JAEA-Research
2024-008
DOI:10.11484/jaea-research-2024-008

JAEA-Research

SIMMER-III and SIMMER-IV: Computer Codes for LMFR Core Disruptive Accident Analysis

---

Satoru KONDO, Yoshiharu TOBITA, Koji MORITA, Kenji KAMIYAMA
Hidemasa YAMANO, Tohru SUZUKI, Hirotaka TAGAMI, Joji SOGABE
and Shinya ISHIDA

Fast Reactor Cycle System Research and Development Center
Oarai Research and Development Institute

October 2024
Japan Atomic Energy Agency

日本原子力研究開発機構

国立研究開発法人日本原子力研究開発機構　研究開発推進部　科学技術情報課
〒 319-1112　茨城県那珂郡東海村大字村松 4 番地 49
E-mail: ird-support@jaea.go.jp

Library, Institutional Repository and INIS Section,
Research and Development Promotion Department,
Japan Atomic Energy Agency.
4-49 Muramatsu, Tokai-mura, Naka-gun, Ibaraki-ken 319-1112, Japan
E-mail: ird-support@jaea.go.jp

JAEA-Research 2024-008

SIMMER-III and SIMMER-IV: Computer Codes for LMFR Core Disruptive Accident Analysis

Satoru KONDO*1, Yoshiharu TOBITA*2, Koji MORITA*3, Kenji KAMIYAMA+1,
Hidemasa YAMANO, Tohru SUZUKI*4, Hirotaka TAGAMI, Joji SOGABE
and Shinya ISHIDA

Fast Reactor Cycle System Research and Development Center
Oarai Research and Development Institute
Japan Atomic Energy Agency
Oarai-machi, Higashiibaraki-gun, Ibaraki-ken

(Received June 6, 2024)

The SIMMER-III and SIMMER-IV computer codes, developed at the Japan Atomic Energy Agency are the codes with two- and three-dimensional, multi-field, multi-component fluid-dynamics models, coupled with a space- and time-dependent neutron kinetics model. The codes have been used widely for simulating complex phenomena during core-disruptive accidents in liquid-metal fast reactors. Advanced features of the codes in comparison with the former codes include: stable and robust fluid-dynamics algorithm with up to 8 velocity fields, improved representation of structures and multi-phase flow topology, comprehensive treatment of complex heat and mass transfer processes, accurate analytic equations of state, a stable and efficient neutron flux shape solution method and decay heat model.

This report describes the models and methods of SIMMER-III and SIMMER-IV. For those individual models, the details of which have been reported elsewhere, only the outlines of the models are presented. The reports of code verification and validation have been already published.

Keywords: Multi-component Flow, Multi-phase Flow, Fluid Dynamics, Heat and Mass Transfer, SIMMER-III, SIMMER-IV, Quasi-static Method, Diffusion Synthetic Acceleration, Severe Accidents, CDA, LMFR Safety

---

+1 Policy Planning and Administration Department
*1 Fast Reactor Cycle System Research and Development Center until March 31, 2023
*2 Karlsruhe Institute of Technology, Germany
*3 Kyushu University
*4 Tokyo City University

JAEA-Research 2024-008

高速炉炉心崩壊事故解析コード **SIMMER-III** 及び **SIMMER-IV**

日本原子力研究開発機構　大洗研究所
高速炉サイクル研究開発センター

近藤　悟[*1]、飛田　吉春[*2]、守田　幸路[*3]、神山　健司[+1]、山野　秀将、鈴木　徹[*4]、
田上　浩孝、曽我部　丞司、石田　真也

（2024 年 6 月 6 日受理）

日本原子力研究開発機構が開発した SIMMER-III 及び SIMMER-IV は、2 次元／3 次元、多速度場、多成分流体力学モデルを空間・時間依存の核動特性モデルと結合した計算コードであり、液体金属高速炉の炉心崩壊事故の解析に広く利用されている。従来コードに対して次のような高度化したモデルが採用されている。すなわち、安定かつ頑健な流体力学アルゴリズム、最大 8 までの多速度場モデル、構造材及び多相流幾何形状の取扱いの改善、熱及び質量移行過程の包括的取扱い、高精度の状態方程式、高精度かつ高効率の中性子束計算モデル、崩壊熱モデルなどである。

本報告書では SIMMER-III 及び SIMMER-IV のモデル及び解法の詳細を記述する。別途詳細が報告されている個別モデルについてはその概要をまとめる。なお、コードの検証及び妥当性確認についてはすでに報告済みである。

大洗研究所：〒311-1393　茨城県東茨城郡大洗町成田町 4002
+1 経営企画部
*1 高速炉サイクル研究開発センター（2023 年 3 月 31 日迄在籍）
*2 カールスルーエ工科大学
*3 九州大学
*4 東京都市大学

Contents

1. Introduction 1
    1.1. Perspective and Objectives 1
    1.2. Summary of SIMMER-III/SIMMER-IV Models 2
    1.3. Previous Reports and Structure of Present Report 3
2. SIMMER-III/SIMMER-IV Code Framework 5
    2.1. Scope of SIMMER-III/SIMMER-IV Models 5
    2.2. Code Framework and Geometry 7
        2.2.1. Overview 7
        2.2.2. Computational geometry 8
        2.2.3. Fluid-dynamics mesh cell 8
    2.3. SIMMER-III/SIMMER-IV Components 9
    2.4. Verification and Validation 11
3. Fluid Convection Algorithm 18
    3.0. Overview 18
        3.0.1. Background of models and methods 18
        3.0.2. Interaction with other models 19
    3.1. Fluid-Dynamics Method 19
        3.1.1. Fluid-dynamics components 19
        3.1.2. Fundamental differential equations 19
        3.1.3. Overall solution procedure (4 step method) 22
        3.1.4. Fluid convection algorithm 23
        3.1.5. Geometries and coordinates 24
    3.2. End-of-Time-Step Estimate (Step 2) 24
        3.2.1. Mass and energy equation updates 25
        3.2.2. Setup for momentum equation 28
        3.2.3. Velocity solution procedure 31
    3.3. Pressure Iteration (Step 3) 36
        3.3.1. Background 36
        3.3.2. Expressions for residual errors 37
        3.3.3. Expansion of residual errors 38
        3.3.4. Formulation of pressure equation 40
        3.3.5. Solution of changes in cell variables 50
        3.3.6. Convergence criteria for pressure iteration 52
        3.3.7. Matrix solvers for pressure iteration 53
        3.3.8 Optional acceleration technique for pressure iteration 53
    3.4. End-of-Time-Step Values (Step 4) 54
        3.4.1. Final mass update 54
        3.4.2. Intermediate updates of internal energies 54

3.4.3. Interfacial area convection 56
3.4.4. Mass and energy outflows 57
3.4.5. Setup for momentum equation 58
3.4.6. End-of-time-step velocities 59
3.4.7. Interfacial drag heating 61
3.4.8. Final operation 63
3.5. Momentum Diffusion Model (Viscous Drag Term) 64
3.5.1. Background 64
3.5.2. Formulation of viscous drag term 65
3.5.3. Implementation in SIMMER-III/SIMMER-IV 68
3.5.4. On turbulence modeling 68
3.6. Some Observations on Convection Algorithm 69
3.6.1. General validity of fluid convection algorithm 69
3.6.2. Source-term decoupling problem 69
3.6.3. Drawbacks in cylindrical geometry 70
3.6.4. Mass and energy conservation 70
4. Intra-Cell Transfer Models 72
4.0. Overview 72
4.0.1. Background of models and methods 72
4.0.2. Interaction with other models 72
4.1. Models of Intra-Cell Transfers 73
4.1.1. Mass and energy equations 73
4.1.2. Modes of mass transfers 74
4.1.3. Relationships among Step 1 operations 75
4.1.4. Computational flow of Step 1 76
4.2. Multi-Phase Flow Topology and Interfacial Areas Mode 77
4.2.1. Flow regimes and topology model 77
4.2.2. Interfacial area convection model 78
4.2.3. Determination of binary contact areas 79
4.3. Momentum Exchange Functions Model 80
4.3.1. Fluid-fluid momentum exchange function model 80
4.3.2. Fluid-structure momentum exchange function model 81
4.3.3. Averaging and interpolation of momentum exchange functions 82
4.3.4. Effect of particles on flow resistance 82
4.3.5. Additional model improvement 83
4.3.6. Evaluation of virtual mass term 83
4.4. Heat-Transfer Coefficients Model 83
4.4.1. Heat-transfer correlations 84
4.4.2. Interpolation between flow regimes 85
4.5. Heat and Mass Transfer Model 86
4.5.1. Basic concept of non-equilibrium mass transfer model 86

4.5.2. Effects of noncondensable gases and multicomponent mixtures 87
4.5.3. Non-equilibrium melting/freezing transfers 88
4.5.4. Non-equilibrium vaporization/condensation transfers 89
4.5.5. Equilibrium melting/freezing transfers 89
4.5.6. Recent model changes 90
4.6. Structure Configuration and Related Heat and Mass Transfer Models 90
4.7. Improved Freezing Model 91
4.7.1. Background 91
4.7.2. Fundamental physics of solidification 92
4.7.3. Improved freezing model 92
4.7.4. Non-equilibrium melting/freezing with improved freezing model 94
4.7.5. Correlation for supercooling temperature 95
4.8. Improved Crust Formation Model 96
4.8.1. Background and assumptions 96
4.8.2. Calculative flow and procedure 97
4.8.3. Mass and energy equations of crust fuel 97
4.8.4. Update of crust and can wall mass and energy 98
4.8.5. Geometrical consideration of crust stability 99
4.8.6. Can wall heat transfer calculations 99
4.9. Inter-cell Heat Transfer Model 100
4.9.1. Inter-cell heat transfer model 100
4.9.2. Axial heat transfer in structure 101
4.9.3. Axial heat transfer between fluids and structures 101
4.10. Miscellaneous Intra-Cell Transfer Updates 102
4.10.1. Nuclear heating updates 102
4.10.2. Fuel related model improvement 103
4.10.3. Updates of velocities and interfacial areas 103
4.10.4. Special treatment of single-phase cells 104
5. Fuel-Pin and Structure Model 116
5.0. Overview 116
5.0.1. Background of models and methods 116
5.0.2. Interaction with other models 116
5.1. Outline of Fuel Pin Model 117
5.1.1. Fuel-pin structure configuration 117
5.1.2. Fuel-pin heat transfer 117
5.2. Outline of Can Wall Model 118
5.2.1. Can-wall structure configuration 118
5.2.2. Can-wall heat transfer 120
5.2.3. Structure volume fraction and hydraulic diameter 120
5.2.4. Hydraulic diameter to simulate transient heat transfer 121
5.3. Structure Melting, Breakup and Other Modes of Mass Transfer 122

- 5.3.1. Modes of structure-related mass transfer 122
- 5.3.2. Equilibrium melting of solid components 123
- 5.3.3. Equilibrium freezing of liquid components 123
- 5.3.4. Fission-gas release from liquid-field fuel 124
- 5.3.5. Fuel-pin breakup 124
- 5.3.6. Collapse of unsupported pin fuel 124
- 5.3.7. Can-wall and crust fuel breakup 124

5.4. Multi-node Can Wall Heat-Transfer Model 125
- 5.4.1. Background and objectives 125
- 5.4.2. Multi-node representation 125
- 5.4.3. Can wall configuration 126
- 5.4.4. Multi-node can wall heat transfer model 133

5.5. Can Wall and Crust Fuel Breakup Model 134
- 5.5.1. Background 134
- 5.5.2. Breakup of thin can wall in adjacent cell (NC1/NC2) 135
- 5.5.3. Breakup of cladding (NC3) 136
- 5.5.4. Breakup of can wall (NC4/NC5) 137
- 5.5.5. Mechanical failure of can wall (NC6/NC7) 138
- 5.5.6. Mechanical breakup of can wall (NC8/NC9) 138
- 5.5.7. Breakup of suspended can wall (NC8B/NC9B) 139
- 5.5.8. Breakup of crust fuel 139
- 5.5.9. Lateral fluid flow restraint 140

5.6. Detailed Fuel-Pin Model 141
- 5.6.1. Background 141
- 5.6.2. Geometry and assumptions 141
- 5.6.3. Fuel pin structure configuration 142
- 5.6.4. Radial heat transfer model and solution method 143
- 5.6.5. Time step control 144
- 5.6.6. Molten cavity model 145
- 5.6.7. Options for input specifications 146

5.7. Other Model Development 146
- 5.7.1. Fuel swelling model 146
- 5.7.2. Improvement of fission-gas release model 147

6. Equations of State and Thermophysical Properties Models 157

6.0. Overview 157
- 6.0.1. Background of models and methods 157
- 6.0.2. Interaction with other models 158

6.1. Analytic Equation-of-State Model 158
- 6.1.1. Outline of the EOS model 158
- 6.1.2. Fitting-free EOS model 160
- 6.1.3. Treatment of EOS sub-materials and EOS regions 160

6.2. Analytic Thermophysical Properties Model 161
    6.2.1. Outline of the TPP model 161
7. Neutronics Model 169
    7.0. Overview 169
        7.0.1. Background of models and methods 169
        7.0.2. Interaction with other models 170
    7.1. Fundamental Models 170
        7.1.1. Time-dependent neutron transport equation 170
        7.1.2. Cross-section model 172
    7.2. Cross-Section Methods 173
        7.2.1. Introduction to the cross-section model 173
        7.2.2 Neutronics mesh structure and coupling with fluid dynamics 173
        7.2.3. Calculation of macroscopic cross sections 174
        7.2.4. Determination of shielding factors 176
        7.2.5. Use of neutronics preprocessor 177
    7.3. Quasistatic Method Equations 177
        7.3.1. Flux factorization 177
        7.3.2. Procedure for fluid-dynamics/neutronics. coupling 178
        7.3.3. Flux-shape equations 179
        7.3.4. Delayed-neutron precursor equations 180
        7.3.5. Amplitude equation 181
        7.3.6. Flux-shape/amplitude coupling terms 181
        7.3.7. Fluid-dynamics/neutronics coupling terms 183
    7.4. Flux Shape Solution Method 184
        7.4.1. Iterative solution procedure for flux shape 184
        7.4.2. Negative flux treatment 185
        7.4.3. Adjoint equation solution method 186
    7.5. Quasistatic Calculative Procedure 186
        7.5.1. Overall calculative flow 186
        7.5.2. Time-step controls 187
        7.5.3. Initialization 188
        7.5.4. Transient-state initialization 189
        7.5.5. Reactivity evaluation steps 189
        7.5.6. Flux-shape evaluation steps 190
    7.6. Decay Heat Model 191
        7.6.1. Model and method 191
        7.6.2. Input and initialization of decay heat model 193
        7.6.3. Update of power shape with decay heat power 193
    7.7. Recent Model Addition 194
        7.7.1. Isotope-wise delayed neutron yields 194
        7.7.2. Flexible fuel isotope composition (Pu vector) 195

7.8. Special Models for External Control ... 197
    7.8.1. External neutron source ... 197
    7.8.2. Specified external reactivity ... 197
    7.8.3. Specified power history ... 198
    7.8.4. Restart and neutronics re-initialization ... 198
8. Initial and Boundary Conditions, and Time Step Control ... 202
8.1. Initial Conditions and Initialization ... 202
    8.1.1. Fluid-dynamics cell initialization ... 202
    8.1.2. Neutronics initialization ... 203
8.2. Boundary Conditions ... 204
    8.2.1. Fluid-dynamics boundary conditions ... 204
    8.2.2. Virtual wall model ... 204
    8.2.3. Internal boundary conditions ... 205
    8.2.4. Simple primary loop and pump model ... 205
    8.2.5. Neutronics boundary conditions ... 205
8.3. Time Step Control ... 206
    8.3.1. Fluid-dynamics time step control ... 206
    8.3.2. Fuel-pin heat-transfer time step control ... 208
    8.3.3. Neutronics shape time-step control ... 209
    8.3.4. Neutronics reactivity time-step control ... 211
9. Special Models ... 215
9.1. Inter-Subassembly Gap Model ... 215
    9.1.1. Background ... 215
    9.1.2. Model outline ... 215
9.2. SIMMER-LT ... 216
    9.2.1. Background ... 216
    9.2.2. Performance measurement of SIMMER-III ... 217
    9.2.3. Parallelization ... 218
    9.2.4. Time-step control ... 218
    9.2.5. Simplification of the heat- and mass-transfer model ... 218
9.3. SIMMER-SW ... 219
    9.3.1. Background ... 219
    9.3.2. Model outline ... 220
10. Concluding Remarks ... 221
Acknowledgments ... 222
References ... 223
Nomenclature ... 227

目　次

1. 序論……1
   - 1.1. 背景と目的……1
   - 1.2. SIMMER-III/SIMMER-IV モデルの要約……2
   - 1.3. 既刊報告書及び本報告書の構成……3
2. SIMMER-III/SIMMER-IV コードの枠組み……5
   - 2.1. SIMMER-III/SIMMER-IV のモデル化の範囲……5
   - 2.2. コードの枠組みと幾何形状……7
     - 2.2.1. 概要……7
     - 2.2.2. 計算体系……8
     - 2.2.3. 流体力学計算メッシュ……8
   - 2.3. SIMMER-III/SIMMER-IV の成分……9
   - 2.4. 検証及び妥当性確認……11
3. 流体対流アルゴリズム……18
   - 3.0. 概要……18
     - 3.0.1. モデル及び手法の背景……18
     - 3.0.2. 他のモデルとの関係……19
   - 3.1. 流体力学の解法……19
     - 3.1.1. 流体力学成分……19
     - 3.1.2. 基礎微分方程式……19
     - 3.1.3. 解法の全体的流れ（4 ステップ法）……22
     - 3.1.4. 流体対流計算アルゴリズム……23
     - 3.1.5. 計算体系及び座標……24
   - 3.2. タイムステップ末値の予測（ステップ 2）……24
     - 3.2.1. 質量及びエネルギーの更新……25
     - 3.2.2. 運動量式の設定……28
     - 3.2.3. 速度の解法手順……31
   - 3.3. 圧力反復（ステップ 3）……36
     - 3.3.1. 背景……36
     - 3.3.2. 残差の定式化……37
     - 3.3.3. 残差の展開……38
     - 3.3.4. 圧力方程式の定式化……40
     - 3.3.5. セル変数の変化量の計算……50
     - 3.3.6. 圧力反復の収束クライテリア……52
     - 3.3.7. 圧力反復の行列解法……53
     - 3.3.8. 圧力反復の加速オプション……53
   - 3.4. タイムステップ末値の評価（ステップ 4）……54
     - 3.4.1. 最終的な質量の更新……54

3.4.2. 内部エネルギーの中間更新 54
3.4.3. 境界面積の対流 56
3.4.4. 質量及びエネルギーの体系外流出 57
3.4.5. 運動量式の設定 58
3.4.6. タイムステップ末の速度 59
3.4.7. 界面間のドラグ発熱 61
3.4.8. 最終更新 63
3.5. 運動量拡散モデル（粘性ドラグ項） 64
3.5.1. 背景 64
3.5.2. 粘性ドラグ項の定式化 65
3.5.3. SIMMER-III/SIMMER-IV への組込み 68
3.5.4. 乱流モデルについて 68
3.6. 対流アルゴリズムに関する考察 69
3.6.1. 流体力学モデルの一般的妥当性 69
3.6.2. 熱及び質量ソース項の分離に係る問題 69
3.6.3. 円筒座標系に係る問題 70
3.6.4. 質量及びエネルギー保存について 70
4. セル内熱及び質量移行モデル. 72
4.0. 概要 72
4.0.1. モデル及び手法の背景 72
4.0.2. 他のモデルとの関係 72
4.1. セル内移行のモデル 73
4.1.1. 質量及びエネルギーの保存式 73
4.1.2. 質量移行モード 74
4.1.3. セル内移行モデル間の関係 75
4.1.4. セル内移行モデルの計算手順 76
4.2. 多相流幾何形状及び境界面積モデル 77
4.2.1. 流動様式及び幾何形状モデル 77
4.2.2. 境界面積対流モデル 78
4.2.3. エネルギー成分間接触面積の計算 79
4.3. 運動量交換関数モデル 80
4.3.1. 流体－流体間運動量交換関数 80
4.3.2. 流体－構造材間運動量交換関数 81
4.3.3. 運動量交換関数の平均化及び内挿 82
4.3.4. 固体粒子の流動抵抗への影響 82
4.3.5. 追加のモデル改良 83
4.3.6. 仮想質量項の計算 83
4.4. 熱伝達係数モデル 83
4.4.1. 熱伝達係数相関式 84
4.4.2. 流動様式間の内挿 85

4.5. 熱及び質量移行モデル 86
4.5.1. 非平衡質量移行モデルの基本概念 86
4.5.2. 非凝縮性ガス及び多成分混合物の影響 87
4.5.3. 非平衡溶融／固化モデル 88
4.5.4. 非平衡蒸発／凝縮モデル 89
4.5.5. 平衡溶融／固化モデル 89
4.5.6. 最近のモデル改良 90
4.6. 構造材配置及び関連する熱及び質量移行モデル 90
4.7. 改良固化モデル 91
4.7.1. 背景 91
4.7.2. 凝固に関する基礎物理 92
4.7.3. 改良固化モデル 92
4.7.4. 改良固化モデルによる非平衡溶融／固化 94
4.7.5. 過冷却温度に関する相関式 95
4.8. 改良クラスト形成モデル 96
4.8.1. 背景 96
4.8.2. 計算手順 97
4.8.3. クラスト燃料に関する質量及びエネルギー式 97
4.8.4. クラスト燃料及び管壁の質量及びエネルギーの更新 98
4.8.5. クラスト安定性に関する幾何形状の考慮 99
4.8.6. 管壁熱移行の計算 99
4.9. セル間熱移行モデル 100
4.9.1. セル間熱移行モデル 100
4.9.2. 構造材成分の軸方向セル間熱移行 101
4.9.3. 流体・構造材間の軸方向セル間熱移行 101
4.10. セル内移行に伴う他の更新 102
4.10.1. 核加熱によるエネルギー更新 102
4.10.2. 燃料関連のモデル改良 103
4.10.3. 速度及び対流境界面積の更新 103
4.10.4. 単相セルの取扱い 104
5. 燃料ピン及び構造材モデル 116
5.0. 概要 116
5.0.1. モデル及び手法の背景 116
5.0.2. 他のモデルとの関係 116
5.1. 燃料ピンモデルの概要 117
5.1.1. 燃料ピンの構造配置 117
5.1.2. 燃料ピン熱移行モデル 117
5.2. 管壁モデルの概要 118
5.2.1. 管壁の構造配置 118
5.2.2. 管壁熱移行モデル 120

5.2.3. 構造材体積割合及び水力直径 120
5.2.4. 過渡伝熱の模擬 121
5.3. 構造材に関わる溶融、破損、その他の質量移行モード 122
5.3.1. 構造材に関わる質量移行モード 122
5.3.2. 固体成分の平衡溶融 123
5.3.3. 液体成分の平衡固化 123
5.3.4. 液体場燃料からの FP ガス放出 124
5.3.5. 燃料ピンの崩壊 124
5.3.6. 支持を失ったピン燃料の崩落 124
5.3.7. 管壁及びクラスト燃料の崩壊 124
5.4. 多ノード管壁熱移行モデル 125
5.4.1. 背景及び目的 125
5.4.2. 多ノード分割 125
5.4.3. 管壁の形状 126
5.4.4. 多ノード管壁熱移行モデル 133
5.5. 管壁及びクラスト燃料の崩壊及び破損モデル 134
5.5.1. 背景 134
5.5.2. 隣接セルの薄い管壁の崩壊 135
5.5.3. 被覆管の崩壊 136
5.5.4. 管壁の崩壊 137
5.5.5. 管壁の機械的破損 138
5.5.6. 管壁の機械的崩壊 138
5.5.7. 支持を失った管壁の崩壊 139
5.5.8. クラスト燃料の崩壊 139
5.5.9. 横方向の流動抑制 140
5.6. 詳細燃料ピンモデルの状況 141
5.6.1. 背景 141
5.6.2. 幾何形状及び仮定 141
5.6.3. 燃料ピンの構造配置 142
5.6.4. 径方向熱移行モデル及び解法 143
5.6.5. タイムステップ制御 144
5.6.6. 溶融キャビティモデル 145
5.6.7. 入力設定 146
5.7. その他のモデル開発 146
5.7.1. 燃料スエリングモデル 146
5.7.2. FP ガス放出モデルの改良 147
6. 状態方程式及び熱物性モデル 157
6.0. 概要 157
6.0.1. モデル及び手法の背景 157
6.0.2. 他のモデルとの関係 158

6.1. 解析的状態方程式モデル 158
6.1.1. 状態方程式モデルの概要 158
6.1.2. フィッティング不要モデル 160
6.1.3. 異なる物質の取扱いと EOS 領域 160
6.2. 解析的熱物性モデル 161
6.2.1. 熱物性モデル概要 161
7. 核計算モデル 169
7.0. 概要 169
7.0.1. モデル及び手法の背景 169
7.0.2. 他のモデルとの関係 170
7.1. 基礎モデル 170
7.1.1. 時間依存の中性子輸送方程式 170
7.1.2. 核断面積モデル 172
7.2. 核断面積の計算手法 173
7.2.1. 核断面積モデル 173
7.2.2. 核計算の計算メッシュ及び流体力学との対応 173
7.2.3. マクロ断面積の計算 174
7.2.4. 自己遮蔽因子の計算 176
7.2.5. 核計算前処理プログラムについて 177
7.3. 準静近似のモデル 177
7.3.1. 中性子束の因数分解 177
7.3.2. 流体力学－核計算結合手順 178
7.3.3. 中性子束形状関数方程式 179
7.3.4. 遅発中性子先行核の方程式 180
7.3.5. 振幅関数方程式 181
7.3.6. 形状関数・振幅関数の結合項 181
7.3.7. 流体力学・核計算結合項 183
7.4. 中性子束の解法 184
7.4.1. 中性子束の反復計算手順 184
7.4.2. 負の中性子束の取扱い 185
7.4.3. 随伴中性子束の解法 186
7.5. 準静近似の計算手順 186
7.5.1. 計算の流れ 186
7.5.2. タイムステップ制御 187
7.5.3. 初期化 188
7.5.4. 過渡状態初期化 189
7.5.5. 反応度計算ステップ 189
7.5.6. 中性子束形状計算ステップ 190
7.6. 崩壊熱モデル 191
7.6.1. モデル及び手法 191

7.6.2. 崩壊熱に係る入力及び初期化 193
7.6.3. 崩壊熱を含む出力分布の更新 193
7.7. 最近のモデル追加 194
7.7.1. 核種毎の遅発中性子生成量 194
7.7.2. 燃料同位体組成の多様化（Pu ベクター） 195
7.8. 外部からの制御に関するモデル 197
7.8.1. 外部中性子源 197
7.8.2. 反応度の外部入力 197
7.8.3. 出力履歴の外部入力 198
7.8.4. リスタート及び核計算の再初期化 198
8. 初期条件、境界条件及びタイムステップ制御 202
8.1. 初期条件及び初期化 202
8.1.1. 流体力学の初期化 202
8.1.2. 核計算の初期化 203
8.2. 境界条件 204
8.2.1. 流体力学の境界条件 204
8.2.1. 仮想壁モデル 204
8.2.3. 計算体系内境界条件 205
8.2.4. 外部ループ及びポンプの簡易モデル 205
8.2.5. 核計算の境界条件 205
8.3. タイムステップ制御 206
8.3.1. 流体力学のタイムステップ制御 206
8.3.2. 燃料ピン伝熱計算のタイムステップ制御 208
8.3.3. 核計算中性子束計算のタイムステップ制御 209
8.3.4. 核計算反応度計算のタイムステップ制御 211
9. 特殊なモデル 215
9.1. 集合体間ギャップモデル 215
9.1.1. 背景 215
9.1.2. モデル概要 215
9.2. SIMMER-LT 216
9.2.1. 背景 216
9.2.1. SIMMER-III の性能測定 217
9.2.3. 並列化 218
9.2.4. タイムステップ制御の改良 218
9.2.5. 熱及び質量移行の簡易モデル 218
9.3. SIMMER-SW 219
9.3.1. 背景 219
9.3.2. モデル概要 220
10. 結論 221
謝辞 222

参考文献 223
記号説明 227

Former Contributors

[Major contributors formerly involved in the SIMMER-III/SIMMER-IV development]

N. Shirakawa: Fluid-dynamics convection algorithm
(on loan from Toshiba Corp.)

S. Fujita: Neutronics and cross sections
(present address: Nuclear Regulation Agency)

E. Kiefhaber and G. Buckel: Coupling of DANTSYS neutronics
(Karlsruhe Institute of Technology)

D. J. Brear: Heat-transfer coefficients, fuel freezing, film boiling
(International Fellows, Power Reactor and Nuclear Fuel Development Corporation)

E.A. Fischer: Equations of state and thermophysical properties
(International Fellows, Power Reactor and Nuclear Fuel Development Corporation)

W. R. Bohl and F. R. Parker: Initial fluid-dynamics modeling and code design
(Los Alamos National Laboratory)

1. Introduction

1.1. Perspective and Objectives

The consequences of postulated core disruptive accidents (CDAs) have been one of major concerns in the safety of liquid-metal fast reactors (LMFRs). Although the extensive safety design effort for accident prevention has made the occurrence of such an event extremely unlikely, the importance of CDAs is emphasized from the viewpoint of safety design and evaluation to appropriately mitigate and accommodate their consequences and thereby to minimize the risk to the public. A mechanistic analysis of CDA sequences requires a comprehensive simulation of transient heat-up, melting, interactions and motion of reactor core materials, and their influence on the reactor neutronic behavior. The SIMMER-II code1), 2) developed at the Los Alamos National Laboratory (LANL) was the first of a kind that calculates a coupled behavior of multi-field, multi-component, fluid dynamics and space-dependent neutron kinetics. The code has played a pioneering role in mechanistically analyzing the CDA sequences and phenomena. Successful and useful applications of the code, on the other hand, have identified several limitations in the major areas of fluid dynamics, particularly in: the number of velocity fields, mass, momentum and energy constitutive relationships; the numerical solution methods; the equation-of-state (EOS) formalism; etc. To improve some of these limitations, an international research program was performed to develop a prototype three-field fluid-dynamics code, Advanced Fluid Dynamics Model (AFDM)3), with advanced models and solution methods. Although some of the AFDM technology are well advanced, but the code is of limited scope and cannot be applied to reactor calculations.

Based on these experiences, the development of a next-generation code, SIMMER-III, was initiated at the Japan Nuclear Cycle Development Institute (JNC), the present Japan Atomic Energy Agency (JAEA), initially in collaboration with LANL under the agreement with the United States Nuclear Regulatory Commission. After the LANL effort, led by the SIMMER-II and AFDM developers W. R. Bohl and F. R. Parker, was terminated with completion of an adiabatic version (three-field fluid convection with no heat and mass transfer nor neutronics models), the model elements necessary for SIMMER-III have been developed at JAEA and incorporated into Version 1. SIMMER-III was then coupled with the SIMMER-II based neutronics module for Version 24), which was ready for reactor accident calculations. Since the completion of Version 1 of SIMMER-III, the code development and assessment program has been joined by AEA Technology, United Kingdom (for two years only), Forschungszentrum Karlsruhe (FZK)[1], Germany, and Commissariat à l'Energie Atomique (CEA)[2], France. The CEA partner also included Institute of Protection and Nuclear Safety (IPSN)[3]. The two-dimensional SIMMER-III fluid dynamics was extended to three dimensions in SIMMER-IV and was interfaced with the two-dimensional neutronics in Version 15). Retaining the same physical models and solution methods except for the dimensions of fluid motion and the treatment of structure walls, SIMMER-III and SIMMER-IV have been further developed and upgraded

---

[1] the present Karlsruhe Institute of Technology (KIT), Germany
[2] the present Commissariat à l'Énergie Atomique et aux énergies alternatives (CEA), France
[3] the present Institut de Radioprotection et de Sûreté Nucléaire (IRSN), France

to Version 3$^{6)}$ and Version 2$^{7)}$, respectively. SIMMER-IV Version 2 has the three-dimensional neutronics model contributed by the KIT.

The purpose of SIMMER-III/SIMMER-IV is to alleviate some of the above limitations in the previous codes and thereby to provide the next-generation tool for more reliable analysis of CDAs. The SIMMER-III/SIMMER-IV codes are two-/three-dimensional, multi-velocity-field, multiphase, multicomponent, Eulerian, fluid-dynamics codes coupled with a two-/three-dimensional space- and energy-dependent neutron kinetics model. A code development task could be easy to get into the situation that fundamental issues are studied endlessly for a long time. To avoid such situations, a modeling scope was carefully selected to make the code be the state of the art but still based on the achievable technologies. The codes are intended to be a generalized code that is useful for analyzing relatively short-time-scale multiphase flow problems with or without neutronics. Although the original objective is primarily to resolve some of the key LMFR CDA issues, their flexible framework enables us to apply the codes to various areas of interest including: accident analyses of any types of future or advanced fast reactors, severe-accident thermohydraulic problems in current- and future-generation light water reactors, and general types of multiphase flow problems.

It is noted again SIMMER-III and SIMMER-IV completely retain the same physical models except for the dimensions and the treatment of can walls at cell boundaries. Therefore, in many parts of this report, the code name is referred to only as SIMMER-III, unless noted differently.

1.2. Summary of SIMMER-III/SIMMER-IV Models

The features of SIMMER-III/SIMMER-IV models are summarized in this section. A more detailed description of the code framework and modeling scope is presented in **Chapter 2**, emphasizing salient and improved features over the previous SIMMER-II.

The multiphase fluid-dynamics approach is based on the four-step algorithm developed and successfully implemented in AFDM$^{8)}$, in which complex intra-cell heat and mass transfer calculations are separated from the inter-cell fluid convection. Intra-cell heat and mass transfer updates are modularized such that future improvement can be implemented easily. A multi-velocity-field convection algorithm is based on Eulerian, semi-implicit, staggered-mesh treatment. The number of velocity fields is increased up to eight (7 liquids and 1 vapor). A higher-order spatial differencing scheme is employed for improved spatial resolution by reducing numerical diffusion, while the first-order donor cell differencing is available as well. The solution procedure is similar to AFDM, but is further advanced with an improved pressure iteration scheme. For the equations of state (EOS) and thermophysical properties, efficient and accurate analytic equations, typically simple temperature polynomials, are used and they are fit over a wide temperature range up to the critical point based on the available experimental data base. A non-ideal gas EOS is used for vapor components, especially for better modeling sodium vapor at high temperature.

The model for multi-phase flow topology covers both the pool and channel flow regimes with smooth transition between flow regimes for the entire void fraction and flow conditions. Convection of interfacial areas is modeled by extending AFDM approach by defining as many as 11 convectible interfacial areas with source terms that model the phenomena such as generation, breakup and coalescence of fluid particles. Binary contact areas are defined for each pair of components among fluid energy components and structure surfaces. The heat-transfer coefficients are defined for all the binary contacts using available engineering correlations. The coefficients are interpolated for the interpolated flow regimes. Using the binary contact area and heat-transfer coefficient, the heat and mass transfer is calculated from the energy balance at the contact interface, which determines the rates of non-equilibrium melting/freezing and vaporization/condensation, or heat transfer. An accurate and stable solution method is employed in calculating non-linear and non-equilibrium vaporization/condensation processes.

For the structure model, a fuel pin is represented by two-node pin fuel and cladding in the standard simple model. A model for detailed fuel-pin representation with radial temperature distribution is also developed as an option, but the model still requires further elaboration. A can wall, with two-node representation, is placed on each of lateral mesh-cell boundaries and fluid is not allowed to flow across the cell boundary when the wall is intact. The melting and breakup of the structure components are modeled mostly by a thermal condition. The lateral inter-cell heat transfer is treated when a can wall becomes thin.

The neutron kinetics is modeled by an improved quasi-static method, in which a time-dependent neutron transport equation is factorized into: a shape function that represents the neutron flux distribution but changes only slowly with time, and an amplitude function that accounts for time evolution of the reactivity and reactor power. The neutron cross sections are updated based on the distributions of material densities and energies calculated in the fluid-dynamics and structure models. A basic approach of the neutronics model is the same as the former SIMMER-II code, except that the former S_n transport solution method is replaced with a more advanced and efficient model using the diffusion-synthesis acceleration technique9) and the neutron diffusion and point-kinetics options are no longer included. From the power distribution determined in the neutronics calculation, the energies of the fluid-dynamics components are updated for internal nuclear heating.

A verification and validation program for SIMMER-III has been conducted since the beginning of the code development. The program, called the “code assessment program”, was conducted in two phases. The Phase 1 assessment is intended to verify individual fluid-dynamics models of the code, while Phase 2 is for comprehensive validation of integral and inter-related accident phenomena. In this stepwise approach, SIMMER-III coding was largely debugged and verified in Phase 1 stage. The program was conducted in collaboration with KIT, Germany and CEA, France and the results and major achievement are jointly synthesized and documented in detail10), 11).

1.3. Previous Reports and Structure of Present Report

The development of SIMMER-III and SIMMER-IV has been a long-lasting effort starting from at around 1990. A full code documentation was repeatedly proposed but has never been initiated due mainly to frequent personnel changes in JAEA. Some of the individual models are written as JNC reports. For other models, some drafts of the reports or informal technical memoranda were written either in English or Japanese. The documentations of the recent model addition and changes have not always been complete. Thus, the purpose of this reports is to provide a complete documentation of the SIMMER-III/SIMMER-IV models and methods.

The reports of individual models already published or under preparation are listed below (available from the web site of JAEA[4]). The model descriptions available in these reports are not reproduced in the present report; however, the model summary and the changes after the issuance of the original reports are included. The use of the codes with brief program and input/output descriptions are available as well 6), 7).

- Analytic Equation-of-State Model: JNC TN9400 2000-005 (1999)12)
- Analytic Thermophysical Property Model: JNC TN9400 2000-004 (1999)13)
- Heat- and Mass-Transfer Model JNC TN9400 2003-047 (2003)14)
- Structure Model: JNC TN9400 2004-043 (2004)15)
- Heat Transfer Coefficients Model: JAEA-Research 2024-009 (2024)16)
- Multi-phase Flow Topology and Interfacial Areas Model: JAEA-Research 2024-010 (2024)17)
- Momentum Exchange Functions Model: JAEA-Research 2024-011 (2024)18)

In the rest of this report, the overall code framework and geometrical model of SIMMER-III and SIMMER-IV are introduced in **Chapter 2**. The area of major improvement over the previous SIMMER-II is also reviewed. In **Chapter 3**, the solution procedure of fluid-dynamics model is presented, followed by detailed description of fluid convection algorithm. The intra-cell heat and mass transfer processes is covered in **Chapter 4**. **Chapter 5** describes the fuel-pin and structure model. The equations-of-state and thermophysical properties models are given in **Chapter 6**, and the neutronics model and method in **Chapter 7**, the initial and boundary conditions in **Chapter 8**, the special models of a limited scope in **Chapter 9**, and the concluding remarks in **Chapter 10**.

---

[4] https://jopss.jaea.go.jp/

2. SIMMER-III/SIMMER-IV Code Framework

2.1. Scope of SIMMER-III/SIMMER-IV Models

At the beginning of the SIMMER-III development project, the guidelines were set up such that a new project should be well-focused. First, the most important purpose of SIMMER-III is to provide a new LMFR safety analysis code that can replace the former SIMMER-II, which had been used widely through the 1980s. Hence the new code is intended to resolve major problem areas in SIMMER-II. At the same time, SIMMER-III is oriented towards, not a basic research tool, but a safety analysis tool sufficiently reliable and practical for full reactor materials and geometries. Second, the first full-scope code version should utilize achievable technologies then. It was felt inappropriate to initiate long-term research activities because they are easy to hit dead rocks, even though it was challenged to make a new code as advanced as practicably achievable. Third, experience in the AFDM project is reflected as far as reasonable. The lessons learned, positive or negative, from the project were valuable in designing SIMMER-III. Forth, the new code must be designed to be versatile and flexible. Although SIMMER-III is primarily applied to LMFR safety analyses, its application areas should not be restricted. This aspect is especially important since the code must be extensively tested against various experiments, many of which use non-reactor materials and geometries. Fifth, as a coupled code system the accuracy or modeling details of individual models are suitably balanced. Also computing cost as a system must be compatible with the computer technology available then. Finally, the code assessment (verification and validation) program is performed in parallel with code development.

Major model improvement and extension, such as three-dimension SIMMER-IV and more than 3 velocity fields, have been made after the first fluid-dynamics version of SIMMER-III with the initially planned scope was completed. The resultant scope of SIMMER-III/SIMMER-IV and salient features are summarized as follows:

(1) Dimensionality. Two dimensions (SIMMER-III) or three dimensions (SIMMER-IV).

(2) Full LMFR core materials. Five main materials are: fuel, steel, sodium, control and fission gas, in possible solid, liquid and vapor states. Different sets of other materials can be defined as sub-materials.

(3) Multiple velocity fields. The three-velocity-field approach of AFDM was extended to up to eight fields (7 liquids and 1 vapor), allowing different components to move at different velocities.

(4) Fluid-dynamics algorithm taken from AFDM. This includes Eulerian staggered mesh, semi-implicit scheme with higher-order spatial differencing, time-factorization technique (a four-step algorithm) for temporal differencing, virtual mass treatment, etc.

(5) Momentum diffusion terms. A viscous drag term is included in the momentum equation to treat momentum diffusion along a velocity gradient.

(6) Pool and channel flow regimes, by extension of the interfacial-area convection model with time-dependent source terms. Flow properties of ill-defined flow topologies are determined by interpolation between well-defined topologies.

(7) Heat transfer coefficients based on quasi-steady-state heat transfer correlations. Fluid particles are treated as rigid spheres but the effects of internal circulation and oscillation are considered. Film boiling heat transfer on hot droplets or particles is modeled.

(8) All the dominant mass transfer paths, due to melting/freezing, vaporization/condensation, fission-gas release and structure breakup are modeled.

(9) An improved fuel freezing model, taking into account the imperfect contact between molten fluid with structure surface and the resulting supercooling of fluid upon freezing inception.

(10) Improved analytic equations of state (EOS), from solid to super-critical point, that are sufficiently accurate and thermodynamically consistent, with modeling a non-ideal gas law for vapors and liquid compressibility.

(11) Thermophysical properties (TPP) defined by analytic functions such as simple temperature dependent functions.

(12) EOS region concept. Different EOS and TPP data can be specified for the same material in different regions.

(13) Two-node representation of the structures that interact with fluid. The can walls to simulate the fuel subassembly duct walls are distinguished between left and right (SIMMER-III) plus front and back (SIMMER-IV).

(14) Detailed treatment of fuel pellet interior for future possible extension of a detailed pin model. A multi-node radial heat-transfer model has been developed, and other advanced features are further to be developed.

(15) Inter-cell heat transfer between the same liquid components, axial heat conduction in the structure components, and axial fluid-to-structure heat transfer.

(16) Flexible and versatile boundary conditions for fluid dynamics. Virtual walls can be placed on any mesh-cell boundaries to restrict fluid flows.

(17) Simple pump and loop model to simulate an external loop.

(18) Improved quasi-static method for time-dependent neutron kinetics. The modeling basis is adopted from SIMMER-II, and a simple decay heating model was added.

(19) Cross-section method taken from SIMMER-II but has been enhanced to include neutron up-scattering.

(20) Internal heat sources given by the neutronics model or by user-specified power-vs-time table and power density distribution.

(21) The neutron flux shape solution method is based on a diffusion-synthesis-approximation method taken from the DANTSYS package. External neutron sources can be defined.

(22) Improved user friendliness. This includes: easy input specifications (free-format NAMELIST and built-in default values), improved robustness with automated self-diagnosis and time-step control and trouble-shooting, variety of output files for post-processing, and so on.

(23) Parallelization of parts of fluid dynamics, matrix solvers, and neutronics for efficient parallel computing.

Many of the problem areas and shortcoming of the former SIMMER-II have been improved.in SIMMER-III/SIMMER-IV. These improved features are listed in **Table 2-1**.

2.2. Code Framework and Geometry

2.2.1. Overview

The conceptual overall framework of SIMMER-III/SIMMER-IV is shown in **Fig. 2-1**. The entire code consists of three modules: the fluid-dynamics module, the structure (fuel pin) module, and the neutronics module. The fluid-dynamics portion, which constitutes about two thirds of the code, is interfaced with the structure model through heat and mass transfer at structure surfaces. The neutronics portion provides nuclear heat sources based on the mass and energy distributions calculated by the other code elements. The nuclear heat source, without calculating the neutronics, can be optionally provided by power-versus-time table based on input specification and specific power density distribution.

To increase the computational efficiency, an optimized hierarchy of three-level time-step control is implemented; that is, the fluid-dynamics, reactivity (and fuel pin heat transfer), and flux-shape time steps in the order from the smallest. Each level of time steps is automatically determined in the code depending on changes in dominant physical properties. No non-physical time step control is implemented. In general, one shape step contains several reactivity steps, and one reactivity step contains several fluid-dynamics steps. The power amplitude equation is solved at every reactivity step for smaller internal steps and the calculated amplitudes are parabolically fitted to determine internal heat generation rates projected over the next several fluid-dynamics steps.

The calculation of fuel-pin heat transfer is separated from the fluid dynamics. This idea was taken because the fuel pellet interior responds to change in ex-pin fluid thermal state only slowly. Future elaboration of a detailed pin model would be merited if excessive computing cost is reduced. Because of the tight relationship between fuel temperature and reactivity, these two calculations are operated at the same time steps in a standard option. For a simple pin model (SPIN), however, there is an option to force the fuel-pin heat transfer time steps to fluid-dynamics time steps. This option might be recommended since the computing cost of SPIN is negligibly small.

The overall calculational flow of SIMMER-III/SIMMER-IV is depicted in **Fig. 2-2**. After reading input data, fluid-dynamics mesh cells are initialized. Then the initial neutronics calculation is performed, stationary or transient depending on input specification, to determine the neutron flux shape and power distribution. The overall computational flow is controlled by successive fluid-dynamics cycles. When the reactivity step is reached, the control is transferred to the neutronics model. The fuel-pin heat transfer is calculated first to account for the effect of fuel temperature on reactivity. After a series of reactivity steps, each of which contains a series of fluid-dynamics steps, and when a shape step is reached, a neutron flux shape is re-evaluated.

2.2.2. Computational geometry

For two-dimensional SIMMER-III and three-dimensional SIMMER-IV, either cylindrical or Cartesian coordinate systems can be used. As an example, a basic geometric structure of SIMMER-III for a two-dimensional *r-z* system is shown in **Fig. 2-3**. An *x-z* or one-dimensional system can optionally be used for various fluid-dynamics calculations. The direction of gravity is set, by default, to an axial *z* direction, but an inclined (tilted) geometry is optionally used for an *x-z* system. Fluid-dynamics mesh cells are indexed radially by i and axially by j, with their input maximums *IB* and *JB*, respectively. Each cell is surrounded by four adjacent cells from left, right, bottom and top. To handle problem boundary cells, for example i = 1 or *IB*, in the same manner as the interior cells, fictitious boundary cells are defined outside the real mesh cells. In other words, the fluid dynamics treats (*IB*+2) times (*JB*+2) cells. This is so even in one-dimensional cases. The cell variables are stored in a one-dimensional array with index *IJ*. The four adjacent cells are indexed: *IJ*-1 for left, *IJ*+1 for right, *IJ*-*IB*-2 for below, and *IJ*+*IB*+2 for above.

The SIMMER-IV code is a direct extension of 2D model to either r-θ-z (cylindrical) or *x-y-z* (Cartesian) geometry. The geometric structure of SIMMER-IV for a three-dimensional *x-y-z* system is shown in **Fig. 2-4**. To retain the code structure and programming commonly between the two codes, the same geometry index and velocity variable are used for an axial direction as shown in **Table 2-2**. The geometry index and velocity of the added coordinate (either y or θ) are k and w, respectively. The axial index j and the velocity v are used commonly to the 2D and 3D systems.

The neutronics mesh is a sub-region of the fluid-dynamics computational mesh. In a typical calculation of an LMFR core, the neutronics model only simulates the reactor core where the fuel exists and the calculation is reasonable; however, the fluid-dynamics simulation covers regions outside the core as well. When an accurate calculation is necessary for a neutron flux shape, each fluid-dynamics cell can be further sub-divided into multiple neutronics cells having equal volume. It is noted that the neutronics mesh should cover those regions where the fuel can present during a course of transient calculation. Otherwise, the reactivity worth of the fuel escaping from the computational mesh is simply lost, and this can be non-physical.

2.2.3. Fluid-dynamics mesh cell

In a mesh cell of SIMMER-III/SIMMER-IV fluid dynamics, an amount of each material is specified by its volume fraction and temperature. The specified temperature and pressure are used in the EOS model to calculate the specific volume. Then the macroscopic (smear) density of material M, $\bar{\rho}_M$, is calculated by:

$$\bar{\rho}_M = \alpha_M / \upsilon_M \,, \qquad (2\text{–}1)$$

where α_M and υ_M are the volume fraction and specific volume of material M, respectively.

In each mesh cell, the structure-field volumes are defined for the fuel pin and can wall components, which are stationary and provides walls containing fluid flow. Unlike SIMMER-II, the can walls with refrozen crust fuel attached on them are distinguished between left and right cell boundaries for improved simulation of a core melt-out behavior. In addition, the structure surface nodes are separated from the interior nodes, except for the cladding, to better simulate their thermal response upon contact with the fluid. To model the void spaces inside the fuel pin and the gaps outside the left and right can walls, no-flow volume fractions α_{NF} are specified. These volume fractions sum up to form the total structure volume fraction α_S, the volume that cannot be used by fluid flow.

The remaining volume $(1-\alpha_S)$ is occupied by fluid having three velocity fields. When the cell vapor volume fraction falls below a certain small non-zero value α_0, the mesh cell is regarded as single phase. This treatment is necessary, even in SIMMER-III, for the numerical reason that a vapor state is explicitly treated even in a single-phase liquid cell. The treatment of single-phase cells consistent with two-phase cells eliminates such problems observed in SIMMER-II as vapor mass non-conservation and unphysical pressure behavior upon phase transition. The value of α_0 can be made reasonably small (for example, 10^{-4}), compared with the former codes (typically 0.05), so that any errors associated with this approximation are negligible.

2.3. SIMMER-III/SIMMER-IV Components

The complete lists of the structure-, liquid- and vapor-field components are shown in **Tables 2-3** through **2-5**. In these tables, the lower-case subscripts denote density components while the upper-case subscripts denote energy components commonly used throughout SIMMER-III/SIMMER-IV.

The changes and improvements made from the previous SIMMER-II are as follows:

- The crust fuel, re-frozen fuel from once-molten state, is distinguished between left and right can wall surfaces.
- The can walls are distinguished between left and right cell boundaries.
- The fluid-dynamics structure field only treats the pin fuel surface node. The interior of pin fuel and fission gas in a pin are modeled in a pin model separately outside the fluid dynamics.
- Each can wall has two nodes, surface and interior.
- The control material (typically B_4C) is assumed to stay in solid state as structure pellets or solid control particles.
- Fission gas can be present both in liquid fuel and fuel particles, in consistency with the initiating phase code SAS4A.

Similarly to SIMMER-II, the fuel components are divided into fertile and fissile in their mass (density components) to represent different enrichment zones in the core. However, the two materials are assumed to be mixed intimately, and hence the single temperature is assigned (energy components). Namely, the macroscopic (smeared) densities of a fuel component have the following equivalence:

$\bar{\rho}_{S1} = \bar{\rho}_{s1} + \bar{\rho}_{s2}$, for pin fuel surface node,

$\bar{\rho}_{S3} = \bar{\rho}_{s5} + \bar{\rho}_{s6}$, for left crust fuel,

$\bar{\rho}_{S2} = \bar{\rho}_{s3} + \bar{\rho}_{s4}$, for right crust fuel,

$\bar{\rho}_{S4} = \bar{\rho}_{s7} + \bar{\rho}_{s8}$, for front crust fuel (SIMMER-IV only),

$\bar{\rho}_{S5} = \bar{\rho}_{s9} + \bar{\rho}_{s10}$, for back crust fuel (SIMMER-IV only) ,

$\bar{\rho}_{L1} = \bar{\rho}_{l1} + \bar{\rho}_{l2}$, for liquid fuel,

$\bar{\rho}_{L4} = \bar{\rho}_{l5} + \bar{\rho}_{l6}$, for solid fuel particles,

$\bar{\rho}_{L7} = \bar{\rho}_{l9} + \bar{\rho}_{l10}$, for solid fuel chunks, and

$\bar{\rho}_{G1} = \bar{\rho}_{g1} + \bar{\rho}_{g2}$, for fuel vapor.

A common practice used for dividing fuel isotopes into two in mixed oxide LMFRs is to assign UO_2 to fertile fuel and PuO_2 and other minor actinides to fissile fuel.

Since the component specific volumes are used in the SIMMER-III/SIMMER-IV EOS model, macroscopic densities are converted to volume fractions by:

$$\alpha_m = \bar{\rho}_m v_m \, . \tag{2-2}$$

It is noted that microscopic densities, $\rho_m = 1/v_m$, used in SIMMER-II are not used.

The pin fuel interior component is not included in **Table 2-3**, because it is treated only in the fuel-pin model. The pin interior is modeled by one-point temperature node in a standard simple model (SPIN) or a radial temperature distribution is calculated in an optional detailed model (DPIN). The components defined in the pin models are listed in **Table 2-5**. The intra-granular and inter-granular fission gas components in the former SIMMER-II are not distinguished in SIMMER-III, because such detailed treatment is judged to be beyond the scope of this code. Improvement exists, however, in the modeling of fission gas in the liquid-field fuel components and this eliminates a problem of instantaneous release upon fuel breakup and unphysical pressurization observed in SIMMER-II.

The default assignment of fluid components to the three velocity fields is also shown in **Tables 2-3** and **2-4**. Velocity field 1 contains heavier liquids and field 2 lighter liquids. This default and standard selection is made such that the relative motion of fuel with either steel or coolant can be simulated. The assignment of liquid components can be modified by user-specified input. Velocity field 3 represents the vapor mixture. It is noted that the three-velocity-field model in a SIMMER-III multi-component system differs in concept from a three-fluid model in advanced single-component two-phase flow codes. In the latter case, liquid is distinguished between liquid film on the structure surfaces and droplets in an annular dispersed flow, while in SIMMER-III multiple liquid components are simply grouped into two liquid velocity fields. The vapor species are assumed to be completely mixed and a single energy is assigned to the vapor field. The number of velocity fields are later increased to 8 (7 liquids and 1 vapor), so that all the fluid energy components are allowed to move at different velocities.

In the EOS and TPP models, properties are defined for the five basic materials: fuel, steel, sodium, control and fission gas. There is no distinction in properties between fertile and fissile fuel, namely between UO_2 and PuO_2. However the current EOS model has a concept of EOS regions, and different properties can be assigned for a same material in different regions.

Finally, the internal heat sources due to nuclear heating are defined for the five heat source materials: fertile fuel, fissile fuel, steal, sodium and control. No heat source modeled for fission gas is considered to be a reasonable assumption.

2.4. Verification and Validation

A verification and validation (V&V) program for SIMMER-III has been conducted since the beginning of the code development. The program, called the "code assessment program", was conducted in two phases. The Phase 1 assessment is intended to verify individual fluid-dynamics models of the code, while Phase 2 is for comprehensive validation of integral and inter-related accident phenomena. In this stepwise approach, SIMMER-III coding was largely debugged and verified in Phase 1 stage. The program was conducted in collaboration with the KIT, Germany and CEA, France and the results and major achievement are synthesized and documented in detail10),11). The most of the assessment results of SIMMER-III hold in SIMMER-IV as well, since the physical models verified and validated are common to both the codes except for difference in dimensions.

The assessment program has confirmed that the performance of SIMMER-III and SIMMER-IV is mostly satisfactory. The codes therefore are reliably applicable to a variety of integrated problems in reactor safety analyses. However, it should be noted, at the same time, that the assessment study has identified many problem areas and model deficiencies that require code improvement. This is especially true for the Phase 1 assessment, in which early SIMMER versions then available were used and some of the unsuccessful calculations were later revised in the Phase 2 stage. In addition, there are fundamental difficulties in Phase 2 in which complex and inter-related phenomena were studied, because available experimental data base were very limited in both scale and material simulation. All the negative conclusions were documented in the assessment reports as proposed by the individual authors, so that the codes must be used carefully in reactor calculations knowing the limitations and model deficiencies. The V&V study is a continuing effort as long as the codes are usefully applied to reactor and other calculations.

Table 2-1. SIMMER-III/SIMMER-IV models.

Items	SIMMER-II	SIMMER-III/SIMMER-IV
Dimensions	2	2/3
No. of velocity fields	2	up to 8 (7 liquids and 1 vapor)
Pin fuel nodes	1	2 (surface and interior)
No. of can wall components	1	2/4 (left and right/left and right /+front and back)
No. of can wall nodes	1	2 (surface and interior)
Fuel-clad gap conductance	No	Yes
Fission gas in pin fuel	Intra- and inter-granular gas	Fission gas in pin fuel
Fission gas in liquid field	No	Fission gas in liquid fuel, fuel particles and fuel chunks
Control	Pin fuel and liquid	Pin fuel and control particles
Equation of state (EOS)	Simple analytic EOS functions	Accurate analytic functions consistent with thermodynamics
No. of EOS materials	5 (fuel, steel, sodium, control and fission gas)	5 each for different regions and sub-materials
Thermophysical properties	Mostly constant except for liquid density and sound speed)	Accurate analytic functions consistent with thermodynamics
Gas EOS	Ideal gas	Non-ideal gas
Single- to two-phase transition	No explicit treatment of vapor state causing abrupt change	Vapor state in single-phase cell treated consistently with two-phase cell
Fluid convection algorithm	Combined explicit (single-phase flow) and implicit method	Consistent semi-implicit method
Spatial differencing	First-order donor cell	Higher-order scheme
Intra-cell mass and energy updates	Rates of change determined at the beginning of cycle	Intra-cell updates separately from fluid convection in the four-step algorithm
Multi-phase flow topology	Dispersed (droplet) flow regime only	Both pool and channel flow regimes with smooth transition
Interfacial areas	Instantaneous	Convection with source terms
Melting and freezing (M/F)	Equilibrium transfer except for fuel crust freezing	Both equilibrium (bulk) and non-equilibrium (contact interface) transfer
Fuel freezing	Solid particles (bulk) and crust (conduction-limited) formation	Solid particles (bulk) and fuel-caps freezing (incomplete contact and fuel supercooling) for crust formation
Vaporization and condensation (V/C)	Only at liquid-vapor interface	All the dominant interfaces including between different materials
Neutron kinetics	Improved quasi-static method	Improved quasi-static method
Cross-section method	Down-scattering only	Full scattering
Flux shape solution method	S_n transport (TWOTRAN) or diffusion	S_n transport (TWODANT/THREE-DANT)
External neutron source	No	Yes
Decay heat	No	Yes
Input specifications	Classical card image	Free-format NAMELIST with built-in default/recommended values
Parallelization	Scalar	Parallelized as far as possible

Table 2-2. SIMMER-III/SIMMER-IV geometry indices and velocities.

Direction	SIMMER-III (2D)				SIMMER-IV (3D)			
	index	Cartesian	cylindrical	velocities	index	Cartesian	cylindrical	velocities
Transverse (left-right)	i	x	r	u	i	x	r	u
Transverse (front-back)	-	-	-	-	k	y	θ	w
Axial (down-up)	j	z	z	v	j	z	z	v

Table 2-3. SIMMER-III/SIMMER-IV structure-field components.

Density components (MCSR)		**Energy components (MCSRE)**	
S-III/S-IV*		**S-III/S-IV***	
$s1/s1$	Fertile pin fuel surface node	$S1/S1$	Pin fuel surface node
$s2/s2$	Fissile pin fuel surface node		
$s3/s3$	Left fertile crust fuel	$S2/S2$	Left crust fuel
$s4/s4$	Left fissile crust fuel		
$s5/s5$	Right fertile crust fuel	$S3/S3$	Right crust fuel
$s6/s6$	Right fissile crust fuel		
--/$s7$	Front fertile crust fuel*	--/$S4$	Front crust fuel*
--/$s8$	Front fissile crust fuel*		
--/$s9$	Back fertile crust fuel*	--/$S5$	Back crust fuel*
--/$s10$	Back fissile crust fuel*		
$s7$/s11	Cladding	$S4/S6$	Cladding
$s8/s12$	Left can wall surface node	$S5/S7$	Left can wall Surface node
$s9/s13$	Left can wall interior node	$S6/S8$	Left can wall Interior node
$s10/s14$	Right can wall surface node	$S7/S9$	Right can wall Surface node
$s11/s15$	Right can wall interior node	$S8/S10$	Right can wall Interior node
--/$s16$	Front can wall surface node*	--/$S11$	Front can wall surface node*
--/$s17$	Front can wall interior node*	--/$S12$	Front can wall interior node*
--/$s18$	Back can wall surface node*	--/$S13$	Back can wall surface node*
--/$s19$	Back can wall interior node*	--/$S14$	Back can wall interior node*
$s12/s20$	Control	$S9/S15$	Control

Table 2-4. SIMMER-III/SIMMER-IV liquid and vapor components.

Density components "*m*"		Energy components "*M*"		Velocity fields "*q*"	
(MCLR)		**(MCLRE)**		**default**	**recommended**
*l*1	Liquid fertile fuel	*L*1	Liquid fuel	*q*1	*q*1
*l*2	Liquid fissile fuel			*q*1	*q*1
*l*3	Liquid steel	*L*2	Liquid steel	*q*2	*q*2
*l*4	Liquid sodium	*L*3	Liquid sodium	*q*2	*q*3
*l*5	Fertile fuel particles	*L*4	Fuel particles	*q*1	*q*1
*l*6	Fissile fuel particles			*q*1	*q*1
*l*7	Steel particles	*L*5	Steel particles	*q*1	*q*2
*l*8	Control particles	*L*6	Control particles	*q*2	*q*4
*l*9	Fertile fuel chunks	*L*7	Fuel chunks	*q*2	*q*5
*l*10	Fissile fuel chunks			*q*2	*q*5
*l*11	Fission gas in liquid fuel			*q*1	*q*1
*l*12	Fission gas in fuel particles			*q*1	*q*1
*l*13	Fission gas in fuel chunks			*q*2	*q*5
(MCGR)		**(material component) ***			
*g*1	Fertile fuel vapor	*G*1	Fuel vapor	*q*3	*q*6
*g*2	Fissile fuel vapor			*q*3	*q*6
*g*3	Steel vapor	G2	Steel vapor	*q*3	*q*6
*g*4	Sodium vapor	*G*3	Sodium vapor	*q*3	*q*6
*g*5	Fission gas	*G*4	Fission gas	*q*3	*q*6

* *All vapor components, behaving as a vapor mixture and having the same temperature, are treated as a single energy component* "*G*" *and assigned to the same velocity field.*

Table 2-5. SIMMER-III/SIMMER-IV fuel-pin components.

Simple model (standard)		Detailed model (optional)	
a	Pin fuel interior node	(*NP*)	Pin fuel radial nodes
b	Pin fuel surface node (= *S*1)	(*NPB*)	Pin fuel surface node (= *S*1)
c	Cladding (= *S*4)	(*NPB*+1)	Cladding (= *S*4)
	Fission gas in pin fuel	(*NP*)	Fission gas in pin fuel
		Fuel-Pin Cavity (MCCR)	
		*c*1	Fertile cavity fuel
		*c*2	Fissile cavity fuel
		*c*3	Dissolved fission gas in cavity
		*c*4	Free fission gas in cavity

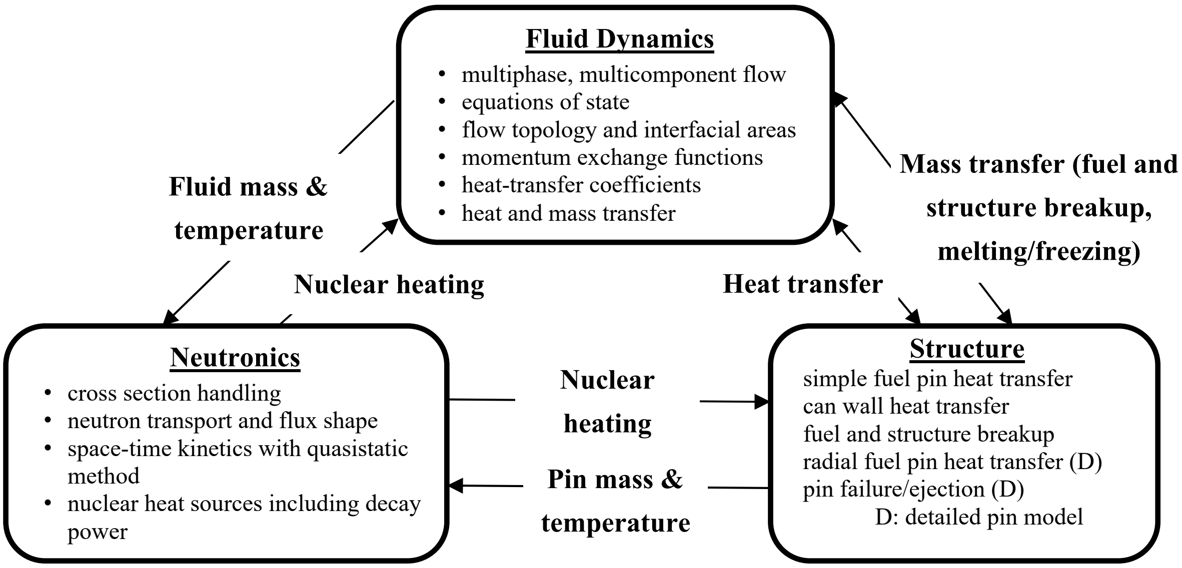

Fig. 2-1. SIMMER-III/SIMMER-IV overall-l code structure.

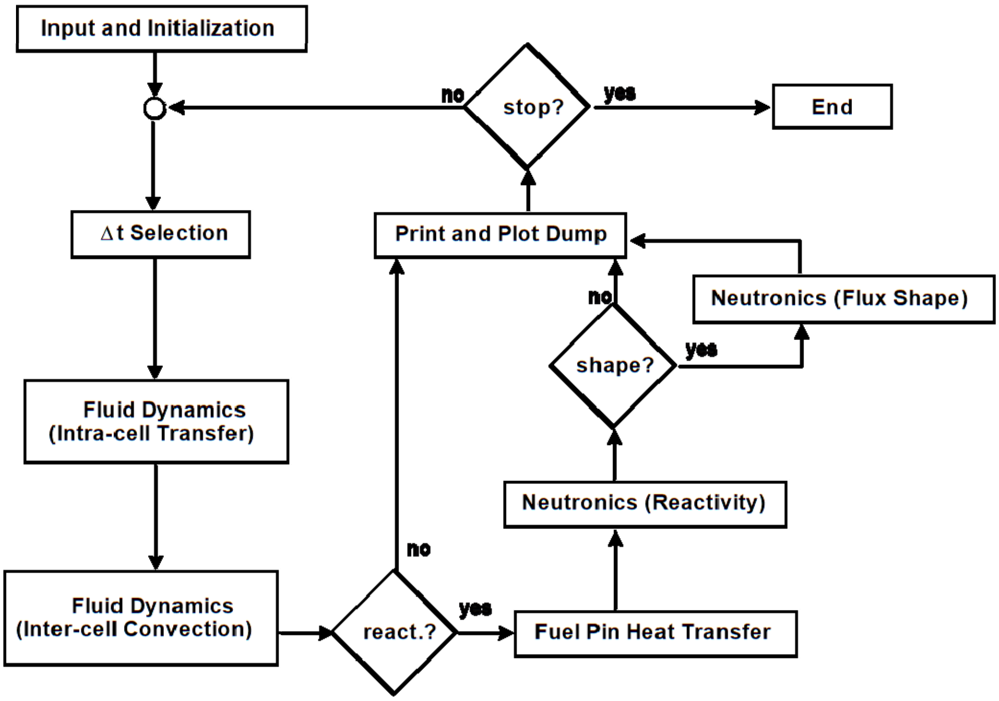

Fig. 2-2. SIMMER-III/SIMMER-IV calculational flow.

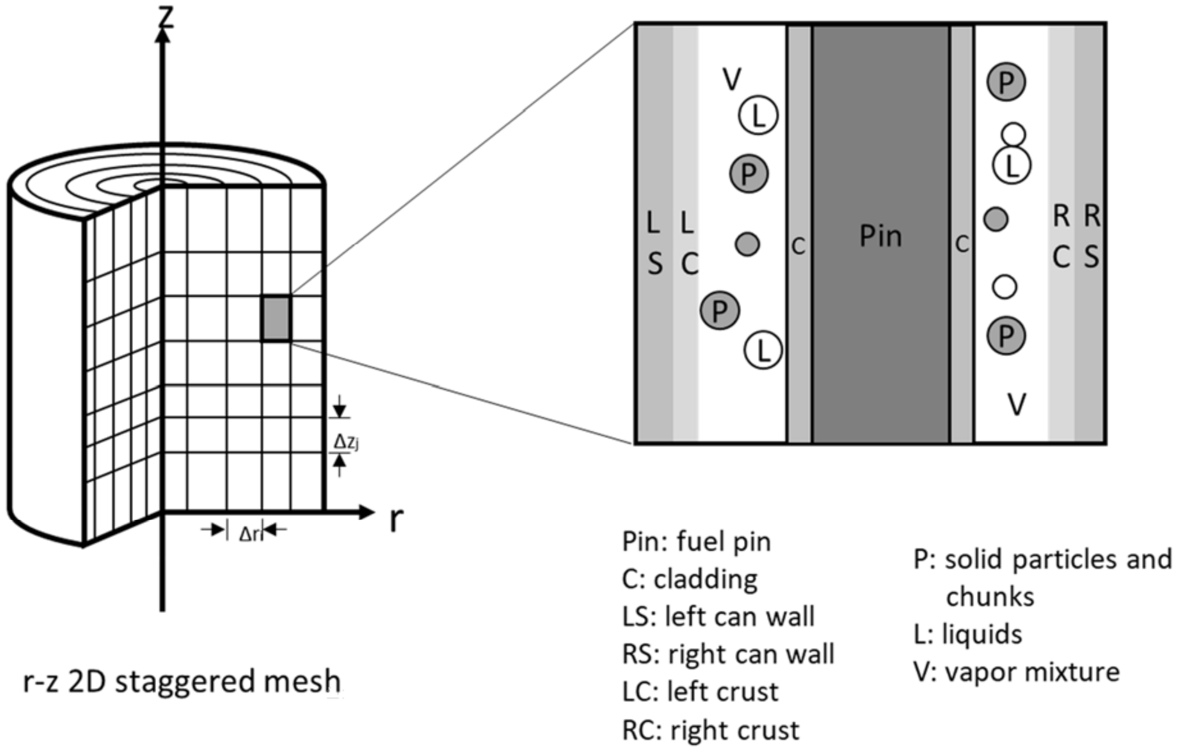

Fig. 2-3. SIMMER-III r-z geometry and mesh cell configuration.
(Dispersed flow regime and intact structure)

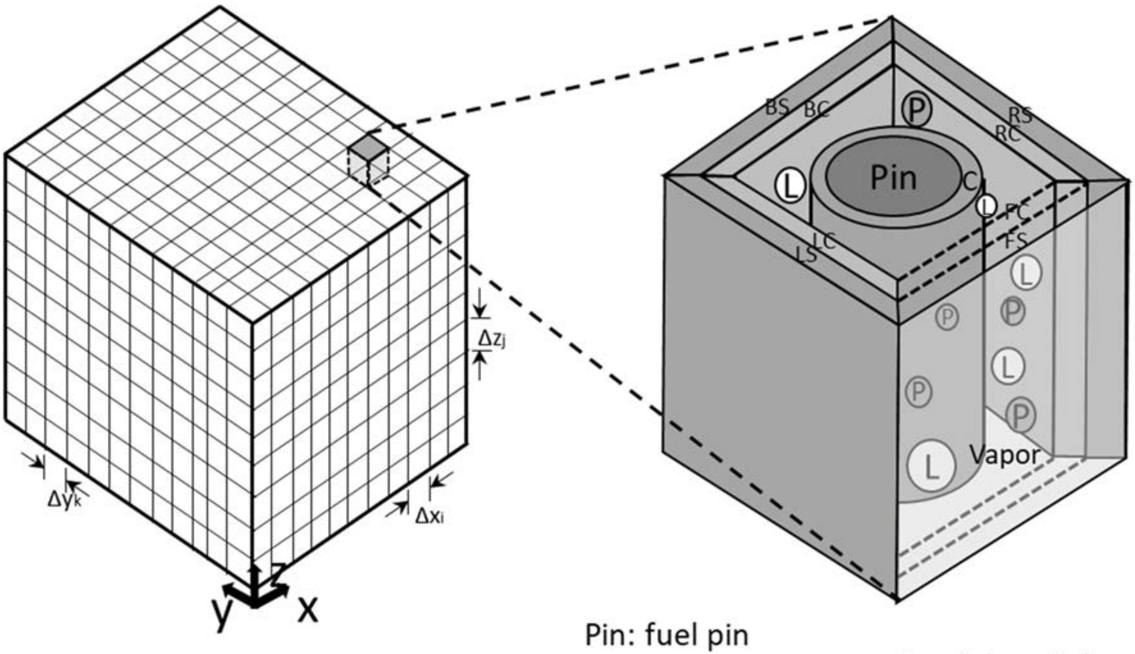

x-y-z 3D staggered mesh

Pin: fuel pin
C: cladding
LS: left can wall
RS: right can wall
FS: front can wall
BS: back can wall
LC: left crust
RC: right crust
FC: front crust
BC: back rust

P: solid particles and chunks
L: liquids
Vapor: vapor mixture

Fig. 2-4. SIMMER-IV x-y-z geometry and mesh cell configuration.
(Dispersed flow regime and intact structure)

3. Fluid Convection Algorithm

3.0. Overview

3.0.1. Background of models and methods

The central portion of the SIMMER-III code is a generalized framework of multiphase, multicomponent fluid dynamics that models time-dependent, interacting flows of all the LMFR core materials in physical states (phases) predicted in severe accident sequences. A fluid component exchanges heat and mass with other fluid components and structure surfaces. Internal heat sources are provided by nuclear heating calculated by the neutronics model. The basic concept of the multiphase, multicomponent flow representation is the same as the former SIMMER-II1), but the modeling framework and solution algorithm were totally re-designed and significantly advanced by taking advantage of experience gained in the AFDM project3), which demonstrated that a computational approach for two-dimensional, three-velocity-field, multiphase flow is technically feasible.

Some of the unique features of the SIMMER-III/SIMMER-IV fluid-dynamics algorithm are summarized below:

- Two dimensions (r-z or x-z) for SIMMER-III, or three dimensions (x-y-z or r-θ-z) for SIMMER-IV;
- Full LMFR core materials (fuel, steel, sodium, control and fission gas);
- Up to eight velocity fields (7 liquids and 1 vapor) with flexible velocity-field assignment for liquid-field components;
- Semi-implicit method for consistent and accurate mass and energy convection;
- First-order donor-cell or higher-order spatial differencing with Eulerian staggered mesh;
- Time-factorization technique, the so-called four-step method, which decouples the treatment of complex intra-cell transfer processes (in Step 1) from fluid convection (Steps 2-4);
- Multiple flow regimes for both the pool and channel flows with interfacial area convection;
- Improved and thermodynamically consistent analytic equations of state (EOS) with a non-ideal gas law and liquid compressibility;
- Improved pressure iteration procedure that eliminates internal iterations for mechanical equilibrium;
- Virtual mass terms for improving numerical stability;
- Robust characteristics with physics-based time-step control and time-step recalculation capability; and
- Flexible and versatile boundary conditions with optional internal virtual walls.

The fluid-dynamics model has been designed to retain generality and modularity as far as practicable, and hence future extension and improvement or model replacement are well possible.

3.0.2. Interaction with other models

In the four-step algorithm, the inter-cell fluid convection calculations solve the fluid-dynamic equations for mass, momentum and energy conservation without source terms due to intra-cell heat and mass transfers (Step 1). Calculations of Step 1, which are decoupled in the present four-step algorithm, provide the initial conditions for fluid convection. End-of-time-step updates of densities, energies, velocities and pressure due to convection are then used in the next time step.

To solve the convection equations, the following information is required:

- Component macroscopic densities and specific internal energies updated through Step 1;
- Component specific volumes and volume fractions, EOS pressure, and other thermophysical properties (TPP) calculated by the EOS and TPP models;
- Hydraulic diameter for each cell updated by the structure model (in Step 1); and
- Momentum exchange functions and interfacial areas evaluated and updated through Step 1.

The convection provides the following information to other code models:

- The end-of-time-step macroscopic densities, specific internal energies, velocities and cell pressure to be used in the next cycle; and
- Component macroscopic densities and temperatures to be used in the neutronics model.

In **Section 3.1**, the fundamental differential equations are described first with presenting the overall solution algorithm and the summary of Step 1 operations. The detailed description of Step 1 models and methods are given in **Chapter 4**. **Sections 4.2**, **4.3** and **4.4** provide the formulation of fluid convection calculations in Steps 2, 3 and 4, respectively.

3.1. Fluid-Dynamics Method

3.1.1. Fluid-dynamics components

The SIMMER-III/SIMMER-IV codes treat, in two/three dimensions, multi-velocity-fields, multiphase fluid flows that exchange mass, momentum and energy with structures through various transfer processes with and without phase transition. Nuclear heating provides internal heat sources to fluid components. The SIMMER-III/SIMMER-IV fluid components (liquids and vapors) are listed in **Table 2-3**. The components are categorized into three: density components written as subscripts “m”, energy components “M”, and momentum (velocity) components “q”. The number of velocity fields (momentum components) was initially 3 in early SIMMER-III versions, and has been extended up to 8, by which all the fluid energy components (7 liquid and 1 vapor mixture) can be assigned separately. An example velocity field assignment recommended for reactor calculations is also shown in **Table 2-3**.

3.1.2. Fundamental differential equations

The independent variables representing mass and energy are macroscopic (smear) densities and specific internal energies, respectively. This selection was made of these independent variables based on experience and consideration in the AFDM program. The macroscopic densities are written with the bar over the symbol $\bar{\rho}_m$ and they are defined by the volume fractions and the specific volumes υ_m as:

$$\bar{\rho}_m = \frac{\alpha_m}{\upsilon_m}. \tag{3-1}$$

In SIMMER-III, the specific volumes are generally used in the EOS model, in contrast to the microscopic (thermodynamic) densities, $\rho_m = 1/\upsilon_m$, used in SIMMER-II and AFDM.

The fundamental differential equations approximated and solved in the SIMMER-III fluid dynamics are given below. In addition to the mass, momentum and energy equations, additional EOS relationship is required for closing the fluid-dynamics equations set that correlates internal energy to pressure, for instance.

(1) Mass conservation equation

The general form of the mass conservation equations is, in abbreviated form:

$$\frac{\partial \bar{\rho}_m}{\partial t} + \nabla \cdot \left(\bar{\rho}_m \boldsymbol{v}_q\right) = -\Gamma_m\,, \tag{3-2}$$

where Γ_m is the total mass-transfer rate per unit volume from component m. The structure components are stationary and hence the second term of Eq. (3-2) is zero. Many mass-transfer paths exist in the SIMMER-III multicomponent system, such as melting/freezing, vaporization/condensation, fission-gas release and structure breakup.

(2) Momentum equations

A momentum equation is required for each velocity field. In the standard 3-velocity-field treatment, the liquid-field components are assigned to either velocity field 1 or 2, and all the vapor-field components are assigned to velocity field 3. This treatment of velocity field assignment has been enhanced, allowing up to 8 liquid velocity fields. A conservative form of the convective term is used in SIMMER-III, because it is more advantageous for transient multiphase flows that are the main application area of the code.

$$\begin{aligned} \frac{\partial \bar{\rho}_q \boldsymbol{v}_q}{\partial t} + \sum_{m \in q} \nabla \cdot \left(\bar{\rho}_m \boldsymbol{v}_q \boldsymbol{v}_q\right) + \alpha_q \nabla p - \bar{\rho}_q \boldsymbol{g} + K_{qS} \boldsymbol{v}_q - \sum_{q'} K_{qq'} \left(\boldsymbol{v}_{q'} - \boldsymbol{v}_q\right) - \boldsymbol{VM}_q \\ = -\sum_{q'} \Gamma_{qq'} \left[\mathrm{H}\left(\Gamma_{qq'}\right) \boldsymbol{v}_q + \mathrm{H}\left(\Gamma_{q'q}\right) \boldsymbol{v}_{q'}\right], \end{aligned} \tag{3-3}$$

where the term on the right-hand side is the momentum sources due to mass transfer and H(x) is the Heaviside unit function defined by $\mathrm{H}(x) = 0$ for $x < 0$, $\mathrm{H}(0) = 1/2$ for $x = 0$ and $\mathrm{H}(x) = 1$ for $x > 0$. The K_{qS} and $K_{qq'}$ terms on the left side are the momentum exchanges of velocity field q with the structure and another velocity field, respectively. $\boldsymbol{VM}_q$ is the virtual mass term for velocity field q and the treatment of this term is discussed later in this chapter. The structure components are assumed to be fixed in space and hence acts as an infinite momentum sink. This means the total momentum of a system cannot be conserved in SIMMER-III/SIMMER-IV.

The viscous drag term is not included in Eq. (3-3); in fact, in early SIMMER-III versions the viscous shear force between the liquid-field flows in laterally adjacent mesh cells was not modeled. The turbulence model is not included, either. Even though these terms may become important for such situations that small-scale experiments are modeled in small cells, they are known to be less important for reactor application with employing rather large mesh cells. In later SIMMER-III versions, explicit modeling of the viscous diffusion term has been attempted and made available as an input option, despite the difficulty to generalize the formulation in multi-component, multiphase systems. To avoid complexity the viscous model is described separately in **Section 3.5**.

(3) Internal energy equations

An internal energy equation is required for each of the structure and fluid energy components. A single equation is solved for the vapor internal energy which is defined as a mixture of vapor species. However, the convective term treats the individual vapor density components; this is required with higher-order differencing. Similarly to the momentum equations, a conservative form of the convective terms is used in SIMMER-III.

$$\begin{aligned}\frac{\partial \bar{\rho}_M e_M}{\partial t} &+ \sum_{m\in M} \nabla\cdot\left(\bar{\rho}_m e_m \boldsymbol{v}_q\right) + p\left[\frac{\partial \alpha_M}{\partial t} + \nabla\cdot\left(\alpha_M \boldsymbol{v}_q\right)\right] \\ &- \frac{\bar{\rho}_M}{\bar{\rho}_m}\left[\sum_{q} K_{q'q}\left(\boldsymbol{v}_q - \boldsymbol{v}_{q'}\right)\cdot\left(\boldsymbol{v}_q - \boldsymbol{v}_{q'q}\right) + K_{qS}\boldsymbol{v}_q\cdot\left(\boldsymbol{v}_q - \boldsymbol{v}_{qS}\right) + \boldsymbol{VM}_q \right. \\ &\left. \cdot\left(\boldsymbol{v}_q - \boldsymbol{v}_{GL}\right)\right] = Q_N + Q_M(\Gamma_M) + Q_H(h, a, \Delta T)\,, \end{aligned} \tag{3-4}$$

where the terms on the right-hand side of the equation denote the specific energy sources due to nuclear heating, mass transfer, and heat transfer to energy component *M*. No convective term is necessary for the structure components that are stationary. The third term on the left-hand side is the pressure-volume work term that accounts for the volume change of the fluid components. The work term also appears in an equation of a liquid component because the liquid compressibility is modeled in SIMMER-III/SIMMER-IV. The fourth term on the left side represents the energy transfer due to interfacial momentum exchange (drag heating).

(4) Interfacial area equations

The convection of interfacial areas (IFA) is modeled in SIMMER-III/SIMMER-IV. The method used is basically the same as one developed for AFDM, but has been improved by increasing the number of convectible IFAs for more flexible and consistent treatment. A basic concept of the model is to convect dominant IFAs at the velocities of associating fluid energy components. In other words, surface areas of some energy components are convected and thereby transient evolution of IFAs is traced. This treatment is expected to allow better simulations of transient multiphase flows where heat and mass transfers are occurring at component interfaces. The equations for convective IFAs are written as

$$\frac{\partial A_M}{\partial t} + \nabla \cdot (A_M \boldsymbol{v}) = \sum_k S_{M,k} \ , \tag{3-5}$$

where A_M and $S_{M,k}$ are the convectible IFAs and IFA source terms, respectively. The changes of interfacial areas are treated as source terms due to hydrodynamic breakup, flashing, turbulence-driven breakup, coalescence, and production of droplets or bubbles. The subscript M represents a fluid energy component associating the relevant convectible IFA. The source terms are calculated first without convection term and the convectible IFAs are then updated using the end-of-time-step fluid velocities.

3.1.3. Overall solution procedure (4 step method)

The overall fluid-dynamics solution algorithm is based on a time-factorization approach, so called the four-step method, developed for AFDM, in which intra-cell interfacial area source terms, heat and mass transfer, and momentum exchange functions are determined separately from inter-cell fluid convection. There are four steps in this algorithm as shown in **Fig. 3-1**.

Step 1 updates Eqs. (3-2) to (3-5) for intra-cell transfers while ignoring the convection terms. The models and methods of individual Step 1 operations are described separately in **Chapter 4**. Here the overall calculative flow through Step 1 has the following operations:

(1) Call EOS routines to initialize component volume fractions and thermodynamic state of each cell.

(2) Perform energy and mass transfer operations associated with fuel-pin or can-wall breakup whenever a break-up criterion is satisfied.

(3) Determine structure configuration and calculate structure heat-transfer coefficients and hydraulic diameter.

(4) Update convectible interfacial areas and determine binary contact areas between energy components.

(5) Calculate momentum-exchange functions.

(6) Calculate fluid heat-transfer coefficients.

(7) Calculate fission-gas release from liquid and particulate fuel.

(8) Update internal energies due to nuclear heating.

(9) Perform heat and mass transfer operations due to intra-cell heat transfer, melting/freezing and vaporization/condensation.

(10) Calculate can-wall heat transfer.

(11) Calculate inter-cell heat transfer.

(12) Update velocities and interfacial areas based on mass transfers.

These operations are performed in series in the order listed above. Macroscopic densities and specific internal energies are updated successively at each operation of intra-cell transfers. One exception is the calculation of inter-cell heat transfer due to heat conduction. This is an inter-cell transfer but is evaluated in Step 1 because the transfer is independent of inter-cell fluid convection. There is no direct coupling between two or more operations and this may potentially introduce inconsistencies. For example, the operation for can-wall heat transfer changes the wall temperature and hence possibly influences the heat and mass transfer on the structure surface. Such inconsistencies cannot be adjusted in the same time step but are only corrected in the next time step. Since rather fine time step sizes are used especially for highly transient cases, the Step 1 procedure is considered well acceptable. More coupled procedure might be theoretically possible, but the cost-effectiveness of such additional development efforts may have to be carefully judged.

The most complexed operation in Step 1 is the vaporization and condensation model. This is due mainly to non-linear nature of phase transition processes where the thermodynamic state and saturation properties of the vapor mixture are very sensitive to small variations in heat and mass being transferred. For this reason, an iterative solution procedure is implemented to obtain converged and consistent solution. This complex procedure and models of Step 1 operations are the characteristics of transient multiphase multicomponent flows simulated by SIMMER-III and the central reason why the intra-cell transfer is decoupled from the inter-cell convection. Finally, it is mentioned that the Step 1 is normally responsible for more than a half of the total computing cost of SIMMER-III even with the neutronics model.

3.1.4. Fluid convection algorithm

Steps 2, 3 and 4 are to solve fluid convection by integrating Eqs. (3-2) - (3-5) while ignoring the source terms on the right-hand sides. The equations solved in the convection part of the fluid-dynamics algorithm are:

$$\frac{\partial \bar{\rho}_m}{\partial t} + \nabla \cdot \left(\bar{\rho}_m \boldsymbol{v}_q\right) = 0\,, \tag{3-6}$$

$$\frac{\partial \bar{\rho}_q \boldsymbol{v}_q}{\partial t} + \sum_{m \in q} \nabla \cdot \left(\bar{\rho}_m \boldsymbol{v}_q \boldsymbol{v}_q\right) + \alpha_q \nabla p - \bar{\rho}_q g + K_{qS} \boldsymbol{v}_q - \sum_{q'} K_{qq'} \left(\boldsymbol{v}_{q'} - \boldsymbol{v}_q\right) - \boldsymbol{VM}_q = 0\,, \tag{3-7}$$

$$\begin{aligned}\frac{\partial \bar{\rho}_M e_M}{\partial t} + \sum_{m \in M} \nabla \cdot \left(\bar{\rho}_m e_m \boldsymbol{v}_q\right) + p\left[\frac{\partial \alpha_M}{\partial t} + \nabla \cdot \left(\alpha_M \boldsymbol{v}_q\right)\right] \\ - \frac{\bar{\rho}_M}{\bar{\rho}_m}\left[\sum_q K_{q'q}\left(\boldsymbol{v}_q - \boldsymbol{v}_{q'}\right) \cdot \left(\boldsymbol{v}_q - \boldsymbol{v}_{q'q}\right) + K_{qS} \boldsymbol{v}_q \cdot \left(\boldsymbol{v}_q - \boldsymbol{v}_{\boldsymbol{qS}}\right) + \boldsymbol{VM}_q \right. \\ \left. \cdot \left(\boldsymbol{v}_{\boldsymbol{q}} - \boldsymbol{v}_{GL}\right)\right] = 0\,, \text{and}\end{aligned} \tag{3-8}$$

$$\frac{\partial A_M}{\partial t} + \nabla \cdot \left(A_M \boldsymbol{v}_q\right) = 0\,. \tag{3-9}$$

The summary of the fluid convection algorithm is described in this section, and the full description of detailed formulation with differenced equations are given in **Sections 3.2** through **3.4**. First Step 2 explicitly estimates the end-of-time-step variables to initialize for the pressure iteration. While the first-order donor-cell differencing scheme is optionally used, a higher-order spatial differencing is the standard scheme to reduce numerical diffusion. The latter was based on the AFDM formulation and is described in the AFDM manual$^{8)}$.

Step 3 performs the pressure iteration that obtains consistent end-of-time-step velocities and pressure using a multivariate Newton-Raphson method. During the pressure iteration, only selected sensitive variables are allowed to change from the Step 2 estimates to limit the number of necessary operations. These variables are: the total density of fuel components, the density of steel, the density of sodium (and control particles), the total density of vapor mixture, the vapor temperature, and the difference between EOS pressure and cell pressure. In addition, an advantage over the previous AFDM approach is the elimination of an inefficient internal EOS iteration to obtain mechanical equilibrium among compressible fluid components. This is done by defining the EOS pressure as a function of the cell pressure, which is related to the amount of liquid compression.

Finally Step 4 performs mass, momentum and energy convection consistently based on the semi-implicit algorithm. The interfacial areas also convect consistently at the converged end-of-time-step velocities. A summary of the above four step updates of variables is schematically shown in an abridged form in **Table 3-1**, where a parenthesized number denotes the corresponding step in which a variable is updated.

3.1.5. Geometries and coordinates

As already shown in **Table 2-1**, a consistent use of geometry indices and velocity variables is maintained for SIMMER-III and SIMMER-IV. Even for a 3D system, the same axial index j and velocity v are used as 2D. The third dimension added for SIMMER-IV is represented by the index k and velocity w. In the staggered mesh cell formulation, the macroscopic densities, internal energies and cell pressure are defined at the cell center, and the velocities are defined at cell boundaries. An example for the 2D SIMMER-III case is shown in **Fig. 3-1**.

For typical reactor calculations, a cylindrical geometry is used in 2D SIMMER-III simulation. For 3D simulations with SIMMER-IV, a use of a Cartesian (rectangular) coordinate is recommended instead of a cylindrical coordinate, which has non-uniform mesh-cell volumes, becoming very small near the centerline.

3.2. End-of-Time-Step Estimate (Step 2)

The second step of the SIMMER-III four-step algorithm is an initial preparation for the fluid convection equation solutions. Step 2 estimates the end-of-time-step field variables by integrating the conservation equations without source terms in Eqs. (3-6), (3-7) and (3-8). The convection terms are treated explicitly in Step 2, with ignoring the interfacial drag heating terms that are included later in Step 4. The purpose of Step 2 is to initialize the pressure iteration in Step 3.

3.2.1. Mass and energy equation updates

The EOS information necessary for Step 2 is evaluated at the end of Step 1 that updates field variables based on intra-cell heat and mass transfer. Namely, based on $\tilde{\bar{\rho}}_m$ and $\tilde{T}_M$ updated in Step 1 transfers, the specific internal energies $\tilde{e}_M^n$ are determined. Consistent values for the macroscopic densities and the energy component volume fractions are also determined.

There are two options for a spatial differencing scheme: a first-order donor-cell differencing method and a higher-order differencing method. A basic concept of the latter option is to convect a slope of the variables in each donor cell in each direction, which is calculated from the values of these variables in the neighboring cells. The latter option is the standard option in SIMMER-III/SIMMER-IV since the experience with AFDM suggested that the scheme retain much higher accuracy with reduced numerical diffusion and is well acceptable for both the computing cost and stability. However, because of complexity of the formulations of the higher-order differencing, the equations for the first-order donor-cell differencing are mainly presented in the rest of this chapter unless stated differently. The original formulation of higher-order differencing in AFDM is described in detail in Appendix C of the AFDM document[8)].

Equation (3-6) for mass convection is expressed in finite-difference form as:

$$\tilde{\bar{\rho}}_m^{n+1} = \tilde{\bar{\rho}}_m^{n} - \Delta t \left[\frac{\Delta_i \left\langle \tilde{\bar{\rho}}_m^n r_i^\zeta \tilde{u}_q^n \right\rangle_{kj}}{r_i^\zeta \Delta x_i} + \frac{\Delta_k \left\langle \tilde{\bar{\rho}}_m^n \tilde{w}_q^n \right\rangle_{ji}}{r_i^\zeta \Delta y_k} + \frac{\Delta_j \left\langle \tilde{\bar{\rho}}_m^n \tilde{v}_q^n \right\rangle_{ik}}{\Delta z_j} \right], \tag{3-10}$$

where

$$\Delta_i f_{kj} = f_{i+1/2,k,j} - f_{i-1/2,k,j},\ \Delta_k f_{ji} = f_{i,k+1/2,j} - f_{i,k-1/2,j},\ \Delta_j f_{ik} = f_{i,k,j+1/2} - f_{i,k,j-1/2}\ ,$$

$\zeta = 1$ for the cylindrical geometry, and

$\zeta = 0$ for the rectangular geometry.

A general Cartesian coordinate system (*x*,*y*,*z*) is used in this chapter, but this might be better written as (*r*,*θ*,*z*) for the cylindrical geometry. In the documentation of former two-dimensional codes, SIMMER-II and AFDM, the coordinate system (r,z) were constantly used and the directions are called “radial” and “axial”. Since the model description of this report has taken advantage of the previous documentations of the two-dimensional codes, the words radial and axial are sometimes used to indicate x and z directions, respectively. The brackets notation in Eq. (3-10) indicates a variation of donor-cell differencing. For the first-order donor-cell option, they are:

$$\left\langle f r^\zeta u \right\rangle_{i+1/2,k,j} = r_{i+1/2,k,j}^\zeta u_{i+1/2,k,j} \begin{cases} f_{i,k,j} & \text{if } u_{i+1/2,k,j} \geq 0 \\ f_{i+1,k,j} & \text{if } u_{i+1/2,k,j} < 0 \end{cases}, \tag{3-11a}$$

$$\left\langle f w \right\rangle_{i,k+1/2,j} = w_{i,k+1/2,j} \begin{cases} f_{i,k,j} & \text{if } w_{i,k,j+1/2} \geq 0 \\ f_{i,k+1,j} & \text{if } w_{i,k,j+1/2} < 0 \end{cases} \text{, and} \tag{3-11b}$$

$$\langle fv\rangle_{i,k,j+1/2} = v_{i,k,j+1/2}\begin{cases} f_{i,k,j} & \text{if } v_{i,k,j+1/2} \geq 0 \\ f_{i,k,j+1} & \text{if } v_{i,k,j+1/2} < 0 \end{cases}. \tag{3-11c}$$

For the higher-order differing option, they are expressed as:

$$\langle fr^{\zeta}u\rangle_{i+\frac{1}{2},k,j} = r^{\zeta}_{i+\frac{1}{2},k,j}u_{i+\frac{1}{2},k,j}$$

$$\begin{cases} \left[f_{ijk} + \frac{r^{\zeta}_{ikj}\Delta x_i}{2}\left(\frac{\partial f}{\partial x}\right)_{ikj}\right] - \frac{\Delta t}{2}\left(r^{\zeta}_{i+1/2,k,j}u_{i+1/2,k,j}\right)^2\left(\frac{\partial f}{\partial x}\right)_{ikj} & \text{if } u_{i+1/2,k,j} \geq 0 \\ \left[f_{ikj} + \frac{r^{\zeta}_{ij}\Delta x_i}{2}\left(\frac{\partial f}{\partial x}\right)_{i+1,k,j}\right] - \frac{\Delta t}{2}\left(r^{\zeta}_{i+\frac{1}{2},k,j}u_{i+\frac{1}{2},k,j}\right)^2\left(\frac{\partial f}{\partial r}\right)_{i+1,k,j} & \text{if } u_{i+\frac{1}{2},k,j} < 0 \end{cases}, \tag{3-12a}$$

$$\langle fw\rangle_{i,k+\frac{1}{2},j} = w_{i,k+\frac{1}{2},j}$$

$$\begin{cases} \left[f_{ikj} + \frac{\Delta y_k}{2}\left(\frac{\partial f}{\partial y}\right)_{ikj}\right] - \frac{\Delta t}{2}\left(w_{i,k+\frac{1}{2},j}\right)^2\left(\frac{\partial f}{\partial y}\right)_{ikj} & \text{if } w_{i,k+1/2,j} \geq 0 \\ \left[f_{ikj} + \frac{\Delta y_k}{2}\left(\frac{\partial f}{\partial y}\right)_{i,k+1,j}\right] - \frac{\Delta t}{2}\left(w_{i,k+\frac{1}{2},j}\right)^2\left(\frac{\partial f}{\partial y}\right)_{i,k+1,j} & \text{if } w_{i,k+1/2,j} < 0 \end{cases}, \text{and} \tag{3-12b}$$

$$\langle fv\rangle_{i,k,j+\frac{1}{2}} = v_{i,k,j+\frac{1}{2}}$$

$$\begin{cases} \left[f_{ikj} + \frac{\Delta z_j}{2}\left(\frac{\partial f}{\partial z}\right)_{ikj}\right] - \frac{\Delta t}{2}\left(v_{i,k,j+1/2}\right)^2\left(\frac{\partial f}{\partial z}\right)_{ikj} & \text{if } v_{i,k,j+1/2} \geq 0 \\ \left[f_{ikj} + \frac{\Delta z_j}{2}\left(\frac{\partial f}{\partial z}\right)_{i,k,j+1}\right] - \frac{\Delta t}{2}\left(v_{i,k,j+1/2}\right)^2\left(\frac{\partial f}{\partial z}\right)_{i,k,j+1} & \text{if } v_{i,k,j+1/2} < 0 \end{cases}. \tag{3-12c}$$

The field variables on the right side of Eq. (3-10) are those obtained from Step 1. The spatial derivatives in the above equations are described in Appendix C of the AFDM manual Volume V[8)], together with the detailed derivation of the higher-order differencing. It is noted that if the spatial derivatives are ignored, Eqs. (3-12a) - (3-12c) reduce to the first-order donor-cell differencing in Eqs. (3-11a) - (3-12c).

For the energy equation, the liquid energy component densities are used as:

$\bar{\rho}_{L1} = \bar{\rho}_{l1} + \bar{\rho}_{l1}$,

$\bar{\rho}_{L2} = \bar{\rho}_{l3}$,

$\bar{\rho}_{L3} = \bar{\rho}_{l4}$,

$\bar{\rho}_{L4} = \bar{\rho}_{l5} + \bar{\rho}_{l6}$,

$\bar{\rho}_{L5} = \bar{\rho}_{l7}$,

$\bar{\rho}_{L6} = \bar{\rho}_{l8}$, and

$\bar{\rho}_{L7} = \bar{\rho}_{l9} + \bar{\rho}_{l10}$.

The estimated end-of-time-step volume fractions are determined from the densities calculated in Eq. (3-10), as:

$$\tilde{\alpha}_{Lm}^{n+1} = \frac{\tilde{\bar{\rho}}_{Lm}^{n+1}}{\tilde{\rho}_{Lm}^{n}} \text{, and} \tag{3-13}$$

$$\tilde{\alpha}_{G}^{n+1} = 1 - \alpha_{S}^{n+1} - \sum_{m} \tilde{\alpha}_{Lm}^{n+1} \,. \tag{3-14}$$

Then the energy equation in Eq. (3-8) is expressed in a finite-difference form as:

$$\begin{aligned} \tilde{e}_{r,ikj}^{n+1} = \frac{1}{\tilde{\bar{\rho}}_{r,ikj}^{n+1}} \Bigg\{ & \tilde{e}_{r,ijk}^{n} \tilde{\bar{\rho}}_{r,ikj}^{n} - \Delta t \left[\frac{\Delta_i \left\langle \tilde{\bar{\rho}}_r^n \tilde{e}_r^n r_i^{\zeta} \tilde{u}_q^n \right\rangle_{kj}}{r_i^{\zeta} \Delta x_i} + \frac{\Delta_k \left\langle \tilde{\bar{\rho}}_r^n \tilde{e}_r^n \tilde{v}_q^n \right\rangle_{ji}}{r_i^{\zeta} \Delta y_k} + \frac{\Delta_j \left\langle \tilde{\bar{\rho}}_r^n \tilde{e}_r^n \tilde{v}_q^n \right\rangle_{ik}}{\Delta z_j} \right] \\ & - p_{r,ikj} \left(\tilde{\alpha}_{r,ikj}^{n+1} - \alpha_{r,ikj}^{n} \right) \\ & - \Delta t p_{r,ikj} \left[\frac{\Delta_i \left\langle \tilde{\alpha}_r^n r_i^{\zeta} \tilde{u}_q^n \right\rangle_{kj}}{r_i^{\zeta} \Delta x_i} + \frac{\Delta_k \left\langle \tilde{\alpha}_r^n \tilde{v}_q^n \right\rangle_{ji}}{r_i^{\zeta} \Delta y_k} + \frac{\Delta_j \left\langle \tilde{\alpha}_r^n \tilde{v}_q^n \right\rangle_{ik}}{\Delta z_j} \right] \Bigg\} , \end{aligned} \tag{3-15}$$

where the subscript *r* denotes the energy component. The convection terms with bracket notation are expressed similarly to the mass equation for both the first-order donor-cell and higher-order differencing schemes, by defining

$$\left\langle \tilde{\bar{\rho}}_r^n \tilde{e}_r^n r^{\zeta} \tilde{u}_q^n \right\rangle_{kj} = \left\langle \tilde{\bar{\rho}}_r^n r^{\zeta} \tilde{u}_q^n \right\rangle_{kj} \langle \tilde{e}_r^n \rangle \,, \tag{3-16a}$$

$$\left\langle \tilde{\bar{\rho}}_r^n \tilde{e}_r^n \widetilde{w}_q^n \right\rangle_{ji} = \left\langle \tilde{\bar{\rho}}_r^n \widetilde{w}_q^n \right\rangle_{ji} \langle \tilde{e}_r^n \rangle \text{, and} \tag{3-16b}$$

$$\left\langle \tilde{\bar{\rho}}_r^n \tilde{e}_r^n \tilde{v}_q^n \right\rangle_{ik} = \left\langle \tilde{\bar{\rho}}_r^n \tilde{v}_q^n \right\rangle_{ik} \langle \tilde{e}_r^n \rangle \,. \tag{3-16c}$$

The remaining field variables on the right side of Eq. (3-15) are those obtained from Step 1. The pressure appearing in the pressure-volume work term is taken from Step 3 of the previous time step.

$$p_{r,ikj} = p_{ikj}^{n} \text{, for } r = L1, L2, \ldots, L7 \,. \tag{3-17}$$

It is noted that the work term is evaluated by only for the liquid energy components. Based on the experience with the previous AFDM code, evaluating the work term for the vapor field in Step 2 turned out to be not cost-effective and hence is omitted. The terms convecting the volume fractions are evaluated similarly to the mass convection and hence are not repeated here.

To avoid numerical problems with “underflow”, all smear (macroscopic) densities evaluated using Eq. (3-10) are limited to a minimum of 10^{-20} kg/m^3. When the density minimum occurs, setting the internal energies to a minimum value predetermined for each material. The present choices are the sublimation energies of the materials defined in the EOS model. The vapor field should be present even in a single-phase cell, and hence no adjustment is made for the vapor energy.

After Eqs. (3-10) and (3-15) are evaluated, the EOS is inverted to obtain the temperatures and volume fractions consistent with the new densities and energies.

3.2.2. Setup for momentum equation

The next operation in Step 2 is to use the momentum equations to calculate new velocities and velocity derivatives with respect to pressure. The SIMMER-III/SIMMER-IV allows to assign each of the seven liquid energy components arbitrarily to one of up to seven liquid velocity fields. In the standard procedure with the three velocity fields, defaulted in the code, the heavy fluid components (liquid fuel, fuel and steel particles) are assigned to $q1$, the light fluid components (liquid steel, liquid sodium and control particles) to $q2$ and the vapor mixture to $q3$.

$\bar{\rho}_{q1,ikj} = \bar{\rho}_{L1,ikj} + \bar{\rho}_{L4,ikj} + \bar{\rho}_{L5,ikj} + \bar{\rho}_{L7,ikj}$,

$\bar{\rho}_{q2,ikj} = \bar{\rho}_{L2,ikj} + \bar{\rho}_{L3,ikj} + \bar{\rho}_{L6,ikj}$, and

$\bar{\rho}_{q8,ikj} = \bar{\rho}_{G,ikj} = \bar{\rho}_{g1,ikj} + \bar{\rho}_{g2,ikj} + \bar{\rho}_{g3,ikj} + \bar{\rho}_{g4,ikj} + \bar{\rho}_{g5,ikj}$.

For an extended procedure with eight velocity-field assignment, the liquid energy components, $L1$ to $L7$, can be assigned respectively to different velocity fields, $q1$ to $q7$, and thereby the motion of individual liquid components can be traced independently. It is noted the increased number of velocity fields requires more computing cost. By increasing the number of velocity fields from 3 to 8, the number of inter-field momentum coupling terms increases from 3 to 28 and the number of fluid-structure friction terms increases from 9 to 24 for SIMMER-III (15 to 40 for SIMMER-IV). The volume fractions for the velocity fields are defined similarly.

To set up velocity calculations, the following four coupled preliminary operations are performed: to adjust momentum exchange coefficients, to average cell centered quantities, to evaluate virtual mass coefficients, and to evaluate convective terms of the momentum equations explicitly.

First, the momentum exchange coefficients are adjusted if a two-phase to single-phase transition has occurred. In Step 1, the $a_{qq'}$ and $b_{qq'}$ were determined for eventual use in the expression of the momentum-exchange function:

$$K_{qq'} = a_{qq'} + b_{qq'}\left|\vec{v}_{q'} - \vec{v}_q\right| . \tag{3-18}$$

If a single-phase cell is predicted, $\tilde{\alpha}_G^{n+1} < 0$, the momentum coupling with the vapor field is tightened for the liquid velocity field M having the largest volume fraction, by resetting $a_{qq'}$ as.

$$a_{qM,G} = 10^{10}(1 - \alpha_S)/\left(\bar{\rho}_{qM}^n \bar{\rho}_G^n\right) \text{, where } M = \left\{m \middle| \max_m\left[\alpha_{qm}\right]\right\} . \tag{3-19}$$

Second, because the velocities are evaluated on cell boundaries, cell-centered quantities are averaged. The results are:

$$\bar{\bar{\rho}}_{q,\lambda+} = \frac{\bar{\bar{\rho}}_{q,ikj} r_i^{\zeta} \Delta x_i + \bar{\bar{\rho}}_{q,i+1,k,j} r_{i+1}^{\zeta} \Delta x_{i+1}}{(r'_{i+1/2})^{\zeta} (\Delta x_i + \Delta x_{i+1})}, \tag{3-20a}$$

$$\bar{\bar{\rho}}_{q,\tau+} = \frac{\bar{\bar{\rho}}_{q,ikj} \Delta y_k + \bar{\bar{\rho}}_{q,i,k+1,j} \Delta y_{k+1}}{(r'_{i+1/2})^{\zeta} (\Delta y_i + \Delta y_{i+1})} \text{ , and} \tag{3-20b}$$

$$\bar{\bar{\rho}}_{q,\theta+} = \frac{\bar{\bar{\rho}}_{q,ikj} \Delta z_j + \bar{\bar{\rho}}_{q,i,k,j+1} \Delta z_{j+1}}{\Delta z_j + \Delta z_{j+1}}, \tag{3-20c}$$

where

$$\left(r'_{i+1/2}\right)^{\zeta} = \left(r_i^{\zeta} + r_{i+1}^{\zeta}\right)/2 \text{ , and}$$

$$\lambda+ = (i+1/2, k, j) \text{ , } \tau+ = (i, k+1/2, j) \text{ and } \theta+ = (i, k, j+1/2) \text{ .}$$

The a_{qS} and b_{qS} components of the fluid-structure momentum-exchange functions K_{qS} and the $a_{qq'}$ and $b_{qq'}$ components of the interfield momentum-exchange functions $K_{qq'}$ are averaged similarly to the densities for consistency. Because of the large fractional changes can take place over a time step, the loss/gain of mass and momentum in a cell requires a further adjustment on the interfield momentum coupling. To maintain a similar force per unit mass on the estimated end-of-time-step densities, the adjustments are

$$\tilde{a}_{qq'}^{n+1} = \tilde{a}_{qq'}^{n} \left[\left(\tilde{\bar{\bar{\rho}}}_q^{n+1} \tilde{\bar{\bar{\rho}}}_{q'}^{n+1}\right) / \left(\tilde{\bar{\bar{\rho}}}_q^{n} \tilde{\bar{\bar{\rho}}}_{q'}^{n}\right)\right], \tag{3-21a}$$

$$\tilde{b}_{qq'}^{n+1} = \tilde{b}_{qq'}^{n} \left[\left(\tilde{\bar{\bar{\rho}}}_q^{n+1} \tilde{\bar{\bar{\rho}}}_{q'}^{n+1}\right) / \left(\tilde{\bar{\bar{\rho}}}_q^{n} \tilde{\bar{\bar{\rho}}}_{q'}^{n}\right)\right], \tag{3-21b}$$

$$\tilde{a}_{qS}^{n+1} = \tilde{a}_{qS}^{n} \left(\tilde{\bar{\bar{\rho}}}_q^{n+1} / \tilde{\bar{\bar{\rho}}}_q^{n}\right) \text{ , and} \tag{3-22a}$$

$$\tilde{b}_{qS}^{n+1} = \tilde{b}_{qS}^{n} \left(\tilde{\bar{\bar{\rho}}}_q^{n+1} / \tilde{\bar{\bar{\rho}}}_q^{n}\right) . \tag{3-22b}$$

The volume fractions are averaged differently. Namely, the straight area averaging determines α_S on cell boundaries. This means, for the radial boundary (*x* direction),

$$\alpha_{S,\lambda+} = \frac{\alpha_{S,ikj} r_i^{\zeta} \Delta x_i + \alpha_{S,i+1,k,j} r_{i+1}^{\zeta} \Delta x_{i+1}}{r_i^{\zeta} \Delta x_i + r_{i+1}^{\zeta} \Delta x_{i+1}} . \tag{3-23}$$

Since the cell-dependent structure volume fractions are time independent during convection, no tilde notation is required. The vapor volume fractions on radial cell boundaries are calculated as

$$\alpha_{G,\lambda+} = \left(1 - \alpha_{S,\lambda+}\right) \begin{cases} \alpha_{G,ikj} / \left(1 - \alpha_{S,ikj}\right) & \text{for } p_{ikj} \geq p_{i+1,k,j} \\ \alpha_{G,i+1,k,j} / \left(1 - \alpha_{S,i+1,k,j}\right) & \text{for } p_{ikj} < p_{i+1,k,j} \end{cases} . \tag{3-24}$$

Because the volume fractions must sum to unity,

$$\alpha_{L,\lambda+} = 1 - \alpha_{S,\lambda+} - \alpha_{G,\lambda+} . \tag{3-25}$$

The component-wise effective vapor volume fractions are averaged on radial cell boundaries as

$$\alpha_{qm,\lambda+} = \frac{\hat{\alpha}_{qm,\lambda+}}{\sum_{m=1}^{8} \hat{\alpha}_{qm,\lambda+}} \alpha_{G,\lambda+} , \tag{3-26}$$

where

$$\hat{\alpha}_{qm,\lambda+} = \alpha_{qm,ikj} r_i \Delta x_i + \alpha_{qm,i+1,k,j} r_{i+1} \Delta x_{i+1} . \tag{3-27}$$

A similar procedure is taken to average the variables at the other boundaries (in *y* and *z* directions).

Third, the virtual mass terms calculated in Step 1 are used. The physical background and purpose of implementing the model are discussed in Appendix A of the AFDM manual Vol. V[8].

Fourth, the convection terms of the momentum equations are evaluated explicitly. For the radial (x) direction, the convection term is given by

$$\begin{aligned} C\tilde{V}_{q,\lambda+} &= \frac{1}{r^\zeta}\frac{\partial}{\partial x}\left(\bar{\rho}_q r^\zeta {u_q}^2\right) + \frac{1}{r^\zeta}\frac{\partial}{\partial y}\left(\bar{\rho}_q u_q w_q\right) + \frac{\partial}{\partial z}\left(\bar{\rho}_q u_q v_q\right) \\ &= \frac{1}{\left({r'}_{i+1/2}\right)^\zeta \Delta x_{i+1/2}} \left[\left\langle \tilde{\bar{\rho}}_q^n r^\zeta \tilde{u}_q^n \right\rangle_{i+1,k,j} \left\langle \tilde{u}_q^n \right\rangle_{i+1,k,j} - \left\langle \tilde{\bar{\rho}}_q^n r^\zeta \tilde{u}_q^n \right\rangle_{ikj} \left\langle \tilde{u}_q^n \right\rangle_{ikj}\right] \\ &+ \frac{1}{\left({r'}_{i+1/2}\right)^\zeta \Delta y_k} \left[\left\langle \tilde{\bar{\rho}}_q^n \widetilde{w}_q^n \right\rangle_{i+1/2,k+1/2,j} \left\langle \tilde{u}_q^n \right\rangle_{i+1/2,k+1/2,j} \right. \\ &\left. - \left\langle \tilde{\bar{\rho}}_q^n \widetilde{w}_q^n \right\rangle_{i+1/2,k-1/2,j} \left\langle \tilde{u}_q^n \right\rangle_{i+1/2,k-1/2,j}\right] \\ &+ \frac{1}{\Delta z_j} \left[\left\langle \tilde{\bar{\rho}}_q^n \tilde{v}_q^n \right\rangle_{i+1/2,k,j+1/2} \left\langle \tilde{u}_q^n \right\rangle_{i+1/2,k,j+1/2} \right. \\ &\left. - \left\langle \tilde{\bar{\rho}}_q^n \tilde{v}_q^n \right\rangle_{i+1/2,k,j-1/2} \left\langle \tilde{u}_q^n \right\rangle_{i+1/2,k,j-1/2}\right] , \end{aligned} \tag{3-28}$$

where the donor cell evaluation of the terms with bracket is

$$\left\langle \bar{\rho} r^\zeta u_q \right\rangle_{i+1,k,j} = \left[\left\langle \bar{\rho} r^\zeta u_q \right\rangle_{i+1/2,k,j} + \left\langle \bar{\rho} r^\zeta u_q \right\rangle_{i+3-2,k,j}\right]/2 , \tag{3-29a}$$

$$\left\langle \bar{\rho} w_q \right\rangle_{i+1/2,k+1/2,j} = \left[\left\langle \bar{\rho} w_q \right\rangle_{i,k+1/2,j} + \left\langle \bar{\rho} w_q \right\rangle_{i+1,k+1/2,j}\right]/2 , \tag{3-29b}$$

$$\left\langle \bar{\rho} v_q \right\rangle_{i+1/2,kj+1/2} = \left[\left\langle \bar{\rho} v_q \right\rangle_{i,k,j+1/2} + \left\langle \bar{\rho} v_q \right\rangle_{i+1,k,j+1/2}\right]/2 , \tag{3-29c}$$

$$\langle u \rangle_{i+1,k,j} = \begin{cases} u_{i+1/2,k,j} & \text{for } \left\langle \bar{\rho} r^\zeta u \right\rangle_{i+1,k,j} \geq 0 \\ u_{i+3-2,k,j} & \text{for } \left\langle \bar{\rho} r^\zeta u \right\rangle_{i+1,k,j} < 0 \end{cases} , \tag{3-29d}$$

$$\langle u \rangle_{i+1/2,k+1/2,j} = \begin{cases} u_{1+1/2,k,j} & \text{for } \langle \bar{\rho} w \rangle_{ii+1/2,k+1/2,j} \geq 0 \\ u_{i+1/2,k+1,j} & \text{for } \langle \bar{\rho} w \rangle_{ii+1/2,k+1/2,j} < 0 \end{cases} \text{, and} \tag{3-29e}$$

$$\langle u\rangle_{i+1/2,k+1/2,j} = \begin{cases} u_{i+1/2,k,j} & \text{for } \langle\bar{\rho}v\rangle_{i+1/2,k,j+1/2} \geq 0 \\ u_{i+1/2,k,j+1} & \text{for } \langle\bar{\rho}v\rangle_{i+1/2,k,j+1/2} < 0 \end{cases}. \tag{3-29f}$$

For the *y* direction, the convection terms are given by

$$\begin{aligned} C\tilde{V}_{q,\tau+} &= \frac{1}{r^\zeta}\frac{\partial}{\partial x}\left(\bar{\rho}_q w_q r^\zeta u_q\right) + \frac{\partial}{\partial y}\left(\bar{\rho}_q w_q^2\right) + \frac{\partial}{\partial z}\left(\bar{\rho}_q w_q u_q\right) \\ &= \frac{1}{r^\zeta \Delta x_i}\Big[\left\langle\tilde{\bar{\rho}}_q^n r^\zeta \tilde{u}_q^n\right\rangle_{i+1/2,k+1/2,j}\left\langle\tilde{w}_q^n\right\rangle_{i+1/2,k+1/2,j} \\ &- \left\langle\tilde{\bar{\rho}}_q^n r^\zeta \tilde{u}_q^n\right\rangle_{i-1/2,k+1/2,j}\left\langle\tilde{w}_q^n\right\rangle_{i-1/2,k+1/2,j}\Big] \\ &+ \frac{1}{r^\zeta \Delta y_{k+1/2}}\Big[\left\langle\tilde{\bar{\rho}}_q^n \tilde{w}_q^n\right\rangle_{i,k+1,j}\left\langle\tilde{w}_q^n\right\rangle_{i,k+1,j} - \left\langle\tilde{\bar{\rho}}_q^n \tilde{w}_q^n\right\rangle_{ikj}\left\langle\tilde{w}_q^n\right\rangle_{ikj}\Big] \\ &+ \frac{1}{\Delta z_j}\Big[\left\langle\tilde{\bar{\rho}}_q^n \tilde{v}_q^n\right\rangle_{i,k+1/2,j+1/2}\left\langle\tilde{w}_q^n\right\rangle_{i,k+1/2,j+1/2} \\ &- \left\langle\tilde{\bar{\rho}}_q^n \tilde{v}_q^n\right\rangle_{i,k+1/2,j-1/2}\left\langle\tilde{w}_q^n\right\rangle_{i,k+1/2,j-1/2}\Big]. \end{aligned} \tag{3-30}$$

For the axial (*z*) direction, the convection terms are given by

$$\begin{aligned} C\tilde{V}_{q,\theta+} &= \frac{1}{r^\zeta}\frac{\partial}{\partial x}\left(\bar{\rho}_q v_q r^\zeta u_q\right) + \frac{\partial}{\partial y}\left(\bar{\rho}_q v_q w_q\right) + \frac{\partial}{\partial z}\left(\bar{\rho}_q v_q^2\right) \\ &= \frac{1}{r^\zeta \Delta x_i}\Big[\left\langle\tilde{\bar{\rho}}_q^n r^\zeta \tilde{u}_q^n\right\rangle_{i+1/2,k,j+1/2}\left\langle\tilde{v}_q^n\right\rangle_{i+1/2,k,j+1/2} \\ &- \left\langle\tilde{\bar{\rho}}_q^n r^\zeta \tilde{u}_q^n\right\rangle_{i-1/2,k,j+1/2}\left\langle\tilde{v}_q^n\right\rangle_{i-1/2,k,j+1/2}\Big] \\ &+ \frac{1}{r^\zeta \Delta y_k}\Big[\left\langle\tilde{\bar{\rho}}_q^n r^\zeta \tilde{w}_q^n\right\rangle_{i,k+1/2,j+1/2}\left\langle\tilde{v}_q^n\right\rangle_{i,k+1/2,j+1/2} \\ &- \left\langle\tilde{\bar{\rho}}_q^n r^\zeta \tilde{w}_q^n\right\rangle_{i,k-1/2,j+1/2}\left\langle\tilde{v}_q^n\right\rangle_{i,k-1/2,j+1/2}\Big] \\ &+ \frac{1}{\Delta z_{j+1/2}}\Big[\left\langle\tilde{\bar{\rho}}_q^n \tilde{v}_q^n\right\rangle_{i,k,j+1}\left\langle\tilde{v}_q^n\right\rangle_{i,k,j+1} - \left\langle\tilde{\bar{\rho}}_q^n \tilde{v}_q^n\right\rangle_{ikj}\left\langle\tilde{v}_q^n\right\rangle_{ikj}\Big]. \end{aligned} \tag{3-31}$$

The donor cell evaluation of the terms with bracket in Eqs. (3-30) and (3-31) is obtained similarly to the *x* direction. The velocities in the above definitions are obtained from dividing the momentum fluxes at the appropriate boundaries by a momentum-averaged density. In the reduction to the first-order differencing, where the velocity derivatives are zero, it is only the sign of the velocities that is important.

3.2.3. Velocity solution procedure

After setting up the momentum equations in the previous section, the momentum equations are solved explicitly for velocities. In SIMMER-III there are up to eight momentum fields (three in the standard option) that are coupled each other through interfacial drag. Because of the direct relationship between velocities and interfacial drag, the momentum equations are solved using an iterative procedure. If strong interfield coupling is applied to previously loosely coupled fields, more iterations can be required to achieve the convergence necessary to allow later determination of interfacial energy dissipation using the calculated velocities.

There are three operations performed in this section. First, momentum averaging is applied to couple momentum fields. Two momentum fields are regarded as coupled if the momentum exchange coefficient is sufficiently large, namely

$$\alpha_{qq'} \geq 10^9(1-\alpha_S)\,. \tag{3-32}$$

The averaged velocity from two coupled momentum fields, for example for the axial boundary, is given by

$$\tilde{V}^n_{q,\xi} = \tilde{V}^n_{q',\xi} = \frac{\tilde{\bar{\rho}}_{q,\xi}\tilde{v}_{q,\xi} + \tilde{\bar{\rho}}_{q',\xi}\tilde{v}_{q',\xi}}{\tilde{\bar{\rho}}_{q,\xi} + \tilde{\bar{\rho}}_{q',\xi}}\,, \tag{3-33}$$

where the quantity ξ can represent either $\theta+1$, $\tau+1$ or $\lambda+1$ momentum cell in *x* (radial), *y* or *z* (axial) direction. This must be done on all the boundaries of the cell. The number of interfield momentum couplings is 3 for the standard three-velocity-field model, but it increases as many as 28 for the eight-field model. In Eq. (3-33) and the solution procedure below, the velocities used in the equations of motion are indicated using upper-case *V* for all the directions.

Second, the finite difference representation of the momentum equations may be placed in the general form

$$\begin{aligned}\tilde{\bar{\rho}}^{n+1}_{q,\xi}\tilde{V}^{n+1}_{q,\xi} + \Delta t K_{qS,\zeta} V_{q,\xi} - \tilde{\beta}^{n+1}_{q,\xi}\left[\tilde{V}^{n+1}_{G,\xi} - \sum_m \tilde{\alpha}^{n+1}_{qm,eff,\xi}\tilde{V}^{n+1}_{qm,\xi}\right]& \\ - \Delta t \sum_{q'}\left(\tilde{a}^{n+1}_{q'q,\xi} + \tilde{b}^{n+1}_{q'q,\xi}\left|V^*_{q'q,\xi}\right|\right)\, V_{q'q,\xi}& \\ = \tilde{\bar{\rho}}^{n}_{q,\xi}\tilde{V}^{n}_{q,\xi} - \Delta t C\tilde{V}_{q,\xi} - \tilde{\beta}^{n+1}_{q,\xi}\left[\tilde{V}^{n}_{G,\xi} - \sum_m \tilde{\alpha}^{n+1}_{qm,eff,\xi}\tilde{V}^{n}_{qm,\xi}\right] + \tilde{\eta}^{n+1}_{q,\xi}\,,&\end{aligned} \tag{3-34}$$

where $K_{qS,\xi} = \tilde{a}^{n+1}_{qS,\xi} + \tilde{b}^{n+1}_{qS,\xi}\left|V^*_{q,\xi}\right|$, and the summation over *m* is only for liquid fields. The last term on the RHS of Eq. (3-34) is defined in three directions as

$$\tilde{\eta}^{n+1}_{q,\lambda+} = -\Delta t\tilde{\alpha}^{n+1}_{q,\lambda+}\frac{\tilde{p}^{n+1}_{i+1,k,j} - \tilde{p}^{n+1}_{ikj}}{\Delta x_{i+\frac{1}{2}}}\,, \tag{3-35a}$$

$$\tilde{\eta}^{n+1}_{q,\tau+} = -\Delta t\tilde{\alpha}^{n+1}_{q,\tau+}\frac{\tilde{p}^{n+1}_{i,k+1,j} - \tilde{p}^{n+1}_{ikj}}{(r'_{i+\frac{1}{2}})^{\xi}\Delta y_{i+\frac{1}{2}}}\,, \text{and} \tag{3-35b}$$

$$\tilde{\eta}^{n+1}_{q,\theta+} = \Delta t\tilde{\bar{\rho}}^{n+1}_{q,\theta+}g - \Delta t\tilde{\alpha}^{n+1}_{q,\theta+}\frac{\tilde{p}^{n+1}_{i,k,j+1} - \tilde{p}^{n+1}_{ikj}}{\Delta z_{j+\frac{1}{2}}}\,. \tag{3-35c}$$

The gravity term appears only in the axial direction. Although they are not explicitly shown, the centrifugal force and Coriolis's force may be added to Eqs. (3.39) and (3.40), respectively, when a three-dimensional cylindrical model is to be used.

The virtual mass coefficients are then defined and the vapor virtual mass term is given by

$$\tilde{\beta}_{q,\xi}^{n+1} = \alpha_{q,eff}\alpha_{G,\xi}VM_{\xi} \text{ , and} \tag{3-36}$$

$$\tilde{\beta}_{G,\xi}^{n+1} = -\alpha_{G,\xi}VM_{\xi} \text{ ,} \tag{3-37}$$

where

$$\alpha_{q,eff} = \alpha_G \Big/ \sum_m \alpha_{qm} \text{ .} \tag{3-38}$$

The term VM_ζ is the cell averaged virtual mass coefficient computed in Step 1.

The velocity differences in the inter-field drag terms in Eq. (3-34) are simply evaluated by

$$V^*_{q'q,\xi} = \tilde{V}^n_{q',\xi} - \tilde{V}^n_{q,\xi} \text{ ,} \tag{3-39a}$$

$$V_{q'q,\xi} = \tilde{V}^{n+1}_{q',\xi} - \tilde{V}^{n+1}_{q,\xi} \text{ ,} \tag{3-39b}$$

$$V^*_{q,\xi} = \tilde{V}^n_{q,\xi} \text{ , and} \tag{3-39c}$$

$$V_{q,\xi} = \tilde{V}^{n+1}_{q,\xi} \text{ .} \tag{3-39d}$$

Because the pressures are those at the beginning of the time step, $\tilde{p}_{ij}^{n+1} = \tilde{p}_{ij}^{n}$.

These reduce the momentum equations to a simultaneous set of three linear equations in three unknowns, which is expressed in a matrix equation of the form:

$$\underline{S_\xi}\,\underline{\tilde{V}_\xi}^{n+1} = \underline{D_\xi} \text{ , or} \tag{3-40a}$$

$$\begin{bmatrix} s_{11} & s_{12} & s_{13} \\ s_{21} & s_{22} & s_{23} \\ s_{31} & s_{32} & s_{33} \end{bmatrix} \begin{bmatrix} \tilde{V}_{1,\xi} \\ \tilde{V}_{2,\xi} \\ \tilde{V}_{3,\xi} \end{bmatrix} = \begin{bmatrix} d_{1,\xi} \\ d_{2,\xi} \\ d_{3,\xi} \end{bmatrix} \text{ .} \tag{3-40b}$$

This matrix is 3 by 3 for the standard three-velocity-field model, where the elements of the matrix $\underline{S_\xi}$ are given by:

$$s_{11,\xi} = \tilde{\rho}_{1,\xi}^{n+1} + \Delta t K_{1S,\xi} + \Delta t(K_{12,\xi} + K_{13,\xi}) - (\tilde{\alpha}_{1,eff,\xi}^{n+1})^2 \tilde{\beta}_{G,\xi}^{n+1} \text{ ,} \tag{3-41a}$$

$$s_{12,\xi} = s_{21,\xi} = -\Delta t K_{12,\xi} - \tilde{\alpha}_{1,eff,\xi}^{n+1} \tilde{\beta}_{G,\xi}^{n+1} \tilde{\alpha}_{2,eff,\xi}^{n+1} \text{ ,} \tag{3-41b}$$

$$s_{22,\xi} = \tilde{\rho}_{2,\xi}^{n+1} + \Delta t K_{2S,\xi} + \Delta t(K_{12,\xi} + K_{23,\xi}) - (\tilde{\alpha}_{2,eff,\xi}^{n+1})^2 \tilde{\beta}_{G,\xi}^{n+1} \text{ ,} \tag{3-41c}$$

$$s_{13,\xi} = s_{31,\xi} = -\Delta t K_{13,\xi} + \tilde{\alpha}_{1,eff,\xi}^{n+1} \tilde{\beta}_{G,\xi}^{n+1} \text{ ,} \tag{3-41d}$$

$$s_{23,\xi} = s_{32,\xi} = -\Delta t K_{23,\xi} + \tilde{\alpha}_{2,eff,\xi}^{n+1} \tilde{\beta}_{G,\xi}^{n+1} \text{ , and} \tag{3-41e}$$

$$s_{33,\xi} = \tilde{\tilde{\rho}}_{3,\xi}^{n+1} + \Delta t K_{3S,\xi} + \Delta t\left(K_{13,\xi} + K_{23,\xi}\right) - \tilde{\beta}_{G,\xi}^{n+1}\,, \tag{3-41f}$$

where $K_{q'q,\xi} = \tilde{a}_{q'q,\xi}^{n+1} + \tilde{b}_{q'q,\xi}^{n+1}\left|V_{q'q,\xi}^{*}\right|$. The vector $\underline{D}_{\xi}$ is given by

$$d_{q,\xi} = \tilde{\tilde{\rho}}_{q,\xi}^{n}\tilde{V}_{q,\xi}^{n} - \Delta t C\tilde{V}_{q,\xi} - \tilde{\beta}_{q,\xi}^{n+1}\left[\tilde{V}_{G,\xi}^{n} - \tilde{\alpha}_{q1,eff,\xi}^{n+1}\tilde{V}_{q1,\xi}^{n} - \tilde{\alpha}_{q2,eff,\xi}^{n+1}\tilde{V}_{q2,\xi}^{n}\right] + \tilde{\eta}_{q,\xi}^{n+1}\,. \tag{3-42}$$

The extension up to an 8 by 8 matrix equation for more than the standard three velocity fields is straightforward and hence not repeated here. The matrix equation is solved for velocities using a Gaussian elimination method.

The iterative procedure is performed in the following way. After initial pass we examine if the estimated velocities are too large, again for the case of three fields,

$$\begin{aligned}\frac{1}{2}\{\tilde{a}_{GS}^{n+1} + \tilde{b}_{GS}^{n+1}\left|\tilde{V}_{GS}^{n+1} + \tilde{V}_{GS}^{n}\right| + \tilde{a}_{13,\xi}^{n+1}& \\ + \tilde{b}_{13}^{n+1}\left|\tilde{V}_{G}^{n+1} - \tilde{V}_{q1}^{n+1} + \tilde{V}_{G}^{n} - \tilde{V}_{q1}^{n}\right| + \tilde{a}_{23,\xi}^{n+1}& \\ + \tilde{b}_{23}^{n+1}\left|\tilde{V}_{G}^{n+1} - \tilde{V}_{q2}^{n+1} + \tilde{V}_{G}^{n} - \tilde{V}_{q2}^{n}\right|\} > K_{GS} + K_{13} + K_{23}\,.&\end{aligned} \tag{3-43a}$$

For the eight velocity-field case, a general expression is given by

$$\begin{aligned}\frac{1}{7}\left\{\tilde{a}_{GS}^{n+1} + \tilde{b}_{GS}^{n+1}\left|\tilde{V}_{GS}^{n+1} + \tilde{V}_{GS}^{n}\right| + \sum_{m=1}^{7}\tilde{a}_{qm,G}^{n+1} + \tilde{b}_{qm,G}^{n+1}\left|\tilde{V}_{G}^{n+1} - \tilde{V}_{qm}^{n+1} + \tilde{V}_{G}^{n} - \tilde{V}_{qm}^{n}\right|\right\}& \\ > K_{GS} + \sum_{q\neq q'}K_{qq'}\,.&\end{aligned} \tag{3-43b}$$

If this is the case, the beginning-of-time-step velocities are insufficient to determine the drag, and hence iteration must be performed using velocities estimated at $t = t^{n} + 1/2\,\Delta t$,

$$V_{q'q,\xi} = V_{q'q,\xi}^{*} = \frac{1}{2}\left[\tilde{V}_{q',\xi}^{n+1} - \tilde{V}_{q,\xi}^{n+1} + \tilde{V}_{q',\xi}^{n} - \tilde{V}_{q,\xi}^{n}\right], \text{and} \tag{3-44a}$$

$$V_{q,\xi} = V_{q,\xi}^{*} = \frac{1}{2}\left[\tilde{V}_{q,\xi}^{n+1} + \tilde{V}_{q,\xi}^{n}\right]. \tag{3-44b}$$

Now, we solve the equation

$$\underset{\sim}{\underline{S}}_{\xi}^{k}\,\delta\underset{\sim}{\underline{V}}_{\xi}^{n+1} = \underset{\sim}{\underline{D}}_{\xi}^{k}\,, \tag{3-45}$$

where $\delta\underset{\sim}{\underline{\tilde{V}}}_{\xi}^{n+1}$are the correction to $\underset{\sim}{\underline{\tilde{V}}}_{\xi}^{n+1}$. The matrix coefficients, again for the three-field case, are

$$s_{11,\xi}^{k} = \tilde{\tilde{\rho}}_{1,\xi}^{n+1} + \Delta t K_{1S,\xi}^{k} + \Delta t(K_{12,\xi}^{k} + K_{13,\xi}^{k}) - (\tilde{\alpha}_{1,eff,\xi}^{n+1})^{2}\tilde{\beta}_{G,\xi}^{n+1}\,, \tag{3-46a}$$

$$s_{12,\xi}^{k} = s_{21,\xi}^{k} = -\Delta t K_{12,\xi}^{k} - \tilde{\alpha}_{1,eff,\xi}^{n+1}\tilde{\beta}_{G,\xi}^{n+1}\tilde{\alpha}_{2,eff,\xi}^{n+1}\,. \tag{3-46b}$$

$$s_{22,\xi}^{k} = \tilde{\tilde{\rho}}_{2,\xi}^{n+1} + \Delta t K_{2S,\xi}^{k} + \Delta t(K_{12,\xi}^{k} + K_{23,\xi}^{k}) - (\tilde{\alpha}_{2,eff,\xi}^{n+1})^{2}\tilde{\beta}_{G,\xi}^{n+1}\,, \tag{3-46c}$$

$$s_{13,\xi}^{k} = s_{31,\xi}^{k} = -\Delta t K_{13,\xi}^{k} + \tilde{\alpha}_{1,eff,\xi}^{n+1}\tilde{\beta}_{G,\xi}^{n+1}\,, \tag{3-46d}$$

$$s_{23,\xi}^{k} = s_{32,\xi}^{k} = -\Delta t K_{23,\xi}^{k} + \tilde{\alpha}_{2,eff,\xi}^{n+1}\tilde{\beta}_{G,\xi}^{n+1} \text{, and} \tag{3-46e}$$

$$s_{33,\xi}^{k} = \tilde{\tilde{\rho}}_{3,\xi}^{n+1} + \Delta t K_{3S,\xi}^{k} + \Delta t\left(K_{13,\xi}^{k} + K_{23,\xi}^{k}\right) - \tilde{\beta}_{G,\xi}^{n+1}. \tag{3-46f}$$

where

$$K_{qS}^{k} = \frac{1}{2}\left[\tilde{a}_{qS}^{n+1} + \tilde{b}_{qS}^{n+1}\left|\tilde{V}_{q,\xi}^{k} + V_{q,\xi}^{n}\right|\right] \text{, and} \tag{3-47}$$

$$K_{qq',\xi}^{k} = \frac{1}{2}\left[\tilde{a}_{qq',\xi}^{n+1} + \tilde{b}_{qq',\xi}^{n+1}\left|\tilde{V}_{q',\xi}^{k} - \tilde{V}_{q,\xi}^{k} + \tilde{V}_{q',\xi}^{n} - \tilde{V}_{q,\xi}^{n}\right|\right]. \tag{3-48}$$

The $\underline{D}_{\xi}^{k}$ vector is given by

$$\begin{aligned} d_{q,\xi} = {} & \tilde{\tilde{\rho}}_{q,\xi}^{n}\tilde{V}_{q,\xi}^{n} - \tilde{\tilde{\rho}}_{q,\xi}^{n+1}\tilde{V}_{q,\xi}^{k} - \Delta t C\tilde{V}_{q,\xi} + \tilde{\eta}_{q,\zeta}^{n+1} \\ & + \tilde{\beta}_{q,\xi}^{n+1}\left[\tilde{V}_{G,\xi}^{k} - \tilde{V}_{G,\xi}^{n} - \tilde{\alpha}_{q1,eff,\xi}^{n+1}(\tilde{V}_{q1,\xi}^{k} - \tilde{V}_{q1,\xi}^{n}) - \tilde{\alpha}_{q2,eff,\xi}^{n+1}(\tilde{V}_{q2,\xi}^{k} - \tilde{V}_{q2,\xi}^{n}\right] \\ & - \Delta t\left[\tilde{a}_{qS,\xi}^{n+1} + \tilde{b}_{qS,\xi}^{n+1}\left|\frac{\tilde{V}_{q,\xi}^{k} + \tilde{V}_{q,\xi}^{n}}{2}\right|\right]\left(\frac{\tilde{V}_{q,\xi}^{k} + \tilde{V}_{q,\xi}^{n}}{2}\right) \\ & + \Delta t\sum_{q'}\left(\tilde{a}_{q'q,\xi}^{n+1} + \tilde{b}_{q'q,\xi}^{n+1}\left|\tilde{V}_{q'q,\xi}^{k}\right|\right)\tilde{V}_{q'q,\xi}^{k}, \end{aligned} \tag{3-49}$$

where

$$V_{q'q,\xi}^{k} = \frac{1}{2}\left[\tilde{V}_{q',\xi}^{k} - \tilde{V}_{q,\xi}^{k} + \tilde{V}_{q',\xi}^{n} - \tilde{V}_{q,\xi}^{n}\right]. \tag{3-50}$$

Absolute convergence would be on a suitably small value of $d_{q,\xi}$, but relative convergence of the vapor velocity is considered to be sufficient.

$$\left|\delta\tilde{V}_{G}^{n+1}/\tilde{V}_{G}^{n+1}\right| < \varepsilon_{v} \ . \tag{3-51}$$

The typical and default value for the convergence precision ε_{v} is 10^{-4}.

Following the velocity calculation, the velocity derivatives with respect to pressure must be calculated for use in Step 3. Assuming that the inter-field differences between the beginning and end-of-time-step velocities remain in the same sign, they can be obtained by differentiating the matrix equation for the velocities. Namely, we got in a matrix form

$$\underline{S}\frac{\partial V}{\partial p} = \underline{R}\,. \tag{3-52}$$

Equation (3-52) has the same coefficient matrix as before. Namely, for the first calculation the matrix is ***S*** in Eq. (3-40); for later iterations it is $\boldsymbol{S}^{k}$ in Eq. (3-45). The ***R*** vector is simply given by

$$r_{q,\lambda+} = \tilde{\alpha}_{q,\lambda+}^{n+1}\frac{\Delta t}{(r'_{i+1/2})^{\zeta}\Delta x_{i+1/2}}, \tag{3-53a}$$

$$r_{q,\tau+} = \tilde{\alpha}_{q,\tau+}^{n+1} \frac{\Delta t}{(r'_{i+1/2})^{\zeta} \Delta y_{k+1/2}} \text{, and} \tag{3-53b}$$

$$r_{q,\theta+} = \tilde{\alpha}_{q,\theta+}^{n+1} \frac{\Delta t}{\Delta z_{j+1/2}} . \tag{3-53c}$$

The evaluation of the velocity derivatives with respect to pressure in the three directions completes the major operation in Step 2.

Finally, the estimated vapor velocities obtained from converging the momentum equations are limited to 1.4 times the Courant velocity criterion. This is because vapor velocities can sometimes become large if step reductions in momentum coupling are determined in Step 1. A large increase in liquid/vapor slip cannot lead to an increase in surface area and associated momentum coupling until the next time step. Limiting the estimated vapor velocity allows the pressure iteration to converge, although without necessarily eliminating the pressure difference driving the velocity increase. Then the large vapor velocities can reappear in Step 4. Accommodation is accomplished in subsequent time steps by reducing the time-step size and/or increasing momentum coupling.

3.3. Pressure Iteration (Step 3)

Step 3 of the SIMMER-III four-step algorithm performs an iteration to obtain the end-of-time-step cell-edge velocities that are consistent with cell-centered pressures. During the pressure iteration, errors in some important variables are reduced to near zero. Since this is the central step of the fluid convection algorithm, a historical perspective is reviewed first. Then the following operations performed in Step 3 are described.

(1) Define expressions whose residuals are reduced,

(2) Expand each expression in the independent variables,

(3) Express all changes in terms of the cell pressure changes, which are obtained from a system of linear equations,

(4) Solve a system of equations for the cell pressure changes and update the other cell variables, and

(5) Check the convergence of pressure iteration.

Finally, the options for matrix solvers are described. The EOS model provides the state variables and their derivatives that are necessary to complete the pressure iterations. The definition and functional forms of these quantities are documented in the EOS model description[12].

3.3.1. Background

In SIMMER-II, it was attempted, in the pressure iteration, to reduce the error to near zero in the overall liquid mass for single-phase cells or the overall vapor mass for two-phase cells assuming that the derivatives of density with respect to pressure were constant. This approach resulted in inaccuracies in some situations requiring very short time steps or problems in vapor convection at two-phase/single-phase boundaries.

In AFDM, it was attempted to eliminate the SIMMER-II problems by forcing consistency between end-of-time-step pressure and the EOS. The important conservation relationships selected for AFDM to be reduced to near zero were: the overall densities of heavy liquid components, the density of a light liquid component and the overall densities of vapor mixture, and the vapor internal energy. Separated treatment of heavy and light liquid densities and conservation of vapor internal energy with the pressure-volume work term were crucial for obtaining stable and consistent results of pressure iteration. Other variables were extrapolated at the beginning of the pressure iteration and then re-evaluated using the converged velocities and pressure. Since compressibility of liquid components were modeled in the AFDM EOS, an internal EOS iteration was required within pressure iteration for obtaining the mechanical equilibrium between liquid volume fractions and EOS pressure such that the vapor volume fraction was computed consistently with the EOS pressure. This procedure sometimes had unacceptable computational penalty especially when a tabular EOS option was used in AFDM.

In SIMMER-III/SIMMER-IV, a basic approach for pressure iteration is direct extension of AFDM to a full multi-component system. The conservation relationships to be reduced to zero are further elaborated to separate liquids into three. Even after the numbers of liquid components and velocity fields are increased during later code improvement, a policy of grouping liquids into three is retained. A major improvement over AFDM is elimination of the internal EOS iteration to obtain mechanical equilibrium. This is done by compressing liquids by the cell pressure, not the EOS pressure, in the pressure iteration. As a result, the present EOS model defines the EOS pressure as a function of the cell pressure. The procedure set up then for the pressure iteration is to reduce the difference between the EOS pressure and the cell pressure to zero, without requiring the internal iteration.

3.3.2. Expressions for residual errors

The mathematical expressions providing residual errors that are to be reduced to zero in the pressure iteration are described. The absolute values are reduced of the results of six calculations to the residual quantities: the pressure residual, the four density residuals and the vapor internal energy residual with work term. These residuals were selected based on consideration on their sensitivities on pressure iteration and experience in AFDM.

First, to obtain a consistent pressure, the residual error in pressure is given by

$$\varepsilon_{ikj}^{k} = p_{EOS,ikj}^{k} - p_{cell,ikj}^{k} \, , \tag{3-54}$$

where $p_{EOS,ikj}^{k}$ denotes the EOS pressure and $p_{cell,ikj}^{k}$ the cell pressure, and k is the iteration index. The quantity $p_{EOS,ikj}^{k}$ calculated by the EOS model is defined as a function of

$$p_{EOS,ikj}^{k} = f\left(\alpha_S,\ \tilde{\bar{\rho}}_{Lm}^{k},\ (\tilde{e}_{Lm}^{n+1})_0,\ \tilde{\bar{\rho}}_{Gm}^{k},\ \tilde{T}_G^{k},\ \tilde{p}_{cell}^{k}\right), \tag{3-55}$$

where the structure volume fraction α_S was determined in Step 1, and the liquid internal energies are determined in Step 2. The other quantities are varied during the pressure iteration.

A call to the EOS routine provides $p^k_{EOS,ikj}$, $\tilde{v}^k_{Lm}$, $\tilde{\alpha}^k_G$ and $\tilde{e}^k_G$, and the derivatives of p^k_{EOS}, α^k_G and e^k_G with respect to $\bar{\rho}_{R1}$, $\bar{\rho}_{R2}$, $\bar{\rho}_{R3}$, $\bar{\rho}_G$, p_{cell} and T_G, where the subscripts R1 to R3 indicate three liquid groups. The expressions for these quantities are given in the EOS description[12)]. To avoid oscillation between single phase and two phase in successive iterations, a special adjustment procedure is implemented when a previously two-phase cell goes into single phase. This adjustment is performed for those cells where $\tilde{\alpha}^n_G > 0$ and $\tilde{\alpha}^k_G \tilde{\alpha}^{k-1}_G < 0$ such that the vapor field is coupled to one of the liquid fields in a similar fashion to Eq. (3.19) as described in **Section 3.2.2**. This must be done on all four boundaries of the cell by mass averaging both the velocities and the velocity derivatives with respect to pressure.

Second, the errors in mass conservation are reduced for the following four densities, which represent fuel material, steel material, sodium and vapor, respectively.

$$\bar{\rho}_{R1} = \bar{\rho}_{L1} + \bar{\rho}_{L4} + \bar{\rho}_{L6} + \bar{\rho}_{L7}\,, \tag{3-56a}$$

$$\bar{\rho}_{R2} = \bar{\rho}_{L2} + \bar{\rho}_{L5}\,, \tag{3-56b}$$

$$\bar{\rho}_{R3} = \bar{\rho}_{L3}\,, \text{and} \tag{3-56c}$$

$$\bar{\rho}_G = \bar{\rho}_{G1} + \bar{\rho}_{G2} + \bar{\rho}_{G3} + \bar{\rho}_{G4}\,. \tag{3-56d}$$

Then the errors in mass conservation are given in the general form by

$$D_{m,ikj} = \frac{\tilde{\bar{\rho}}^k_m - \tilde{\bar{\rho}}^n_m}{\Delta t} + \nabla \cdot \left(\tilde{\bar{\rho}}^n_m v^{n+1}_q\right), \tag{3-57}$$

for m=$R1$, $R2$, $R3$, G.

Third, the error in the vapor internal energy with pressure-volume work term is calculated by

$$\begin{aligned} D_{e_{G,ikj}} = {} & \frac{(\tilde{\bar{\rho}}^{n+1}_{G,ikj})_0 \tilde{e}^k_{G,ikj} - \tilde{\bar{\rho}}^n_{G,ikj} \tilde{e}^n_{G,ikj}}{\Delta t} + \nabla \cdot (\tilde{\bar{\rho}}^n_G \tilde{e}^n_G v^{n+1}_G) + p^k_{G,ikj} \nabla \cdot v^{n+1}_G \\ & + p^k_{G,ikj} \frac{\tilde{\alpha}^k_{G,ikj} - \tilde{\alpha}^n_{G,ikj}}{\Delta t}\,. \end{aligned} \tag{3-58}$$

The $\tilde{e}^k_{G,ikj}$ term is obtained from the EOS call necessary to evaluate Eq. (3-58). The pressure $p^k_{G,ikj}$ is calculated for the first pass to the pressure iteration (k=1) as

$$p^{k=1}_{G,ikj} = \mathrm{CVMGT}\left(p^k_{cell,ikj},\ 0,\ \hat{\alpha}_{G,ikj} > 0 \text{ and } \tilde{\alpha}^k_{G,ikj} > 0\right), \tag{3-59}$$

where $\hat{\alpha}_{G,ikj} = \tilde{\alpha}^n_{G,ikj}$ from Step 3 on the previous time step, and for the subsequent iterations calculated as

$$p^{k>1}_{G,ikj} = \mathrm{CVMGT}\left(p^k_{cell,ikj},\ 0,\ \tilde{\alpha}^k_{G,ikj} > 0 \text{ and } p^{k-1}_{G,ikj} > 0\right). \tag{3-60}$$

Here $\mathrm{CVMGT}(A,\ B,\ T)$ is a function that returns A if T is true, and B if T is false.

3.3.3. Expansion of residual errors

The six relationships defined in the previous section are each expanded to first order in a Taylor series, with assuming the macroscopic densities, the temperatures and the cell pressure being the independent variables. Namely, the six expressions are expanded in terms of $\Delta\bar{\rho}_{R1}$, $\Delta\bar{\rho}_{R2}$, $\Delta\bar{\rho}_{R3}$, $\Delta\bar{\rho}_G$, ΔT_G

and Δp_{cell}. After obtaining $\Delta\bar{\rho}_{R1}$, $\Delta\bar{\rho}_{R2}$ and $\Delta\bar{\rho}_{G}$, the individual material density components are obtained by assuming that the macroscopic density ratios within a given material to define mass residual are constant, or

$$\Delta_{L1} = \left(\frac{\tilde{\bar{\rho}}_{L1}^{n+1}}{\tilde{\bar{\rho}}_{R1}^{n+1}}\right)_0 \Delta\bar{\rho}_{R1} = x_{L1}\Delta_{R1}\ , \tag{3-61a}$$

$$\Delta\bar{\rho}_{L2} = \left(\frac{\tilde{\bar{\rho}}_{L2}^{n+1}}{\tilde{\bar{\rho}}_{R2}^{n+1}}\right)_0 \Delta\bar{\rho}_{R2} = x_{L2}\Delta\bar{\rho}_{R2}\ , \tag{3-61b}$$

$$\Delta\bar{\rho}_{L3} = \Delta\bar{\rho}_{R3}\ , \tag{3-61c}$$

$$\Delta\bar{\rho}_{L4} = \left(\frac{\tilde{\bar{\rho}}_{L4}^{n+1}}{\tilde{\bar{\rho}}_{R1}^{n+1}}\right)_0 \Delta\bar{\rho}_{R1} = x_{L4}\Delta\bar{\rho}_{R1}\ , \tag{3-61d}$$

$$\Delta\bar{\rho}_{L5} = \left(\frac{\tilde{\bar{\rho}}_{L5}^{n+1}}{\tilde{\bar{\rho}}_{R2}^{n+1}}\right)_0 \Delta\bar{\rho}_{R2} = x_{L5}\Delta\bar{\rho}_{R2}\ , \tag{3-61e}$$

$$\Delta\bar{\rho}_{L6} = \left(\frac{\tilde{\bar{\rho}}_{L6}^{n+1}}{\tilde{\bar{\rho}}_{R1}^{n+1}}\right)_0 \Delta\bar{\rho}_{R1} = x_{L6}\Delta\bar{\rho}_{R1} \tag{3-61f}$$

$$\Delta\bar{\rho}_{L7} = \left(\frac{\tilde{\bar{\rho}}_{L7}^{n+1}}{\tilde{\bar{\rho}}_{R1}^{n+1}}\right)_0 \Delta\bar{\rho}_{R1} = x_{L7}\Delta\bar{\rho}_{R1}\ \text{, and} \tag{3-61g}$$

$$\Delta\bar{\rho}_{Gm} = \left(\frac{\tilde{\bar{\rho}}_{Gm}^{n+1}}{\tilde{\bar{\rho}}_{G}^{n+1}}\right)_0 \Delta\bar{\rho}_{G} = x_{Gm}\Delta\bar{\rho}_{G}\ \text{, for } m\text{=1, 2, 3 and 4.} \tag{3-61h}$$

The resultant expressions are given by

$$\varepsilon_{ikj} + \frac{\partial\varepsilon_{ikj}}{\partial p_{cell,ikj}}\Delta p_{cell,ikj} + \sum_{m=R1}^{G}\frac{\partial\varepsilon_{ikj}}{\partial\bar{\rho}_{m,ikj}}\Delta\bar{\rho}_{m,ikj} + \frac{\partial\varepsilon_{ikj}}{\partial T_{G,ikj}}\Delta T_{G,ikj} = 0\ , \tag{3-62}$$

for the expansion of EOS,

$$D_{m,ikj} + \frac{\partial D_{m,ikj}}{\partial\bar{\rho}_{m,ikj}}\Delta\bar{\rho}_{m,ikj} + \frac{\partial D_{m,ijk}}{\partial p_{cell,ikj}}\Delta p_{cell,ikj} + \frac{\partial D_{m,ijk}}{\partial p_{cell,i\pm1,k\pm1,j\pm1}}\Delta p_{cell,i\pm1,k\pm1,j\pm1} = 0\ , \tag{3-63}$$

for the expansion of the mass conservation relationships for m= $R1$, $R2$, $R3$ and G, and

$$\begin{aligned} D_{e_{G,ikj}} &+ \frac{\partial D_{e_{G,ikj}}}{\partial e_{G,ikj}} \left[\sum_{m=R1}^{G} \frac{\partial e_{G,ikj}}{\partial \vec{\rho}_{m,ikj}} \Delta \vec{\rho}_{m,ikj} + \frac{\partial e_{G,ikj}}{\partial T_{G,ikj}} \Delta T_{G,ikj} + \frac{\partial e_{G,ikj}}{\partial p_{cell,ikj}} \Delta p_{cell,ikj} \right] \\ &+ \frac{\partial D_{e_{G,ikj}}}{\partial T_{G,ikj}} \Delta T_{G,ikj} + \sum_{m=R1}^{G} \frac{\partial D_{e_{G,ikj}}}{\partial \bar{\rho}_{m,ikj}} \Delta \bar{\rho}_{m,ikj} + \frac{\partial D_{e_{G,ikj}}}{\partial p_{cell,ikj}} \Delta p_{cell,ikj} \\ &+ \frac{\partial D_{e_{G,ikj}}}{\partial p_{cell,i\pm1,k\pm1,j\pm1}} \Delta p_{cell,i\pm1,k\pm1,j\pm1} = 0 \,, \end{aligned} \tag{3-64}$$

for the expansion of the vapor energy equation, where (*i*±1, *k*±1, *j*±1) means that six terms are summed for (*i*+1, *k*, *j*), (*i*-1, *k*, *j*), (*i*, *k*+1, *j*), (*i*, *k*-1, *j*), (*i*, *k*, *j*+1) and (*i*, *k*, *j*-1).

3.3.4. Formulation of pressure equation

The equations (3-62) - (3-64) are solved using the EOS derivatives, the derivatives from the higher-order differencing and the constraint that the velocities depend only on pressure using the velocity derivatives from Step 2. Algebraic manipulation of Eqs. (3-62) - (3-64) resulted in a matrix equation of a form

$$\begin{aligned} \underline{A}_{ikj} \Delta \vec{x}_{ikj} = &- \vec{B}_{1,ikj} \Delta p_{i-1,k,j} - \vec{B}_{2,ij} \Delta p_{i+1,k,j} - \vec{B}_{3,ikj} \Delta p_{i,k-1,j} - \vec{B}_{4,ikj} \Delta p_{i,k+1,j} \\ &- \vec{B}_{5,ikj} \Delta p_{i,k,j-1} - \vec{B}_{6,ikj} \Delta p_{i,k,j+1} - \vec{S}_{ikj} \,, \end{aligned} \tag{3-65}$$

where the vector $\Delta \vec{x}_{ikj}$ represents the six residuals, $\Delta p_{cell,ikj}$, $\Delta \bar{\rho}_{R1,ikj}$, $\Delta \bar{\rho}_{R2,ikj}$, $\Delta \bar{\rho}_{R3,ikj}$, $\Delta \bar{\rho}_{G,ikj}$ and $\Delta T_{G,ij}$. The coefficient matrix $\underline{A}_{ikj}$ is 6 by 6, and expressed as

$$\underline{A}_{ikj} = \begin{bmatrix} a_{11} & a_{12} & a_{13} & a_{14} & a_{15} & a_{16} \\ a_{21} & a_{22} & 0 & 0 & 0 & 0 \\ a_{31} & 0 & a_{33} & 0 & 0 & 0 \\ a_{41} & 0 & 0 & a_{44} & 0 & 0 \\ a_{51} & 0 & 0 & 0 & a_{55} & 0 \\ a_{61} & a_{62} & a_{63} & a_{64} & a_{65} & a_{66} \end{bmatrix} . \tag{3-66}$$

The values of coefficients involve the derivatives of ε_{ikj}, $D_{m,ikj}$ and $D_{e_{G,ikj}}$ given in a generalized form by

$$a_{rs} = \frac{\partial \Psi_r}{\partial \xi_s} \text{ for } r\text{=1, 2, ..., 5 and } s\text{=1,2, ..., 6} \,, \tag{3-67}$$

where

$$\Psi_1 = \varepsilon_{ikj} \,, \tag{3-68a}$$

$$\Psi_2 = D_{R1,ikj} \,, \tag{3-68b}$$

$$\Psi_3 = D_{R2,ikj} \,, \tag{3-68c}$$

$$\Psi_4 = D_{R3,ikj} \,, \tag{3-68d}$$

$$\Psi_5 = D_{G,ikj} \text{,} \tag{3-68e}$$

$$\xi_1 = p_{cell,ikj} \text{,} \tag{3-69a}$$

$$\xi_2 = \bar{\rho}_{R1,ikj} \text{,} \tag{3-69b}$$

$$\xi_3 = \bar{\rho}_{R2,ikj} \text{,} \tag{3-69c}$$

$$\xi_4 = \bar{\rho}_{R3,ikj} \text{,} \tag{3-69d}$$

$$\xi_5 = \bar{\rho}_{G,ikj} \text{,} \tag{3-69e}$$

$$\xi_6 = T_{G,ikj} \text{, and} \tag{3-69f}$$

$$a_{6s} = \frac{\partial D_{e_{G,ikj}}}{\partial \xi_s} + \frac{\partial D_{e_{G,ikj}}}{\partial e_{G,ikj}} \frac{\partial e_{G,ikj}}{\partial \xi_s} \text{.} \tag{3-70}$$

The B vectors of Eq. (3.65) are given by

$$\vec{B}_{1,ikj} = \begin{bmatrix} \partial\Psi_1/\partial p_{i-1,k,j} \\ \partial\Psi_2/\partial p_{i-1,k,j} \\ \partial\Psi_3/\partial p_{i-1,k,j} \\ \partial\Psi_4/\partial p_{i-1,k,j} \\ \partial\Psi_5/\partial p_{i-1,k,j} \\ \partial D_{e_{G,ikj}}/\partial p_{i-1,k,j} \end{bmatrix}, \vec{B}_{2,ikj} = \begin{bmatrix} \partial\Psi_1/\partial p_{i+1,k,j} \\ \partial\Psi_2/\partial p_{i+1,k,j} \\ \partial\Psi_3/\partial p_{i+1,k,j} \\ \partial\Psi_4/\partial p_{i+1,k,j} \\ \partial\Psi_5/\partial p_{i+1,k.j} \\ \partial D_{e_{G,ijk}}/\partial p_{i+1,k,j} \end{bmatrix}, \vec{B}_{3,ikj} = \begin{bmatrix} \partial\Psi_1/\partial p_{i,k-1,j} \\ \partial\Psi_2/\partial p_{i,k-1,j} \\ \partial\Psi_3/\partial p_{i,k-1,j} \\ \partial\Psi_4/\partial p_{i,k-1,j} \\ \partial\Psi_5/\partial p_{i,k-1,j} \\ \partial D_{e_{G,ijk}}/\partial p_{i,k-1,j} \end{bmatrix},$$

$$\vec{B}_{4,ikj} = \begin{bmatrix} \partial\Psi_1/\partial p_{i,k+1,j} \\ \partial\Psi_2/\partial p_{i,k+1,j} \\ \partial\Psi_3/\partial p_{i,k+1,j} \\ \partial\Psi_4/\partial p_{i,k+1,j} \\ \partial\Psi_5/\partial p_{i,k+1,j} \\ \partial D_{e_{G,ikj}}/\partial p_{i,k+1,j} \end{bmatrix}, \vec{B}_{5,ikj} = \begin{bmatrix} \partial\Psi_1/\partial p_{i,k,j-1} \\ \partial\Psi_2/\partial p_{i,k,j-1} \\ \partial\Psi_3/\partial p_{i,k,j-1} \\ \partial\Psi_4/\partial p_{i,k,j-1} \\ \partial\Psi_5/\partial p_{i,k,j-1} \\ \partial D_{e_{G,ikj}}/\partial p_{i,k,j-1} \end{bmatrix}, \vec{B}_{6,ikj} = \begin{bmatrix} \partial\Psi_1/\partial p_{i,k,j+1} \\ \partial\Psi_2/\partial p_{i,k,j+1} \\ \partial\Psi_3/\partial p_{i,k,j+1} \\ \partial\Psi_4/\partial p_{i,k,j+1} \\ \partial\Psi_5/\partial p_{i,k,j+1} \\ \partial D_{e_{G,ikj}}/\partial p_{i,k,j+1} \end{bmatrix},$$

$$\vec{S}_{ikj} = \begin{bmatrix} \varepsilon_{ikj} \\ D_{R1,ikj} \\ D_{R2,ikj} \\ D_{R3,ikj} \\ D_{G,ikj} \\ D_{e_{G,ikj}} \end{bmatrix} \text{, and } \Delta\vec{x}_{ikj} = \begin{bmatrix} \Delta p_{ikj} \\ \Delta\bar{\rho}_{R1,ikj} \\ \Delta\bar{\rho}_{R2,ikj} \\ \Delta\bar{\rho}_{R3,ikj} \\ \Delta\bar{\rho}_{G,ikj} \\ \Delta T_{G,ikj} \end{bmatrix} \text{.} \tag{3-71}$$

To examine these in more in detail, the first row of $\underline{A}_{ikj}$ involves the derivatives of ε_{ikj} defined by

$$\varepsilon_{ikj} = p_{EOS.ikj}(\alpha_S,\ \tilde{\bar{\rho}}_{Lm}^{n+1},\ (\tilde{e}_{Lm}^{n+1})_0,\ \tilde{\bar{\rho}}_{Gm}^{n+1},\ \tilde{T}_G^{n+1},\ \tilde{p}_{cell}^{n+1}) - \tilde{p}_{cell,ikj}^{n+1}\,. \tag{3-72}$$

In the EOS model, both the two-phase and single-phase pressures, $p_{2\varphi,ikj}$ and $p_{1\varphi,ikj}$, are computed and the maximum is taken to get $p_{EOS,ikj}$, unless specified otherwise by user input. Let us obtain the derivatives for the two-phase case first. The element a_{11} is written as

$$a_{11} = \frac{\partial \varepsilon_{ikj}}{\partial p_{cell,ikj}} = \frac{\partial p_{EOS,ikj}}{\partial p_{cell,ikj}} - 1\,, \tag{3-73}$$

where $p_{EOS,ikj}$ comes from the EOS as

$$p_{EOS,ikj} = \sum_m \left[\frac{\rho_{Gm} R_M T_G}{1 - a_{G1,M}\rho_{Gm}} - \frac{\rho_{Gm}^2 a_{G2,M} \left(\frac{T_G}{T_{Crt,M}}\right)^{0.2}}{1 - a_{G3,M}\rho_{Gm}} \right] = \sum_m p_{Gm}\,. \tag{3-74}$$

Then the partial derivative of $p_{EOS,ikj}$ with respect to $p_{cell,ikj}$ is defined as

$$\frac{\partial p_{EOS,ikj}}{\partial p_{ccll,ikj}} = \sum_{Gm} \frac{\partial p_{Gm}}{\partial \rho_{Gm}} \left[\sum_{Lm} \frac{\partial \rho_{Gm}}{\partial v_{Lm}} \frac{\partial v_{Lm}}{\partial p_{cell}} \right]. \tag{3-75}$$

where the specific volume is defined as the inverse of microscopic density $v_{Lm} = 1/\rho_{Lm}$. Using the current EOS functions, the derivatives of the partial pressure of vapor components with respect to the vapor microscopic density is given be

$$\frac{\partial p_{Gm}}{\partial \rho_{Gm}} = \frac{R_M T_G}{(1 - a_{G1,M}\rho_{Gm})^2} - \frac{(2 + a_{G3M}\rho_{Gm})\rho_{Gm} a_{G2,M} \left(\frac{T_G}{T_{Crt,M}}\right)^{0.2}}{(1 + a_{G3M}\rho_{Gm})^2}\,, \tag{3-76}$$

where

$$\rho_{Gm} = \frac{\bar{\rho}_{Gm}}{(1 - \alpha_S)} \quad \text{if} \quad \alpha_G < 0\,, \text{or}$$

$$\rho_{Gm} = \frac{\bar{\rho}_{Gm}}{1 - \alpha_S - (1 - \alpha_0)\sum_m \bar{\rho}_{Lm} v_{Lm}}\,, \text{ if } \quad \alpha_0 \geq 0\,, \text{and}$$

$$\frac{\partial \rho_{Gm}}{\partial v_{Lm}} = 0\,, \text{ if } \quad \alpha_G < 0\,, or$$

$$\frac{\partial \rho_{Gm}}{\partial v_{Lm}} = \frac{\rho_{Gm}}{1 - \alpha_S - (1 - \alpha_0)\alpha_L}[(1 - \alpha_0)\bar{\rho}_{Lm}]\ , \text{ if } \quad \alpha_0 \geq 0\,,$$

where

$$\alpha_L = \sum_m \bar{\rho}_{Lm} v_{Lm}\,.$$

The derivatives of the liquid specific volumes with respect to cell pressure is

$$\frac{\partial v_{Lm}}{\partial p_{cell}} = \left(\frac{\partial v_{LM}}{\partial p}\right)_{e_{Lm}}, \tag{3-77}$$

as given by the EOS relationships. This completes the necessary expressions for a_{11} for the two-phase case.

The coefficient a_{12} is given as

$$\begin{aligned} a_{12} = \frac{\partial \varepsilon_{ikj}}{\partial \bar{\rho}_{R1,ikj}} = \frac{\partial p_{EOS,ikj}}{\partial \bar{\rho}_{R1,ikj}} \\ = \left(\frac{\bar{\rho}_{L1}}{\bar{\rho}_{R1}}\right)_0 \frac{\partial p_{EOS,ikj}}{\partial \bar{\rho}_{L1,ikj}} + \left(\frac{\bar{\rho}_{L4}}{\bar{\rho}_{R1}}\right)_0 \frac{\partial p_{EOS,ikj}}{\partial \bar{\rho}_{L4,ikj}} + \left(\frac{\bar{\rho}_{L6}}{\bar{\rho}_{R1}}\right)_0 \frac{\partial p_{EOS,ikj}}{\partial \bar{\rho}_{L6,ikj}} \\ + \left(\frac{\bar{\rho}_{L7}}{\bar{\rho}_{R1}}\right)_0 \frac{\partial p_{EOS,ikj}}{\partial \bar{\rho}_{L7,ikj}}, \end{aligned} \tag{3-78}$$

where the derivative of $p_{EOS,ikj}$ with respect to the liquid density is described as

$$\frac{\partial p_{EOS}}{\partial \bar{\rho}_{Lm}} = \sum_{Gm} \frac{\partial p_{Gm}}{\partial \rho_{Gm}} \left(\frac{\partial \rho_{Gm}}{\partial \bar{\rho}_{Lm}}\right), \tag{3-79}$$

for the two-phase case, where ρ_{Gm} is the microscopic density of vapor component *m*. The new expression in the parenthesis is

$$\frac{\partial \rho_{Gm}}{\partial \bar{\rho}_{Lm}} = 0 \quad \text{if} \quad \alpha_G < 0\text{, and} \tag{3-80}$$

$$\frac{\partial \rho_{Gm}}{\partial \bar{\rho}_{Lm}} = \frac{(1-\alpha_0)\rho_{Gm} v_{Lm}}{1-\alpha_S-(1-\alpha_0)\sum_m \bar{\rho}_{Lm} v_{Lm}}, \text{ if } \alpha_G \geq 0 \tag{3-81}$$

Similar expressions can be written for a_{13} and a_{14} as

$$a_{13} = \left(\frac{\bar{\rho}_{L2}}{\bar{\rho}_{R2}}\right)_0 \frac{\partial p_{EOS,ikj}}{\partial \bar{\rho}_{L2,ikj}} + \left(\frac{\bar{\rho}_{L5}}{\bar{\rho}_{R2}}\right)_0 \frac{\partial p_{EOS,ikj}}{\partial \bar{\rho}_{L5,ikj}}\text{, and} \tag{3-82}$$

$$a_{14} = \frac{\partial p_{EOS,ij}}{\partial \bar{\rho}_{L3,ij}}. \tag{3-83}$$

The derivative with respect to the vapor density is

$$a_{15} = \frac{\partial p_{EOS,ikj}}{\partial \bar{\rho}_{G,ikj}} = \sum_{Gm} \left(\frac{\bar{\rho}_{Gm,ikj}}{\bar{\rho}_{G,ikj}}\right)_0 \frac{\partial p_{EOS,ikj}}{\partial \bar{\rho}_{Gm,ikj}}, \tag{3-84}$$

where

$$\frac{\partial p_{EOS}}{\partial \bar{\rho}_{Gm}} = \frac{\partial p_{Gm}}{\partial \rho_{Gm}} \left(\frac{\partial \rho_{Gm}}{\partial \bar{\rho}_{Gm}}\right), \tag{3-85a}$$

with

$$\frac{\partial \rho_{Gm}}{\partial \bar{\rho}_{Gm}} = \frac{1}{max[\alpha_0(1-\alpha_S),\ 1-\alpha_S-(1-\alpha_0)\sum_m \bar{\rho}_{Lm} v_{Lm}]} . \tag{3-85b}$$

Similarly, a_{16} is expressed as

$$a_{16} = \frac{\partial \varepsilon_{ikj}}{\partial T_{G,ikj}} = \frac{\partial p_{EOS,ikj}}{\partial T_{G,ikj}} = \sum_{Gm} \frac{\partial p_{Gm,ikj}}{\partial T_G} , \tag{3-86a}$$

for the two-phase case, with

$$\frac{\partial p_{Gm}}{\partial T_G} = \frac{\rho_{Gm} R_M}{1-a_{G1,M}\rho_{Gm}} - \frac{0.2\rho_{Gm}^2 a_{G2,M}}{(1+a_{G3M}\rho_{Gm})T_{Crt,M}} \left(\frac{T_{Crt,M}}{T_G}\right)^{0.8} . \tag{3-86b}$$

The definition of the single-phase case is the $p_{1\phi} > p_G$, where

$$p_{1\phi} = p_{cell} - \frac{\alpha_G}{\partial \alpha_G / \partial p_{cell}} , \tag{3-87a}$$

such that

$$\varepsilon = -\frac{\alpha_G}{\partial \alpha_G / \partial p_{cell}} . \tag{3-87b}$$

In determining the derivatives for the expression of ε, only the numerator is differentiated. This makes the expansion equation become

$$\alpha_{G,ikj} + \frac{\partial \alpha_{G,ikj}}{\partial p_{cell,ikj}} \Delta p_{cell,ikj} + \sum_{m=R1}^{G} \frac{\partial \alpha_{G,ikj}}{\partial \bar{\rho}_{m,ikj}} \Delta \bar{\rho}_{m,ikj} + \frac{\partial \alpha_{G,ikj}}{\partial T_{G,ikj}} \Delta T_{G,ikj} = 0 . \tag{3-88}$$

Convergence of the iteration means $\alpha_G \approx 0$. For a flag, when $p_{1\varphi} > p_G$ and a cell is single-phase, the α_G returned from the EOS should be set to -10^{-20}. However, a positive value while in the EOS is still acceptable. Because the vapor volume fraction is defined by

$$\alpha_G = 1 - \alpha_S - \sum_{Lm} \bar{\rho}_{Lm} v_{Lm} , \tag{3-89}$$

the derivative with respect to cell pressure is given by the EOS as

$$\frac{\partial \alpha_G}{\partial p_{cell}} = -\sum_{Lm} \bar{\rho}_{Lm} \left(\frac{\partial v_{Lm}}{\partial p}\right)_{e_{Lm}} . \tag{3-90}$$

Then, with the above prescription, for the single-phase case, the coefficients a_{11}- a_{16} are

$$a_{11} = \frac{\partial \varepsilon_{ikj}}{\partial p_{cell,ikj}} = -1 \tag{3-91}$$

$$a_{12} = \frac{\partial \varepsilon_{ikj}}{\partial \bar{\rho}_{R1,ikj}} = -\frac{(\partial \alpha_G / \partial \bar{\rho}_{R1})_{ikj}}{(\partial \alpha_G / \partial p_{cell})_{ikj}} \text{, with} \tag{3-92a}$$

$$\frac{\partial \alpha_G}{\partial \bar{\rho}_{R1}} = -\left[\left(\frac{\bar{\rho}_{L1}}{\bar{\rho}_{R1}}\right)_0 v_{L1} + \left(\frac{\bar{\rho}_{L4}}{\bar{\rho}_{R1}}\right)_0 v_{L4} + \left(\frac{\bar{\rho}_{L6}}{\bar{\rho}_{R1}}\right)_0 v_{L6} + \left(\frac{\bar{\rho}_{L7}}{\bar{\rho}_{R1}}\right)_0 v_{L7}\right] \tag{3-92b}$$

$$a_{13} = \frac{1}{(\partial \alpha_G / \partial p_{cell})}\left[\left(\frac{\bar{\rho}_{L2}}{\bar{\rho}_{R2}}\right)_0 v_{L2} + \left(\frac{\bar{\rho}_{L5}}{\bar{\rho}_{R2}}\right)_0 v_{L5}\right] \tag{3-93}$$

$$a_{14} = \frac{v_{L3}}{(\partial \alpha_G / \partial p_{cell})}\text{ , and} \tag{3-94}$$

$$a_{15} = a_{16} = 0\,. \tag{3-95}$$

For a_{21}, defined as

$$a_{21} = \frac{\partial D_{R1,ikj}}{\partial p_{cell}}, \tag{3-96a}$$

we need the expression for $D_{R1,ikj}$

$$D_{R1,ikj} = \frac{\tilde{\bar{\rho}}_{R1}^{n+1} - \tilde{\bar{\rho}}_{R1}^{n}}{\Delta t} + \sum_{m \in R1}\left[\frac{\Delta_i \langle \tilde{\bar{\rho}}_m^n r^\zeta \tilde{u}_{R1}^{n+1} \rangle_{k,j}}{r_i^\zeta \Delta x_i} + \frac{\Delta_k \langle \tilde{\bar{\rho}}_m^n \tilde{w}_{R1}^{n+1} \rangle_{i,k}}{\Delta y_k} + \frac{\Delta_j \langle \tilde{\bar{\rho}}_m^n \tilde{v}_{R1}^{n+1} \rangle_{i,k}}{\Delta z_j}\right]. \tag{3-96b}$$

For the donor-cell differencing, there are no non-linear terms and we can sum all the $\tilde{\bar{\rho}}_m^n$ to $\tilde{\bar{\rho}}_{R1}^n$ inside the brackets. This means, for the donor-cell case,

$$a_{21} = \frac{1}{r^\zeta \Delta x_i}\left[\Delta_i \frac{\partial \langle \tilde{\bar{\rho}}_{R1}^n r^\zeta \tilde{u}_{R1}^{n+1} \rangle_{k,j}}{\partial p_{ikj}}\right] + \frac{1}{\Delta y_j}\left[\Delta_k \frac{\partial \langle \tilde{\bar{\rho}}_{R1}^n \tilde{w}_{R1}^{n+1} \rangle_{j,i}}{\partial p_{ikj}}\right] + \frac{1}{\Delta z_j}\left[\Delta_j \frac{\partial \langle \tilde{\bar{\rho}}_{R1}^n \tilde{v}_{R1}^{n+1} \rangle_{i,k}}{\partial p_{ikj}}\right]. \tag{3-97}$$

where

$$\begin{aligned} \Delta_i \frac{\partial \langle \tilde{\bar{\rho}}_{R1}^n r^\zeta \tilde{u}_{R1}^{n+1} \rangle_{k,i}}{\partial p_{ikj}} \\ &= r_{i+1/2}^\zeta \frac{\partial u_{i+1/2,k,j}}{\partial p_{ikj}} \begin{cases} \tilde{\bar{\rho}}_{R1,ikj}^n & \tilde{u}_{i+1/2,k,j}^{n+1} \geq 0 \\ \tilde{\bar{\rho}}_{R1,i+1,j}^n & \tilde{u}_{i+1/2,k,j}^{n+1} < 0 \end{cases} \\ &- r_{i+1/2}^\zeta \frac{\partial u_{i-1/2,k,j}}{\partial p_{ikj}} \begin{cases} \tilde{\bar{\rho}}_{R1,ikj}^n & \tilde{u}_{i-1/2,k,j}^{n+1} < 0 \\ \tilde{\bar{\rho}}_{R1,i-1,k,j}^n & \tilde{u}_{i-1/2,k,j}^{n+1} \geq 0 \end{cases} \end{aligned} \tag{3-98a}$$

$$\Delta_k \frac{\partial \langle \tilde{\bar{\bar{\rho}}}_{R1}^{n} \widetilde{w}_{R1}^{n+1} \rangle_{j,i}}{\partial p_{ikj}} = \frac{\partial \widetilde{w}_{i,k+1/2,j}}{\partial p_{ij}} \begin{cases} \tilde{\bar{\bar{\rho}}}_{R1,ikj}^{n} & \widetilde{w}_{i,k+1/2,j}^{n+1} \geq 0 \\ \tilde{\bar{\bar{\rho}}}_{R1,i,k+1,j}^{n} & \widetilde{w}_{i,k+1/2,j}^{n+1} < 0 \end{cases} - \frac{\partial w_{i,k-\frac{1}{2},j}}{\partial p_{ikj}} \begin{cases} \tilde{\bar{\bar{\rho}}}_{R1,ikj}^{n} & \widetilde{w}_{i,k-\frac{1}{2},j}^{n+1} < 0 \\ \tilde{\bar{\bar{\rho}}}_{R1,i,k-1,j}^{n} & \widetilde{w}_{i,k-\frac{1}{2},j}^{n+1} \geq 0 \end{cases} \tag{3-98b}$$

$$\Delta_j \frac{\partial \langle \tilde{\bar{\bar{\rho}}}_{R1}^{n} \tilde{v}_{R1}^{n+1} \rangle_{i,k}}{\partial p_{ikj}} = \frac{\partial v_{i,k,j+1/2}}{\partial p_{ikj}} \begin{cases} \tilde{\bar{\bar{\rho}}}_{R1,ikj}^{n} & \tilde{v}_{i,k,j+1/2}^{n+1} \geq 0 \\ \tilde{\bar{\bar{\rho}}}_{R1,i,k,j+1}^{n} & \tilde{v}_{i,k,j+1/2}^{n+1} < 0 \end{cases} - \frac{\partial v_{i,k,j-1/2}}{\partial p_{ikj}} \begin{cases} \tilde{\bar{\bar{\rho}}}_{R1,ikj}^{n} & \tilde{v}_{i,k,j-1/2}^{n+1} < 0 \\ \tilde{\bar{\bar{\rho}}}_{R1,i,k,j-1}^{n} & \tilde{v}_{i,k,j-1/2}^{n+1} \geq 0 \end{cases} \tag{3-98c}$$

The velocity derivatives with respect to pressure come from Step 2. We have

$$\frac{\partial u_{i-1/2,k,j}}{\partial p_{ikj}} = -\frac{\partial u_{i-1/2,k,j}}{\partial p_{i-1,k,j}} \;, \tag{3-99a}$$

$$\frac{\partial w_{i,k-1/2,j}}{\partial p_{ikj}} = -\frac{\partial w_{i,k-1/2,j}}{\partial p_{i,k-1,j}} \text{, and} \tag{3-99b}$$

$$\frac{\partial v_{i,k,j-1/2}}{\partial p_{ikj}} = -\frac{\partial v_{i,k,j-1/2}}{\partial p_{i,k,j-1}} , \tag{3-99c}$$

for determining derivatives on the left and right boundaries.

The terms a_{22}, a_{31} and a_{33} are given by

$$a_{22} = \frac{\partial D_{R1,ikj}}{\partial \tilde{\bar{\bar{\rho}}}_{R1,ikj}^{n+1}} = \frac{1}{\Delta t}, \tag{3-100}$$

$$a_{3-1} = \frac{\partial D_{R2,ikj}}{\partial p_{cell,ikj}} \text{, and} \tag{3-101}$$

$$a_{3-1} = \frac{1}{\Delta t}. \tag{3-102}$$

where a_{3-1} is evaluated similarly to a_{21} with $R2$ replacing $R1$. The terms a_{41}, a_{44}, a_{51} and a_{55} all involve errors of density equations and can be obtained similarly. The term a_{61} involves an error in vapor energy equation and is written as

$$a_{61} = \frac{\partial D_{e_{G,ikj}}}{\partial p_{cell,ikj}} + \frac{\partial D_{e_{G,ikj}}}{\partial e_{G,ikj}} \frac{\partial e_{G,ikj}}{\partial p_{cell,ikj}} . \tag{3-103}$$

The error $D_{e_{G,ikj}}$ is expressed, for the donor-cell option, as

$$\begin{aligned} D_{e_{G,ikj}} = & \frac{(\tilde{\bar{\rho}}^{n+1}_{G,ikj})_0 \tilde{e}^n_{G,ikj} - \tilde{\bar{\rho}}^n_{G,ikj} \tilde{e}^n_{G,ikj}}{\Delta t} \\ & + \left[\frac{\Delta_i \left\langle \tilde{\bar{\rho}}^n_G \tilde{e}^n_G r^\zeta \tilde{u}^n_G \right\rangle_{k,j}}{r_i^\zeta \Delta x_i} + \frac{\Delta_k \langle \tilde{\bar{\rho}}^n_G \tilde{e}^n_G \widetilde{w}^n_G \rangle_{j,i}}{\Delta y_k} + \frac{\Delta_j \langle \tilde{\bar{\rho}}^n_G \tilde{e}^n_G \tilde{v}^n_G \rangle_{i,k}}{\Delta z_j} \right] \\ & + \frac{\tilde{p}^{n+1}_{2\varphi,ikj} \left[\tilde{\alpha}^{n+1}_{G,ikj} - \alpha^n_{G,ikj} \right]}{\Delta t} \\ & + \tilde{p}^{n+1}_{2\varphi,ikj} \left[\frac{\Delta_i \left\langle \tilde{\alpha}^n_G r^\zeta \tilde{u}^{n+1}_G \right\rangle_{k,j}}{r_i^\zeta \Delta x_i} + \frac{\Delta_k \langle \tilde{\alpha}^n_G \widetilde{w}^{n+1}_G \rangle_{j,i}}{\Delta y_k} + \frac{\Delta_j \langle \tilde{\alpha}^n_G \tilde{v}^{n+1}_G \rangle_{i,k}}{\Delta z_j} \right], \end{aligned} \tag{3-104}$$

where $\tilde{p}^{n+1}_{2\varphi,ikj} = \tilde{p}^{n+1}_{cell,ikj}$ for a cell that has been two-phase throughout the pressure iteration, and $\tilde{p}^{n+1}_{2\varphi,ikj} =$ 0 otherwise. The derivative with respect to cell pressure is given by

$$\begin{aligned} \frac{\partial D_{e_{G,ikj}}}{\partial p_{cell,ikj}} = & \frac{1}{\Delta t} \left\{ \left[\tilde{\alpha}^{n+1}_{G,ikj} - \tilde{\alpha}^n_{G,ikj} \right] + \tilde{p}^{n+1}_{ceell,ikj} \left(\frac{\partial \alpha^{n+1}_{G,ikj}}{\partial p_{cell,ikj}} \right) \right\} \\ & + \left[\frac{\Delta_i \left\langle \tilde{\alpha}^n_G r^\zeta \tilde{u}^n_G \right\rangle_{k,j}}{r_i^\zeta \Delta x_i} + \frac{\Delta_k \langle \tilde{\alpha}^n_G \widetilde{w}^n_G \rangle_{j,i}}{\Delta y_k} + \frac{\Delta_j \langle \tilde{\alpha}^n_G \tilde{v}^n_G \rangle_{i,k}}{\Delta z_j} \right] \\ & + \tilde{p}^{n+1}_{ceell,ikj} \left\{ \frac{1}{r_i^\zeta \Delta x_i} \left[\Delta_i \frac{\partial \left\langle \tilde{\alpha}^n_G r^\zeta \tilde{u}^{n+1}_G \right\rangle_{k,j}}{\partial p_{ikj}} \right] + \frac{1}{\Delta y_j} \left[\Delta_k \frac{\partial \langle \tilde{\alpha}^n_G \widetilde{w}^{n+1}_G \rangle_{i,k}}{\partial p_{ikj}} \right] \right. \\ & \left. + \frac{1}{\Delta z_j} \left[\Delta_j \frac{\partial \langle \tilde{\alpha}^n_G \tilde{v}^{n+1}_G \rangle_{i,k}}{\partial p_{ikj}} \right] \right\} , \end{aligned} \tag{3-105}$$

for $p_{2\varphi,ikj} = p_{cell,ikj}$, or

$$\frac{\partial D_{e_{G,ikj}}}{\partial p_{cell,ikj}} = 0 \text{ for } p_{2\varphi,ikj} = 0 . \tag{3-106}$$

With the vapor volume fraction playing the role of density, all terms in the above expression can be determined using relationships already defined. The second term in a_{61} is only non-zero when $\alpha_G > 0$. The derivatives with respect to vapor energy is given by

$$\frac{\partial D_{e_{G,ikj}}}{\partial e_{G,ikj}} = \left(\tilde{\bar{\rho}}^{n+1}_{G,ikj} \right)_0 / \Delta t , \tag{3-107}$$

and the derivative of the vapor internal energy with respect to cell pressure is given by

$$\frac{\partial e_{G,ikj}}{\partial p_{cell,ikj}} = \frac{1}{\tilde{\bar{\rho}}^{n+1}_{G,ikj}} \sum_{Gm} \tilde{\bar{\rho}}^{n+1}_{Gm} \left(\frac{\partial e_{Gm}}{\partial \rho_{Gm}} \right) \left[\sum_{Lm'} \frac{\partial \rho_{Gm}}{\partial v_{Lm'}} \frac{\partial v_{Lm'}}{\partial p_{cell}} \right], \tag{3-108a}$$

where

$$\frac{\partial e_{Gm}}{\partial \rho_{Gm}} = -\frac{0.8 a_{G2,M}\left(\frac{T_G}{T_{Crt,M}}\right)^{0.2}}{a_{G3M}(1 + a_{G3M})}, \tag{3-108b}$$

and the other derivative components are already known. The term a_{62} also involves an error in vapor energy equation and is written by

$$a_{62} = \frac{\partial D_{e_{G,ikj}}}{\partial \bar{\rho}_{R1,ikj}} + \frac{\partial D_{e_{G,ikj}}}{\partial e_{G,ikj}} \frac{\partial e_{G,ikj}}{\partial \bar{\rho}_{R1,ikj}}, \tag{3-109a}$$

where

$$\frac{\partial D_{e_{G,ikj}}}{\partial \bar{\rho}_{R1,ikj}} = \frac{\tilde{p}_{2\varphi,ikj}^{n+1}}{\Delta t}\left(\frac{\partial \tilde{\alpha}_G^{n+1}}{\partial \bar{\rho}_{R1,ikj}}\right), \tag{3-109b}$$

for which the expressions exist. The derivatives of the vapor internal energy with respect to densities are

$$\begin{aligned} \frac{\partial \tilde{\alpha}_G^{n+1}}{\partial \bar{\rho}_{R1,ikj}} = \sum_{Gm} \frac{\partial e_{G,ikj}}{\partial \rho_{Gm,ikj}} \Bigg[& \left(\frac{\bar{\rho}_{L1}}{\bar{\rho}_{R1}}\right)_0 \frac{\partial \rho_{Gm}}{\partial \bar{\rho}_{L1}} + \left(\frac{\bar{\rho}_{L4}}{\bar{\rho}_{R1}}\right)_0 \frac{\partial \rho_{Gm}}{\partial \bar{\rho}_{L4}} + \left(\frac{\bar{\rho}_{L5}}{\bar{\rho}_{R1}}\right)_0 \frac{\partial \rho_{Gm}}{\partial \bar{\rho}_{L5}} \\ & + \left(\frac{\bar{\rho}_{L6}}{\bar{\rho}_{R1}}\right)_0 \frac{\partial \rho_{Gm}}{\partial \bar{\rho}_{L6}} + \left(\frac{\bar{\rho}_{L7}}{\bar{\rho}_{R1}}\right)_0 \frac{\partial \rho_{Gm}}{\partial \bar{\rho}_{L7}} \Bigg], \end{aligned} \tag{3-110a}$$

where

$$\frac{\partial e_{G,ikj}}{\partial \rho_{Gm,ikj}} = \left(\frac{\bar{\rho}_{Gm,ikj}}{\bar{\rho}_{G,ikj}}\right) \left(\frac{\partial e_{Gm,ikj}}{\partial \rho_{Gm,ikj}}\right). \tag{3-110b}$$

The terms a_{63} and a_{64} are similar to a_{62}, and the term a_{65} is

$$a_{65} = \frac{\partial D_{e_{G,ikj}}}{\partial \bar{\rho}_{G,ikj}} + \left(\frac{\partial D_{e_{G,ikj}}}{\partial e_{G,ikj}}\right) \frac{\partial e_{G,ikj}}{\partial \bar{\rho}_{G,ikj}}, \tag{3-111a}$$

with

$$\frac{\partial D_{e_{G,ikj}}}{\partial \bar{\rho}_{G,ikj}} = 0, \tag{3-111b}$$

and

$$\frac{\partial e_{G,ikj}}{\partial \bar{\rho}_{G,ikj}} = \sum_{Gm} \left(\frac{\bar{\rho}_{Gm}}{\bar{\rho}_G}\right)_0 \frac{\partial e_G}{\partial \bar{\rho}_{Gm}}. \tag{3-111c}$$

Finally, the term a_{66} is written as

$$a_{66} = \frac{\partial D_{e_{G,ikj}}}{\partial T_G} + \left(\frac{\partial D_{e_{G,ikj}}}{\partial e_{G,ikj}}\right) \frac{\partial e_{G,ikj}}{\partial T_{G,ikj}}, \tag{3-112a}$$

with

$$\frac{\partial D_{e_{G,ikj}}}{\partial T_G} = 0\,. \tag{3-112b}$$

The derivative of the vapor internal energy with respect to vapor temperature requires the expression of the vapor internal energy

$$e_G(T_G) = \sum_m \tilde{\bar{\rho}}_{Gm}^{n+1}\, e_{Gm}(T_G) / \sum_m \tilde{\bar{\rho}}_{Gm}^{n+1}\,, \tag{3-113a}$$

where

$$e_{Gm} = e_{Gm}^{+} + \frac{0.8 a_{G2,M}\left(\dfrac{T_G}{T_{Crt,M}}\right)^{0.2}}{a_{G3M}} \ln\left[\frac{1 + a_{G2,M}\rho_{Gm}^{+}}{\rho_{Gm}}\right] \text{, and} \tag{3-113b}$$

$$\rho_{\mathrm{Gm}} = \frac{\tilde{\bar{\rho}}_{Gm}^{n+1}}{max[\alpha_0(1-\alpha_S), 1-\alpha_S-(1-\alpha_0)\alpha_L]}, \tag{3-113c}$$

with

$$\alpha_L = \sum_m \frac{\tilde{\bar{\rho}}_{Lm}^{n+1}}{\rho_{Lm}}, \tag{3-114a}$$

where

$$\rho_{Lm} = \rho_{Lm}(p_{cwll},\ e_{Lm})\,. \tag{3-114b}$$

Thus, the derivative is expressed by

$$\frac{\partial e_{Gm}}{\partial T_G} = \frac{\partial e_{GM}^{+}}{\partial T_G} + \frac{a_{G2,M}}{a_{G3,M} T_{crt,M}^{0.2}}\left\{\frac{0.16}{T_G^{0.8}} \ln\left[\frac{1 + a_{G3,M}\rho_{G,M}^{+}}{1 + a_{G3,M}\rho_{Gm}}\right]\right\} + 0.8 T_G^{0.2}\left[\frac{a_{G3,M}}{1 + a_{G3,M}\rho_{G,M}^{+}} \frac{\partial \rho_{G,M}^{+}}{\partial T_G}\right], \tag{3-115}$$

with

$$\frac{\partial e_{GM}^{+}}{\partial T_G} \text{ and } \frac{\partial \rho_{G,M}^{+}}{\partial T_G},$$

from the EOS relationships. This completes the terms in the matrix $\underline{A}_{ikj}$.

For the vectors $\vec{B}_{1,ikj}, \ldots, \vec{B}_{6,ikj}$, the pressures in the neighboring cells affect the velocities in the convective terms. Many repetitious formulas could be written. Here only one example is written for a typical term, the fourth component of $\vec{B}_{2,ikj}$, defined as

$$\frac{\partial \Psi_4}{\partial p_{i+1,k,j}} = \frac{\partial D_{R3,ikj}}{\partial p_{i+1,k,j}}\,. \tag{3-116}$$

For the donor-cell case, the expression for $D_{R3,ikj}$ and the derivative are

$$D_{R3,ikj} = \frac{\tilde{\bar{\rho}}_{R3,ikj}^{n+1} - \tilde{\bar{\rho}}_{R3,ikj}^{n}}{\Delta t} + \frac{\Delta_i\left\langle \tilde{\bar{\rho}}_{R3}^{n} r^{\zeta} \tilde{u}_{R3}^{n+1}\right\rangle_{k,j}}{r_i^{\zeta}\Delta x_i} + \frac{\Delta_k\langle \tilde{\bar{\rho}}_{R3}^{n} \tilde{w}_{R3}^{n+1}\rangle_{j,i}}{r_i^{\zeta}\Delta y_k} + \frac{\Delta_j\langle \tilde{\bar{\rho}}_{R3}^{n} \tilde{v}_{R3}^{n+1}\rangle_{i,k}}{\Delta z_j}, \tag{3-117}$$

$$\frac{\partial D_{R3,ikj}}{\partial p_{i+1,k,j}} = \frac{1}{r_i^{\zeta}\Delta x_i}\left[\Delta_i \frac{\partial \left\langle \tilde{\bar{\rho}}_{R3}^{n} r^{\zeta} \tilde{u}_{R3}^{n+1} \right\rangle_{k,j}}{\partial p_{i+1,k,j}}\right]$$
$$= \frac{r^{\zeta}_{i+\frac{1}{2}}}{r_i^{\zeta}\Delta x_i} \frac{\partial u_{q2,i+\frac{1}{2},k,j}}{\partial p_{i+1,k,j}} \begin{cases} \tilde{\bar{\rho}}_{R3,ikj}^{n} & u_{R3,i+1/2,k,j} \geq 0 \\ \tilde{\bar{\rho}}_{R3,i+1,k,j}^{n} & u_{R3,i+1/2,k,j} < 0 \end{cases}, \tag{3-118}$$

where

$$\frac{\partial u_{R3,i+1/2,k,j}}{\partial p_{i+1,k,j}} = -\frac{\partial u_{R3,i+\frac{1}{2},k,j}}{\partial p_{ikj}}. \tag{3-119}$$

3.3.5. Solution of changes in cell variables

By multiplying Eq. (3.65) by $\underline{A}_{ikj}^{-1}$, the vector $\Delta\vec{x}_{ikj}$ is expressed as

$$\Delta\vec{x}_{ikj} = -\underline{A}_{ikj}^{-1}\big[\vec{B}_{1,ikj}\Delta p_{i-1,k,j} + \vec{B}_{2,ikj}\Delta p_{i+1,k,j} + \vec{B}_{3,ikj}\Delta p_{i,k-1,j}$$
$$+ \vec{B}_{4,ikj}\Delta p_{i,k+1,j} + \vec{B}_{5,ikj}\Delta p_{i,k,j-1} + \vec{B}_{6,ikj}\Delta p_{i,k,j+1} + \vec{S}_{ikj}\big]. \tag{3-120}$$

This equation represents six equations, one for each element in $\Delta\vec{x}_{ikj}$. The first equation is an implicit relationship between cell pressure changes and neighboring cell pressure changes. The change in cell pressure can be computed if the first row of $\underline{A}_{ij}^{-1}$ is available. The inversion of 6 by 6 matrix $\underline{A}_{ikj}$ is performed by a band matrix solver. At the same time, the matrix multiplications are performed to determine the four off-diagonal elements for the subset of Eq. (3-120) describing the cell pressure variations. Since Eq. (3-120) couples the pressure changes with neighboring cells, treatment of boundary cells must be explained. The pressure in all boundary cells is assumed to remain constant throughout Step 3, regardless the boundary condition option selected by the user. This means that $\vec{B}_{1,ikj} = 0$ on the left boundary, $\vec{B}_{2ikj} = 0$ on the right boundary, $\vec{B}_{3,ikj} = 0$ on the front boundary, $\vec{B}_{4ikj} = 0$ on the back boundary, and $\vec{B}_{5,ikj} = \vec{B}_{6,ijj} = 0$ on the bottom and top boundaries. As a result, Eq. (3-120) only couples real cells. Also values of $\vec{S}_{ikj}$ are zeroed to eliminate these boundary cells from the convergence criteria.

Three solution methods are available for solving the set of *N* equations describing the pressure changes, where *N* is the number of real computational cells. These matrix solvers are described later in **Section 3.3.7**. Once the pressure changes Δp_{ikj} are determined, they are back-substituted into the other expansions to obtain Δ_{R1}, $\Delta\bar{\rho}_{R2}$, $\Delta\bar{\rho}_{R3}$, $\Delta\bar{\rho}_{G}$ and ΔT_G. A limiter is introduced to clip densities during the two-phase to single-phase transition. Here, an estimated end-of-time-step liquid volume fraction is computed as

$$(\tilde{\alpha}_{L,ij}^{n+1})_{est} = \frac{\tilde{\bar{\rho}}_{L1}^{n+1} + x_{L1}\Delta\bar{\rho}_{R1}}{\tilde{\bar{\rho}}_{R1}^{n+1}} + \frac{\tilde{\bar{\rho}}_{L2}^{n+1} + x_{L2}\Delta\bar{\rho}_{R2}}{\tilde{\bar{\rho}}_{R2}^{n+1}} + \frac{\tilde{\bar{\rho}}_{L3}^{n+1} + x_{L3}\Delta_{R3}}{\tilde{\bar{\rho}}_{R3}^{n+1}} + \frac{\tilde{\bar{\rho}}_{L4}^{n+1} + x_{L4}\Delta\bar{\rho}_{R1}}{\tilde{\bar{\rho}}_{R1}^{n+1}}$$
$$+ \frac{\tilde{\bar{\rho}}_{L5}^{n+1} + x_{L5}\Delta\bar{\rho}_{R2}}{\tilde{\bar{\rho}}_{R2}^{n+1}} + \frac{\tilde{\bar{\rho}}_{L6}^{n+1} + x_{L6}\Delta\bar{\rho}_{R1}}{\tilde{\bar{\rho}}_{R1}^{n+1}} + \frac{\tilde{\bar{\rho}}_{L7}^{n+1} + x_{L7}\Delta\bar{\rho}_{R1}}{\tilde{\bar{\rho}}_{R1}^{n+1}}. \tag{3-121}$$

Then if $(\tilde{\alpha}_{L,ikj}^{n+1})_{est} + \alpha_{S,ikj} > 1$ and $\tilde{\alpha}_{G,ikj}^{k} > 0$, we apply the limiter to $\Delta\bar{\rho}_q$ as

$$\Delta\bar{\rho}_q = min\left[\Delta\bar{\rho}_q,\ \left(\frac{1-\alpha_S+10^{-9+k}}{1-\alpha_S-\tilde{\alpha}_G^k}-1\right)\tilde{\bar{\rho}}_q^k\right], \tag{3-122}$$

where k is the iteration index and q=$R1$, $R2$ and $R3$. The velocity changes are determined by

$$\tilde{u}^k_{i+1/2,k,j} = \tilde{u}^{k-1}_{i+1/2,k,j} - \left(\frac{\partial u}{\partial p}\right)_{i+1/2,k,j}\left[\Delta p_{i+1,k,j} - \Delta p_{ikj}\right], \tag{3-123a}$$

$$\tilde{w}^k_{i,k+1/2,j} = \tilde{w}^{k-1}_{i,k+1/2,j} - \left(\frac{\partial u}{\partial p}\right)_{i,k+1/2,j}\left[\Delta p_{i,k+1,j} - \Delta p_{ikj}\right], \text{and} \tag{3-123b}$$

$$\tilde{v}^k_{i,k,j+1/2} = \tilde{v}^{k-1}_{i,k,j+1/2} - \left(\frac{\partial v}{\partial p}\right)_{i,k,j+1/2}\left[\Delta p_{i,k,j+1} - \Delta p_{ikj}\right]. \tag{3-123c}$$

Then on the left, front, bottom, right, back and top boundaries,

$$\tilde{u}^k_{3/2,k,j} = \tilde{u}^{k-1}_{3/2,k,j} - \left(\frac{\partial u}{\partial p}\right)_{3/2,k,j}\Delta p_{2,k,j}, \tag{3-124a}$$

$$\tilde{w}^k_{i,3/2,j} = \tilde{w}^{k-1}_{i,3/2,j} - \left(\frac{\partial w}{\partial p}\right)_{i,3/2,j}\Delta p_{i,2,j}, \tag{3-124b}$$

$$\tilde{v}^k_{i,k,3/2} = \tilde{v}^{k-1}_{i,k,3/2} - \left(\frac{\partial v}{\partial p}\right)_{i,k,3/2}\Delta p_{i,k,2}, \tag{3-124c}$$

$$\tilde{u}^k_{IB+3/2,k,j} = \tilde{u}^{k-1}_{B+3/2,k,j} - \left(\frac{\partial u}{\partial p}\right)_{B+3/2,k,j}\Delta p_{IB+1,k,j}, \tag{3-124d}$$

$$\tilde{w}^k_{i,KB+3/2,j} = \tilde{w}^{k-1}_{i,KB+3/2,j} - \left(\frac{\partial w}{\partial p}\right)_{i,KB+3/2,j}\Delta p_{i,KB+1,j}, \text{and} \tag{3-124e}$$

$$\tilde{v}^k_{i,k,JB+3/2} = \tilde{v}^{k-1}_{i,k,JB+3/2} - \left(\frac{\partial v}{\partial p}\right)_{i,k,JB+3/2}\Delta p_{i,k,JB+1}. \tag{3-124f}$$

In the above equations the velocity derivatives come from Step 2. After unfolding the changes in the densities, temperatures and velocities based on Δp_{ij}, all the variables are updated as

$$\tilde{\bar{\rho}}^k_{L1} = \tilde{\bar{\rho}}^{k-1}_{L1} + x_{L1}\Delta\bar{\rho}_{R1}, \tag{3-125a}$$

$$\tilde{\bar{\rho}}^k_{L2} = \tilde{\bar{\rho}}^{k-1}_{L2} + x_{L2}\Delta\bar{\rho}_{R2}, \tag{3-125b}$$

$$\tilde{\bar{\rho}}^k_{L3} = \tilde{\bar{\rho}}^{k-1}_{L3} + x_{L3}\Delta\bar{\rho}_{L3}, \tag{3-125c}$$

$$\tilde{\bar{\rho}}^k_{L4} = \tilde{\bar{\rho}}^{k-1}_{L4} + x_{L4}\Delta\bar{\rho}_{R1}, \tag{3-125d}$$

$$\tilde{\bar{\rho}}^k_{L5} = \tilde{\bar{\rho}}^{k-1}_{L5} + x_{L5}\Delta\bar{\rho}_{R2}, \tag{3-125e}$$

$$\tilde{\bar{\rho}}_{L6}^{k} = \tilde{\bar{\rho}}_{L6}^{k-1} + x_{L6}\Delta\bar{\rho}_{R1} \,, \tag{3-125f}$$

$$\tilde{\bar{\rho}}_{L7}^{k} = \tilde{\bar{\rho}}_{L7}^{k-1} + x_{L7}\Delta\bar{\rho}_{R1} \,, \tag{3-125g}$$

$$\tilde{\bar{\rho}}_{Gm}^{k} = \tilde{\bar{\rho}}_{Gm}^{k-1} + x_{Gm}\Delta\bar{\rho}_{G} \,, \text{ for } m\text{=1, 2, 3 and 4, and} \tag{3-125h}$$

$$\tilde{T}_{G}^{k} = \tilde{T}_{G}^{k-1} + x_{Gm}\Delta T_{G} \,. \tag{3-125i}$$

The only additional limit is that the overall vapor density cannot be decreased by more than 90% in one iteration. The individual density components are updated based on the assumed constant mass ratios existing within a momentum field. All densities and temperatures are then reflected from the last real cell into the boundary cells in the radial direction.

3.3.6. Convergence criteria for pressure iteration

Two convergence criteria are basically used for the pressure iteration. First, the absolute values of each component of the $\vec{S}_{ikj}$ vector are compared to input convergence criteria.

$$\left|\varepsilon_{ikj}^{k}\right| < \epsilon_{p} \,, \tag{3-126a}$$

$$\left|D_{R1}^{k}\right| < \epsilon_{\rho} \,, \tag{3-126b}$$

$$\left|D_{R2}^{k}\right| < \epsilon_{\rho} \,, \tag{3-126c}$$

$$\left|D_{R3}^{k}\right| < \epsilon_{\rho} \,, \tag{3-126d}$$

$$\left|D_{G}^{k}\right| < \epsilon_{\rho} \,, \text{and} \tag{3-126e}$$

$$\left|D_{e_G}^{k}\right| < \epsilon_{T} \,. \tag{3-126f}$$

Here it is noted that if the user sets these criteria too tightly or the coefficient matrix form Eq. (3-120) is sufficiently ill-conditioned, enough significant figures may not be available to achieve the attempted accuracy. The standard convergence criteria currently defaulted in the code are:

$$\epsilon_{p} = 10 \ [\text{Pa}] \,, \tag{3-127a}$$

$$\epsilon_{\rho} = 10^{-4} [\text{kg/m}^3] \,, \text{and} \tag{3-127b}$$

$$\epsilon_{T} = 10 \ [\text{J/kg}] \,. \tag{3-127c}$$

For the vapor specific internal energy, the convergence criterion roughly corresponds to a temperature precision of 1.0 K or less.

The second convergence criterion examines satisfaction of the inequality,

$$\frac{max\left[\left|\eta_{ikj}\right|,\ \left|10 \times \Delta p_{ikj}^{k}\right|\right]}{max\left[\left|p_{ikj}^{k}\right|,\ 10^{-20}\right]} < \epsilon_c\ , \tag{3-128}$$

where η_{ikj} is the first element of $\underline{A}_{ikj}^{-1}\vec{S}_{ikj}$. If more than one iteration has been done and inequality in Eq. (3-128) is satisfied, further iteration is judged to be impractical. If further iterations are required, control is transferred to the calculation of new residual derivatives.

3.3.7. Matrix solvers for pressure iteration

There are three matrix solvers currently available in SIMMER-III/SIMMER-IV. For a one-dimensional problem, the pressure change equation in Eq. (3-120) is reduced to a tridiagonal matrix, in which each cell is coupled with two adjacent cells. A standard tridiagonal matrix solver is employed in this case.

For a two- or three-dimensional problem, two types of matrix solvers are optionally used: a direct banded-matrix solver based on an outer-product Gaussian elimination method; and an iterative solution method based on the partial conjugate-gradient, either an ILUBCG or ILUCR type. The former banded-matrix solver is taken from AFDM and the detailed description is available in AFDM Manual Vol. V, Appendix X. In the latter method, the convergence criterion taken for a matrix equation,

$$\underline{A}\vec{x} = \vec{b} \tag{3-129}$$

is written as

$$\frac{\left|\underline{A}\vec{x} = \vec{b}\right|}{\left|\vec{b}\right|} < \epsilon_{itrf}\ , \tag{3-130}$$

where the typical value of ϵ_{itrf} is 10^{-6} to 10^{-8}.

It is noted that the experience in using the options for matrix solvers has suggests that the direct solution method be faster when the number of mesh cells of the problem is smaller than about 1,000. On the other hand, the iterative partial conjugate gradient method is obviously faster when the number of mesh cells exceeds about 1,500. Based on experience of using the two types of iterative solvers, ILUBCG has a better convergence property than ILUCR.

3.3.8 Optional acceleration technique for pressure iteration

An optional acceleration technique based on Steffensen's method is implemented for cases when difficulty is encountered in converging the pressure iteration. The method is known to be effective, in general, when an oscillatory behavior is encountered between iterations. In this method, a new estimate in an iteration variable x^k is defined from the previous two iterations as

$$x_{new}^{k} = x^{k-2} - \frac{(x^{k-1} - x^{k-2})^2}{x^k - 2x^{k-1} - x^{k-2}}\ . \tag{3-131}$$

For application to the present pressure iteration, Eq. (3-131) is reduced to

$$\delta_{new}^{k} = \frac{\delta^{k}\delta^{k-1}}{\delta^{k} - \delta^{k-1}}, \tag{3-132}$$

and is applied individually to each of six independent variables separately by user specification. Note that the use of this acceleration technique is not always effective and hence is not recommended for a standard use.

3.4. End-of-Time-Step Values (Step 4)

The fourth step (Step 4) of the SIMMER-III/SIMMER-IV four-step algorithm does the final update for densities, velocities and material temperatures. The basic approach is to use the results of Step 3 to re-evaluate the conservation equations and invert the EOS. Step 4 also interweaves several other operations. The interfacial areas used in Step 1 are also convected with the same velocities used for mass, momentum and energy convection. The mass/energy outflows/inflows at the boundaries of the problem are evaluated. Finally, using the end-of-time-step velocities, the interfacial frictional dissipation terms are determined.

3.4.1. Final mass update

An EOS call at the beginning of Step 4 is omitted to save computational effort. The liquid specific volumes $\tilde{v}_{Lm}^{n+1}$ required are taken from the values determined on the final iteration in Step 3. This is justified by the fact that liquid specific volumes have only weak dependence on the pressure.

Using the velocities $\tilde{u}_q^{n+1}$, $\widetilde{w}_q^{n+1}$ and $\tilde{v}_q^{n+1}$ from Step 3, the end-of-time-step densities must be updated for all components. The finite difference equations are

$$\tilde{\bar{\rho}}_{m,ikj}^{n+1} = \tilde{\bar{\rho}}_{m,ikj}^{n} - \Delta t \left[\frac{\Delta_i \left\langle \tilde{\bar{\rho}}_m^n r^{\zeta} \tilde{u}_q^{n+1} \right\rangle_{k,j}}{r_i^{\zeta} \Delta x_i} + \frac{\Delta_k \left\langle \tilde{\bar{\rho}}_m^n \widetilde{w}_q^{n+1} \right\rangle_{j,i}}{r_i^{\zeta} \Delta y_k} + \frac{\Delta_j \left\langle \tilde{\bar{\rho}}_m^n \tilde{v}_q^{n+1} \right\rangle_{i,k}}{\Delta z_j} \right], \tag{3-133}$$

where the convective terms are evaluated similarly to Step 2, although the velocities used are those determined in Step 3. The beginning-of-time-step densities in Eq. (3-133) are those from Step 1. After determining the energy component densities, $\bar{\rho}_{Lm}^{n+1}$, estimated end-of-time-step liquid volume fractions can be obtained from

$$\tilde{\alpha}_{Lm}^{n+1} = \tilde{v}_{Lm}^{n+1} \bar{\rho}_{Lm}^{n+1}. \tag{3-134}$$

3.4.2. Intermediate updates of internal energies

New estimates for the internal energies for liquids and vapor are

$$\begin{aligned} \tilde{e}_{r,ikj}^{n+1} = \frac{1}{\bar{\rho}_{r,ikj}^{n+1}} \Bigg\{ & \tilde{e}_{r,ikj}^{n} \tilde{\bar{\rho}}_{r,ikj}^{n} \\ & - \Delta t \left[\frac{\Delta_i \left\langle \tilde{\bar{\rho}}_r^n r^{\zeta} \tilde{e}_r^n \tilde{u}_q^{n+1} \right\rangle_{k,j}}{r_i^{\zeta} \Delta x_i} + \frac{\Delta_k \left\langle \tilde{\bar{\rho}}_m^n \tilde{e}_r^n \widetilde{w}_q^{n+1} \right\rangle_{j,i}}{r_i^{\zeta} \Delta y_j} + \frac{\Delta \left\langle \tilde{\bar{\rho}}_m^n \tilde{e}_r^n \tilde{v}_q^{n+1} \right\rangle_{i,k}}{\Delta z_j} \right] \\ & - W_{r,ikj} + X_{r,ikj} \Bigg\}, \end{aligned} \tag{3-135}$$

where the convection terms are evaluated similarly to Step 2, although the velocities used are those determined in Step 3. Again, the beginning-of-time-step densities in Eq. (3-135) are those from Step 1. In Eq. (3-135), $W_{r,ikj}$ denotes the pressure-volume work term and $X_{r,ikj}$ is an addition to the liquid equations when the vapor pressure-volume work term is zero. The latter is included to conserve energy. The values of $W_{r,ikj}$ are given by

$$\begin{aligned} W_{r,ikj} = p_{r,ikj}^{n+1} \Bigg\{ & \left(\tilde{\alpha}_{r,ikj}^{n+1} - \alpha_{r,ikj}^{n}\right) \\ & + \Delta t \left[\frac{\Delta_i \left\langle \tilde{\alpha}_r^n r^\zeta \tilde{u}_q^{n+1} \right\rangle_{k,j}}{r_i^\zeta \Delta x_i} + \frac{\Delta_k \left\langle \tilde{\alpha}_r^n \widetilde{w}_q^{n+1} \right\rangle_{j,i}}{r_i^\zeta \Delta y_k} + \frac{\Delta_j \left\langle \tilde{\alpha}_r^n \tilde{v}_q^{n+1} \right\rangle_{i,k}}{\Delta z_j} \right] \Bigg\}, \end{aligned} \tag{3-136}$$

where

$$p_{r,ikj} = p_{ikj}^{n+1} \text{ for the liquid components}\,, \tag{3-137a}$$

$$p_{ikj}^{n+1} \text{ is the final cell pressure in Step 3}\,, \tag{3-137b}$$

$$p_{G,ikj} = p_{ikj}^{n+1} \text{ if } p_{G,ikj}^{k} > 0 \text{ in Step 3}\,\text{, and} \tag{3-137c}$$

$$p_{G,ikj} = 0 \text{ if } p_{G,ikj}^{k} = 0 \text{ in Step 3}\,. \tag{3-137d}$$

Using the overall liquid volume fraction,

$$\tilde{\alpha}_L^{n+1} = \sum_m \tilde{\alpha}_{Lm}^{n+1}\,. \tag{3-138}$$

$X_{r,ikj}$ is defined by

$$\begin{aligned} X_{r,ikj} = \frac{\tilde{\alpha}_r^{n+1}}{\tilde{\alpha}_L^{n+1}} p_{ikj}^{n+1} \Bigg\{ & \left(\tilde{\alpha}_{G,ikj}^{n+1} - \tilde{\alpha}_{G,ikj}^{n}\right) \\ & + \Delta t \left[\frac{\Delta_i \left\langle \tilde{\alpha}_G^n r^\zeta \tilde{u}_G^{n+1} \right\rangle_{k,j}}{r_i^\zeta \Delta x_i} + \frac{\Delta_k \langle \tilde{\alpha}_G^n \widetilde{w}_G^{n+1} \rangle_i}{r_i^\zeta \Delta y_k} + \frac{\Delta_j \langle \tilde{\alpha}_G^n \tilde{v}_G^{n+1} \rangle_i}{\Delta z_j} \right] \Bigg\}. \end{aligned} \tag{3-139}$$

When $p_{G,ikj} = 0$ and consequently $W_G = 0$ for the vapor component,

$$X_r = 0\,\text{, if } p_{G,ikj} = p_{ikj}^{n+1}\text{, and always} \tag{3-140a}$$

$$X_G = 0\,.. \tag{3-140b}$$

The vapor volume fraction is recalculated as

$$\tilde{\alpha}_{G,ikj}^{n+1} = 1 - \alpha_S - \tilde{\alpha}_L^{n+1}\,. \tag{3-141}$$

These are the same method as used in Step 2, except that the non-linear terms use end-of-time-step velocities. Again, for the higher-order differencing of the vapor, the “*r*” subscript identifying the vapor energy field is replaced by an “*m*” subscript to indicate that the convected value for each individual density component must be determined. As in Step 2, the convective terms involving density components must be summed to obtain the terms involving the convection of the density associated with an energy component. The bracket terms involving $\tilde{\alpha}_r^n$ are evaluated with end-of-time-step velocities analogous to Step 2 for the liquid components and similarly to a density for the vapor volume fraction where a direct spatial derivative is determined. The internal energies calculated in Eq. (3-135) become the end-of-time-step values after addition of the interfacial heating terms described in **Section 3.4.7**.

3.4.3. Interfacial area convection

The operation is performed in Step 4 to convect interfacial areas per unit volume with the same velocities as used to convect densities and internal energies. The convection equation used is given by

$$\frac{\partial A_M}{\partial t} + \nabla \cdot \left(A_M \boldsymbol{v}_q \right) = 0 , \tag{3-142}$$

where A_M is the convectible interfacial areas per unit volume. Before introducing the convectible interfacial areas, a concept of multiphase flow topology is explained. A SIMMER-III/SIMMER-IV mesh cell is generally represented by the combination of a bubbly- (liquid-continuous) flow region and a dispersed (vapor-continuous) region. The eight fluid energy components are distributed in the cell as continuous liquid or vapor phase, bubbles, droplets and particles, and their surface areas flow with associating fluids. The total of 11 convectible interfacial areas are defined in SIMMER-III/SIMMER-IV[17]. These are:

- Surface areas of 3 real liquid components (fuel, steel and sodium) in the dispersed region ($A_{L1,D}$, $A_{L2,D}$, $A_{L3,D}$) and bubbly region ($A_{L1,B}$, $A_{L2,B}$, $A_{L3,B}$),
- Surface areas of fuel particles, steel particles and fuel chunks (A_{L4}, A_{L5}, A_{L7}),
- Surface areas of bubbles in the bubbly region ($A_{G,B}$), and
- Interface area between the bubbly and dispersed regions ($A_{B,D}$). This area is not actually convected but is defined as an additional area to be treated similarly to other convectible interfacial areas.

The control particles is not convectible and its surface area is determined instantaneously from the volume fraction and radius. The convectible interfacial area of a liquid-field component is convected at the velocity of the momentum field to which the associating component is assigned. The $A_{G,B}$ is convected at the velocity of the vapor field.

The differenced form of Eq. (3-142) is handled in a similar way as the mass convection. For the first-order donor-cell differencing option, the interfacial areas are explicitly updated.

$$A_M^{n+1} = \tilde{A}_M^n - \Delta t \left[\frac{\Delta_i \left\langle \tilde{A}_M^n r^\zeta \tilde{u}_q^{n+1} \right\rangle_{k,j}}{r_i^\zeta \Delta x_i} + \frac{\Delta_k \left\langle \tilde{A}_M^n \tilde{w}_q^{n+1} \right\rangle_{j,i}}{r_i^\zeta \Delta y_k} + \frac{\Delta_j \left\langle \tilde{A}_M^n \tilde{v}_q^{n+1} \right\rangle_{i,k}}{\Delta z_j} \right] . \tag{3-143}$$

3.4.4. Mass and energy outflows

Determination of the convective fluxes for Eqs. (3-133) and (3-135) provides the necessary information to compute mass and energy outflows across the problem boundaries. These are evaluated before the velocities are solved. Only the two-dimensional case is shown in this section. To give the expressions for the boundaries, the bottom real cell is denoted by a *j* of 2, the top real cell by a *j* of *J*+1, the left real cell by a *i* of 2, and the right real cell by a *i* of *I*+1. Then the net mass outflow for each component over a time step is

$$\begin{aligned}\frac{\Delta M_m}{\Delta t} = \sum_{i=2}^{I+1} A_i \left[\langle \tilde{\bar{\rho}}_m^n \tilde{v}_q^{n+1} \rangle_{i,J+3/2} - \langle \tilde{\bar{\rho}}_m^n \tilde{v}_q^{n+1} \rangle_{i,3/2} \right] \\ + \sum_{j=2}^{J+1} 2\pi \Delta z_j \left[\langle \tilde{\bar{\rho}}_m^n r^{\varsigma} \tilde{u}_q^{n+1} \rangle_{I+3/2,j} - \langle \tilde{\bar{\rho}}_m^n r^{\varsigma} \tilde{u}_q^{n+1} \rangle_{3/2,j} \right],\end{aligned} \tag{3-144}$$

where the convective terms have the same definition as before, A_i is the area and

$\pi = 3.14159265...$ for $\zeta = 1$, or 0.5 for $\zeta = 0$.

To maintain an account of overall energy conservation, the energy outflow is computed as the sum of the internal energies, the kinetic energies and the work done by pressure at the problem boundaries. The resultant net energy outflow for a component over a time step is

$$\begin{aligned}\frac{\Delta E_r}{\Delta t} = \sum_{i=2}^{I+1} A_i \left[\langle \tilde{\bar{\rho}}_r^n \left(\tilde{e}_r^n + \frac{1}{2} \left(\tilde{v}_q^n \right)^2 \right) \tilde{v}_q^{n+1} \rangle_{i,J+3/2} - \langle \tilde{\bar{\rho}}_r^n \left(\tilde{e}_r^n + \frac{1}{2} \left(\tilde{v}_q^n \right)^2 \right) \tilde{v}_q^{n+1} \rangle_{i,3/2} \right] \\ + \sum_{i=2}^{I+1} A_i \left[\frac{p_{i,J+1}^{n+1} + p_{i,J+2}^{n+1}}{2} \langle \tilde{\alpha}_r^n \tilde{v}_q^{n+1} \rangle_{i,J+3/2} - \frac{p_{i,1}^{n+1} + p_{i,2}^{n+1}}{2} \langle \tilde{\alpha}_r^n \tilde{v}_q^{n+1} \rangle_{i,3/2} \right] \\ + \sum_{j=2}^{J+1} 2\pi \Delta z_j \left[\langle \tilde{\bar{\rho}}_r^n r^{\varsigma} \left(\tilde{e}_r^n + \frac{1}{2} \left(\tilde{u}_q^n \right)^2 \right) \tilde{u}_q^{n+1} \rangle_{I+3/2,j} \right. \\ \left. - \langle \tilde{\bar{\rho}}_r^n r^{\varsigma} \left(\tilde{e}_r^n + \frac{1}{2} \left(\tilde{u}_q^n \right)^2 \right) \tilde{u}_q^{n+1} \rangle_{3/2,j} \right] \\ + \sum_{j=2}^{J+1} 2\pi \Delta z_j \left[\frac{p_{I+1,j}^{n+1} + p_{I+2,j}^{n+1}}{2} \langle \tilde{\alpha}_r^n r^{\varsigma} \tilde{u}_q^{n+1} \rangle_{I+3/2,j} \right. \\ \left. - \frac{p_{1,j}^{n+1} + p_{2,j}^{n+1}}{2} \langle \tilde{\alpha}_r^n r^{\varsigma} \tilde{u}_q^{n+1} \rangle_{3/2,j} \right].\end{aligned} \tag{3-145}$$

The formulas for the kinetic energy transfer across the problem boundaries are rather arbitrary. No transfers of the work term from the vapor field component to the liquid components are made in these summations for single-phase cells, as they should be small in practical cases and do not affect the overall energy balance.

3.4.5. Setup for momentum equation

The procedure to set up velocity calculations is similar to Step 2, although a more implicit relationship is used for drag terms in the momentum equations. The five coupled preliminary operations to set up momentum equations in Step 2 are changed as follows.

First, no further adjustment to the momentum-exchange coefficients are performed for a two-phase to single-phase transition, since the final pressures were determined and accommodation of any cell to the transition to single-phase pressures was performed already in Step 3.

Second the momentum densities, $\bar{\rho}^{n+1}_{q,\theta+}$, $\bar{\rho}^{n+1}_{q,\tau+}$ and $\bar{\rho}^{n+1}_{q,\lambda+}$, are averaged similarly to Step 2 as

$$\bar{\rho}^{n+1}_{q,\lambda+} = \frac{\bar{\rho}^{n+1}_{q,ikj} r_i^{\zeta} \Delta x_i + \bar{\rho}^{n+1}_{q,i+1,k,j} r_{i+1}^{\zeta} \Delta x_{i+1}}{(r'_{i+1/2})^{\zeta} (\Delta x_i + \Delta x_{i+1})}, \tag{3-146a}$$

$$\bar{\rho}^{n+1}_{q,\tau+} = \frac{\bar{\rho}^{n+1}_{q,ikj} \Delta y_k + \bar{\rho}^{n+1}_{q,i,k+1,j} \Delta y_{k+1}}{(r'_{i+1/2})^{\zeta} (\Delta y_k + \Delta y_{k+1})} \text{, and} \tag{3-146b}$$

$$\bar{\rho}^{n+1}_{q,\theta+} = \frac{\bar{\rho}^{n+1}_{q,ikj} \Delta z_j + \bar{\rho}^{n+1}_{q,i,k,j+1} \Delta z_{j+1}}{\Delta z_j + \Delta z_{j+1}}. \tag{3-146c}$$

where the momentum densities are determined by summing over the same components as used in Step 2.

Third, the $a_{qq'}$ and $b_{qq'}$ are multiplied by $\bar{\rho}^{n+1}_q \bar{\rho}^{n+1}_{q'}$ to obtain values partially corrected for mass transfers. The a_{qS} and b_{qS} are multiplied by $\bar{\rho}^{n+1}_q$. The $a_{qq'}$, $b_{qq'}$, a_{qS}, b_{qS}, and the virtual mass terms are averaged similarly to the densities. The volume fractions are averaged as in Step 2 with p^{n+1} determining the donor cell for α_G.

Fourth, the convective terms are defined by using the end-of-time-step velocities only in the mass fluxes. These terms become

$$\begin{aligned} CV^{n+1}_{q,\lambda+} == & \frac{1}{\left(r'_{i+1/2}\right)^{\zeta} \Delta x_{i+1/2}} \left[\left\langle \tilde{\bar{\rho}}^n_q r^{\zeta} \tilde{u}^n_q \right\rangle_{i+1,k,j} \left\langle \tilde{u}^n_q \right\rangle_{i+1,k,j} - \left\langle \tilde{\bar{\rho}}^n_q r^{\zeta} \tilde{u}^n_q \right\rangle_{ikj} \left\langle \tilde{u}^n_q \right\rangle_{ikj} \right] \\ & + \frac{1}{\left(r'_{i+1/2}\right)^{\zeta} \Delta y_k} \left[\left\langle \tilde{\bar{\rho}}^n_q \widetilde{w}^n_q \right\rangle_{i+1/2,k+1/2,j} \left\langle \tilde{u}^n_q \right\rangle_{i+1/2,k+1/2,j} \right. \\ & \left. - \left\langle \tilde{\bar{\rho}}^n_q \widetilde{w}^n_q \right\rangle_{i+1/2,k-1/2,j} \left\langle \tilde{u}^n_q \right\rangle_{i+1/2,k-1/2,j} \right] \\ & + \frac{1}{\Delta z_j} \left[\left\langle \tilde{\bar{\rho}}^n_q \tilde{v}^n_q \right\rangle_{i+1/2,k,j+1/2} \left\langle \tilde{u}^n_q \right\rangle_{i+1/2,k,j+1/2} \right. \\ & \left. - \left\langle \tilde{\bar{\rho}}^n_q \tilde{v}^n_q \right\rangle_{i+1/2,k,j-1/2} \left\langle \tilde{u}^n_q \right\rangle_{i+1/2,k,j-1/2} \right], \end{aligned} \tag{3-147a}$$

$$\begin{aligned} CV^{n+1}_{q,\tau+} = & \frac{1}{r^{\zeta}\Delta x_i}\Big[\big\langle\tilde{\bar{\rho}}^n_q r^{\zeta}\tilde{u}^n_q\big\rangle_{i+1/2,k+1/2,j}\big\langle\tilde{w}^n_q\big\rangle_{i+1/2,k+1/2,j} \\ & - \big\langle\tilde{\bar{\rho}}^n_q r^{\zeta}\tilde{u}^n_q\big\rangle_{i-1/2,k+1/2,j}\big\langle\tilde{w}^n_q\big\rangle_{i-1/2,k+1/2,j}\Big] \\ & + \frac{1}{r^{\zeta}\Delta y_{k+1/2}}\Big[\big\langle\tilde{\bar{\rho}}^n_q\tilde{w}^n_q\big\rangle_{i,k+1,j}\big\langle\tilde{w}^n_q\big\rangle_{i,k+1,j} - \big\langle\tilde{\bar{\rho}}^n_q\tilde{w}^n_q\big\rangle_{ikj}\big\langle\tilde{w}^n_q\big\rangle_{ikj}\Big] \\ & + \frac{1}{\Delta z_j}\Big[\big\langle\tilde{\bar{\rho}}^n_q\tilde{v}^n_q\big\rangle_{i,k+1/2,j+1/2}\big\langle\tilde{w}^n_q\big\rangle_{i,k+1/2,j+1/2} \\ & - \big\langle\tilde{\bar{\rho}}^n_q\tilde{v}^n_q\big\rangle_{i,k+1/2,j-1/2}\big\langle\tilde{w}^n_q\big\rangle_{i,k+1/2,j-1/2}\Big]\ \text{, and} \end{aligned} \tag{3-147b}$$

$$\begin{aligned} CV^{n+1}_{q,\theta+} = & \frac{1}{r^{\zeta}\Delta x_i}\Big[\big\langle\tilde{\bar{\rho}}^n_q r^{\zeta}\tilde{u}^n_q\big\rangle_{i+1/2,k,j+1/2}\big\langle\tilde{v}^n_q\big\rangle_{i+1/2,k,j+1/2} \\ & - \big\langle\tilde{\bar{\rho}}^n_q r^{\zeta}\tilde{u}^n_q\big\rangle_{i-1/2,k,j+1/2}\big\langle\tilde{v}^n_q\big\rangle_{i-1/2,k,j+1/2}\Big] \\ & + \frac{1}{r^{\zeta}\Delta y_k}\Big[\big\langle\tilde{\bar{\rho}}^n_q r^{\zeta}\tilde{w}^n_q\big\rangle_{i,k+1/2,j+1/2}\big\langle\tilde{v}^n_q\big\rangle_{i,k+1/2,j+1/2} \\ & - \big\langle\tilde{\bar{\rho}}^n_q r^{\zeta}\tilde{w}^n_q\big\rangle_{i,k-1/2,j+1/2}\big\langle\tilde{v}^n_q\big\rangle_{i,k-1/2,j+1/2}\Big] \\ & + \frac{1}{\Delta z_{j+1/2}}\Big[\big\langle\tilde{\bar{\rho}}^n_q\tilde{v}^n_q\big\rangle_{i,k,j+1}\big\langle\tilde{v}^n_q\big\rangle_{i,k,j+1} - \big\langle\tilde{\bar{\rho}}^n_q\tilde{v}^n_q\big\rangle_{ikj}\big\langle\tilde{v}^n_q\big\rangle_{ikj}\Big]\ . \end{aligned} \tag{3-147c}$$

The terms in brackets can then be averaged as was done in Step 2. However, donor-cell velocities now depend on end-of-time-step information. The "~" velocities are defined as in Step 2 (the momentum flux is divided by a momentum-averaged density), except that they now use the Step 3 end-of-time-step values, rather than the Step 1 tilde estimates.

3.4.6. End-of-time-step velocities

The iterative calculation for the end-of-time-step velocities proceeds similarly to Step 2, although derivatives of velocity with respect to pressure are not required this time. The initial estimates for the velocities are those from Step 3, or

$\tilde{u}^{n+1}_{q,i+1/2,k,j}$ $\tilde{w}^{n+1}_{q,i,k+1/2,j}$ and $\tilde{v}^{n+1}_{q,i,k,j+1/2}$.

These estimates are then adjusted if tight coupling exists at an interface. Two fields are assumed to be tightly coupled if the $a_{qq'}$ for the interface is greater than $10^9(1-\alpha_S)$. For two fields being tightly coupled, the adjustment formula is

$$\tilde{V}^{n+1}_{q,\xi} = \tilde{V}^{n+1}_{q',\xi} = \frac{\tilde{V}^k_{q,\xi}\bar{\rho}^{n+1}_{q,\xi} + \tilde{V}^k_{q',\xi}\bar{\rho}^{n+1}_{q',\xi}}{\bar{\rho}^{n+1}_{q,\xi} + \bar{\rho}^{n+1}_{q',\xi}}, \tag{3-148}$$

where

$\tilde{V}^{n+1}_{q,\xi} = \tilde{u}^{n+1}_{q,i+1/2,k,j}$ in the x (radial) direction,

$\tilde{V}_{q,\xi}^{n+1} = \tilde{w}_{q,i,k+1/2,j}^{n+1}$ in the *y* direction, and

$\tilde{V}_{q,\xi}^{n+1} = \tilde{v}_{q,i,k,j+1/2}^{n+1}$ in the *z* (axial) direction.

For all three fields tightly coupled in a three-velocity-field model,

$$\tilde{V}_{1,\xi}^{n+1} = \tilde{V}_{2,\xi}^{n+1} = \tilde{V}_{G,\xi}^{n+1} = \frac{\tilde{V}_{1,\xi}^{k}\bar{\rho}_{1,\xi}^{n+1} + \tilde{V}_{2,\xi}^{k}\bar{\rho}_{2,\xi}^{n+1} + \tilde{V}_{G,\xi}^{k}\bar{\rho}_{G,\xi}^{n+1}}{\bar{\rho}_{1,\xi}^{n+1} + \bar{\rho}_{2,\xi}^{n+1} + \bar{\rho}_{G,\xi}^{n+1}} . \tag{3-149}$$

In Step 4, it is intended to implicitly treat the velocities in the interfacial drag terms. This means the finite difference representation for the momentum equation is

$$\begin{aligned}\tilde{\bar{\rho}}_{q,\xi}^{n+1}\tilde{V}_{q,\xi}^{n+1} + \Delta t K_{qS,\zeta} V_{q,\xi} - \tilde{\beta}_{q,\xi}^{n+1}\left[\tilde{V}_{G,\xi}^{n+1} - \sum_{m} \tilde{\alpha}_{qm,eff,\xi}^{n+1}\tilde{V}_{qm,\xi}^{n+1}\right] \\ - \Delta t \sum_{q'} \left(\tilde{a}_{q'q,\xi}^{n+1} + \tilde{b}_{q'q,\xi}^{n+1}\left|V_{q'q,\xi}^{*}\right|\right) V_{q'q,\xi} \\ = \tilde{\bar{\rho}}_{q,\xi}^{n}\tilde{V}_{q,\xi}^{n} - \Delta t C\tilde{V}_{q,\xi} - \tilde{\beta}_{q,\xi}^{n+1}\left[\tilde{V}_{G,\xi}^{n} - \sum_{m} \tilde{\alpha}_{qm,eff,\xi}^{n+1}\tilde{V}_{qm,\xi}^{n}\right] + \tilde{\eta}_{q,\zeta}^{n+1} .\end{aligned} \tag{3-150}$$

The velocity difference in the interfacial drag term is evaluated from

$$V_{q'q,\xi} = V_{q',\xi}^{n+1} - V_{q,\xi}^{n+1} = V_{q',\xi}^{k} - V_{q,\xi}^{k} , \tag{3-151a}$$

for the *k*-th iteration, and

$$K_{qS,\xi}^{k} = a_{qS,\xi} + b_{qS,\xi}V_{q,\xi}^{k} , \tag{3-151b}$$

$$(V\tilde{C})_{q,\xi}^{n+1} = \alpha_{q,eff}\alpha_{G,\xi}VM_{\xi} \text{ for } q=1 \text{ and } 2 , \tag{3-151c}$$

$$(V\tilde{C})_{G,\xi}^{n+1} = -\alpha_{G,\xi}VM_{\xi} \text{ for } q=G, \text{and} \tag{3-151d}$$

$$\alpha_{q,eff} = \frac{\alpha_q}{\alpha_{q1} + \alpha_{q2}} , \tag{3-151e}$$

and VM_{ξ} is the cell-averaged virtual mass coefficient computed in Step 1. The iteration procedure for solving Eq. (3-150) is the same as Step 2. Namely, the equation can be expressed in the form of a matrix,

$$\underset{\sim}{S}_{\xi}^{k}\,\delta\underset{\sim}{\tilde{V}}_{\xi}^{n+1} = \underset{\sim}{D}_{\xi}^{k} , \tag{3-152}$$

where $\delta\underset{\sim}{\tilde{V}}_{\xi}^{n+1}$ are corrections to $\underset{\sim}{\tilde{V}}_{\xi}^{n+1}$. The matrix coefficients, for the standard three-velocity-field model, are

$$s_{11,\xi}^{k} = \tilde{\bar{\rho}}_{1,\xi}^{n+1} + \Delta t(K_{1S,\xi}^{k} + K_{12,\xi}^{k} + K_{13,\xi}^{k}) - (\tilde{\alpha}_{1,eff,\xi}^{n+1})^2\tilde{\beta}_{G,\xi}^{n+1} , \tag{3-153a}$$

$$s_{12,\xi}^{k} = s_{21,\xi}^{k} = -\Delta t K_{12,\xi}^{k} - \tilde{\alpha}_{1,eff,\xi}^{n+1}\tilde{\alpha}_{2,eff,\xi}^{n+1}\tilde{\beta}_{G,\xi}^{n+1} , \tag{3-153b}$$

$$s_{22,\xi}^{k} = \tilde{\bar{\rho}}_{2,\xi}^{n+1} + \Delta t(K_{2S,\xi}^{k} + K_{12,\xi}^{k} + K_{23,\xi}^{k}) - (\tilde{\alpha}_{2,eff,\xi}^{n+1})^{2}\tilde{\beta}_{G,\xi}^{n+1} \,, \tag{3-153c}$$

$$s_{13,\xi}^{k} = s_{3-1,\xi}^{k} = -\Delta t K_{13,\xi}^{k} + \tilde{\alpha}_{1,eff,\xi}^{n+1}\tilde{\beta}_{G,\xi}^{n+1} \,, \tag{3-153d}$$

$$s_{23,\xi}^{k} = s_{32,\xi}^{k} = -\Delta t K_{23,\xi}^{k} + \tilde{\alpha}_{2,eff,\xi}^{n+1}\tilde{\beta}_{G,\xi}^{n+1} \text{ , and} \tag{3-153e}$$

$$s_{33,\xi}^{k} = \tilde{\bar{\rho}}_{3,\xi}^{n+1} + \Delta t(K_{3S,\xi}^{k} + K_{13,\xi}^{k} + K_{23,\xi}^{k}) - \tilde{\beta}_{G,\xi}^{n+1} \,, \tag{3-153f}$$

where

$$K_{qS,\xi}^{k} = a_{qS,\xi} + 2b_{qS,\xi}\left|\tilde{V}_{q,\xi}^{k}\right| \text{, and} \tag{3-154a}$$

$$K_{qq',\xi}^{k} = a_{qq',\xi} + 2b_{qq',\xi}\left|\tilde{V}_{q',\xi}^{k} - \tilde{V}_{q,\xi}^{k}\right| . \tag{3-154b}$$

The $\underline{D}_{\xi}^{k}$ vector is given by

$$d_{q,\zeta} = \tilde{\bar{\rho}}_{q,\xi}^{n}\tilde{V}_{q,\xi}^{n} - \Delta t C\tilde{V}_{q,\xi} - \tilde{\beta}_{q,\xi}^{n+1}\left[\tilde{V}_{G,\xi}^{n} - \tilde{\alpha}_{q1,eff,\xi}^{n+1}\tilde{V}_{q1,\xi}^{n} - \tilde{\alpha}_{q2,eff,\xi}^{n+1}\tilde{V}_{q2,\xi}^{n}\right] + \tilde{\eta}_{q,\zeta}^{n+1} . \tag{3-155}$$

For optional multi-velocity-field model, the extension of Eqs. (3-158) – (3-160) up to 8 by 8 matrix is straightforward like in Step 2. The identical convergence criteria are employed in Step 4 as well. When convergence is obtained for the momentum equations, the end-of-time-step velocities are all known.

3.4.7. Interfacial drag heating

Following the convergence to the final velocities, interfacial drag heating is calculated. From the differential equations, the general form of the interfacial energy production on a unit mass basis for an energy component belonging to momentum field q is

$$\Theta_q = \frac{\Delta t}{\bar{\rho}_q}\left[\sum_{q'} K_{qq'}(v_q - v_{q'}) \cdot (v_q - v_{qq'}) + K_{qS}v_q \cdot (v_q - v_{qS}) - VM_q \cdot (v_q - v_{GL})\right], \tag{3-156a}$$

$$\Theta_S = \frac{\Delta t}{\bar{\rho}_q}\sum_{q} K_{qS}v_q \cdot v_{qS} \,, \tag{3-156b}$$

where Θ_q and Θ_S represent drag heating on fluid/fluid interface and fluid/structure interface, respectively.

The interfacial velocities are defined as follows. The velocity in the virtual mass term v_{GL} is best represented by some liquid velocity because of the inertia in the liquids. Since the virtual mass concept is based on component volumes, v_{GL} is defined by the volume averaged velocity, for a case of the three-velocity-field model,

$$v_{GL} = \frac{\alpha_{q1}}{\alpha_{q1} + \alpha_{q2}}v_{q1} + \frac{\alpha_{q2}}{\alpha_{q1} + \alpha_{q2}}v_{q2} . \tag{3-157}$$

In the cases of fluid/fluid interface and fluid/structure drag heating, the choice was made to interpolate velocities based on momentum-field volume fractions because of the stability that this approach gives, again for the three-velocity-field case.

$$v_{qq'} = \frac{\alpha_q}{\alpha_q + \alpha_{q'}} v_{q'} + \frac{\alpha_{q'}}{\alpha_q + \alpha_{q'}} v_q \text{ , and} \qquad \text{(3-158)}$$

$$v_{qS} = \frac{\alpha_S}{\alpha_q + \alpha_S} v_q \, . \qquad \text{(3-158)}$$

The resultant expressions for Θ_q and Θ_S are

$$\begin{aligned}\Theta_{q,\xi} = \frac{\Delta t}{\bar{\rho}_{q,\xi}^{n+1}} \Bigg\{ & \sum_{q'} \left(a_{qq',\xi} + b_{qq',\xi} \left| V_{q',\xi}^{n+1} - V_{q,\xi}^{n+1} \right| \right) \frac{\tilde{\alpha}_{q,\xi}^{n+1}}{\tilde{\alpha}_{q,\xi}^{n+1} + \tilde{\alpha}_{q',\xi}^{n+1}} \left| V_{q',\xi}^{n+1} - V_{q,\xi}^{n+1} \right|^2 \\ & + \left(a_{qS,\xi} + b_{qS,\xi} \left| V_{q,\xi}^{n+1} \right| \right) \frac{\tilde{\alpha}_{q,\xi}^{n+1}}{\tilde{\alpha}_{q,\xi}^{n+1} + \tilde{\alpha}_{S,\xi}^{n+1}} \left| V_{q,\xi}^{n+1} \right|^2 \\ & + \tilde{\beta}_{q,\xi}^{n+1} \left[\frac{V_{G,\xi}^{n+1} - V_{G,\xi}^{n}}{\Delta t} \right. \\ & \left. - \tilde{\alpha}_{q1,eff}^{n+1} \frac{V_{q1,\xi}^{n+1} - V_{q1,\xi}^{n}}{\Delta t} - \tilde{\alpha}_{q2,eff}^{n+1} \frac{V_{q2,\xi}^{n+1} - V_{q2,\xi}^{n}}{\Delta t} \right] \left[V_{G,\xi}^{n+1} - \tilde{\alpha}_{q1,eff}^{n+1} V_{q1,\xi}^{n+1} \right. \\ & \left. - \tilde{\alpha}_{q2,eff}^{n+1} V_{q2,\xi}^{n+1} \right] \Bigg\} \text{ , and} \end{aligned} \qquad \text{(3-160)}$$

$$\Theta_{S,\xi} = \frac{\Delta t}{\bar{\rho}_{S,\xi}^{n+1}} \sum_{q} \left(a_{qS,\xi} + b_{qS,\xi} \left| V_{q,\xi}^{n+1} \right| \right) \frac{\alpha_{S,\xi}}{\tilde{\alpha}_{q,\xi}^{n+1} + \alpha_{S,\xi}} \left| V_{q,\xi}^{n+1} \right|^2 . \qquad \text{(3-161)}$$

Equation (3-161) is further sub-divided into the three (or five) structure surfaces.

$$a_{SS} = \sum_{j} a_{Sj} \, , \qquad \text{(3-162)}$$

where subscript j denotes the cladding, left and right (or plus front and back) can wall, with the surface areas are given by input. By defining the total volume fractions and densities as

$$\alpha_{SS} = \sum_{j} \alpha_{Sj} \text{ , and} \qquad \text{(3-163)}$$

$$\bar{\rho}_{SS} = \sum_{j} \bar{\rho}_{Sj} \, . \qquad \text{(3-164)}$$

the interfacial heating is then recalculated by

$$\Theta_{Sj,\xi} = \frac{\Delta t}{\bar{\rho}_{SS,\xi}} \frac{a_{j,\xi}}{a_{SS,\xi}} \sum_{q} \left(a_{qS,\xi} + b_{qS,\xi} \left| V_{q,\xi}^{n+1} \right| \right) \frac{\alpha_{SS,\xi}}{\tilde{\alpha}_{q,\xi}^{n+1} + \alpha_{SS,\xi}} \left| V_{q,\xi}^{n+1} \right|^2 , \qquad \text{(3-165)}$$

where $\alpha_{SS,\xi}$ is averaged over two cells of α_{SS}. In the calculation of $\Theta_{q,\xi}$ in Eq. (3-165), $\alpha_{SS,\xi}$ is used instead of $\alpha_{S,\xi}$. After determining the $\Theta_{q,\xi}$ and $\Theta_{S,\xi}$, the cell-centered values are calculated from

$$\Theta_{q,ikj} = \big[\Theta_{q,i-1/2,k,j} + \Theta_{q,i+1/2,k,j} + \Theta_{q,i,k-1/2,j} + \Theta_{q,i,k+1/2,j} + \Theta_{q,i,k,j-1/2} + \Theta_{q,i,k,j+1/2}\big]/2 \text{ , and} \tag{3-166a}$$

$$\Theta_{S,ikj} = \big[\Theta_{S,i-1/2,k,j} + \Theta_{S,i+1/2,k,j} + \Theta_{S,i,k-1/2,j} + \Theta_{S,i,k+1/2,j} + \Theta_{S,i,k,j-1/2} + \Theta_{S,i,k,j+1/2}\big]/2 \text{ .} \tag{3-166b}$$

The internal energies can then be updated by, for the standard three-field model,

$$e^{n+1}_{S,ikj} = \tilde{e}^{n+1}_{S,ikj} + \Theta_{S,ikj} \text{ ,} \tag{3-167a}$$

$$e^{n+1}_{L1,ikj} = \tilde{e}^{n+1}_{L1,ikj} + \Theta_{q1,ikj} \text{ ,} \tag{3-167b}$$

$$e^{n+1}_{L2,ikj} = \tilde{e}^{n+1}_{L2,ikj} + \Theta_{q1,ikj} \text{ ,} \tag{3-167c}$$

$$e^{n+1}_{L3,ikj} = \tilde{e}^{n+1}_{L3,ikj} + \Theta_{q2,ikj} \text{ ,} \tag{3-167d}$$

$$e^{n+1}_{L4,ikj} = \tilde{e}^{n+1}_{L4,ikj} + \Theta_{q1,ikj} \text{ ,} \tag{3-167e}$$

$$e^{n+1}_{L5,ikj} = \tilde{e}^{n+1}_{L5,ikj} + \Theta_{q1,ikj} \text{ ,} \tag{3-167f}$$

$$e^{n+1}_{L6,ikj} = \tilde{e}^{n+1}_{L6,ikj} + \Theta_{q2,ikj} \text{ ,} \tag{3-167g}$$

$$e^{n+1}_{L7,ikj} = \tilde{e}^{n+1}_{L7,ikj} + \Theta_{q1,ikj} \text{ , and} \tag{3-167h}$$

$$e^{n+1}_{G,ikj} = \tilde{e}^{n+1}_{G,ikj} + \Theta_{G,ikj} \text{ .} \tag{3-167i}$$

3.4.8. Final operation

The final operation in Step 4 is to invert the EOS. The liquid temperatures are obtained straightforwardly from the internal energies and the cell pressure. The vapor temperature is obtained with an iteration using

$$T^{k+1}_G = T^k_G - \frac{e_G(T^k_G) - e^{n+1}_G}{\partial e_G / \partial T_G} \text{ ,} \tag{3-168}$$

where

$$e_G(T^k_G) = \sum_m \bar{\rho}^{n+1}_{Gm}\, e_{Gm}(T_G) / \sum_m \bar{\rho}^{n+1}_{Gm} \text{ ,} \tag{3-169}$$

and

$$\frac{\partial e_G}{\partial T_G} = \sum_m \bar{\rho}^{n+1}_{Gm} \frac{\partial e_{Gm}}{\partial T_G} / \sum_m \bar{\rho}^{n+1}_{Gm} \text{ .} \tag{3-170}$$

From the vapor EOS, the vapor internal energies and microscopic densities are

$$e_{Gm} = e_{Gm}^{+} + \frac{0.8a_{G2,M}\left(\frac{T_G}{T_{Crt,M}}\right)^{0.2}}{a_{G1,M}} ln\left[\frac{1 + a_{G3,M}\rho_{GM}^{+}}{\rho_{Gm}}\right] \text{, and} \tag{3-171}$$

$$\rho_{Gm} = \frac{\tilde{\tilde{\rho}}_{Gm}^{n+1}}{max[\alpha_0(1-\alpha_S),\ 1-\alpha_S-(1-\alpha_0)\alpha_L]}, \tag{3-172}$$

where

$$\alpha_L = \sum_m \tilde{\tilde{\rho}}_{Lm}^{n+1}/\rho_{Lm} \text{ , and} \tag{3-173}$$

$$\rho_{Lm} = \rho_{Lm}(p_{cell},\ e_{Lm}) \,. \tag{3-174}$$

Thus, the derivatives of the vapor internal energy with respect to vapor temperature is expressed by

$$\begin{aligned} \frac{\partial e_{Gm}}{\partial T_G} = \frac{\partial e_{Gm}^{+}}{\partial T_G} + \left(\frac{a_{G2,M}}{a_{G3,M}T_{Crt.M}^{0.2}}\right)\Bigg\{\frac{0.16}{T_G^{0.8}} ln\left[\frac{1 + a_{G3,M}\rho_{GM}^{+}}{1 + a_{G3,M}\rho_{Gm}}\right] \\ + 0.8T_G^{0.2}\left[\frac{a_{G3,M}}{1 + a_{G3,M}\rho_{GM}^{+}}\frac{\partial \rho_{GM}^{+}}{\partial T_G}\right]\Bigg\}, \end{aligned} \tag{3-175a}$$

with

$$\frac{\partial e_{Gm}^{+}}{\partial T_G} \text{ and } \frac{\partial \rho_{GM}^{+}}{\partial T_G}, \tag{3-175b}$$

coming from the EOS relationships.

3.5. Momentum Diffusion Model (Viscous Drag Term)

3.5.1. Background

In the early versions of SIMMER-III, the viscous drag term due to molecular diffusion perpendicular to flow velocities was not included in the momentum equations. This is because the effect of inter-cell momentum diffusion is not necessarily important in reactor-scale applications where relatively large mesh cell sizes are used and the transient fluid motion during accident progression is driven mainly by pressure-driven acceleration and the gravity. On the contrary, in analyses of small-scale experiments with fine mesh simulation, the inter-cell momentum coupling has non-negligible effects.

In some of the test problems studied in the phase 1 assessment of SIMMER-III10), in which fundamental small-scale single- and two-phase flow experiments were analyzed, the neglect of momentum diffusion perpendicular to the velocities in the momentum equation has been criticized by some of the authors. Later during the phase 2 assessment program11), a preliminary model of the momentum diffusion was developed and applied to some of the test problems, showing obvious improvement especially in simulating laminar or low velocity flow experiments. Then this model has been extended to three dimensions in SIMMER-IV. The momentum diffusion model with the viscous drag term in SIMMER-III/SIMMER-IV, available as an input option, is described in this section. In the multi-component, multi-velocity fluid dynamics system, involving different flow regimes, implementation of the model requires a rather complex procedure to judge whether the momentum diffusion is to be treated.

Since the early days of SIMMER-III code development and assessment, turbulence modeling has been desired for treating multiphase turbulent flow problems and addressing small-node to large-node scaling questions. However, derivation of the appropriate turbulence closure relationships still requires a research program. Although some preliminary efforts have been conducted for SIMMER-III, no model has yet been developed to a level sufficient for inclusion as a standard model of SIMMER-III/SIMMER-IV.

3.5.2. Formulation of viscous drag term

The momentum equation for the velocity field q solved in the convection part of the fluid-dynamics algorithm, shown in Eq. (3-7), is revised to include the viscous drag term as:

$$\begin{aligned}\frac{\partial \bar{\rho}_q \boldsymbol{v}_q}{\partial t} &+ \sum_{m \in q} \nabla \cdot \left(\bar{\rho}_m \boldsymbol{v}_q \boldsymbol{v}_q\right) + \alpha_q \nabla p - \bar{\rho}_q g + K_{qS} \boldsymbol{v}_q - \sum_{q'} K_{qq'} \left(\boldsymbol{v}_{q'} - \boldsymbol{v}_q\right) - \nabla \cdot \left(\alpha_q \bar{\boldsymbol{\tau}}_q\right) \\ &- \boldsymbol{VM}_q = 0 \,,\end{aligned} \tag{3-176}$$

where $\nabla \cdot \left(\alpha_q \bar{\boldsymbol{\tau}}_q\right)$ is the viscous drag term and $\bar{\boldsymbol{\tau}}_q$ denotes the viscous stress tensor. Since the viscous drag term transfers momentum along a velocity gradient due to viscous shear force, this term is also called the momentum diffusion term. The elements of $\bar{\boldsymbol{\tau}}_q$ are generally defined as:

$$\tau_{lm} = \mu \left(\frac{\partial U_l}{\partial x_m} + \frac{\partial U_m}{\partial x_l} - \frac{2}{3} \frac{\partial U_n}{\partial x_n} \delta_{lm} \right), \tag{3-177}$$

where μ is the viscosity, and δ_{lm} is the Kronecker delta operator, with $\delta_{lm} = 1$ only if $l = m$.

The viscous drag terms in three directions of Cartesian and cylindrical coordinate systems are:

$$\begin{aligned}D_{q,x} &= \frac{\partial}{\partial x_x}\left(\alpha_q \tau_{xm}\right) \\ &= \frac{1}{r^\zeta} \frac{\partial}{\partial x}\left(\alpha_q r^\zeta \tau_{xx}\right) + \frac{1}{r^\zeta} \frac{\partial}{\partial y}\left(\alpha_q \tau_{xy}\right) - \frac{\zeta}{r^\zeta}\left(\alpha_q \tau_{yy}\right) + \frac{\partial}{\partial z}\left(\alpha_q \tau_{xz}\right),\end{aligned} \tag{3-178a}$$

$$D_{q,y} = \frac{\partial}{\partial x_y}\left(\alpha_q \tau_{ym}\right) = \frac{\partial}{\partial x}\left(\alpha_q \tau_{xy}\right) + \frac{1}{r^\zeta} \frac{\partial}{\partial y}\left(\alpha_q \tau_{yy}\right) + \frac{2\zeta}{r^\zeta}\left(\alpha_q \tau_{xy}\right) + \frac{\partial}{\partial z}\left(\alpha_q \tau_{yz}\right), \text{and} \tag{3-178b}$$

$$D_{q,z} = \frac{\partial}{\partial x_z}\left(\alpha_q \tau_{zm}\right) = \frac{1}{r^\zeta} \frac{\partial}{\partial x}\left(\alpha_q r^\zeta \tau_{xz}\right) + \frac{1}{r^\zeta} \frac{\partial}{\partial y}\left(\alpha_q \tau_{yz}\right) + \frac{\partial}{\partial z}\left(\alpha_q \tau_{zz}\right), \tag{3-178c}$$

where $\zeta = 0$ for the Cartesian geometry, and $\zeta = 1$ for the cylindrical geometry. In the cylindrical geometry, coordinates (x, y, z) are read as (r, θ, z). The drag stress tensor is expanded and the above equations are re-written as:

$$\begin{aligned} D_{q,x} = & \frac{1}{r^\zeta}\frac{\partial}{\partial x}\left[\alpha_q r^\zeta \mu_q\left(2\frac{\partial u}{\partial x}-\frac{2}{3}(\nabla\cdot\boldsymbol{v}_q)\right)\right]+\frac{1}{r^\zeta}\frac{\partial}{\partial y}\left[\alpha_q\mu_q\left(r^\zeta\frac{\partial}{\partial x}\left(\frac{w}{r^\zeta}\right)+\frac{1}{r^\zeta}\frac{\partial u}{\partial y}\right)\right] \\ & -\frac{\zeta\alpha_q\mu_q}{r^\zeta}\left[2\left(\frac{1}{r^\zeta}\frac{\partial w}{\partial y}+\frac{u}{r^\zeta}\right)-\frac{2}{3}(\nabla\cdot\boldsymbol{v}_q)\right]+\frac{\partial}{\partial z}\left[\alpha_q\mu_q\left(\frac{\partial v}{\partial x}+\frac{\partial u}{\partial z}\right)\right], \end{aligned} \tag{3-179a}$$

$$\begin{aligned} D_{q,y} = & \frac{\partial}{\partial x}\left[\alpha_q\mu_q\left(r^\zeta\frac{\partial}{\partial x}\left(\frac{w}{r^\zeta}\right)+\frac{1}{r^\zeta}\frac{\partial u}{\partial y}\right)\right] \\ & +\frac{1}{r^\zeta}\frac{\partial}{\partial y}\left[\alpha_q\mu_q\left(2\left(\frac{1}{r^\zeta}\frac{\partial w}{\partial y}+\frac{\zeta u}{r^\zeta}\right)-\frac{2}{3}(\nabla\cdot\boldsymbol{v}_q)\right)\right] \\ & +\frac{2\zeta\alpha_q\mu_q}{r^\zeta}\left[r^\zeta\frac{\partial}{\partial x}\left(\frac{w}{r^\zeta}\right)+\frac{1}{r^\zeta}\frac{\partial u}{\partial y}\right]+\frac{\partial}{\partial z}\left[\alpha_q\mu_q\left(\frac{\partial w}{\partial x}+\frac{1}{r^\zeta}\frac{\partial v}{\partial y}\right)\right] \text{, and} \end{aligned} \tag{3-179b}$$

$$\begin{aligned} D_{q,z} = & \frac{1}{r^\zeta}\frac{\partial}{\partial x}\left[\alpha_q r^\zeta\mu_q\left(\frac{\partial v}{\partial x}+\frac{\partial u}{\partial z}\right)\right]+\frac{1}{r^\zeta}\frac{\partial}{\partial y}\left[\alpha_q\mu_q\left(\frac{\partial w}{\partial z}+\frac{1}{r^\zeta}\frac{\partial v}{\partial y}\right)\right] \\ & +\frac{\partial}{\partial z}\left[\alpha_q\mu_q\left(2\frac{\partial v}{\partial z}-\frac{2}{3}(\nabla\cdot\boldsymbol{v}_q)\right)\right], \end{aligned} \tag{3-179c}$$

where

$$(\nabla\cdot\boldsymbol{v}_q)=\frac{1}{r^\zeta}\frac{\partial(r^\zeta u_q)}{\partial x}+\frac{1}{r^\zeta}\frac{\partial w_q}{\partial y}+\frac{\partial v_q}{\partial z}, \tag{3-180}$$

and μ_q is the mixture viscosity of velocity field q and is defined by a volume average of the viscosities of fluid components constituting the velocity field. In two-dimensional SIMMER-III, the equation in the y direction $D_{q,y}$ and the terms with the coordinate y and velocity w are simply omitted.

It is noted that the above formulation would better fit in the momentum equation if the macroscopic density could be used instead of the volume fraction using the relation $\bar{\rho}_q = \alpha_q \upsilon_q$, where υ_q is the specific volume. Then the viscosity μ_q is simply replaced by the kinematic viscosity ν_q, for $\mu_q\alpha_q = \nu_q\bar{\rho}_q$. The SIMMER-II formulation of the viscous drag term employed the kinematic viscosity and the input constant value is used for each of the liquid materials. However, for SIMMER-III and SIMMER-IV, it is preferred to use temperature-dependent viscosities, to be consistent with the analytic thermophysical property model.[13] Thus, the above formulation using the volume fractions is employed.

The discretization of the Eq. (3-179) requires lengthy manipulation of the equations and hence only an example in the x direction is shown below. The four terms of the right side of Eq. (3-179a) are respectively discretized as:

$$
\begin{aligned}
&\frac{1}{r^{\zeta}}\frac{\partial}{\partial x}\left[\alpha_q r^{\zeta}\mu_q\left(2\frac{\partial u}{\partial x}-\frac{2}{3}(\nabla\cdot\boldsymbol{v}_q)\right)\right]\\
&\qquad=\frac{1}{{r_{i+1/2}}^{\zeta}}\frac{1}{(\Delta x_i+\Delta x_{i+1})/2}\Bigg[\alpha_{q,i+1,k,j}{r_{i+1}}^{\zeta}\mu_{q,i+1,k,j}\Bigg\{2\frac{u_{q,i+3/2,k,j}-u_{q,i+1/2,k,j}}{\Delta x_{i+1}}\\
&\qquad-\frac{2}{3}\Bigg(\frac{1}{{r_{i+1}}^{\zeta}}\frac{{r_{i+3/2}}^{\zeta}u_{q,i+3/2,k,j}-{r_{i+1/2}}^{\zeta}u_{q,i+1/2,k,j}}{\Delta x_{i+1}}\\
&\qquad+\frac{1}{{r_{i+1}}^{\zeta}}\frac{w_{q,i+1,k+1/2,j}-w_{q,i+1,k-1/2,j}}{\Delta y_k}+\frac{v_{q,i+1,k,j+1/2}-v_{q,i+1,k,j-1/2}}{\Delta z_i}\Bigg)\Bigg\}\\
&\qquad-\alpha_{q,i,k,j}{r_{i+1}}^{\zeta}\mu_{q,i,k,j}\Bigg\{2\frac{u_{q,i+1/2,k,j}-u_{q,i-1/2,k,j}}{\Delta x_i}\\
&\qquad-\frac{2}{3}\Bigg(\frac{1}{{r_i}^{\zeta}}\frac{{r_{i+1/2}}^{\zeta}u_{q,i+1/2,k,j}-{r_{i-1/2}}^{\zeta}u_{q,i-1/2,k,j}}{\Delta x_i}+\frac{1}{{r_i}^{\zeta}}\frac{w_{q,i,k+1/2,j}-w_{q,i,k-1/2,j}}{\Delta y_k}\\
&\qquad+\frac{v_{q,i,k,j+1/2}-v_{q,i,k,j-1/2}}{\Delta z_j}\Bigg)\Bigg\}\Bigg],
\end{aligned}
\tag{3-181a}
$$

$$
\begin{aligned}
&\frac{1}{r^{\zeta}}\frac{\partial}{\partial y}\left[\alpha_q\mu_q\left(r^{\zeta}\frac{\partial}{\partial x}\left(\frac{w}{r^{\zeta}}\right)+\frac{1}{r^{\zeta}}\frac{\partial u}{\partial y}\right)\right]\\
&\qquad=\frac{1}{{r_{i+1/2}}^{\zeta}}\frac{1}{\Delta y_k}\Bigg[\alpha_{q,i+1/2,k+1/2,j}\mu_{q,i+1/2,k+1/2,j}\Bigg\{\frac{{r_{i+1/2}}^{\zeta}}{(\Delta x_i+\Delta x_{i+1})/2}\Bigg(\frac{w_{q,i+1,k+1/2,j}}{{r_{i+1}}^{\zeta}}\\
&\qquad-\frac{w_{q,i,k+1/2,j}}{{r_i}^{\zeta}}\Bigg)+\frac{1}{{r_{i+1/2}}^{\zeta}}\frac{u_{q,i+1/2,k+1,j}-u_{q,i+1/2,k,j}}{(\Delta y_k+\Delta y_{k+1})/2}\Bigg\}\\
&\qquad-\alpha_{q,i+1/2,k-1/2,j}\mu_{q,i+1/2,k-1/2,j}\Bigg\{\frac{{r_{i+1/2}}^{\zeta}}{(\Delta x_i+\Delta x_{i+1})/2}\Bigg(\frac{w_{q,i+1,k-1/2,j}}{{r_{i+1}}^{\zeta}}-\frac{w_{q,i,k-1/2,j}}{{r_i}^{\zeta}}\Bigg)\\
&\qquad+\frac{1}{{r_{i+1/2}}^{\zeta}}\frac{u_{q,i+1/2,k,j}-u_{q,i+1/2,k,j}}{(\Delta y_k+\Delta y_{k-1})/2}\Bigg\}\Bigg],
\end{aligned}
\tag{3-181b}
$$

$$
\begin{aligned}
&\frac{\zeta\alpha_q\mu_q}{r^{\zeta}}\left[2\left(\frac{1}{r^{\zeta}}\frac{\partial w}{\partial y}+\frac{u}{r^{\zeta}}\right)-\frac{2}{3}(\nabla\cdot\boldsymbol{v}_q)\right]\\
&\qquad=\frac{\zeta}{{r_{i+1/2}}^{\zeta}}\alpha_{q,i+1/2,k,j}\mu_{q,i+1/2,k,j}\Bigg[2\Bigg\{\frac{1}{{r_{i+1/2}}^{\zeta}}\frac{1}{\Delta y_k}\Bigg(\frac{w_{q,i+1,k+1/2,j}-w_{q,i,k+1/2,j}}{2}\\
&\qquad-\frac{w_{q,i+1,k-1/2,j}-w_{q,i+3/2,k-1/2,j}}{2}\Bigg)+\frac{u_{q,i+1/2,k,j}}{{r_{i+1/2}}^{\zeta}}\Bigg\}\\
&\qquad-\frac{2}{3}\Bigg\{\frac{1}{{r_{i+1/2}}^{\zeta}}\frac{{r_{i+3/2}}^{\zeta}u_{q,i+1/2,k,j}-{r_{i-1/2}}^{\zeta}u_{q,i-1/2,k,j}}{\Delta x_i+\Delta x_{i+1}}\\
&\qquad+\frac{1}{{r_{i+1/2}}^{\zeta}}\frac{1}{\Delta y_k}\Bigg(\frac{w_{q,i+1,k+1/2,j}+w_{q,i,k+1/2,j}}{2}-\frac{w_{q,i+1,k-1/2,j}+w_{q,i+1,k-1/2,j}}{2}\Bigg)\\
&\qquad+\frac{1}{\Delta z_j}\Bigg(\frac{v_{q,i+1,k,j+1/2}+v_{q,i,k,j+1/2}}{2}-\frac{v_{q,i+1,k,j-1/2}+v_{q,i+1,k,j-1/2}}{2}\Bigg)\Bigg\}\Bigg]\ \text{, and}
\end{aligned}
\tag{3-181c}
$$

$$
\begin{aligned}
&\frac{\partial}{\partial z}\left[\alpha_q \mu_q \left(\frac{\partial v}{\partial x} + \frac{\partial u}{\partial z}\right)\right] \\
&\qquad = \frac{1}{\Delta z_j}\left[\alpha_{q,i+1/2,k,j+1/2}\mu_{q,i+1/2,k,j+1/2}\left(\frac{v_{q,i+1,k,j+1/2} - v_{q,i,k,j+1/2}}{(\Delta x_i + \Delta x_{i+1})/2}\right.\right. \\
&\qquad \left. + \frac{u_{q,i+1/2,k,j+1} - u_{q,i+1/2,k,j}}{(\Delta x_i + \Delta x_{i+1})/2}\right) \\
&\qquad - \alpha_{q,i+1/2,k,j-1/2}\mu_{q,i+1/2,k,j-1/2}\left(\frac{v_{q,i+1,k,j-1/2} - v_{q,i,k,j-1/2}}{(\Delta x_i + \Delta x_{i+1})/2}\right. \\
&\qquad \left.\left. + \frac{u_{q,i+1/2,k,j} - u_{q,i+1/2,k,j-1}}{(\Delta z_j + \Delta z_{j-1})/2}\right)\right].
\end{aligned}
\tag{3-181d}
$$

Equations (3-179b) and (3-179c) are discretized similarly in the *y* and *z* directions, respectively.

3.5.3. Implementation in SIMMER-III/SIMMER-IV

The momentum diffusion occurs only in a continuous real liquid or gas phase where viscous shear force acts perpendicular to the velocities. There is no momentum diffusion occurring between dispersed components or between dispersed component and continuous phase. This means, in a multi-component, multi-velocity fluid dynamics system, involving different flow regimes, implementation of the model requires a rather complex procedure to judge whether the momentum diffusion is to be treated between pairs of mesh cells potentially having different flow conditions. Determination of a liquid component constituting the continuous phase, the volume fractions of real liquids and vapor mixture are calculated first. Since the momentum cells in certain directions are shifted by half a mesh size, the volume fractions are calculated by averaging the values of the real cells. In a similar procedure to the flow topology and interfacial area model, based mainly on the calculated component volume fractions, the continuous phase component and volume fraction are determined. Then at each mesh cell boundary, a flag to calculate momentum diffusion is set.

The momentum equation is solved twice in SIMMER-III/SIMMER-IV. In Step 2, the end-of-time-step velocities are iteratively estimated, using the beginning-of-time-step pressure, to initiate the pressure iteration in Step 3. The viscous drag term is added to the momentum equation in Step 2 before the velocity iteration operation. After the converged end-of-time-step pressure is computed in Step 3, the momentum equation is solved again in Step 4 to obtain the end-of-time-step velocities. The viscous drag term is added before the velocity iteration. The viscous drag term is kept unchanged during these iterations.

The SIMMER-III code with the momentum diffusion model was validated for a Poiseuille flow in a two-dimensional slab geometry. SIMMER-III completely reproduced the theoretical solution of the velocity profile. The same problem was recalculated by SIMMER-IV with a two-dimensional representation and the almost identical result was obtained.

3.5.4. On turbulence modeling

Since the early days of SIMMER-III code development and assessment, a model of turbulence diffusion has been desired for treating multiphase turbulent flow problems. However, an appropriate turbulence model applicable to multi-phase flows is not available and the inclusion of turbulence closure relationships in SIMMER-III still requires a research program. Although some preliminary efforts have been conducted for SIMMER-III, as briefly explained below, no model has yet been developed to a level sufficiently generalized for implementation in SIMMER-III.

Pigny and Coste of CEA-Grenoble developed a simple turbulence model, which is applicable to single- or two-phase flows, by replacing the momentum diffusion term with the turbulence diffusion term. The model was applied to some of the Phase-2 SIMMER assessment program, that is, the Burty and SEBULON experiments (Problems 1.5 and 1.4)11). The model is specific and of limited use, controlled by the input parameters that depend on computational geometries, and hence is not included as a standard option of SIMMER-III. Horie and Shirakawa of Toshiba, under contracts with JAEA, have developed a one-equation, turbulence diffusion model (*k*-equation model), based on an early idea provided by Bohl of Los Alamos. A preliminary formulation and discretization of the turbulence transport equation was attempted19) for possible future inclusion in SIMMER-III. However, these preliminary studies have not been conclusive and a generalized model suitable for implementation as a standard model for SIMMER have not been made available.

3.6. Some Observations on Convection Algorithm

3.6.1. General validity of fluid convection algorithm

The SIMMER-III/SIMMER-IV fluid dynamics is based on technologies available in the 1990s, based on the experience in SIMMER-II and the outcome of the AFDM development program. The modeling choices made for inclusion in the AFDM convection algorithm were discussed in detail and documented in the AFDM Manual Vol. V8). Many of the deficiencies and shortcomings in SIMMER-II have been improved in AFDM. Although more advanced computational fluid dynamics technologies can be applied taking advantage of today's parallel supercomputers, our original purpose of the SIMMER-III/SIMMER-IV development is to provide a next-generation reactor safety analysis code that replaces the former SIMMER-II.

The verification and validation program (code assessment) program has been conducted for SIMMER-III in two phases10),11). Although the fundamental issues, such as numerical instabilities generic to fluid dynamics codes and ill-posedness of a multiphase flow equation set, were not addressed in detail, it was generally confirmed, from many of the test problems analyzed, the fluid-dynamics convection algorithm is basically valid, accurate, numerically stable and robust.

3.6.2. Source-term decoupling problem

In the four-step algorithm of SIMMER-III, the mass and energy source terms are evaluated in Step 1, separately from fluid convection. The reason for choosing this time-factorization technique is that fully coupling the complex intra-cell transfer processes with the fluid convection algorithm was judged to be impractical. Further, a modular code structure of the intra-cell transfer processes, independent of inter-cell convection, would facilitate any future model improvement or addition for local phenomena. A drawback of the time-factorization algorithm is that feedback from convection on intracell heat and mass transfer will not occur within one time step. As a result, it is known that this algorithm may introduce a time-step-size sensitivity issue. From the Phase 1 code assessment calculations10), we have identified one of the causes of this problem. When very rapid coolant boiling occurs and its rate competes fluid convection, the use of a large time-step size underestimates the rate of vaporization because the mesh cell state cannot be relaxed by convection until the next time step. It was concluded that with the time step sizes of 10^{-4} to 10^{-5} s, vaporization/condensation dominant cases are accurately traced. For simulations of fuel-coolant interactions, single phase pressurization, and other highly transient situations, even smaller time step sizes may be desired.

For a slow transient or a near steady-state problem when vaporization/condensation mass transfer is not dominant, time step sizes can be relaxed and this might be desired. For this purpose, a couple of special remedies (Method-1 and Method-2) have been programmed in SIMMER-III. A basic idea is to update a part of intra-cell mass transfer source term within the convection algorithm based on the rate of mass transfer evaluated in Step 1. However, the determination of fractional update is problem dependent, and moreover this procedure may potentially introduce additional time-step size sensitivity. Therefore, even though some provision is made in the code, these special methods must be carefully used.

3.6.3. Drawbacks in cylindrical geometry

The 2D cylindrical representation of two-phase flows introduces the so-called “centerline-problem”, in which liquid tends to be collected along the centerline of the computational cylinder. It is speculated that this problem has been caused by the lack of centrifugal force in an r-z system. In a 3D rectangular simulation, however, there observed no such singular behavior along the centerline. A 3D cylindrical simulation is possible, but the models for a centrifugal force and a Coliolis force may have to be implemented in circumferential fluid convection.

3.6.4. Mass and energy conservation

The mush improved mass and energy conservation in SIMMER-III was achieved by: the small value limiter (10^{-20}) to control numerical underflows and cutting-off of missing components; consistent mass and energy convection using the semi-implicit method; single-phase cell treatment consistent with two-phase cells; mass conservation more than satisfactory with pressure iteration residual $<10^{-2}$; and so on. Energy conservation is less satisfactory, with an order of non-conservation for the system total energy is 10^{-4} and this order of energy may well compete the kinetic energy. The source of this non-conservation comes not from the errors in kinetic energy evaluated by the velocities and masses of fluid convection, which are computed reasonably accurate. The main reason of the 10^{-4} system energy error is attributed to errors in internal energy, coming from the convergence precisions for vapor energy in pressure iteration and the temperature precision in vaporization/condensation iteration. The above 10^{-4} system energy error roughly corresponds to the errors in temperature of the order of 1.0 K and this level of temperature precision should be well acceptable for most of the code application problems.

Table 3-1. Update procedure in four-step algorithm.

Step 1: Calculate intra-cell transfers from the end of the previous time step.

$$\left(\bar{\rho}^{(1)}, v^{(1)}, e^{(1)}\right) \leftarrow \left(\bar{\rho}^{n}, v^{n}, e^{n}\right)$$

Step 2: Estimate end-of-time-step values $\left(\bar{\rho}^{(2)}, v^{(2)}, e^{(2)}\right)$ without intra-cell source terms.

$$\frac{\bar{\rho}^{(2)} - \bar{\rho}^{(1)}}{\Delta t} + \nabla \cdot \left(\bar{\rho}^{(1)} v^{(1)}\right) = 0$$

$$\frac{\bar{\rho}^{(2)} v^{(2)} - \bar{\rho}^{(1)} v^{(1)}}{\Delta t} + \nabla \cdot \left(\bar{\rho}^{(1)} v^{(1)} v^{(1)}\right) + \nabla p^{n} = 0$$

$$\frac{\bar{\rho}^{(2)} e^{(2)} - \bar{\rho}^{(1)} e^{(1)}}{\Delta t} + \nabla \cdot \left(\bar{\rho}^{(1)} e^{(1)} v^{(1)}\right) + p^{n} \nabla \cdot v^{(1)} = 0$$

Step 3: Solve for $\left(\bar{\rho}^{(3)}, v^{(3)}, e^{(3)}\right)$ by pressure iteration.

$$\frac{\bar{\rho}^{(3)} - \bar{\rho}^{(1)}}{\Delta t} + \nabla \cdot \left(\bar{\rho}^{(1)} v^{(3)}\right) = 0$$

$$\frac{\bar{\rho}^{(3)} \vec{v}^{(3)} - \bar{\rho}^{(1)} \vec{v}^{(1)}}{\Delta t} + \nabla \cdot \left(\bar{\rho}^{(1)} v^{(1)} v^{(3)}\right) + \nabla p^{(3)} = 0$$

$$\frac{\bar{\rho}^{(2)} e^{(3)} - \bar{\rho}^{(1)} e^{(1)}}{\Delta t} + \nabla \cdot \left(\bar{\rho}^{(1)} e^{(1)} v^{(1)}\right) + p^{(3)} \nabla \cdot v^{(3)} = 0$$

Step 4: Calculate end-of-time-step values $\left(\bar{\rho}^{n+1}, v^{n+1}, e^{n+1}\right)$.

$$\frac{\bar{\rho}^{(3)} v^{(4)} - \bar{\rho}^{(1)} v^{(1)}}{\Delta t} + \nabla \cdot \left(\bar{\rho}^{(1)} v^{(1)} v^{(3)}\right) + \nabla p^{(3)} = 0$$

$$\frac{\bar{\rho}^{(3)} e^{(4)} - \bar{\rho}^{(1)} e^{(1)}}{\Delta t} + \nabla \cdot \left(\bar{\rho}^{(1)} e^{(1)} v^{(3)}\right) + p^{(3)} \nabla \cdot v^{(3)} = 0$$

$$\left(\bar{\rho}^{n+1}, v^{n+1}, e^{n+1}\right) \leftarrow \left(\bar{\rho}^{(3)}, v^{(4)}, e^{(4)}\right)$$

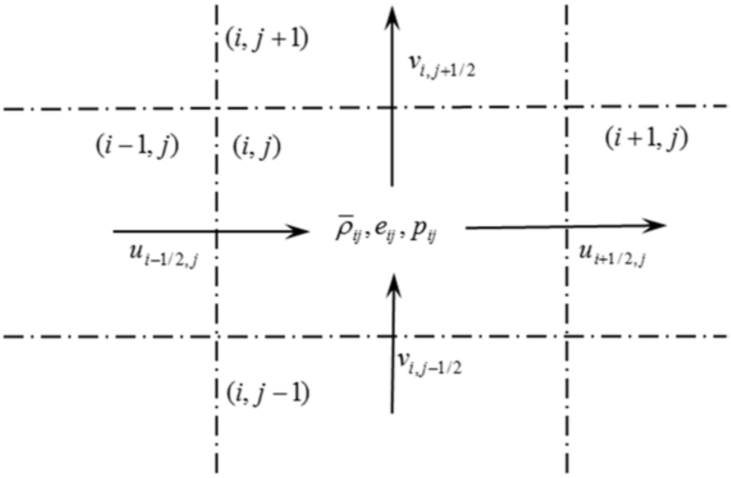

Fig. 3-1. Staggered mesh used for fluid convection (2D SIMMER-III).

4. Intra-Cell Transfer Models

4.0. Overview

4.0.1. Background of models and methods

In the former SIMMER-II[1)], heat and mass exchange rates were determined at the beginning of time step, and the end-of-time-step updates due to convection were calculated assuming these exchange rates stay constant during the time step. This procedure sometimes produced serious stability problems as well as accuracy. A time-factorization, four-step solution algorithm was first developed for the AFDM code[3)]. The complexity associated with modeling the various inter-related phenomena of heat and mass transfer is the main reason of selecting this approach. The successful performance of the algorithm in AFDM has made the decision in SIMMER-III/SIMMER-IV to implement the same algorithm with some improvements made based on the experience in the previous studies with SIMMER-II and AFDM. Even though the time-factorization technique potentially introduces some drawbacks, especially the possibility of time-step-size sensitivity when intra-cell mass transfers compete fluid convection, it is judged the algorithm is practically useful in complex multi-phase flow codes like SIMMER-III/SIMMER-IV.

A most complex portion of the SIMMER-III/SIMMER-IV fluid dynamics is the model for intra-cell heat and mass transfers, which describes the physical phenomena associated with multi-component, multiphase flows. Interactions between different components having different energies take place locally at places where two components come into contact. In SIMMER-III/SIMMER-IV, these local phenomena or interactions are treated as intra-cell transfer processes in fluid-dynamics Step 1, which is separated from the fluid inter-cell fluid convection treated in Steps 2-4. Step 1 solves the mass and energy equations without convection terms, and updates the end-of-time-step mesh cell variables resulted from intra-cell heat and mass transfer. Step 1 also include the models for inter-cell heat conduction, momentum exchange functions to be used in fluid-convection calculations and energy updates due to nuclear heating.

The fluid-dynamics Step 1 consists of a series of operations to calculate: interfacial areas, momentum exchange functions, heat-transfer coefficients, structure configuration, heat and mass transfers, etc. The models for these operations are modularized in different routines, so that future model improvement or replacement can be easily implemented. Because of the complexity of Step 1 operations, the contents and overall calculative procedure are explained in **Section 4.1**, before describing individual models in the subsequent sections.

4.0.2. Interaction with other models

Intra-cell heat and mass calculations in Step 1 (see **Fig. 4-1**) solve the fundamental fluid-dynamic equations for mass and energy conservation without convection terms. End-of-time-step updates of macroscopic densities and specific internal energies due to intra-cell heat and mass transfer are decoupled from fluid convection. The updated densities and energies are used as initial end-of-time-step estimates for fluid convection calculations in Step 2. The component volume fractions, EOS properties, and the cell pressure are also updated. The momentum exchange functions, defined as drag coefficients between a fluid component and other fluids or structure surfaces, are calculated based on the structure configuration and flow regimes and they are later used in Step 2.

The fuel-pin heat-transfer calculations are performed outside the fluid dynamics and operated at larger time steps. This is valid so far as the fuel or control pin is intact. When the structure melting or breakup takes place, the fuel pin must be coupled directly with fluid dynamics. Therefore, the heat and mass transfers associated with fuel or control pin breakup are modeled in Step 1 as well. The can wall heat transfer, on the other hand, is calculated in Step 1, because of quick thermal response due to large thermal conductivity of steel.

The internal energy updates due to nuclear heating are also performed in Step 1. The internal energy generation rate for each heat source component is either: given by the input power-versus-time and distribution tables when the neutronics option is not used; or directly supplied from the neutronics module.

Finally, the models for Step 1 transfers require the information from the equations-of-state and thermophysical properties, and their derivatives as well.

4.1. Models of Intra-Cell Transfers

4.1.1. Mass and energy equations

The mass and energy conservation equations solved in Step 1 are derived from the fundamental differential equations presented in **Chapter 3** by neglecting the convection terms. The mass conservation equation is written in terms of macroscopic densities as:

$$\frac{\partial \bar{\rho}_m}{\partial t} = -\Gamma_m \ , \tag{4-1}$$

which means the change in mass with time corresponds to the mass-transfer rate from the component m. The mass of density component m is represented by macroscopic density, since the equation is written for unit volume. Similarly, the energy equation is written in terms of specific internal energy of energy component M as:

$$\frac{\partial \bar{\rho}_M e_M}{\partial t} = Q_N + Q_M(\Gamma_M) + Q_H(h,\ a,\ \Delta T) \ , \tag{4-2}$$

where the terms on the right-hand side denote the energy transfer rates due to nuclear heating, mass transfer and heat transfer, respectively. The terms for pressure-volume work and interfacial drag heating are eliminated here; however, they are treated in conjunction with fluid convection in Steps 2-4.

The modes of heat and mass transfers currently modeled in SIMMER-III/SIMMER-IV are listed in **Section 4.1.2**. The many of the mass transfer processes occur at interfaces between energy components, and importantly these processes are mainly dominated by heat transfer. A heat transfer process is driven by the temperature difference of a pair of energy components and the rate is determined by a heat-transfer area and heat-transfer coefficient (HTC). Thus, the standard model is the heat-transfer limited model. For this reason, determination the heat-transfer areas and coefficients are key elements to evaluate Step 1 transfers and they are based on binary contact conditions among energy components.

In SIMMER-III, eight fluid energy components (liquid fuel, liquid steel, liquid sodium, solid fuel particles, solid steel particles, solid control particles, fuel chunks and vapor mixture) and three structure surfaces (fuel pin/control pin, left can wall and right can wall) are modeled. In three-dimensional SIMMER-IV, the number of fluid energy components stays the same (eight) but two structure surfaces are added (front and back can walls). The combination of contact modes of a fluid with other fluids or structures needs the total of 52 binary contact interfaces to be defined for SIMMER-III (68 interfaces for SIMMER-IV). The binary contact conditions are determined from topology of multi-phase flows, and hence calculations of interfacial areas (IFAs) are based on flow-regime consideration. Both the pool flow where the effect of structure walls is negligible and the channel flow which is restricted by structure walls are treated. The model to determine IFAs also takes accounts of the history of flows by treating their convection and time-dependent source terms. It is noted the IFA convection is calculated with fluid convection in Step 4.

The momentum equation is also solved in Step 1 without convection terms

$$\frac{\partial \bar{\rho}_q \boldsymbol{v}_q}{\partial t} = -\sum_{q'} \Gamma_{qq'} \left[\mathrm{H}\left(\Gamma_{qq'}\right) \boldsymbol{v}_q + \mathrm{H}\left(\Gamma_{q'q}\right) \boldsymbol{v}_{q'} \right] \ , \tag{4-3}$$

where the right side of the equation denotes the momentum change due to the mass transfer from the velocity field q. The velocities are explicitly updated at the end of Step 1 reflecting intra-cell mass transfers.

4.1.2. Modes of mass transfers

The modes of mass transfers modeled in SIMMER-III are summarized in this section. The mass transfer rate on the right side of Eq. (4-1) includes various modes of mass transfers. The mass transfer rate from density component *m* is further subdivided into:

$$\Gamma_m = \Gamma_m^{BR} + \Gamma_m^{NQ} + \Gamma_m^{NE} + \Gamma_m^{REL} + \Gamma_m^{EJ} + \Gamma_m^{BL} \ , \tag{4-4}$$

where

Γ_m^{BR}	mass-transfer rate due to structure breakup and applies only to structure components,
Γ_m^{NQ}	mass-transfer rate due to equilibrium melting/freezing,
Γ_m^{NE}	mass-transfer rate due to non-equilibrium melting/freezing and vaporization/condensation,
Γ_m^{REL}	mass-transfer rate due to fission gas release from liquid and particle fuel or fission gas mass transfer associated with fuel mass transfer,
Γ_m^{EJ}	mass-transfer rate due to ejection of molten cavity materials from the fuel pin, and is applied when the detailed pin model is used (not currently available), and
Γ_m^{BL}	mass-transfer rate due to plenum fission gas blowdown, and is applied when the detailed pin model is used (not currently available).

The model for melting/freezing (M/F) consists of equilibrium and non-equilibrium processes. The former process takes place when the bulk internal energy of an energy component satisfies the condition for phase transition. The latter process is evaluated from the heat balance and the thermal condition at a binary contact interface between two energy components, regardless of bulk energy conditions. For vaporization/condensation (V/C) processes, only the non-equilibrium mass transfer is modeled. Out of possible binary contact interfaces (52 for SIMMER-III and 68 for SIMMER-IV), only those important non-equilibrium mass transfer paths are modeled based on consideration of importance with respect to reactor accident conditions. The resultant numbers of paths modeled are 22 M/F and 33 V/C paths for SIMMER-III (32 and 35 paths, respectively, for SIMMER-IV).

The term in Eq. (4-2) includes all the modes of energy-transfer rates associated with mass transfer. Exception is the mass transfer relating to fission gas; the internal energy of fission gas in pin fuel and liquid-field fuel is not modeled because it is negligibly small, but the fission gas released to the vapor field should have internal energy. The term for energy-transfer rate due to heat transfer is concerned with all the binary contact areas between pairs of energy components. It is noted that the mass transfers relevant to the detailed pin model, ejection of molten pin fuel and plenum fission gas blowdown, have not been yet fully available and hence they are not documented in this report.

4.1.3. Relationships among Step 1 operations

The individual heat and mass transfer processes are separately calculated in series, because solving the mass and energy equations simultaneously by coupling all the heat and mass transfer modes is impractical. The macroscopic density and specific internal energy are updated every time when a heat and mass transfer process is calculated. Then the updated state is used in the next heat and mass transfer calculation. The result of later updates cannot be fed back to the former calculation in the same time step. Therefore, the order of Step 1 updates is very important and is designed carefully. For example, the structure breakup transfer is calculated at the beginning of Step 1, because it changes the structure configuration and volume fraction that affect the subsequent transfer processes. In general, however, the current approach of sequential updates in Step 1 is well justified because individual mass transfer phenomena are only loosely inter-related. In addition, the fluid dynamics time steps are controlled to be sufficiently small such that any dependent heat and mass transfer can be treated in the next time step.

The initial conditions for Step 1 in the current time step are taken from the end of previous time step (Step 4). If the structure breakup condition is satisfied, the mass transfer due to breakup is calculated. The structure configuration is updated to determine the structure-side heat-transfer coefficients, structure surface areas, the structure volume fraction, and the cell hydraulic diameter. The flow regime is determined from the structure configuration, component volume fractions and the fluid velocities. Then the convectible IFAs, resulted from Step 4 in the previous time step, binary contact areas are determined based on the flow regime. The fluid-side heat-transfer coefficients (HTCs) are calculated also based on the flow regime. The component internal energies are updated due to nuclear heating. The heat and mass transfer processes are then calculated for all the heat-transfer paths and for non-equilibrium mass transfers. The can-wall heat transfer is performed and resultant structure energies are calculated and tested for equilibrium phase transition. The inter-cell heat conduction is then performed. Finally at the end of Step 1, the specific internal energy of each component is checked for possible equilibrium melting/freezing updates.

4.1.4. Computational flow of Step 1

As already mentioned, the calculational order of the Step 1 operations is very important and has been carefully determined. The Step 1 routines are listed below in the order of calculations. The Step 1 operations relating to the detailed pin model, such as molten fuel and gas ejection from a failed fuel pin, are not listed below because they are not fully available.

- EOSPHS and THEPHY (EOS and TPP): Calculate the EOS variables and thermophysical properties to be used in Step 1 operations.
- STRBRK (structure breakup): Calculate the structure breakup transfer (for pin fuel/control, cladding, crust fuel and can wall) when each breakup criterion is satisfied.
- UPDV (update velocities): Update velocities after structure breakup.
- STRCON (structure configuration): Determine structure configuration for the fuel/control pin and can walls, and calculate structure-side heat-transfer coefficients and areas, and the cell hydraulic diameter.
- IFA (interfacial areas): Determine flow regimes for fluid-dynamics mesh cells, update the convectible interfacial areas due to source terms, and calculate binary contact areas between energy components. Call IFASRC to calculate IFA source terms.
- MXF (momentum exchange functions): Calculate the momentum exchange functions and virtual mass coefficients to be used in Steps 2-4.
- HTC (heat-transfer coefficients): Calculate fluid-side heat-transfer coefficients for fluid energy components including film-boiling heat transfer.
- NUCLHT (nuclear heating): Calculate total power and update the specific internal energies due to nuclear heating for all the fluid-dynamics and structure components. The energy of pin fuel interior is extrapolated from the previous heat-transfer step to the fluid-dynamics step.
- MASSPN (fission gas release): Calculate pin fuel interior temperature approximately and fission gas release from the liquid-field fuel components.
- MFHMT (non-equilibrium M/F): Calculate non-equilibrium heat and mass transfer due to M/F.
- VCHMT (V/C): Calculate non-equilibrium heat and mass transfer due to V/C.
- ITCTHR (inter-cell heat transfer): Calculate inter-cell heat transfer between the same liquid components, axial heat conduction in the structure components, and inter-cell fluid-to-structure heat transfer.

- MXFCR (momentum exchange functions): Calculate the momentum exchange functions for traverse flows across a rod bundle (available as an option).
- UPDSTR (update structure and liquid): Calculate can wall heat transfer, and call QHCHTP to calculate and save energy sources for the pin model, and call EQUIMF to calculate heat and mass transfer due to equilibrium M/F.
- EOST (update EOS): Call EOS to calculate temperatures and specific volumes reflecting the result of Step 1 heat and mass transfers.
- IFARGN (update flow regimes): Update flow regimes reflecting the result of Step 1 mass transfer.
- UPDVIA (update velocities and interfacial areas): Update fluid velocities and interfacial areas reflecting the result of Step 1 mass transfer.

All the above mass and energy updates are performed in series, each of which deals with a different transfer process. It is noted again that the structure breakup mass transfer is calculated at the beginning of the fluid-dynamics algorithm, before the structure configuration is updated, because the breakup transfer instantaneously and drastically changes the structure configuration and the cell hydraulic diameter. The equilibrium melting/freezing transfer is calculated at the end of an intra-cell calculation step, to make sure whether the component thermal condition after a series of intra-cell heat-transfer satisfies the phase transition criteria. The Step 1 mass transfers change the mass and volume fractions of the fluid and structure components. The adjustment in IFAs and velocities are required and this is performed at the very end of Step 1.

The models and methods used in Step 1 modules are essentially identical for both SIMMER-III and SIMMER-IV, because local intra-cell phenomena treated are independent of geometrical dimensions, except for the front and back can walls added in SIMMER-IV.

4.2. Multi-Phase Flow Topology and Interfacial Areas Mode

The interfacial area modeling successfully attempted in AFDM[20)] was extended to the SIMMER-III/SIMMER-IV multicomponent system, with more complex and comprehensive representation of flow topologies with up to eight velocity field. Since a detailed description of the model is available in a separate report[17)], only a brief summary is presented in this section.

4.2.1. Flow regimes and topology model

To calculate intra-cell heat and mass transfers in Step 1, the binary contact areas must be determined of 52 possible contact interfaces for SIMMER-III (and 68 for SIMMER-IV) among 8 fluid energy components and 3 structure surfaces (5 for SIMMER-IV). Such binary contact areas are calculated based on the convectible interfacial areas and flow regimes which describe the topology of multiphase flows.

Flow regimes are modeled for both: pool flow, in which the effect of the structure is negligible; and channel flow, which is confined by structure. The flow-regime representation for pool flow is rather simple;

only bubbly, dispersed and in-between transition regimes are modeled, as schematically depicted in **Fig. 4-2**. The upper limit of the bubbly regime and the lower limit of the dispersed regime are defined by user-specified void fractions, α_B and α_D, respectively, with the typical and default values being 0.3 and 0.7. It is generally assumed that a cell consists of two local regions: the bubbly and dispersed regions, and the transition regime is defined as a combination of the two local regions, which always have the void fractions α_B and α_D. This means that the transition regime, commonly called a churn-turbulent flow regime, is defined non-mechanistically as an interpolated flow regime. However, this treatment is very advantageous because the flow characteristics can be determined continuously over an entire void fraction range from 0 to 1, without abrupt change upon flow-regime transition.

As the void fraction increases in a bubbly region, the effect of change in bubble shape from spherical (ellipsoidal) to cap-shaped on momentum coupling becomes large. This effect has been later included in the momentum exchange functions model18), based on an experimental study on high density-ratio two-phase flows that are relevant to LMFR severe accident conditions.

The modeling approach taken for the channel flow regimes is essentially the same, but special flow characteristics resulting from the effects of channel walls have also to be considered. The channel flow regimes are distinguished based the vapor volume fraction and the liquid entrainment fraction as schematically depicted in **Fig. 4-3**. The liquid entrainment is related to the inter-phasic velocity difference, taking into account the flooding criterion for a liquid film on a solid structure. Since a liquid film on a fuel-pin surface cannot be distinguished from one on a can wall, there remain some uncertainties. No geometric picture is given for the interpolated flow regime, where the quantities are estimated purely by mathematical interpolation.

This multiple flow-regime treatment significantly improves the code applicability to reactor and experiment analyses over the previous SIMMER-II, in which only a dispersed droplet flow is modeled. It is also intended to provide a consistent framework of the flow regime map, over the entire range of void fraction, with smooth and stable transitions between flow regimes. In the early modeling, however, an abrupt change of interfacial areas occurred when a component forming the continuous phase changed to other components. To ensure the smooth transition of continuous phase in this situation, a real liquid that has the second largest volume fraction and belongs to a velocity field is defined as the second continuous phase. In order not to introduce excessive complexity, the second continuous phase is calculated after all the convectible interfacial areas are updated. The detailed treatment of the second continuous phase is documented elsewhere17).

4.2.2. Interfacial area convection model

The SIMMER-III/SIMMER-IV codes must be applied to highly transient and dynamic processes of heat and mass transfer processes, which are dominated by contact interface areas between two fluids or fluid and structure surface. Contact areas cannot be determined from local instantaneous conditions alone, but must be calculated considering a time-dependent nature of multi-phase flow topology and the transport of fluid surface areas. The interfacial area convection modeling attempted in AFDM has been extended and significantly improved in SIMMER-III to flexibly trace transport and history of interfaces, and thereby better represents physical phenomena. Ishii[21)] proposed a basic convection equation for the interfacial areas per unit volume (interfacial area concentration) in a general form:

$$\frac{\partial A_M}{\partial t} + \nabla \cdot (A_M \boldsymbol{v}) = \sum_k S_{M,k} \ , \tag{4-5}$$

where A_M is the interfacial area of component *M* per unit volume and $S_{M,k}$ denotes the source terms of the interfacial area. This formulation is difficult to be implemented into a Eulerian code such as SIMMER-III because the real velocity of an interface cannot be determined easily. Therefore, we made a compromise that each convectible interfacial area is defined as a surface area of a fluid energy component and flows at the same velocity of the accompanying component. A total of nine convectible interfacial areas associated to moving energy components are presently defined. These are: the surface areas of real liquids (fuel, steel and sodium) in the bubbly region; the surface areas of real liquids in the dispersed region; the surface areas of fuel and steel particles; and the surface area of bubbles in the bubbly region. A special treatment is modeled to avoid abrupt changes in such situations when the area convection occurs into a cell having a different void fraction. This is done by additional local convection (diffusion) terms between the bubbly and dispersed regions:

$$\frac{\partial A_{M,B}}{\partial t} + \nabla \cdot \left(A_{M,B} \boldsymbol{v}\right) = \sum_k S_{M,B,k} - A_{M,B\rightarrow D} \ \text{, and} \tag{4-6}$$

$$\frac{\partial A_{M,D}}{\partial t} + \nabla \cdot \left(A_{M,D} \boldsymbol{v}\right) = \sum_k S_{M,D,k} - A_{M,D\rightarrow B} \ . \tag{4-7}$$

where $A_{M,B}$ and $A_{M,D}$ are the convectible interfacial areas of component *M* in the bubbly and dispersed regions, respectively. The second term on the right-hand side denotes the diffusion between the two regions. The changes of interfacial areas due to hydrodynamic breakup, flashing, turbulence-driven breakup, coalescence, and production of droplets or bubbles are treated as source terms in the interfacial area convection equation.

The interfacial area convection equation is solved in three steps. First, the equation without convection term is solved in Step 1 with updated source terms based on the convectible interfacial areas from the previous time step. Second, at the end of Step 1 interfacial areas are adjusted for any changes from heat and mass transfer updates. Third, the equation without source terms is solved in Step 4 using the end-of-time-step velocity in the same procedure as the mass convection.

4.2.3. Determination of binary contact areas

The rate of heat and mass transfers occurring at an interface of a pair of two energy components is in proportion to the heat transfer coefficient and the binary contact area. The binary contact areas are calculated, for interfaces of fluid-fluid contacts and fluid-structure contacts, using the convectible interfacial areas, structure surface areas, component volume fractions, physical properties, etc. The present model basically calculates the contact areas based on the volume fractions of the fluids and a "summation rule" that the sum of binary contact areas over a component should be equal to the convectible interfacial area (surface area) of the component. For the fluid-fluid contacts between moving discontinuous components, a theory developed for SIMMER-II, based on collisions of fluid particles, is used.

4.3. Momentum Exchange Functions Model

The SIMMER-III/SIMMER-IV fluid dynamics solves the mass, momentum and energy conservation equations in multi-component, multi-velocity-field systems. The momentum exchange functions (MXFs) appearing in the momentum equation model a drag force between a pair of velocity fields and a friction force between a structure and a velocity field. The modeling concept is similar to the two-velocity SIMMER-II$^{1)}$ and three-velocity AFDM$^{22)}$, the treatment in SIMMER-III/SIMMER-IV becomes more complex, because up-to eight velocity fields can be used with allowing flexible assignment of liquid components to velocity fields.

The momentum equation described in **Chapter 3** is repeated below.

$$\begin{aligned}\frac{\partial \bar{\rho}_q \boldsymbol{v}_q}{\partial t} + \sum_{m\in q} \nabla \cdot \left(\bar{\rho}_m \boldsymbol{v}_q \boldsymbol{v}_q\right) + \alpha_q \nabla p - \bar{\rho}_q \boldsymbol{g} + K_{qS}\boldsymbol{v}_q - \sum_{q'} K_{qq'}\left(\boldsymbol{v}_{q'} - \boldsymbol{v}_q\right) - \boldsymbol{VM}_q \\ = -\sum_{q'} \Gamma_{qq'}\left[\mathrm{H}\left(\Gamma_{qq'}\right)\boldsymbol{v}_q + \mathrm{H}\left(\Gamma_{q'q}\right)\boldsymbol{v}_{q'}\right] ,\end{aligned} \tag{3-3}$$

where the $\boldsymbol{VM}_q$ term is the virtual mass term for velocity field q and the treatment of this term is discussed in **Section 4.3.3**. The MXF between velocity fields q and q', which appears as $K_{qq\prime}$ describes the rate of momentum exchange per unit volume after being multiplied by the velocity difference between the two velocity fields. The MXF between velocity field q and structure K_{qS}. multiplied by velocity, gives the frictional loss by the structure. The MXFs and virtual mass terms are evaluated in Step 1 and are used in solving the momentum equations in Steps 2 to 4.

Compared with water-steam or water-air two-phase flows, both theoretical and experimental knowledge is limited in multicomponent multiple-velocity flows. The formulations developed for SIMMER-III are based on engineering correlations of steady-state two-velocity flows. Since a detailed model description is available elsewhere$^{18)}$, only an outline of the MXF model is presented in this section.

In order to formulate the MXFs between velocity fields (or momentum components), it is necessary to calculate the geometric variables such as interfacial areas, volume fractions of each momentum component and the mixture viscosity. The volume fractions of each momentum component are calculated simply by summing the volume fraction of the energy components which belongs to the momentum field.

4.3.1. Fluid-fluid momentum exchange function model

MXSs between two fluid fields consist of laminar and turbulent terms:

$$K_{qq\prime} = A_{qq\prime} + B_{qq\prime}\left|\boldsymbol{v}_{q'} - \boldsymbol{v}_q\right| , \tag{4-8}$$

where the laminar term $A_{qq\prime}$ is described by Stoke's law, and the turbulent term $B_{qq\prime}\left|\boldsymbol{v}_{q'} - \boldsymbol{v}_q\right|$ is proportional to the inter-phase velocity difference with the drag coefficient based on Ishii's drag similarity hypothesis[23)], which assumes that the drag in a multi-particle system follows the same Reynolds number function as isolated spherical bubbles or droplets using an effective viscosity.

There are three situations in fluid-fluid momentum exchange modes. Between continuous liquid and discontinuous phases (droplets and particles), the MXF coefficients are defined as:

$$A_{C,D}=\frac{3}{2}a_{C,D}\frac{\mu_a}{r_D} \text{ and } B_{qC,qD}=\frac{a_{qC,qD}}{2}\frac{C_D}{4}\rho_{qC}, \tag{4-9}$$

where $a_{C,D}$ and $a_{qC,qD}$ are the interfacial (surface) area between continuous and discontinuous phases and interfacial area between the velocity fields of continuous and discontinuous phases, respectively. The drag coefficient C_d is based on Ishii's drag similarity hypothesis. The MXF between bubbles and continuous liquid, and the MXF between droplets and continuous vapor are defined similarly.

Between discontinuous and discontinuous phases, the MXF coefficients are defined as:

$$A_{D1,D2}=0 \text{ and } B_{D1,D2}=C_{dd}a_{D1,D2}\frac{\bar{\rho}_{D1}+\bar{\rho}_{D2}}{\alpha_{D1}+\alpha_{D2}}, \tag{4-10}$$

where $a_{D1,D2}$ is the interfacial area between discontinuous phases and the drug coefficient $C_{dd}=0.01$ is recommended for SIMMER-III.

Between continuous and continuous phases, the MXF coefficients are defined as:

$$A_{CP,G}=0 \text{ and } B_{CP,G}=C_{cc}a_{CP,G}\frac{\rho_G}{4}, \tag{4-11}$$

where $a_{CP,G}$ is the interfacial area between continuous phases (continuous liquid and vapor) and $C_{cc}=0.005$ is recommended for SIMMER-III.

4.3.2. Fluid-structure momentum exchange function model

The MXF between fluid and structure similarly consists of laminar and turbulent terms:

$$K_{qS}=A_{qS}+B_{qS}|\boldsymbol{v}_q|, \tag{4-12}$$

which is used to evaluated the pressure drop along the flow channel and frictional losses.

For channel flows, the MXFs between continuous liquid components and structure are modeled based on Blasius formula which gives the friction factor for a turbulent flow in a smooth pipe when the Reynolds number of flow is larger than $\mathrm{Re}_0=3000$,

$$f=\frac{0.0791}{\mathrm{Re}^{1/4}}. \tag{4-13}$$

For a laminar flow, in which Reynolds number is less than $Re_0=3000$, the Hagen-Poiseuille law is used as a fiction factor such as,

$$f=\frac{16}{\mathrm{Re}}. \tag{4-14}$$

Using these correlations, the MXF in SIMMER-III could be formulated as follows:

$$A_{Lm,\,S} = \frac{2a_{Lm,\,S}\mu_L}{\alpha_{Lm}} \text{ and } B_{Lm,\,S} = \frac{1}{2}a_{Lm,S}\rho_{Lm}C_{T1}\left(\frac{4\alpha_{Lm}\rho_{Lm}v_{q(Lm)}}{a_{Lm,S}\mu_L}\right)^{C_{T2}} \tag{4-15}$$

where the default values of the parameters are: $C_{T1} = 0.0791$ and $C_{T2} = -0.25$. The viscosity in this equation is obtained simply by averaging the viscosities of existing liquids with the multiplication factor of particle viscosity model. When the flow is regarded as a pool flow, where the effect of structure surface to the flow is small, the MXFs between the continuous phase and structure are simplified as follows:

$$A_{Lm,\,S} = \frac{2a_{Lm,S}\mu_L}{\alpha_{Lm}} \text{ and } B_{Lm,\,S} = \frac{C_{cS}}{2}a_{Lm,S}\rho_{Lm} \tag{4-16}$$

where $C_{cS} = 0.005$ is the recommended value.

Between discontinuous phase and structure, it is assumed that the time scale of the contact between dispersed fluids and structure is too small for laminar boundary layer to form at the contact interface. Thus, only the turbulence term with constant friction factor is used for the MXF coefficients as:

$$A_{dS} = 0 \text{ and } B_{Lm,\,S} = \frac{C_{dS}}{2}a_{Lm,S}\rho_{Lm}S_f\,, \tag{4-17}$$

where $C_{dS} = 0.005$ is the recommended value. The multiplication factor, S_f, is applied here to account for effective increase in the mixture viscosity in the presence of solid particles, as briefly discussed in **Section 4.3.4**.

4.3.3. Averaging and interpolation of momentum exchange functions

Eight fluid energy components are modeled in SIMMER-III, and each of them is assigned to one of up to 8 velocity fields. In a fluid-dynamic mesh cell, there are three continuous regions: bubbly, continuous liquid and second continuous liquid regions. The MXFs defined in the previous sections are calculated for the 8 fluid energy components in the 3 continuous regions. For each velocity field, they are averaged to determine the MXFs to be used in the momentum equations. It is noted a logarithmic interpolation procedure is used between the bubbly (liquid continuous) and dispersed (vapor continuous) regions, because MXFs in the two regions may differ more than an order of magnitude.

4.3.4. Effect of particles on flow resistance

Solid mobile particles in a flow require a special consideration, since the presence of particles in fluid component, depending on their volume fraction, should significantly increase the hydrodynamic resistance of the flow by increasing the apparent viscosity of the fluid component as a result of collision, rotation and friction of the particles. Hence the concept of effective particle viscosity is introduced to particle components as a function of particle volume (packing) fraction and it is used in defining the total viscosity of each liquid velocity field. If the volume fraction of particles in the flow area approaches the maximum packing fraction, the total viscosity is increased significantly and thereby the model is crucial when the fuel blockage formation due to particle jamming is simulated.

The other model related to the behavior of particles was introduced to simulate the phenomenon that the volume fraction of solid particles cannot exceed a maximum packing fraction in the situations where solid particles are deposited on a horizontal surface, for example. This model prohibits the inflow of particles into a mesh cell when the volume fraction of solid particles in that cell reaches the maximum packing fraction. This is modeled by increasing the MXF at the cell interface.

4.3.5. Additional model improvement

Two additional but important model improvements have been implemented after the early versions of SIMMER-III were developed. First, it is known that the pressure drop is enhanced due to the turbulent enhancement due to liquid-vapor interaction. Ueda's model[24)] is introduced to approximately estimate the pressure loss more appropriately by applying a multiplication factor. The model is also available for the bubbly flow.

The effect of bubble shape on the momentum exchange between bubbles and continuous liquid is taken into account[25)]. If the cap-shape bubbles are identified, the drag coefficient using the drift velocity proposed by Kataoka and Ishii is applied to determine the MXF between continuous and discontinuous phases. The model is discussed in detail in the MXF report[18)].

4.3.6. Evaluation of virtual mass term

An important purpose of including the virtual mass term is to improve numerical stability. The physical background and purpose of implementing the model are discussed in Appendix A of the AFDM manual Vol. V[8)]. The same model is implemented in SIMMER-III/SIMMER-IV as AFDM. The virtual mass coefficients are evaluated in Step 1 and are used in Steps 2 and 4.

The virtual mass term in each momentum field is given by

$$\boldsymbol{VM}_{q\notin G} = -\alpha_{q,eff}\,, \tag{4-18}$$

$$\boldsymbol{VM}_G = -\,\alpha_G \bar{\rho}_{eff} C_G \frac{\alpha_L}{\alpha_L + \alpha_P}\left[\frac{\partial \boldsymbol{v}_G}{\partial t} - \sum_{q\notin G} \alpha_{q,eff}\frac{\partial \boldsymbol{v}_q}{\partial t}\right], \text{and} \tag{4-19}$$

where the virtual mass coefficient C_G is defined as,

$$C_G = \begin{cases} \frac{1}{2}\left(1 + \frac{2\alpha_{G,eff}}{1-\alpha_{G,eff}}\right) & \text{for } \alpha_{G,eff} \le \frac{1}{2} \\ 2\left(\frac{\alpha_D - \alpha_{G,eff}}{\alpha_D - 1/2}\right)^2 & \text{for } \frac{1}{2} < \alpha_{G,eff} \le \alpha_D \\ 0 & \text{for } \alpha_D < \alpha_{G,eff} \end{cases}. \tag{4-20}$$

4.4. Heat-Transfer Coefficients Model

Since a complete model description together with collected backing data from the literature is available as a separate JAEA report[16)], only the example of heat transfer coefficient (HTC) correlations and the specific features of the modeling concepts are outlined in this section. A list of major HTCs defined in SIMMER-III/SIMMER-IV for various modes of heat transfers is presented in **Table 4-1**. The structure-side heat-transfer coefficients are defined and included in the structure model (see **Chapter 5**).

4.4.1. Heat-transfer correlations

Heat-transfer coefficients (HTCs) are required to perform the heat and mass transfer calculations. The heat and mass transfer paths between the fluid energy components are illustrated in **Figs. 4-4** and **4-5**, for SIMMER-III and SIMMER-IV, respectively. HTCs are defined for 52 (or 68) binary contact interfaces between the energy components and contribute to 33 (or 35) vaporization/condensation (V/C) paths and 22 (or 31) melting/freezing (M/F) paths for SIMMER-III (or SIMMER-IV). The HTCs control heat transfer between the bulk and interface temperatures for each liquid energy component and vapor mixture. The HTCs are based mostly on quasi-steady state Nusselt number correlations, obtained from various experiments over the past decades in nuclear and non-nuclear engineering fields. The correlations take account of a low Prandtl number range, which is particularly important when calculating heat transfer in liquid metals. It is noted that the heat transfer correlations are mostly based on steady-state experiments and hence they must be carefully applied to transient problems.

Some examples of HTC correlations are described below, and the list of major HTCs are given in **Table 4-1**. The complete description of the HTC correlations in SIMMER-III and SIMMER-IV is available in a separate HTC report$^{16)}$. Solid particles are treated as rigid spheres, and heat transfer is controlled by conduction. The internal HTC to reproduce steady-state heat conduction is obtained by constant Nu

$$\mathrm{Nu}_p = \frac{h_p D_p}{K_p} = a\,, \tag{4-21}$$

where h_p, D_p and K_p denote the HTC, the diameter and thermal conductivity of particles, respectively. The recommended value of $a = 10$ corresponds to heat conduction from the mass centroid of the particle to its surface. Liquid droplets and gas bubbles are also treated as rigid spheres but the augmentation effects due to internal circulation and oscillation of fluid particles are taken into account. For the augmentation due to internal fluid circulation, a factor based on Peclet number correlation is used, and in the latter case heat transfer is augmented by a user input factor. In the dispersed flow regime, the heat transfer between moving droplets is calculated as a function of the contact times in the same way as determination of binary contact area.

Forced convection heat transfer from continuous phase liquids or gas to solid particles is calculated using correlations obtained from forced flow over spheres.

$$\mathrm{Nu}_{cp,p} = b + e_1 \mathrm{Re}_j^{e_2} \mathrm{Pr}_i^{e_3}\left(1 + e_4 \mathrm{Re}_j^{e_5}\right), \tag{4-22}$$

which is composed of a conduction term, b, to describe the minimum heat transfer rate from a particle to a stagnant liquid, and a forced convection term. Subscripts i and j denote continuous phase (cp) and particle (p), respectively. Heat transfer to the particles by natural convection driven by thermal expansion can also be calculated using the Grashof number correlation:

$$\mathrm{Nu}_{cp,p} = b + f_1\left(\mathrm{Gr}_j \mathrm{Pr}_i^{f_3}\right)^{f_2}. \tag{4-23}$$

Heat transfer between continuous phase vapor mixture and structure in the dispersed flow regime is calculated using correlations obtained for forced convection single-phase flow in pipes (the Dittus-Boelter correlation).

$$\mathrm{Nu}_{cp,S} = c + g_1 \mathrm{Re}_i^{g_2} \mathrm{Pr}_i^{g_3} \,. \tag{4-24}$$

Again, the correlation includes the conduction term c to represent the minimum heat transfer in laminar flows. For heat transfer between continuous phase liquid and in the bubbly flow regime, the effective thermal conductivity of a multi-component mixture is considered, assuming that the liquid-field components are uniformly mixed in the continuous region.

Heat transfer correlations include the lengthscale of heat transfer, which is reasonably represented by the standard hydraulic diameter for a channel flow that is surrounded by structure walls. For pool flow configurations, on the other hand, there is an uncertainty in determining a lengthscale in a mesh cell in contact with structure, because a conventional hydraulic diameter cannot be used. In the SIMMER-III structure model16), the hydraulic diameter is set to the mesh cell width in such cells in contact with the pool wall. This treatment is consistent with the use of an optional model of inter-cell heat transfer (see **Section 4.9.1**), when a liquid pool to structure heat transfer is of interest.

If the conditions for film boiling are satisfied for a hot dispersed-phase liquid in contact with a more volatile continuous-phase liquid, film boiling HTCs are calculated. The film boiling can significantly reduce heat fluxes due to the insulating effect of the vapor blanket.

4.4.2. Interpolation between flow regimes

As described in **Section 4.2** and illustrated in **Fig. 4-5** the multiple flow regimes are defied in SIMMER-III/SIMMER-IV. The HTCs are defined for the bubbly, annular and dispersed flow regimes. The intermediate flow regimes (e.g. transition and interpolated flow) are topologically ill-defined and suitable correlations are not available. Consider the transition flow in which the HTC in the liquid phase is defined as h_B and h_D for the bubbly and dispersed flow regimes, respectively. The values of h_B and h_D may differ by several orders of magnitude and a linear interpolation does not give a smooth transition. Therefore, a logarithmic interpolation is implemented in the same way as the logarithmic averaging of the drag coefficients in the well-defined flow regimes. The HTC for the transition flow regime, h_{trans}, is calculated by:

$$\log h_{trans} = \beta \log h_B + (1-\beta) \log h_D \,, \text{where } \beta{=}\left(\frac{\alpha_D - \alpha}{\alpha_D - \alpha_B}\right) \text{ for } 0 < \beta < 1. \tag{4-25}$$

Equation (4-25) gives a sufficiently smooth transition of HTCs between flow regimes.

For channel flow regimes, illustrated in in **Fig. 4-5**, interpolations are made from the well-defined flow regime. The HTCs in slug flow are treated as a logarithmic interpolation between the HTCs in the bubbly and annular flow regimes. The HTCs in annular-dispersed flow are treated by interpolating between the HTCs in the dispersed and annular flow regimes. The interpolated flow regime does not have a well-defined topology at all. The HTCs are obtained by interpolation between the slug and transition flow regimes, In addition, the HTCs of two liquid components are interpolated between the continuous and discontinuous phase HTCs when neither liquid components form a dominant continuous phase. This avoids sudden changes in heat transfer caused by small alterations in volume fractions of the components.

4.5. Heat and Mass Transfer Model

The SIMMER-III/SIMMER-IV heat- and mass-transfer model[14)] is based on the technologies developed and experience gained in the former SIMMER-II[1)] and AFDM[26)]. After the binary contact areas and heat-transfer coefficients between a pair of energy components are obtained, the conservation equations without convection terms are solved for intra-cell heat and mass transfer in two steps. The first step calculates the phase transition processes occurring at interfaces, described by a non-equilibrium heat-transfer-limited model. This is a non-equilibrium process because the bulk temperature does not generally satisfy the phase-transition condition when the mass transfer occurs at the interface. The second step of mass and energy transfer is through an equilibrium process occurring when the bulk temperature satisfies the phase-transition condition. At 52 possible binary contact interfaces defined in SIMMER-III (68 in SIMMER-IV), all the important non-equilibrium mass-transfer processes are modeled, including 22 M/F paths and 32 V/C paths (32 and 39 paths in SIMMER-IV) (see **Table 4-2**). All the non-equilibrium mass transfer paths modeled in SIMMER-III is listed **Table 4-3**. Note that in the V/C transfers condensation processes of fuel or steel vapor on other colder liquids are included to avoid the SIMMER-II/AFDM problem of unphysical presence of subcooled vapor. Combinations of all the possible binary contact interfaces and the heat and mass transfer paths treated in SIMMER-III and SIMMER-IV are shown in **Figs. 4-2** and **4-3**, respectively.

In addition, 16 equilibrium M/F transfers are performed to eliminate super-cooled liquids or meta-stable solids as a result of heat transfer and nuclear heating.

4.5.1. Basic concept of non-equilibrium mass transfer model

The mass-diffusion limited model is employed to represent effects of noncondensable gases and multicomponent mixture on V/C processes. The M/F transfers include the crust formation on a can wall that furnishes thermal resistance, and steel ablation and particle formation that contribute to fluid quenching and bulk freezing. The mass-transfer processes modeled are selected in consideration of their importance in and effects on the behavior of materials in the transition-phase.

The basic concept of the non-equilibrium mass transfer model is described for a binary contact interface of the energy components A and B (see **Fig. 4-6**). This is a heat-transfer-limited process where the phase transition rate is determined from an energy balance at the interface. The heat transfer rates from the interface to components A and B are:

$$q_{A,B} = a_{A,B} h_{A,B} \left(T_{A,B}^{I} - T_A \right) \text{, and} \tag{4-26a}$$

$$q_{B,A} = a_{A,B} h_{B,A} \left(T_{A,B}^{I} - T_B \right) , \tag{4-26b}$$

where $T_{A,B}^{I}$ is the instantaneous contact interface temperature due to heat conduction without phase transition. The net energy transfer rate from the interface is defined as:

$$q^I_{A,B} = q_{A,B} + q_{B,A} \,. \tag{4-27}$$

If the net heat flow $q^I_{A,B}$ is zero, sensible heat is exchanged without phase transition. This is a simple heat-transfer process without phase transition. If $q^I_{A,B}$ is positive, namely the energy is lost at the interface, either a liquid component freezes or a vapor component condenses. Then the mass transfer rate for this case is determined, using the difference of specific enthalpies, from:

$$\Gamma^I_{A,B} = R_{A,B} \frac{q^I_{A,B}}{i_A - i^I_B} \text{ , if the component formed by phase transition is } B \text{, or} \tag{4-28a}$$

$$\Gamma^I_{A,C} = R_{A,B} \frac{q^I_{A,B}}{i_A - i^I_C} \text{ , if the component } C \text{ formed by phase transition is not } B \,. \tag{4-28b}$$

If $q^I_{A,B}$ is negative, on the other hand, namely the energy is gained at the interface, either a solid component melts or a liquid component vaporizes. Then the mass transfer rate for this case is determined from:

$$\Gamma^I_{B,A} = -R_{A,B} \frac{q^I_{A,B}}{i^I_A - i_B} \text{ , if the component formed by phase transition is A, or} \tag{4-29a}$$

$$\Gamma^I_{B,D} = -R_{A,B} \frac{q^I_{A,B}}{i^I_D - i_B} \text{ , if the component } D \text{ formed by phase transition is not } A. \tag{4-29b}$$

In the above four equations, the heat of phase transition (the effective latent heat) is defined as the difference between the enthalpy at the interface and the bulk enthalpy of a component undergoing phase transition. In the above equations, a correction factor $R_{A,B}$ is introduced to take account of the effect of noncondensable gases and multicomponent mixtures on vaporization and condensation at the vapor/liquid and vapor/solid interfaces.

When a phase transition is occurring at the A-B interface, the interface temperature $T^I_{A,B}$ is set to a phase-transition temperature such as melting point and saturation temperature. In cases with no mass transfer, the equivalent interface temperature is defined as:

$$T^I_{A,B} = \frac{h_{A,B} T_A + h_{\mathrm{B,A}} T_B}{h_{A,B} + h_{\mathrm{B,A}}} \,. \tag{4-30}$$

The detailed treatment of individual binary contact interfaces depends on combination of pairs of energy components and is detailed in the original JNC report[14)].

4.5.2. Effects of noncondensable gases and multicomponent mixtures

The physical model to represent the effect of noncondensable gases and multicomponent mixtures on V/C processes is based on a study performed originally for SIMMER-II[1)], which models the quasi-steady, stagnant Couette flow boundary layer to relate the mass and energy fluxes to the overall forces driving heat and mass transfer. This classical Couette-flow model has been shown to provide a good engineering model for single-component vapor condensation in the presence of noncondensable gases, thus confirming the adequacy of its theory for incorporation in several two-phase flow codes. To make the original model suitable for implementing in a multi-component system, an extensive modification was necessary in SIMMER-III/SIMMER-IV.

The model is based on the assumption that the mass-transfer coefficient can be treated in a manner analogous to the heat-transfer coefficients. In the mass-diffusion limited model, the equations of mass and energy transfers at the interface between a vapor mixture and a liquid or structure surface component are:

$$\Gamma_k = -a_i k_k^*\left(\omega_{k,i} - \omega_{k,\infty}\right) + \omega_{k,i}\sum_{j=1}^{N}\Gamma_j \text{, and} \tag{4-31a}$$

$$\sum_{j=1}^{N}\Gamma_j\, i_{lg,j} = a_i\left[h_g^*\left(T_i - T_g\right) + h_o\left(T_i - T_o\right)\right], \tag{4-31b}$$

where k_k^* and h_g^* are the effective mass- and heat-transfer coefficients, respectively, in the presence of mass transfer, ω is the mass fractions of vapor species, i_{lg} is the latent heat of vaporization simply replaced with the effective latent heat as already explained, T_g and T_o are the vapor temperature and the bulk liquid or solid temperature, respectively. The vapor mass fraction is determined from the mole fraction of a non-condensable gas specie at the interface, and is related to the ratio of its saturation pressure to the total pressure.

The correction factor R is introduced to the heat-transfer limited model to represent the mass-diffusion limited behaviors for each mass-transfer rate at the vapor/liquid and vapor/solid interfaces. The correction factor R_k for the component k undergoing phase transition is defined as a factor to correct mass-transfer rate of pure vapor:

$$R_k = \frac{\Gamma_k(T_i)}{\Gamma_k(T_{sat,k})}, \tag{4-32}$$

where

$$\Gamma_k(T_i) = \frac{a_i\left[h_g^*\left(T_i - T_g\right) + h_o\left(T_i - T_o\right)\right]}{i_{lg,k}} \text{, and} \tag{4-33a}$$

$$\Gamma_k(T_{sat,k}) = \frac{a_i\left[h_g\left(T_{sat,k} - T_g\right) + h_o\left(T_{sat,k} - T_o\right)\right]}{i_{lg,k}}. \tag{4-33b}$$

The mass-transfer rate $\Gamma_k(T_i)$ is defined as a function of the interface temperature, while $\Gamma_k(T_{sat,k})$ is obtained assuming that the interface temperature is equal to the bulk saturation temperature $T_{sat,k}$ and the vapor-side heat-transfer coefficient is independent of mass transfer. To avoid convergence problem in the V/C iteration, when an extremely small amount of vapor component is involved, the initial value of the correction factor is also related to the partial pressure of the component.

4.5.3. Non-equilibrium melting/freezing transfers

The non-equilibrium M/F operation performs particle-liquid-structure heat transfer with non-equilibrium M/F, which does not involve the V/C. The mass- and energy-conservation equations are solved for three structure surfaces (five in SIMMER-IV), three real liquids, and four solid particles/chunks. The energy equations include the energy transfer associated with mass transfer and the heat transfer between the two components being in contact. When the phase transition condition is not satisfied at the interface, sensible heat is transferred.

The equations are solved explicitly using beginning-of-time-step values except for liquid sodium. The implicit treatment of sodium energy could mitigate its excessive change due to high thermal conductivity. The solution procedure is to update first the macroscopic densities of structure surfaces, solid particles, and real liquids. Then their energies are evaluated using the updated densities.

4.5.4. Non-equilibrium vaporization/condensation transfers

The non-equilibrium V/C operation performs liquid-vapor-solid heat transfer with nonequilibrium V/C, which does not involve the M/F. The mass- and energy-conservation equations are solved for vapor mixture, three real liquids, and seven solid components. The energy equations also include the heat-transfer terms. In the solution procedure, using a multivariate Newton-Raphson method, five sensitive variables (three condensable vapor densities, sodium energy and vapor temperature) are updated implicitly, whereas the remaining less sensitive variables are updated explicitly following the convergence of the iteration.

In a single-phase cell, vapor is assumed to always exist in a non-zero small volume, $\alpha_0(1-\alpha_S)$, such that its density and energy are calculated consistently with two-phase cells to avoid numerical difficulties upon single to two phase transition. The single-phase V/C calculations are performed using the same procedure as two-phase cells except for the energy transfer between liquids. At a liquid/liquid interface, such as fuel/sodium contact in a two-phase cell, vaporization can occur, and in this case the interface temperature is defined as the saturation temperature of a vaporizing material. In a single-phase cell, however, the interface temperature of the liquid/liquid contact is defined such that no vaporization is caused by the energy transfer between the liquids. Instead, phase transition occurs only when the liquid temperature increases high sufficiently to cause vaporization at a liquid/vapor interface.

The multi-component V/C involves highly transient and non-linear processes which sometimes make the V/C iteration difficult to converge. Several special case treatments are implemented to minimize the numerical difficulties in the V/C iteration, or to eliminate unphysical states. They include: treatment of supersaturated vapor, adjustment of initial vapor and liquid states to stabilize the iteration, applying limiters to heat-transfer coefficients and areas to achieve numerical stabilities, treatment of missing components, and avoidance of overshooting in the explicit solutions.

4.5.5. Equilibrium melting/freezing transfers

The equilibrium M/F operation calculates equilibrium processes resulting from the cell state after the non-equilibrium and other modes of heat and mass transfers that are calculated in series. The equilibrium transfers for fuel-pin structure and can wall interiors are treated in the structure model as described in **Chapter 5**. The mass- and energy-conservation equations are solved for can-wall surfaces, fuel crusts, fuel and steel liquids, and fuel and steel particles. The finite-differenced equations are solved explicitly.

4.5.6. Recent model changes

After issuance of the report on the SIMMER-III/SIMMER-IV heat- and mass-transfer model14), several important model improvements have been implemented in the code as described below.

(1) Improved freezing model

With the former SIMMER-III/SIMMER-IV framework, both the modes of fuel freezing phenomena, conduction-limited freezing and bulk freezing, can be simulated individually or simultaneously. However, it revealed that the fuel penetration into a cold pipe was underestimated due to lack of thermal resistance caused by imperfect contact of molten fuel to the structure surface. Model improvement then implemented is based on the fundamental physics of solidification processes, and models the heat transfer mechanism with discrete contacts of melt on structure and formation of supercooling of melt upon freezing inception. A detailed model description is available in in a separate section (**Section 4.7**).

(2) Improved crust formation model

Frozen fuel crust formation is modeled as a part of non-equilibrium heat and mass transfer processes, in which the rate of crust formation is determined from the energy balance at the interface between liquid fuel and structure surface. The crust is assumed to uniformly cover an entire surface of the structure, even if the amount of crust being formed is very small with its thickness extremely thin. This assumption in the former SIMMER-III/SIMMER-IV might be unphysical because thin oxide crust is unstable in nature and the assumed perfect crust formation overestimates an insulating effect of a crust layer. Model improvement has been made to simulate the effect of imperfect crust formation. The improved crust formation model is documented separately in **Section 4.8**.

(3) Can wall and crust fuel breakup model

The can wall and crust breakup model has been documented in the structure model report15), and the original model is, more or less, based on thermal criteria such as a melt fraction and temperature of the can wall. Other mechanisms of can wall breakup or failure have been later added. All the modes of breakup currently modeled are documented in **Chapter 5**.

4.6. Structure Configuration and Related Heat and Mass Transfer Models

The fuel-pin and structure model has been already documented in detail15), and the model summary and recent improvements will be described separately in **Chapter 5**. Therefore, a short outline of the structure-related model is listed below, since the most of the operations are performed as parts of Step 1 at fluid-dynamics time steps, except for the fuel-pin heat-transfer calculation.

Any changes in structure volume fraction and configuration, and structure-related mass transfers will instantaneously influence the state of fluid-dynamics mesh cell. For this reason, many of the structure related operations must be tightly coupled with fluid-dynamics Step 1, consisting of the following operations in the order of calculations:

(1) Structure breakup: Calculate mass and energy transfers due to structure breakup (for pin fuel/control, cladding, crust fuel and can wall) when one of the breakup criteria is satisfied. Fluid macroscopic densities, internal energies and velocities are updated by reflecting the result of breakup.

(2) Structure configuration: Determine structure configuration for the fuel/control pin and can walls, and calculate structure-side heat-transfer coefficients and areas, and the mesh-cell hydraulic diameter.

(3) Pin fuel interior temperature: Calculate pin fuel interior temperature approximately for heat transfer calculations of the surface node.

(4) Fission gas release: Calculate fission gas release from the liquid-field fuel (liquid fuel, solid fuel particles and fuel chunk).

(5) Non-equilibrium heat and mass transfer: Calculate non-equilibrium melting/freezing and vaporization/condensation processes involving fuel-pin and can-wall components.

(6) Can wall heat transfer: Calculate can wall heat transfer for all the configurations, thin or thick, with or without crust, whether coupled or uncoupled with an adjacent cell.

(7) Update fuel pin heat source: Calculate and save energy sources for the pin model over fluid-dynamics time steps.

(8) Equilibrium melting/freezing: Calculate equilibrium melting of can wall surfaces and fuel particle, steel particles, and fuel chunk.

Model improvement that have been made after the previous report15) are described in **Chapter 5**.

4.7. Improved Freezing Model

4.7.1. Background

With the SIMMER-III/SIMMER-IV framework, both the modes of fuel freezing phenomena, namely conduction-limited freezing and bulk freezing, can be simulated individually or simultaneously. From a series of out-of-pile experiments on molten UO_2 freezing in a steel pipe, conducted at CEA-Grenoble in the 1980s, where a combined freezing mode (crust formation on the wall and bulk freezing at the leading edge) was observed, it was argued that conventional freezing models tended to underestimate the fuel penetration lengths implying the importance of thermal resistance at the molten fuel contact interface27).

To resolve the above problem and because of the importance of fuel freezing in the LMFR safety, a model improvement has been conducted and documented28), 29). This improvement is based on understanding of fundamental physics of solidification (crystallization) processes, and models the heat transfer mechanism with discrete contacts of melt on structure and formation of a chill (supercooling) zone upon freezing inception. The degree of supercooling is material dependent; therefore, a semi-empirical correlation is developed for supercooling temperature.

The improved model is implemented in the non-equilibrium melting/freezing operations in fluid-dynamics Step 1. Although this model improvement was intended to better simulate fuel freezing, it is applicable to non-equilibrium steel freezing on a cold structure surface as well. In the lest of this section, the model description part of the previous report is recompiled.

4.7.2. Fundamental physics of solidification

In the solidification process in a metal mold, three varieties of grain types are observed: solid nuclei appear in the vicinity of the mold wall, grow up to crystals, and form the so-called equiaxed chill zone, where the liquid is supercooled below its liquidus temperature; crystals grow parallel and opposite to heat flow direction, leading to formation of a columnar zone; and an equiaxed zone is formed in the central part to complete the solidification process. These fundamental mechanisms of melt solidification can be correlated to individual freezing phenomena. Namely, from the observation of UO_2 and simulant metal freezing experiments and their analyses, it was deduced that the columnar crystal growth corresponds to the formation of crust layer at the structure wall, and the formation of the equiaxed zone results in blockage formation caused by bulk freezing.

Another important aspect is the fact that the melt makes contacts with the steel wall at discrete points, due possibly to wall surface roughness and poor wettability. This imperfect contact, observed by a micro-structure examination as well, significantly reduces the heat transfer from the melt to structure.

4.7.3. Improved freezing model

Based on the above-described micro-physics of crystallization, two key assumptions, supercooling of melt in the vicinity of the wall and melt-wall contact resistance due to imperfect contact, were introduced. The first assumption is that the interface temperature between the melt and the wall is defined by the temperature of the supercooled layer, T_{scl}^{I}, until the crust forms, which can be deduced from the fact that an equiaxed chill zone has existed at the vicinity of the wall. The second assumption is to consider the thermal resistance which can be deduced from the fact that the melt has contacted the steel wall at discrete points. Since the melt freezing initiates at discrete contact points, the improved model is commonly called as “fuel-caps freezing model” from the shape of solidification nuclei being formed.

The degree of supercooling temperature is represented simply by using an input constant value initially, but later replaced by a semi-empirical correlation. To represent the second assumption, the heat transfer coefficient through discrete contact points is modeled, based on the concept of the interface resistance model developed by Berthoud30). The contact points are idealized as circular discs of radius, a, arranged on a regular grid. The points are characterized by two parameters: a separation distance between points, b, and the ratio of point radius to separation distance, $\xi = a/b$, which are given by the empirical observations. A suitable value of at the UO_2-steel contact is $\xi = 0.1$.

The steady-state thermal resistance for s single contact point is obtained analytically as:

$$R_{\mathrm{ss}} = \frac{1}{4a}\frac{\kappa_c + \kappa_s}{\kappa_c \kappa_s}. \tag{4-34}$$

This equation can be converted to an interface-resistance heat-transfer coefficient for multiple contact points with its areal density N_c.

$$h_{IR} = \frac{N_c}{R_{ss}} = \frac{4\xi\sqrt{N_c}}{\sqrt{\pi}} \frac{\kappa_c \kappa_s}{\kappa_c + \kappa_s}, \tag{4-35}$$

which is then slightly modified to correct for the effect of heat transfer through neighboring contact points[29)]. The resultant interface-resistance heat-transfer coefficient between a crust and a steel wall is given by:

$$h_{IR,\mathrm{c-s}} = \frac{4\xi\sqrt{N_c}}{g(\xi)\sqrt{\pi}} \frac{\kappa_c \kappa_s}{\kappa_c + \kappa_s}, \tag{4-36}$$

where the parameter $g(\xi)$ as a function of ξ and N_c are expressed by:

$$g(\xi) = 1 - G_{p1}\xi + G_{p2}\xi^3 \text{, and}$$

$$N_c = C_{p1} + C_{p2}{V_L}^2 .$$

where V_L is the velocity of liquid. The values of $G_{p1} = 1.40925$, $G_{p2} = 0.40925$, $C_{p1} = 40 \times 10^6$ and $C_{p2} = 2.5 \times 10^6$ are used in SIMMER-III/SIMMER-IV based on experimental analysis. The heat transfer coefficient of the wall side, representing contact resistance, is then given by:

$$h_{IR,s} = \frac{4\xi\kappa_s\sqrt{N_c}}{g(\xi)\sqrt{\pi}}. \tag{4-37}$$

For the non-equilibrium processes to take place, in which the mass transfer occurs at the interface whereas the bulk temperatures of the melt or the wall do not generally satisfy the phase-transition condition, the following criteria are introduced. The non-equilibrium melting of the wall occurs when the following condition is satisfied:

$$h_L(T_L - T_{scl}^I) > h_{IR,s}(T_{Sol,s} - T_s), \tag{4-38}$$

where T_{scl}^I is the temperature of the supercooled layer. This criterion is simply that the energy transferred from the flowing melt to the supercooled layer exceeds the energy which can be extracted by the steel wall without melting of the wall surface. On the other hand, non-equilibrium freezing of the melt occurs when the energy extracted through the supercooled layer exceeds the energy transferred from flowing melt to supercooled layer. This is expressed by the equation

$$h_{scl-s,sum}(T_{scl}^I - T_s) > h_L(T_L - T_{scl}^I), \tag{4-39}$$

where the overall heat-transfer coefficient, $h_{scl-s,sum}$, and the resistance on the melt side, $h_{IR,scl}$, are given by

$$h_{scl-s,sum} = \left(\frac{1}{h_{IR,scl}} + \frac{1}{h_{IR,s}} + \frac{1}{h_s}\right)^{-1} \text{, and} \tag{4-40}$$

$$h_{IR,sci} = \frac{4\xi\kappa_L\sqrt{N_c}}{g(\xi)\sqrt{\pi}}. \tag{4-41}$$

The configurations of above heat transfer coefficients are schematically shown in **Fig. 4-7**. Since the interface temperature is defined by the temperature of the supercooled layer, the heat transfer coefficient of the structure side includes the thermal resistance. The heat transfer coefficient for the melt does not include the resistance.

When the supercooled layer solidifies completely, the energy of the flowing melt is transferred to the crust. The discrete contact between the melt and the wall is transformed into the contact resistance between the crust and the wall. Thus, the overall heat transfer coefficient between the crust and the wall includes the thermal resistance as:

$$h_{c-s,sum} = \left(\frac{1}{h_c} + \frac{1}{h_{IR,scl}} + \frac{1}{h_{IR,s}} + \frac{1}{h_s}\right)^{-1}, \tag{4-42}$$

where h_c is simply determined by the heat conduction in the crust fuel. Concerning the blockage formation at the leading edge of flowing melt, the original model is unchanged, because it is judged that solid particle formation due to the equilibrium mass transfer process and increased viscosity of particle-rich flow can well characterize the phenomena.

4.7.4. Non-equilibrium melting/freezing with improved freezing model

In the original non-equilibrium M/F model, the rate of phase transition is determined by the net energy flow from the binary contact interface. That is, from Eq. (4-17), the net energy flow from the interface between the melt and structure is expressed as

$$q_{L,s}^I = a_{L,s}h_L(T^I - T_L) + a_{L,s}h_s(T^I - T_s), \tag{4-43}$$

where h_L and h_s are the melt-side and structure-side heat-transfer coefficients, respectively, and the instantaneous contact interface temperature T^I is calculated by

$$T^I = \frac{h_L T_L + h_s T_s}{h_L + h_s}. \tag{4-44}$$

If Eq. (4-43) is positive, namely the energy is lost at the interface, the melt freezes to compensate this energy loss. On the other hand, if Eq. (4-43) is negative, namely the energy is gained at the interface, the structure melts to compensate this energy gain.

While only a single equation is used to predict the mode of phase transition, two inequalities are used in the improved freezing model, with replacing the contact interface temperature by the temperature of the supercooled zone. Namely, inequalities (4-38) and (4-39) are used to predict melting of structure and freezing of melt, respectively. The mass-transfer rates are evaluated from the energy balance as:

$$q^{\text{melting}} = a_{L,s}h_L(T_L - T_{scl}^I) - a_{L,s}h_{IR,s}(T_{Sol,s} - T_s), \text{ for structure melting, and} \tag{4-45a}$$

$$q^{\text{freezing}} = a_{L,s}h_{scl-s,sum}(T_{scl}^I - T_s) - a_{L,s}h_L(T_L - T_{scl}^I), \text{ for melt freezing.} \tag{4-45b}$$

When neither Eq. (4-38) nor (4-39) is satisfied, heat transfer is simply calculated without non-equilibrium mass transfer.

4.7.5. Correlation for supercooling temperature

The supercooling temperature, or the degree of supercooling, is defined as the temperature difference between the liquidus temperature and temperature of the supercooled layer, and is dependent on properties of materials. The supercooling temperatures of UO_2 and tin are 180 and 45 K, respectively. It seems obvious that the supercooling temperature increases with increasing the liquidus temperature. First, we define the instantaneous contact interface temperature between melt and structure.

$$T_{con}^{I} = \frac{\sqrt{\left(\rho c_p \kappa\right)_L} T_L + \sqrt{\left(\rho c_p \kappa\right)_s} T_s}{\sqrt{\left(\rho c_p \kappa\right)_L} + \sqrt{\left(\rho c_p \kappa\right)_s}} = \frac{\sqrt{\beta} T_L + T_s}{\sqrt{\beta} + 1}, \tag{4-46}$$

where $\beta = \left(\rho c_p \kappa\right)_L / \left(\rho c_p \kappa\right)_s$. Then the supercooling temperature with no phase transition is defined as

$$\Delta T_{con} = T_{Liq} - T_{con}^{I} \, . \tag{4-47}$$

To obtain an empirical correlation for the supercooling temperature, ΔT_{sc}, the following functional form is assumed, based on a dimensional analysis to extract sensitive parameters:

$$\frac{\Delta T_{sc}}{\Delta T_{con}} = a \beta^{\pi 1} \left(\frac{T_{Liq}}{\Delta T_{con}}\right)^{\pi 2} . \tag{4-48}$$

The equation is re-arranged to obtain the form of the ΔT_{sc} correlation as:

$$\Delta T_{sc} = a \beta^{\pi 1} {T_{Liq}}^{\pi 2} {\Delta T_{con}}^{1-\pi 2} \, . \tag{4-49}$$

In the previous report$^{30)}$, an intermediate form of the correlation is derived for fitting the parameters in Eq. (4-49) using the UO_2, tin and Wood's metal data, but it is not necessary to reproduce this process here. The resultant correlation with the fitted parameter values is:

$$\Delta T_{sc} = 0.083 \beta^{0.275} {T_{Liq}}^{1.147} {\Delta T_{con}}^{-0.147} \, . \tag{4-50}$$

Finally, the semi-empirical correlation for the temperature of subcooling layer is obtained by substituting Eqs. (4-46) and (4-47).

$$T_{scl}^{I} = T_{Liq} - \Delta T_{sc} = T_{Liq} - 0.083 \beta^{0.275} {T_{Liq}}^{1.147} \left(T_{Liq} - \frac{\sqrt{\beta} T_L + T_s}{\sqrt{\beta} + 1}\right)^{-0.147} . \tag{4-51}$$

The material dependent characteristics are included in this correlation by the liquidus temperature and other thermophysical properties. In addition to the experiments used to fit the parameters, the improved freezing model has been successfully applied to other high-temperature freezing experiments with stainless steel and alumina to confirm a wide applicability of the correlation$^{31)}$.

4.8. Improved Crust Formation Model

4.8.1. Background and assumptions

Frozen fuel crust formation is modeled as a part of non-equilibrium heat and mass transfer processes, in which the rate of crust formation is determined from the energy balance at the interface between liquid fuel and structure surface. The crust is assumed to uniformly cover an entire surface of the structure, even if the crust being formed is extremely thin. This assumption in the former SIMMER-III might be unrealistic because thin oxide crust can be unstable in nature and the assumed perfect crust formation overestimates an insulating effect due to a crust layer. This has been identified in a recent experimental knowledge from the EAGLE in- and out-of-pile test program, which simulated LMFR fuel melting and relocation behaviors in relatively large scales32). SIMMER-III was used in analyzing selected experiments. It was shown that the experimentally observed timing of structure wall melting was poorly simulated by the code, but was reproduced by increasing the liquid- to-structure heat-transfer coefficient by a factor of 3 to 533). This means the former SIMMER-III model has significantly underestimated the heat transfer to the structure. This underestimation of the heat transfer to the wall is partly attributed to the assumption that the fuel crust layer formed on the entire structure surface stays stable in the SIMMER model and the effect of thermal resistance reduced the heat flow into the structure. A model improvement specific to this problem was attempted by assuming a part of the structure wall is directly contacted by molten fuel and steel34); however a more mechanistic approach was desired for inclusion in SIMMER-III.

A new approach is based on consideration of an unstable nature of the thin crust layer. It is assumed that frozen crust being formed is brittle and imperfect, covering only a part of the structure surface, and this allows the partial contact of liquid steel and fuel directly to the structure steel, enhancing the heat flow into the structure. In this improved crust formation model, the structure surface is divided into two regions, with and without crust fuel, that exchange heat and mass with the fluid mixture. A noncrusted structure surface allows to calculate direct-contact heat transfer between fluid components and structure wall. There is no major change necessary for the fluid-side heat-transfer coefficient, except that the binary contact areas calculated in the interfacial area model are adjusted to treat the two regions in the same mesh cell.

The following assumptions are made in the improved crust formation model:

- Frozen fuel crust formed on a cold steel structure surface is unable to cover an entire surface of the structure. The structure surface is therefore divided into crusted and noncrusted regions.
- The surface area of the crusted region is determined in consideration of a minimum stable crust thickness.
- The crusted and noncrusted regions are treated separately for calculating non-equilibrium heat and mass transfers from/to fluid components to update the structure surface node mass and energy.
- Even though the heat flows into the can wall are modeled in two paths, the can wall component temperatures in the two regions are assumed to be equilibrated instantaneously. The can wall heat transfer calculation is performed without separating the two regions.

- The equilibrium melting/freezing model and the can wall breakup model are used as in the original code.

4.8.2. Calculative flow and procedure

The calculative procedure of the improved crust formation model is shown below. Since the calculations are performed sequentially, some of changes resulted from Step 1 operations are adjusted only in the next time step. This sequential procedure is well justified with small time step sizes used in the fluid-dynamics calculations.

- Structure breakup (STRBRK): Structure breakup calculations are performed at the beginning of Step 1, based on the results of heat and mass transfer operations in the previous time step.
- Structure configuration (STRCON): The structure configuration is calculated with determination of configuration case, structure-side heat transfer coefficient and area. The structure surface area is partitioned into crusted and noncrusted regions.
- Binary contact areas and fluid-side heat-transfer coefficients (IFA and HTC): The binary contact areas and fluid-side heat-transfer coefficient between fluid energy components and structure surface are calculated separately for the two regions, although no specific model change is necessary.
- Heat and mass transfers (MFHMT and VCHMT): Non-equilibrium heat and mass transfers are calculated at the structure surface including crust formation separately in the two regions. The masses and energies of the crust fuel and can wall surface, respectively in the crusted and noncrusted regions, are updated. The surface area of the crusted region is adjusted for the next time step.
- Can wall heat transfer (UPDSTR): The can wall heat transfer calculations are performed using the same procedure as the original code, without separating the two regions.
- Equilibrium mass transfer (EQUIMF, called from UPDSTR): Equilibrium melting/freezing operations are performed using the updated SIMMER variables.

4.8.3. Mass and energy equations of crust fuel

In the improved crust formation model, the total surface area per unit volume of the structure surface is divided into the crusted and noncrusted areas:

$$a_{k2} = a_{k2,cr} + a_{k2,nocr}, \tag{4-52}$$

for the left structure. In the crusted region, fluid energy components exchange heat and mass with crust fuel (*S*2). In the noncrusted region, fluid energy components are directly in contact with either a surface or an interior can wall node (*S*5 or *S*6) depending on its thickness.

The mass and energy equations of newly formed crust in the noncrusted region are:

$$\frac{\partial \bar{\rho}_{S2,nocr}}{\partial t} = \Gamma_{L1,S2,nocr}, \text{ for } k2 = S5 \text{ or } S6 \text{ , and} \tag{4-53a}$$

$$\frac{\partial \bar{\rho}_{S2,nocr} e_{S2,nocr}}{\partial t} = \Gamma_{L1,S2,nocr} e_{Sol,M(S2)} \text{ , for } k2 = S5 \text{ or } S6 \text{ .} \tag{4-53b}$$

Similarly, the crust mass and energy equations in the crusted region are:

$$\frac{\partial \bar{\rho}_{S2,cr}}{\partial t} = \Gamma_{L1,S2,cr}, \text{ for } k2 = S2 \text{ , and} \tag{4-54a}$$

$$\frac{\partial \bar{\rho}_{S2,cr} e_{S2,cr}}{\partial t} = \Gamma_{L1,S2,cr} e_{Sol,M(S2)} \text{ , for } k2 = S2 \text{ .} \tag{4-54b}$$

where mass transfer rates in the above equations are calculated in the non-equilibrium M/F model.

To determine the surface area of the crusted region, a concept of minimum stable crust thickness is introduced, based on a consideration that a thin crust layer is brittle and unstable in nature until a certain amount is accumulated to become stable. This limiting thickness for stable formation is represented by $W_{cr,min}$. When crust fuel is newly formed on the noncrusted structure surface, the crust thickness is set to this value. Equations (4-53a) and (4-53b) are simply evaluated at the current time step as:

$$\Delta \bar{\rho}_{S2,nocr}^{n+1} = \Delta t \Gamma_{L1,S2,nocr}, \text{ and} \tag{4-55a}$$

$$e_{S2,nocr}^{n+1} = e_{Sol,M(S2)}. \tag{4-55b}$$

The corresponding surface area increase is evaluated by

$$\Delta a_{S2,cr}^{n+1} = \frac{\Delta \alpha_{S2,cr}^{n+1}}{W_{cr,min}} = \frac{\Delta \bar{\rho}_{S2,uncr}^{n+1} v_{M(S2)}}{W_{cr,min}}, \tag{4-56}$$

where $v_{M(S2)}$ is the specific volume of crust fuel. For a cylindrical geometry, a different formula is to be used based on node radii. The surface areas of the crusted and noncrusted regions are updated as:

$$a_{k2,cr}^{n+1} = a_{k2,cr}^{n} + \Delta a_{S2,cr}^{n+1}, \text{ and} \tag{4-57a}$$

$$a_{k2,nocr}^{n+1} = a_{k2} - a_{k2,cr}^{n+1} \text{ .} \tag{4-57b}$$

The newly formed crust in the noncrusted region has been merged into the crusted region.

4.8.4. Update of crust and can wall mass and energy

Updated crust mass and energy are:

$$\bar{\rho}_{S2,cr}^{n+1} = \tilde{\bar{\rho}}_{S2,cr}^{n+1} + \Delta \bar{\rho}_{S2,nocr}^{n+1}, \text{ and} \tag{4-58a}$$

$$e_{S2,cr}^{n+1} = \frac{\tilde{\bar{\rho}}_{S2,cr}^{n+1} \tilde{e}_{S2,cr}^{n+1} + \Delta \bar{\rho}_{S2,nocr}^{n+1} e_{Sol,M(S2)}}{\bar{\rho}_{S2,cr}^{n+1}}, \tag{4-58b}$$

where the variables with "tilde" denote those updated in the heat and mass transfer operations in the same time step. For the noncrusted region, the mass and energy of the can wall surface or interior node, depending on its thickness, are updated.

After the non-equilibrium M/F and V/C calculations are finished by updating the mass and energy of the can wall node in contact with fluids, the can wall mass and energy are integrated. As an example, the local variables of the surface node of left can wall, when it is thick, are integrated to:

$$\bar{\rho}_{S6}^{n+1} = \bar{\rho}_{S6,cr}^{n+1} + \bar{\rho}_{S6,nocr}^{n+1}, \text{and} \tag{4-59a}$$

$$e_{S6}^{n+1} = \frac{\bar{\rho}_{S6,cr}^{n+1} e_{S6,cr}^{n+1} + \bar{\rho}_{S6,nocr}^{n+1} e_{S6,nocr}^{n+1}}{\bar{\rho}_{S6}^{n+1}}. \tag{4-59b}$$

A history of different heat flows in the two regions is lost at this point; however, the current values of partitioned structure surface areas updated in Eqs. (4-57a) and (4-57b) are saved for the next time step.

4.8.5. Geometrical consideration of crust stability

The minimum stable crust thickness, $W_{cr,min}$, should represent the geometrical characteristics, such aa shape and curvature, of the structure surface. For a cylindrical geometry, the stability of frozen crust fuel being formed would depend on shapes of the surface. It is presumed that the crust formed on a convex surface (the left can wall surface), is less stable than on a flat surface. The crust formation on a concave surface (the right can wall surface), on the other hand, may be stabler than on a flat surface.

An input factor, $f_{cr,stab}$, is introduced to adjust the minimum stable crust thickness depending on the shape of structure surface. For the cylindrical geometry, both for SIMMER-III and SIMMER-IV, the shapes of the left and right can wall surfaces are convex and concave, respectively. The minimum stable crust thickness for the cylindrical geometry is evaluated by:

$$W_{cr,min} = \begin{cases} W_{cr,min}^{in}\left(1 + f_{cr,stab}\right) & \text{for left can wall} \\ W_{cr,min}^{in} & \text{for front and back can walls} \\ W_{cr,min}^{in}\left(1 - f_{cr,stab}\right) & \text{for right can wall} \end{cases} \tag{5-60}$$

$W_{cr,min}^{in}$ is an input variable for the minimum stable crust thickness on a flat surface, and a typical value is 0.3 mm. A typical value of $f_{cr,stab}$ is 0.3 for a pipe with a small diameter such as 5 cm and 0.0 for a pipe with a diameter larger than 10 cm. The default value of $f_{cr,stab}$ is 0.0. For simulating hexagonal duct walls in LMFR fuel subassemblies as a flat wall, the value of 0.0 should simply be used.

4.8.6. Can wall heat transfer calculations

In the improved crust formation model, a heat flow to the structure is determined by the non-equilibrium M/F and V/C calculations in the two regions. The mass and energy of the structure surface are updated for crust fuel in the crusted region, and can wall surface or interior in the noncrusted region. Since the heat flow into crust fuel is much less than the heat transfer in the noncrusted region, the separated treatment of can wall heat transfer in the crusted regions is considered unimportant. Therefore, a single-path heat transfer calculation is performed including the crust fuel. The surface area of the crusted region is used as a crust-to-can-wall heat transfer area. If two cells are coupled through a single can wall with crust fuel present on the both sides of the cell boundary of cells *IJ* and *IJ*-1, different values can be used for the surface areas of the crusted regions.

The implementation of the above modeling approach in the multi-node can wall model, described in **Section 5.4**, is straightforward, since the multi-node model is simply to replace a single interior can wall node with multiple temperature nodes.

4.9. Inter-cell Heat Transfer Model

In the original modeling framework of SIMMER-III and SIMMER-IV, inter-cell heat transfer has not been calculated, except for lateral thermal coupling of two adjacent cells through a can wall when one of the can walls at a cell boundary is missing. In a calculation of internally-heated boiling pools, it revealed that treatment of inter-cell heat transfer was necessary to simulate small-scale pool boiling behavior correctly. In such a situation as a large temperature gradient exists in a hot liquid pool, lateral and axial inter-cell heat transfer becomes essential for simulating heat losses from the pool to the structure wall. Another example of requiring inter-cell heat transfer treatment is the situation that the hot liquid is in contact axially with a cold structure. It is for these reasons that the inter-cell heat transfer is modeled in the later versions of SIMMER-III and SIMMER-IV as described in this section.

4.9.1. Inter-cell heat transfer model

In the inter-cell heat transfer model, a transient heat-conduction equation is solved in a simplified way. Although the component energies are updated due to inter-cell transfers, the model is treated as a part of intra-cell transfers in Step 1, because the fluid convection is not involved. In a multi-component and multi-phase system of SIMMER-III and SIMMER-IV, the model is only applied to the same components (materials) such as real liquids (fuel, steel or sodium) and vapor mixture.

The energy equation with no convection term solved in Step 1 is repeated below from Eq. (4-2), with adding the contribution of the inter-cell heat transfer:

$$\frac{\partial \bar{\rho}_M e_M}{\partial t} = Q_N + Q_M + Q_H + Q_{IC} \, , \tag{4-61}$$

where the first three terms on the right side denote the energy sources due to nuclear (internal) heating, energy transfer associating with mass transfer and the intra-cell heat transfer, and Q_{IC} is the heat source due to inter-cell heat transfer per unit volume. Since the intra-cell updates of energy have been calculated individually, step by step, in Step 1, the inter-cell heat transfer is separated from other heat sources and is evaluated simply by the transient heat conduction equation with no other heat sources:

$$\frac{\partial \bar{\rho}_M e_M}{\partial t} = Q_{IC} = \nabla \cdot \boldsymbol{q}_{c,M} \, . \tag{4-62}$$

The heat flux which appears in this equation is calculated by Fourier's law and includes the turbulent thermal conductivity:

$$\boldsymbol{q}_{c,M} = -f_I \left(\kappa_{c,M} + \kappa_{T,M} \right) \nabla T_M \, , \tag{4-63}$$

where $\kappa_{c,M}$ is the thermal conductivity of component M and the turbulent thermal conductivity, $\kappa_{T,M}$, is evaluated by Plandtl's mixing length theory as:

$$\kappa_{T,M} = \frac{c_{p,M}}{\upsilon_M} l^2 , \tag{4-64}$$

where $c_{p,M}$ and υ_M denote the specific heat at constant pressure and the specific volume, respectively, for component M. The mixing length l is determined based on the location, direction, and the nature of the turbulent flow, using either von Karman's similarity hypothesis or Deisler's empirical formulation. The factor f_I in Eq. (4-63) is to adjust the heat-transfer area between two cells where the volume fractions of component M are different from each other. In fact, this factor must be determined for each direction, considering the different heat-transfer areas of mesh cell boundaries.

The internal energy of component M is updated explicitly using the beginning-of-time-step temperatures. An example of inter-cell heat conduction in a rectangular (or axial) direction is given. The energy of cell i is updated due to heat conduction from cell j by:

$$e_{M,i}^{n+1} = e_{M,i}^{n} + \frac{\Delta t}{\bar{\rho}_{M,i}^{n}} f_I \left(\kappa_{c,M} + \kappa_{T,M}\right) \frac{T_{M,j}^{n} - T_{M,i}^{n}}{\Delta x_{i,j}} \quad , \tag{4-65}$$

where $\Delta x_{i,j}$ is the distance between the cell centers (temperature points) of cells i and j. The properties are averaged over the momentum cell in-between. Since the explicit procedure may introduce numerical problems especially with large time step sizes, an arrangement is made to use special time steps that can be smaller than the fluid dynamics time steps.

4.9.2. Axial heat transfer in structure

The model has been later extended to calculate axial heat conduction in structure such as cladding and can walls. This model is useful for simulating axial heat losses from the hot core region through the structure components. A one-dimensional equation for axial heat conduction is expressed as:

$$\frac{\partial \bar{\rho}_{SM} e_{SM}}{\partial t} = f_I \kappa_{c,SM} \nabla T_M , \tag{4-66}$$

where the structure component M represents structure components such as cladding or can wall. The factor f_I again is to adjust the heat-transfer areas between two adjacent cells. The solution procedure is the same as the above for inter-cell heat transfer in fluid components, including the special time-step control.

4.9.3. Axial heat transfer between fluids and structures

In the original SIMMER-III and SIMMER-IV, hot fluids in a cell cannot transfer their energies to the structure in axially adjacent cells. This mechanism of inter-cell heat transfer becomes extremely important in correctly treating axial heat losses or simulating melting attack of the structure due to a contact of hot liquid. When a solid structure is simulated by the can wall component that fills the mesh cell volume, or a mesh cell is plugged by molten steel that has been refrozen as structure, this cell is thermo-hydraulically decoupled completely from the axially adjacent cells. To avoid this unphysical situation, an axial heat transfer model has been developed which models heat transfer between the fluid components in a cell and the structure components in adjacent cells above or below the relevant cell35).

The modeling concept is the same as the intra-cell heat and mass transfer (**Section 4.5**) without phase transition. All the possible heat-transfer paths are treated in a generalized way between 8 fluid components and 9 structure components for SIMMER-III (15 structure components for SIMMER-IV). Binary contact areas are evaluated in the same way as the interfacial area model (**Section 4.2**), with considering only the pool flow regimes. The fluid-side heat-transfer coefficients are evaluated in the same way as **Section 4.4**, and the structure-side heat-transfer coefficients are evaluated in the structure configuration model (**Chapter 5**). Even though the structure melting is neglected in this model, if the bulk thermal condition after heat transfer satisfies the phase transition criterion, an equilibrium melting/freezing operation is performed in the subsequent operation in Step 1.

The concept of the model is almost similar to the intra-cell heat transfer between fluid energy components and the structure in the non-equilibrium M/F heat and mass transfer model. The energy equations for heat transfer across the contact interface without phase change are written as:

$$\frac{\partial \bar{\rho}_{Sn} e_{Sn}}{\partial t} = \sum_{m \in n} a_{Lm,Sn} h_{Sn} \left(T^I_{Sn,Lm} - T_{Sn} \right) \text{ , and} \tag{4-67}$$

$$\frac{\partial \bar{\rho}_{Lm} e_{Lm}}{\partial t} = a_{Sn,Lm} h_{Lm} \left(T^I_{Sn,Lm} - T_{Lm} \right) . \tag{4-68}$$

where *m* and *n* are fluid and structure components, respectively, and the structure-liquid contact interface temperature is defined as:

$$T^I_{S,Lm} = \frac{h_K T_S + h_{S,Lm} T_{Lm}}{h_K + h_{S,Lm}} . \tag{4-69}$$

The characteristic lengths used in the fluid-side heat transfer coefficients for discontinuous and continuous phases are represented by droplet diameter and axial mesh cell size, respectively. The standard fluid-side heat transfer coefficients, based on the empirical correlations for a vertical circular tube, are applied to the present configuration of the horizontal surface in this model as well. Because of uncertainty associated with this, the model is controlled as an input option, with providing the user-specified multipliers to fluid heat-transfer coefficients.

4.10. Miscellaneous Intra-Cell Transfer Updates

In this section, other miscellaneous intra-cell transfer models are described.

4.10.1. Nuclear heating updates

The energy injection into the LMFR core materials is a major mechanism of driving core disruption during a CDA. The reactor power may vary drastically with time, depending on an accident sequence considered, from the decay power level after neutronic shutdown to thousands of the nominal power level when a recriticality event is postulated. In SIMMER-III/SIMMER-IV, nuclear energy release is modeled by the specific internal energy generation rates for the five nuclear heat source materials: fertile fuel, fissile fuel, steel, sodium and control. No heat source can be specified to fission gas, because of the negligibly small contribution.

Depending on whether the neutronics option is used or not, there are two options to define the specific internal energy generation rates. When the space-dependent neutronics option is used, the nuclear heat source is directly supplied from the neutronics module. Based on the initial total power, power distribution based on a neutron flux shape and the power amplitude updated every reactivity time step, the specific internal energy generation rates are extrapolated to fluid-dynamics time steps. The contribution of decay heat generated in fission and capture products is also modeled in a simplified way. Without the neutronics module, nuclear heat source can still be defined by user input. The total power, power partition among the five heat source materials, radial and axial power distributions are specified for the initial conditions. The input power-versus-time table then determines time-dependent nuclear heat source, assuming the initial distribution of specific power is kept unchanged. This means the nuclear heating calculation without neutronics is inaccurate when large-scale material re-distribution takes place.

Consider the specific internal energy generation rate due to nuclear heating $Q_N(M)$ is determined for nuclear heat source material *M*, then the update in the specific internal energy is simply performed by

$$\tilde{e}_M^{n+1} = e_M^n + \Delta t Q_N(M)\,. \tag{4-70}$$

Equation (4-70) applies to energy updates for all the fluid-dynamics and fuel-pin energy components, and there seems to be need to repeat all the equations. The operation of nuclear heating updates for all the energy components including pin fuel is performed only in Step 1 as the first energy update in the series of Step 1 heat and mass transfer operations. The subsequent heat and mass transfer operations are performed based on the updated energy conditions.

4.10.2. Fuel related model improvement

Some fuel-related models are included in Step 1 operations. because they directly affect the component volume fractions and cell vapor state. They include an improved model of fission gas release from liquid-field fuel components and a new model of fuel swelling. Because they are related to the fuel pin (structure) model, further details are described in **Section 5.7**.

4.10.3. Updates of velocities and interfacial areas

The Step 1 heat and mass transfers change the macroscopic densities and volume fractions of the fluid and structure energy components. These changes then require adjustment in IFAs and velocities because of the following reasons. The Step 1 mass transfers include the mass exchange processes between two different velocity fields or a fluid velocity field and structure. To conserve the total momentum of the velocity fields, the mass transferred is assumed to carry its momentum from the transferring field to the transferred field. This results in adjustment of the velocity of the transferred field, whilst the velocity of the transferring field is unchanged. This procedure corresponds to solving the momentum equation without convection terms shown in Eq. (4-3), reflecting the mass transfers.

When the mass is transferred from velocity field q to velocity field q', the updated velocity of the transferred velocity field is expressed by

$$\vec{v}_{q'}^{n+1} = \frac{\bar{\rho}_{q'}^n \vec{v}_{q'}^n + \Delta t \Gamma_{q,q'} \vec{v}_q^n}{\bar{\rho}_{q'}^n + \Delta t \Gamma_{q,q'}}\,, \tag{4-71}$$

where the adjusted velocity does not represent the end-of-time-step update, although it is superscripted as n+1, because the actual velocity update is only made in Steps 2-4 setting the above velocities to the beginning-of-time-step values. Equation (4-71) is applied to all the velocity fields for all the modes of mass transfers, but the velocities are only updated for the transferred fields. The mass transferred from the structure field is assumed to carry zero velocity. The momentum of the mass transferred to the structure field is simply lost, because the structure field, by definition, is always stationary and works as a momentum sink. This means the momentum is not conserved when the mass is transferred from a moving field to the structure.

The Step 1 mass transfers change the component volume fractions, and hence the convectible IFAs and flow regime must be adjusted for these changes. The flow regime is re-evaluated based on the updated volume fractions as in the same procedure described in **Section 4.2.1**. The changes of IFAs of droplets and particles by the changes of volume fractions are assumed to be proportional to volume fraction to the power of 2 over 3.

$$\mathrm{A}_{Lm}^{n+1} = \mathrm{A}_{Lm}^{n}\left(\frac{\alpha_{Lm}^{n+1}}{\alpha_{Lm}^{n}}\right)^{\frac{2}{3}} . \tag{4-72}$$

The newly born components by mass transfer are assumed to have radius which are given by input data. The change of the component volume fractions causes the migration of IFA between bubbly and dispersed flow regions. The amount of this migration generated by mass transfer is calculated in the same way as the migration generated by convection, which is given in the reference17).

4.10.4. Special treatment of single-phase cells

The Step 1 transfers result in changes in component volume fractions. Under some situations, a mesh cell with a small vapor volume fraction at the beginning of time step may turn to single phase with potential cell over-filling, resulting in non-physical spurious pressure spikes. This is normally adjusted in the Step 3 pressure iteration; however, this sometimes requires to cut down time step sizes extremely small in the order of 10^{-6} s or even less. This treatment is still reasonable when single-phase pressurization is to be simulated. On the other hand, the resolution in single-phase pressure propagation is not always important in many cases of SIMMER-III/SIMMER-IV application. Under two-phase dominant conditions, the single-phase pressure, even if it develops, disappears in a very short time scale and it does not affect an overall fluid motion in the system. Thus, in many cases, it is computer-time saving if the cell over-filling situation is relieved.

The method optionally implemented is a simple donor-acceptor approach. In this approach, if mesh-cell over-filling is detected at the end of Step 1, the over-filled mass in a cell is removed from the cell and transferred to the upper adjacent cell, such that the donor cell has the vapor volume fraction corresponding to α_0. If the acceptor cell is over-filled, the cell is scanned further upward. If the top real cell is filled up, then the radial direction is scanned.

This optional method is found to be very effective to reduce computer time, but is of course not physically exact, since the fluid is transferred instantaneously to neighboring cells without solving the momentum equations. Nevertheless, the method is justified because the over-filled mass is small enough that the overall fluid dynamics is essentially unaffected. It is therefore recommended to use this simple method when single-phase pressure spikes generated in Step 1 are reducing the time step sizes seriously.

Table 4-1. Major heat transfer coefficients defined in SIMMER-III/SIMMER-IV. (1/2)

Modes of heat transfer	Heat transfer coefficients model
Rigid particles - internal heat transfer	$H_{P,i} = \frac{K_i}{2R_i} a_i$
Circulating fluid particles - internal heat transfer	$H_{FP,i} = H_{P,i} \left\{ 1 + j_{i1} \left[1 + \tanh \left(j_{i2} \ln \left(\frac{\mathrm{Pe}_i^*}{j_{i3}} \right) \right) \right] \right\}$, for $\mathrm{Re}_{is} < \mathrm{Re}_i \leq \mathrm{Re}_{os}$ $\mathrm{Pe}_i^* = \frac{\mathrm{Pe}_i}{1+\kappa} = \frac{2R_i V_{ij}}{\alpha_i (1+\kappa)}$
Oscillating fluid particles - internal heat transfer	$H_{FP,i} = H_{P,i} k_i$, for $\mathrm{Re}_{os} < \mathrm{Re}_i$
Heat transfer in CP fluid *i* to rigid particles *j* – forced convection	$H_{CPP,i} = \frac{K_i}{2R_i} \left[b_i + e_{i1} \mathrm{Re}_j^{e_{i2}} \mathrm{Pr}_i^{e_{i3}} \left(1 + e_{i4} \mathrm{Re}_j^{e_{i5}} \right) \right]$
Heat transfer in CP fluid *i* to circulating fluid particles *j* – forced convection	$H_{CPP,i} = \frac{K_i}{2R_j} \left\{ b_i + i_{i1} \mathrm{Pe}_j^{i_{i2}} \left[1 - \frac{\left(i_{i3} + i_{i4} \kappa^{i_{i5}} \right)}{\mathrm{Re}_j^{1/2}} \right]^{i_{i6}} \right\}$
Heat transfer in CP fluid *i* to particles *j* – natural convection	$H_{CPP,i} = \frac{K_i}{2R_j} \left[b_i + f_{i1} \left(\mathrm{Gr}_j \mathrm{Pr}^{f_{i3}} \right)^{f_{i2}} \right]$
Heat transfer for gas/vapor in the dispersed flow regime to structure	$H_{CPS,i} = \frac{K_i}{D_h} \left[c_i + g_{i1} \mathrm{Re}_{D_h}^{g_{i2}} \mathrm{Pr}_i^{g_{i3}} \right]$
Heat transfer for bubbly flow CP liquid to structure	$H_{CPS,i} = \frac{K_{mix}}{D_h} h_1 + \frac{K_i}{D_h} \left(g_{i1} \mathrm{Re}_{D_h}^{g_{i2}} \mathrm{Pr}_i^{g_{i3}} \right)$, where $K_{mix}^{h_2} = \left(\sum_{i=1}^{7} \alpha_i K_i^{h_2} + \alpha_{g,bub} K_g^{h_2} \right) \Big/ \alpha_{bub}$
Heat transfer for a liquid film in annular flow to structure	$H_{CPS,i} = \frac{K_i}{W_i} \left[d_i + g_{i1} \mathrm{Re}_{D_h}^{g_{i2}} \mathrm{Pr}_i^{g_{i3}} F \right]$, where $F = \left(\frac{2W_i}{D_h} \right)^{0.743} \frac{\left[1 - \frac{8}{15} \right]}{\left[1 - \frac{8}{15} \left(\frac{2W_i}{D_h} \right) \right]}$

Table 4-1. Major heat transfer coefficients defined in SIMMER-III/SIMMER-IV. (2/2)

Modes of heat transfer	Heat transfer coefficients model
Heat transfer between solid particles and structure	$H_{DPS,i} = \frac{K_{mix}}{D_h} h_i$ for $\frac{\alpha_{pp}}{(1-\alpha_{st})} \geq \alpha_{MP}$ $H_{DPS,i} = 0$ for $\frac{\alpha_{pp}}{(1-\alpha_{st})} < \alpha_{MP}$
Heat transfer between droplets and structure	$H_{DPS,i} = \frac{K_{mix}}{D_h} h_1$ for $\mathrm{Re}_{CP} < 3000$ (laminar), $H_{DPS,i} = \frac{K_i}{2R_i} a_i$, for $\mathrm{Re}_{CP} \geq 3000$ (turbulent)
Heat transfer for droplet-droplet contact	$H_{DF,i} = \frac{K_i}{2R_i} \frac{-3\alpha_i \tau_{ij}^c}{2R_i^2} \Big/ \ln\left[\frac{6}{\pi^2} \sum_{n=1}^{\infty} \frac{1}{n^2} \exp\left(\frac{-n^2\pi^2\alpha_i\tau_{ij}^c}{R_i^2}\right)\right]$, where $\tau_{ij}^c = \frac{2(R_i + R_j)}{\Delta V_{ij}}$

a's, b's, c's, etc.: fitting parameters for heat-transfer correlations

Subscripts:

i	Energy component for which the heat transfer coefficient is being calculated
j	Energy component being interacted with
cp	Continuous phase (external fluid)
dp	Dispersed phase (particle)
ic	Internal circulation
os	Oscillating particle
int	Interface

Table 4-2. Numbers of binary contacts and mass transfer paths in SIMMER-III/SIMMER-IV.

	SIMMER-III	**SIMMER-IV**
No. of binary contact interfaces (total)	52	68
(between fluid components)	(28)	(28)
(between fluid component and structure)	(24)	(40)
No. of melting/freezing heat and mass transfer paths*	22	32
No. of vaporization/condensation heat and mass transfer paths*	33	39

* only important mass transfer paths are actually modeled

Table 4-3. Non-equilibrium mass transfer paths modeled in SIMMER-III. (1/2)

Interface ID	**Interface**	**Processes**	**Mass transfer rate**
*I*1	liquid fuel-vapor	Condense fuel vapor/Vaporize liquid fuel	$\Gamma_{G,L1}^{I1}/\Gamma_{L1,G}^{I1}$
*I*2	liquid steel-vapor	Condense fuel and steel vapor/Vaporize liquid steel	$\Gamma_{G,Lm}^{I2}/\Gamma_{L2,G}^{I2}$ (m=1, 2)
*I*3	liquid sodium-vapor	Condense fuel, steel and sodium vapor/Vaporize liquid sodium	$\Gamma_{G,Lm}^{I3}/\Gamma_{L3,G}^{I3}$ (m=1, 2, 3)
*I*4	fuel particles-vapor	Condense fuel, steel and sodium vapor	$\Gamma_{G,Lm}^{I4}$ (m=1, 2, 3)
*I*5	steel particles-vapor	Condense fuel, steel and sodium vapor	$\Gamma_{G,Lm}^{I5}$ (m=1, 2, 3)
*I*6	control particles-vapor	Condense fuel, steel and sodium vapor	$\Gamma_{G,Lm}^{I6}$ (m=1, 2, 3)
*I*7	fuel chunks-vapor	Condense fuel, steel and sodium vapor	$\Gamma_{G,Lm}^{I7}$ (m=1, 2, 3)
*I*8	liquid fuel-liquid steel	Vaporize liquid steel	$\Gamma_{L2,G}^{I8}$
*I*9	liquid fuel-liquid sodium	Vaporize liquid sodium	$\Gamma_{L3,G}^{I9}$
*I*10	liquid fuel-fuel particles	Form fuel particles/Melt fuel particles	$\Gamma_{L1,L4}^{I10}/\Gamma_{L4,L1}^{I10}$
*I*11	liquid fuel-steel particles	Form fuel particles/Melt steel particles	$\Gamma_{L1,L4}^{I11}/\Gamma_{L5,L2}^{I11}$
*I*13	liquid fuel-fuel chunks	Form fuel chunks/Melt fuel chunks	$\Gamma_{L1,L7}^{I13}/\Gamma_{L7,L1}^{I13}$
*I*14	liquid steel-liquid sodium	Vaporize liquid sodium	$\Gamma_{L3,G}^{I14}$
I16	liquid steel-steel particles	Form steel particles/Melt steel particles	$\Gamma_{L2,L5}^{I16}/\Gamma_{L5,L2}^{I16}$
*I*29	pin-vapor	Condense fuel, steel and sodium vapor	$\Gamma_{G,Lm}^{I29}$ (m=1, 2, 3)

Table 4-3. Non-equilibrium mass transfer paths modeled in SIMMER-III. (2/2)

Interface ID	Interface	Processes	Mass transfer rate
*I*30	pin-liquid fuel	Form fuel particles/Melt cladding	$\Gamma_{L1,L4}^{I30}/\Gamma_{S4,L2}^{I30}$
*I*31	pin-liquid steel	Freeze steel on cladding/Melt cladding	$\Gamma_{L2,S4}^{I31}/\Gamma_{S4,L2}^{I31}$
*I*37	left can wall or crust-vapor	Condense fuel, steel and sodium vapor	$\Gamma_{G,Lm}^{I37}$ (m=1, 2, 3)
*I*38	left can wall or crust-liquid fuel	Form crust/Melt crust/Melt can wall	$\Gamma_{L1,S2}^{I38}/\Gamma_{S2,L1}^{I38}$ $/\Gamma_{S5,L2}^{I38}$ or $\Gamma_{S6,L2}^{I38}$
*I*39	left can wall or crust-liquid steel	Freeze steel to can wall/Melt can wall	$\Gamma_{L2,S5}^{I39}$ or $\Gamma_{L2,S6}^{I39}$ $/\Gamma_{S5,L2}^{I39}$ or $\Gamma_{S6,L2}^{I39}$
*I*45	right can wall or crust-vapor	Condense fuel, steel and sodium vapor	$\Gamma_{G,Lm}^{I45}$ (m=1, 2, 3)
*I*46	right can wall or crust-liquid fuel	Form crust/Melt crust/Melt can wall	$\Gamma_{L1,S3}^{I46}/\Gamma_{S3,L1}^{I46}$ $/\Gamma_{S7,L2}^{I46}$ or $\Gamma_{S8,L2}^{I46}$
*I*47	right can wall or crust-liquid steel	Freeze steel to can wall/Melt can wall	$\Gamma_{L2,S7}^{I47}$ or $\Gamma_{L2,S8}^{I47}$ $/\Gamma_{S7,L2}^{I47}$ or $\Gamma_{S8,L2}^{I47}$

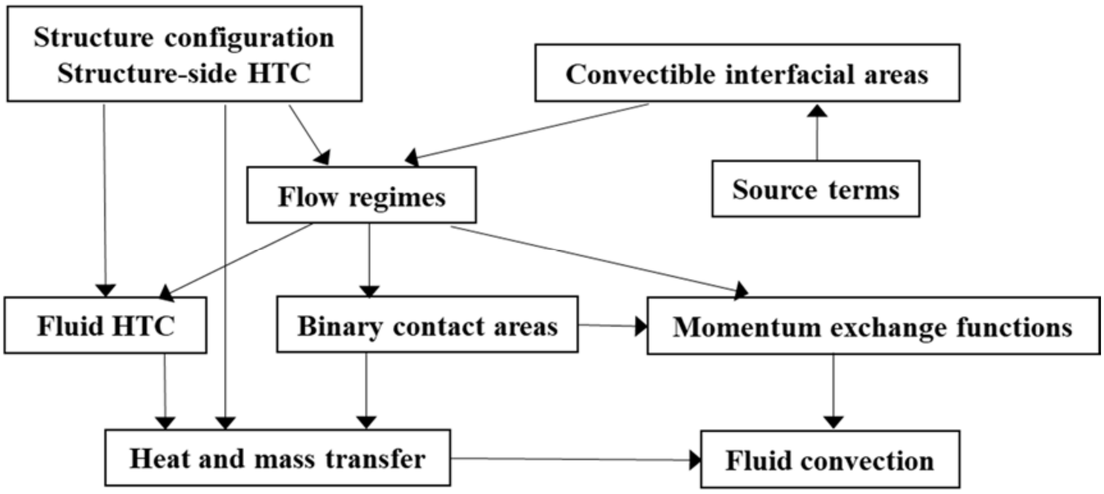

Fig. 4-1. Flow of intra-cell heat and mass transfer calculations (Step 1).

	Energy component	Energy component which is being interacted with:											Mass transfer paths	
		Gas/ Vapor G	Liquid Fuel L1	Liquid Steel L2	Liquid Sodium L3	Fuel Particle L4	Steel Particle L5	Control Particle L6	Fuel Chunk L7	Fuel pin Structure K1	Left Structure K2	Right Structure K3	M/F	V/C
HTC	Gas/ Vapor G		V/C HGLM(1) I1{1}	V/C HGLM(2) I2{2}	V/C HGLM(3) I3{3}	V/C HGLM(4) I4{3}	V/C HGLM(5) I5{3}	V/C HGLM(6) I6{3}	V/C HGLM(7) I7{3}	V/C HGS I29{3}	V/C HGS I37{3}	V/C HGS I45{3}		27
	Liquid Fuel L1	V/C HLMG(1) I1{1}		V/C HRT(1) I8{-}	V/C HRT(2) I9{-}	M/F HRT(3) I10{1}	M/F HRT(4) I11{1}	M/F HRT(5)	M/F HRT(6) I13{1}	M/F HRS(1) I30{1}	M/F HRS(8) I38{1}	M/F HRS(10) I46{1}	6	1
	Liquid Steel L2	V/C HLMG(2) I2{1}	M/F HRT(7) I8{1}		V/C HRT(8) I14{-}	M/F HRT(9)	M/F HRT(10) I16{1}	M/F HRT(11)	M/F HRT(12)	M/F HRS(2) I31{1}	M/F HRS(9) I39{1}	M/F HRS(11) I47{1}	4	2
	Liquid Sodium L3	V/C HLMG(3) I3{1}	M/F HRT(13) I9{1}	M/F HRT(14) I14{1}		M/F HRT(15)	M/F HRT(16)	M/F HRT(17)	M/F HRT(18)	M/F HRS(3)	M/F HRS(3)	M/F HRS(3)		3
	Fuel Particle L4	V/C HPT(1)	M/F HPT(1) I10{1}	M/F HPT(1)	M/F HPT(1)		M/F HPT(1)	M/F HPT(1)	M/F HPT(1)	M/F HRS(4)	M/F HRS(4)	M/F HRS(4)	1	
	Steel Particle L5	V/C HPT(2)	M/F HPT(2) I11{1}	M/F HPT(2) I16{1}	M/F HPT(2)	M/F HPT(2)		M/F HPT(2)	M/F HPT(2)	M/F HRS(5)	M/F HRS(5)	M/F HRS(5)	2	
	Control Particle L6	V/C HPT(3)	M/F HPT(3)	M/F HPT(3)	M/F HPT(3)	M/F HPT(3)	M/F HPT(3)		M/F HPT(3)	M/F HRS(6)	M/F HRS(6)	M/F HRS(6)		
	Fuel Chunk L7	V/C HPT(4)	M/F HPT(4) I13{1}	M/F HPT(4)	M/F HPT(4)	M/F HPT(4)	M/F HPT(4)	M/F HPT(4)		M/F HRS(7)	M/F HRS(7)	M/F HRS(7)	1	
STRCON	Fuel Pin Structure K1	V/C I29{-}	M/F I30{1}	M/F I31{1}	M/F	M/F	M/F	M/F	M/F	Heat and mass transfer calculated in V/C or M/F routine.			2	
	Left Structure K2	V/C I37{-}	M/F I38{2}	M/F I39{1}	M/F	M/F	M/F	M/F	M/F	HTC(n) is an array name and (the number of HTCs).			3	
	Right Structure K3	V/C I45{-}	M/F I46{2}	M/F I47{1}	M/F	M/F	M/F	M/F	M/F	Interface ID and {the number of mass transfer paths}.			3	
										Total number of paths:			22	33

Fig. 4-2. Role of HTCs in SIMMER-III heat and mass transfer

	Energy component	Energy component which is being interacted with:													Mass transfer paths	
		Gas/ Vapor G	Liquid Fuel L1	Liquid Steel L2	Liquid Sodium L3	Fuel Particle L4	Steel Particle L5	Control Particle L6	Fuel Chunk L7	Fuel pin Structure K1	Left Structure K2	Right Structure K3	Front Structure K4	Back Structure K5	M/F	V/C
HTC	Gas/ Vapor G		V/C HGLM(1) I1{1}	V/C HGLM(2) I2{2}	V/C HGLM(3) I3{3}	V/C HGLM(4) I4{3}	V/C HGLM(5) I5{3}	V/C HGLM(6) I6{3}	V/C HGLM(7) I7{3}	V/C HGS I29{3}	V/C HGS I37{3}	V/C HGS I45{3}	V/C HGS I53{3}	V/C HGS I61{3}		33
	Liquid Fuel L1	V/C HLMG(1) I1{1}		V/C HRT(1) I8{-}	V/C HRT(2) I9{-}	M/F HRT(3) I10{1}	M/F HRT(4) I11{1}	M/F HRT(5)	M/F HRT(6) I13{1}	M/F HRS(1) I30{1}	M/F HRS(8) I38{1}	M/F HRS(10) I46{1}	M/F HRS(8) I54{1}	M/F HRS(10) I62{1}	8	1
	Liquid Steel L2	V/C HLMG(2) I2{1}	M/F HRT(7) I8{1}		V/C HRT(8) I14{-}	M/F HRT(9)	M/F HRT(10) I16{1}	M/F HRT(11)	M/F HRT(12)	M/F HRS(2) I31{1}	M/F HRS(9) I39{1}	M/F HRS(11) I47{1}	M/F HRS(9) I55{1}	M/F HRS(11) I63{1}	6	2
	Liquid Sodium L3	V/C HLMG(3) I3{1}	M/F HRT(13) I9{1}	M/F HRT(14) I14{1}		M/F HRT(15)	M/F HRT(16)	M/F HRT(17)	M/F HRT(18)	M/F HRS(3)	M/F HRS(3)	M/F HRS(3)	M/F HRS(3)	M/F HRS(3)		3
	Fuel Particle L4	V/C HPT(1)	M/F HPT(1) I10{1}	M/F HPT(1)	M/F HPT(1)		M/F HPT(1)	M/F HPT(1)	M/F HPT(1)	M/F HRS(4)	M/F HRS(4)	M/F HRS(4)	M/F HRS(4)	M/F HRS(4)	1	
	Steel Particle L5	V/C HPT(2)	M/F HPT(2) I11{1}	M/F HPT(2) I16{1}	M/F HPT(2)	M/F HPT(2)		M/F HPT(2)	M/F HPT(2)	M/F HRS(5)	M/F HRS(5)	M/F HRS(5)	M/F HRS(5)	M/F HRS(5)	2	
	Control Particle L6	V/C HPT(3)	M/F HPT(3)	M/F HPT(3)	M/F HPT(3)	M/F HPT(3)	M/F HPT(3)		M/F HPT(3)	M/F HRS(6)	M/F HRS(6)	M/F HRS(6)	M/F HRS(6)	M/F HRS(6)		
	Fuel Chunk L7	V/C HPT(4)	M/F HPT(4) I13{1}	M/F HPT(4)	M/F HPT(4)	M/F HPT(4)	M/F HPT(4)	M/F HPT(4)		M/F HRS(7)	M/F HRS(7)	M/F HRS(7)	M/F HRS(7)	M/F HRS(7)	1	
STRCON	Fuel Pin Structure K1	V/C I29{-}	M/F I30{1}	M/F I31{1}	M/F	M/F	M/F	M/F	M/F						2	
	Left Structure K2	V/C I37{-}	M/F I38{2}	M/F I39{1}	M/F	M/F	M/F	M/F	M/F						3	
	Right Structure K3	V/C I45{-}	M/F I46{2}	M/F I47{1}	M/F	M/F	M/F	M/F	M/F						3	
	Front Structure K4	V/C I53{-}	M/F I38{2}	M/F I39{1}	M/F	M/F	M/F	M/F	M/F						3	
	Back Structure K5	V/C I61{-}	M/F I46{2}	M/F I47{1}	M/F	M/F	M/F	M/F	M/F						3	
	Total number of paths:														32	39

Heat and mass transfer calculated in V/C or M/F routine.

HTC(n) is an array name and (the number of HTCs).

Interface ID and {the number of mass transfer paths}.

Fig. 4-3. Role of HTCs in SIMMER-IV heat and mass transfer

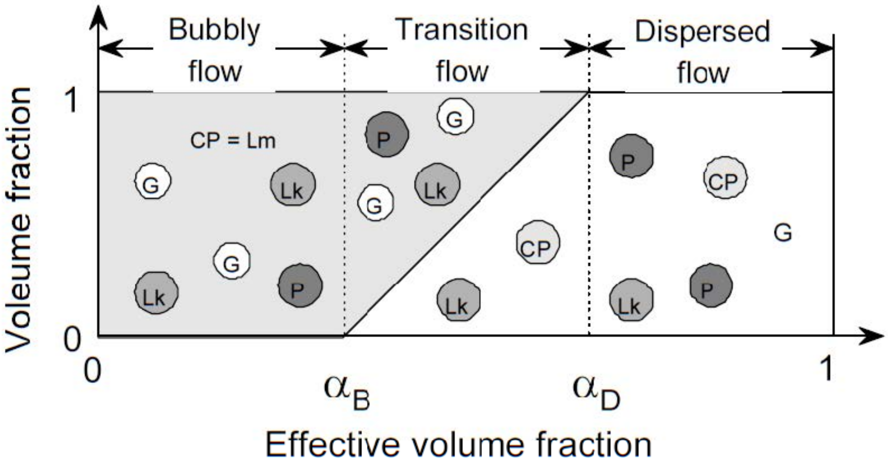

Fig. 4-4. Concept of transition flow and pool flow regime map in SIMMER-III/SIMMER-IV.

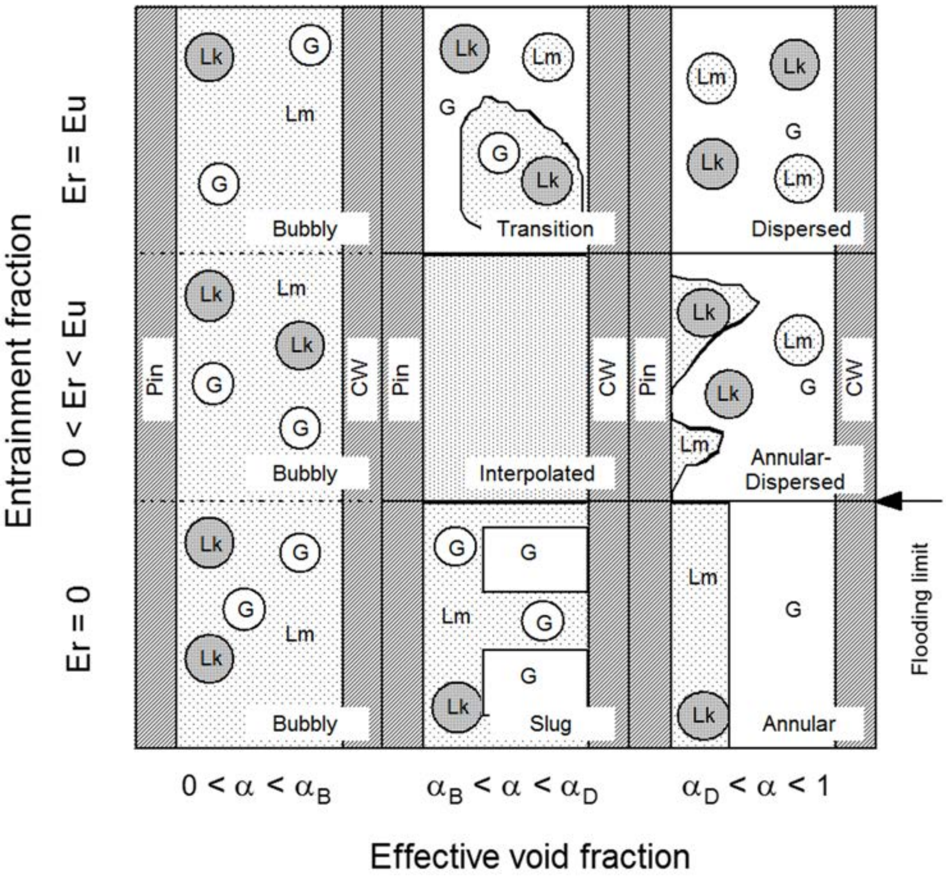

Fig. 4-5. Channel flow regime map for SIMMER-III/SIMMER-IV.

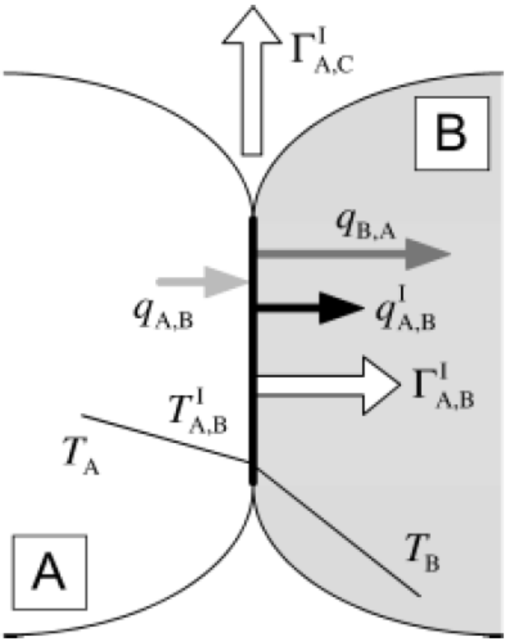

(a) Possible mass transfers at an (A,B) interface with net heat flow to the interface toward Component B: Component A condenses or freezes

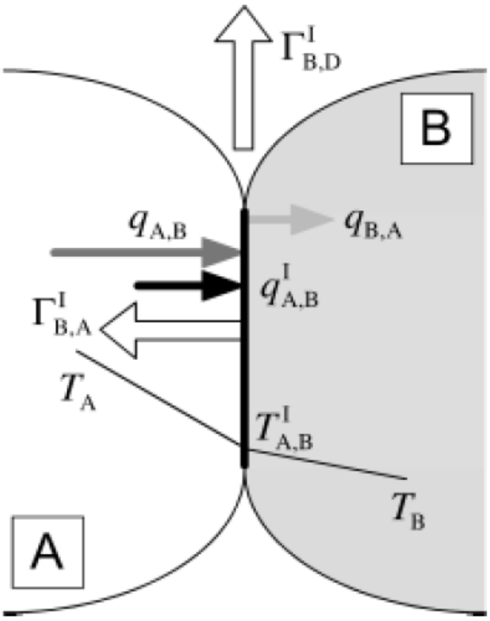

(b) Possible mass transfers at an (A,B) interface with net heat flow to the interface toward Component A: Component B condenses or freezes

Fig. 4-6. Basic concept of heat-transfer limited processes.

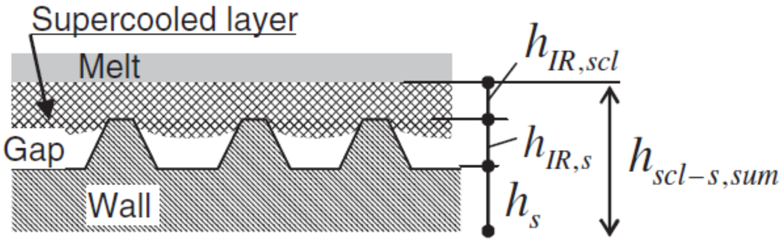

Fig. 4-7. Schematic representation of heat transfer coefficients at the melt-wall interface

5. Fuel-Pin and Structure Model

5.0. Overview

5.0.1. Background of models and methods

The structure field of the SIMMER-III/SIMMER-IV constitutes of solid components that are stationary. In as LMFR core they are fuel pins and subassembly can walls. In the former SIMMER-II[1)], pin fuel and can wall are both represented by a single temperature node. This simplistic assumption has shortcomings that, for example, the surfaces of pin fuel or can walls cannot respond to rapid variations in fluid temperature. In the SIMMER-III/SIMMER-IV structure model, thick structure components (pin fuel and can wall) are divided into a quickly responding surface node and a slowly responding interior node. This two-node representation, together with a more flexible treatment of inter-cell coupling through can wall heat transfer, has significantly improved the analysis of core melt-out behaviors.

Since a detailed model description is available for the SIMMER structure model[15)], only an outline of the fuel pin and can wall models are presented in **Sections 5.1** and **5.2**, respectively. Recent revision of the hydraulic diameter in a pool configuration is included in **Section 5.2**. The original models for structure-related heat and mass transfers are summarized in **Section 5.3**. The model improvements and additions implemented after the issuance of the above report are then presented, including: a multi-node can wall model, improved freezing model, improved crust formation model, additional structure failure and breakup models and other small model improvements. The improved freezing model and the improved crust formation model are parts of the non-equilibrium melting/freezing model in fluid-dynamics Step 1, and hence they are described in **Chapter 4**.

5.0.2. Interaction with other models

The fuel-pin and structure model is not an independent code module, but parts of the model is included in the fluid-dynamics module. Only the fuel-pin heat transfer model is programmed outside the fluid dynamics module. Thus, the model is intimately coupled with the fluid dynamics through heat and mass transfer processes, such as heat transfer between structure surface and fluid flow, melting or breakup of structure components, and freezing of liquid components on the structure surface. Because any changes in structure volume fraction and mass and energy transfer may significantly and immediately influence the state and multi-phase flows in a fluid-dynamics mesh cell, many of the structure related heat and mass transfer operations are directly performed in Step 1 of the fluid dynamics.

The internal heat sources of structure energy components due to nuclear heating are provided by the neutronics model. The macroscopic densities and specific internal energies of all the structure and fluid energy components are transferred to the neutronic model to calculate atom number densities and temperatures necessary for determining the effective shielded macroscopic cross sections.

5.1. Outline of Fuel Pin Model

Since a detailed model description is available for the SIMMER-III structure model$^{15)}$, only an outline of the models is given in this section.

5.1.1. Fuel-pin structure configuration

Axial and radial geometries of the SIMMER fuel-pin configuration are depicted in **Figs. 5-1 and 5-2**, respectively. A fuel pin consists of pin fuel (representing pellets), or control for a control rod assembly, and cladding of steel. No-flow volume can be specified to simulate a volume fraction of the central hole, pellet-cladding gap or the internal volume in the fission gas plenum region. The standard fuel-pin model is rather simple with a pellet interior modeled by a single temperature node and with breakup modeled only by a thermal (melt fraction) criterion. However, the separated treatment of a pellet surface node provides better thermal coupling with the fluid. Because of the relatively large thermal inertia of the pellet interior, the fuel-pin heat-transfer calculation can be performed with time steps larger than the fluid-dynamics steps. This simplified model is considered sufficient for simulating the fuel-pin behavior in a voided channel typical for a loss-of-flow accident. The axial blanket and fission-gas plenum regions can be placed both above and below the core region.

A thickness of the pin-fuel surface node is determined from the thermal penetration length, $2\delta_M$, using the input time constant $\tau_{str,M}$, in consideration of transient thermal response.

$$2\delta_M = 2\sqrt{3}\sqrt{\frac{\kappa_M \tau_{str,M}}{\rho_M c_M}}, \tag{5-1}$$

where the coefficient $2\sqrt{3}$ is determined by assuming a transient temperature profile is parabolic. The temperature points of the cladding and surface node are placed respectively at the radial center of their thickness, and the temperature point of the pin pin-fuel interior node is selected at the mass centroid.

The thickness of can-wall surface node is determined in the same way as Eq. (5-1).

5.1.2. Fuel-pin heat transfer

The basic equations of mass and energy conservation of the fuel-pin component *m* are :

$$\frac{\partial \bar{\rho}_m}{\partial t} = -\Gamma_m \text{ , and} \tag{5-2}$$

$$\frac{\partial \bar{\rho}_m e_m}{\partial t} = h_{m,\mathrm{m-1}} a_{m,\mathrm{m-1}} (T_{m-1} - T_m) + h_{\mathrm{m+1,m}} a_{\mathrm{m+1,m}} (T_{\mathrm{m+1}} - T_m) + Q_{H,\mathrm{m}} + Q_{N,m} \text{ ,} \tag{5-3}$$

where the subscript *m* denotes the fuel-pin radial node, and Eq. (5-2) represent all the modes of mass transfer from the fluid. The $Q_{H,m}$ and $Q_{N,m}$ terms denote the energy transfer rates due to heat transfer from the fluid and nuclear heating, respectively. The heat-conduction equation in a cylindrical geometry is solved for specific internal energies of the three fuel-pin components (interior, surface and cladding). The heat transfer coefficient between pin-fuel surface and cladding includes the gap conductance. There are three options available for the gap conductance as documented in the structure model report$^{15)}$.

- a constant value specified by user input,
- a simple conductance model based on gap gas conduction and radiation heat transfer, and
- a more elaborated model to consider fuel-cladding contact behavior as well as gap gas conductance and radiation.

The solution procedure is implicit, by expanding the end-of-time-step temperatures on the right side of Eq. (5-3) into a Taylor series with respect to specific internal energy. The resultant linear equations are solved directly. The fuel-pin surface (cladding, or pin fuel surface node when cladding is missing) exchanges mass and energy with the contacting fluid and this is operated in the fluid-dynamics Step 1. In the fission-gas plenum region, the gas temperature is represented by one point and the heat transfer is solved explicitly because of its slow thermal response. For a control subassembly, the pin fuel is replaced by the control material (B_4C), which is represented by a single node.

The calculations are conducted outside the fluid-dynamics module at heat-transfer time steps which are larger than fluid-dynamics time steps, because of large thermal inertia of the pin fuel. The heat-transfer time steps are, by default, set equal to the reactivity time steps because the fuel temperature change is closely related to nuclear heating rates. The time-step sizes are controlled based on: the changes in the specific energies of pin fuel and cladding, and the change in the power amplitude.

5.2. Outline of Can Wall Model

A detailed model description is available for this model, only the outlines of the models are given below. Although only the model for left and right can walls are described in this section, the same procedure is implemented for the front and back can walls as well.

A can wall represents fuel subassembly hexagonal duct walls (wrapper tubes) in LMFR simulation or circular pipe in many non-LMFR calculations. Thus, both the slab and cylindrical geometries are optionally available. The latter is applied only to the left and right can walls in the radial direction (index *i*) both in SIMMER-III and SIMMER-IV.

5.2.1. Can-wall structure configuration

A general configuration of the SIMMER-III structure components in a mesh cell *IJ* are depicted in **Fig. 5-3**, together with the can-wall components in the adjacent cells. The SIMMER-III can wall model distinguishes separated left and right can walls (plus front and back can walls in SIMMER-IV), which are placed at the left and right mesh-cell boundaries, respectively. At each mesh-cell boundary, there are two can walls, one from cell *IJ* and the other from an adjacent cell, and no-flow volumes can be specified in between to represent the inter-subassembly gap volume. The presence of the can wall at a cell boundary prohibits fluid flow in the traverse direction and furnishes a structure wall for an axial fluid flow. Fuel crust can grow on a can wall when the fuel solidification on the can-wall surface is predicted by the heat and mass transfer model.

Similarly to the pin-fuel surface node, each can wall is divided into: a surface and interior nodes。 The surface node is to model a quicker thermal response in contact with fluid flow. The thickness of the surface node is determined from Eq. (5-1) as well. When the can wall becomes thin due to mass transfer to fluid (melting and ablation), the two can wall nodes are merged into a single interior node. As long as two can walls are present at a cell boundary, either thick or thin, the two adjacent mesh cells are assumed to be thermally decoupled and no heat transfer is calculated in-between. Inter-cell heat transfer is calculated only when one of the two can walls at a cell boundary is missing. The above requires a complex procedure to define the variations in can-wall structure configuration as summarized in **Table 5-1**. These variations represent different can-wall configurations either: presence of can wall or not, thick or thin, with or without crust fuel, and adjacent cells decoupled or coupled.

There are 8 configuration cases and 4 sub-cases each for Cases 7 and 8. Cases 1 through 6 are for special case treatment of an isolated can wall for the first and the last boundary mesh cells (I=1 or IB) in the radial (traverse) direction. Cases 7 and 8 are for general treatment of the right boundaries of internal mesh cells (I=1, 2, …, IB-1). Two adjacent cells are decoupled in Case 7, where two can walls (right can wall in cell IJ and left can wall in cell IJ+1) are both present. Two cells are coupled when one of the can walls is missing in Case 8. Depending on whether the can wall is thick or thin and whether there exists crust fuel or not, there are 4 sub-cases in Cases in 7 and 8, as shown in **Table 5-1**. For Case 7, the treatment of decoupled can walls in a mesh cell in 4 sub-cases is the same as that for either Cases 1, 2, 4 or 5. In Case 8, the most complex situation with inter-cell coupling, as many as 5 temperature points are defined in Case 8d.

A special treatment is necessary when a thick can wall is coupled with an adjacent cell; a part of the thick can wall interior is transferred to the adjacent cell as the surface node and the macroscopic densities are adjusted. This treatment is somewhat tricky, but is performed only to calculate inter-cell heat and mass transfers. The volume fraction of the surface node set over from the adjacent cell is not added to calculate the total structure volume fraction α_S in the transferred cell (accepter cell) but is accounted in the transferring cell (donor cell). This treatment is necessary to conserve the structure volumes in the two cells as described later.

The thickness of a can wall is calculated, for the left can wall, as

$$W_{LCW} = \begin{cases} \dfrac{\alpha_{S5} + \alpha_{S6}}{a_{LCW}} & \text{for slab geometry} \\ \sqrt{r_{c0}^2 + (r_{c1}^2 - r_{c0}^2)(\alpha_{S5} + \alpha_{S6})} - r_{c0} & \text{for cylindrical geometry} \end{cases}, \tag{5-4a}$$

where a_{LCW} is the surface area of left can wall per unit volume, and r_{c0} and r_{c1} are the radii of the left and right boundaries of the mesh cell, respectively. This equation is valid for an isolated (decoupled) can wall (Cases 1 to 7). However, when a part of the interior node is transferred from cell *IJ* to an adjacent cell like in Case 8, the volume fraction of the set-over can wall is brought back to the original transferring cell.

$$W_{LCW} = \begin{cases} \left(\alpha_{S5} + \alpha_{S6} + \alpha_{S7,ij-1}\dfrac{V_{ij-1}}{V_{ij}}\right) \Big/ a_{LCW} \\ \sqrt{r_{c0}^2 + (r_{c1}^2 - r_{c0}^2)\left(\alpha_{S5} + \alpha_{S6} + \alpha_{S7,ij-1}\dfrac{V_{ij-1}}{V_{ij}}\right)} - r_{c0} \end{cases}, \tag{5-4b}$$

where the volume ratio is necessary to conserve can wall mass. The right can wall is treated in the same way.

Whether a can wall is thick or not is determined by the remaining thickness of interior node which must be larger than $2\delta_S$ to be thick. An isolated can wall (Cases 1 to 7) is regarded as thick if $W_{LCW} > 4\delta_S$ is satisfied. A coupled can wall (Case 8) is regarded as thick if $W_{LCW} > 6\delta_S$ is satisfied, since two surface nodes must be considered.

5.2.2. Can-wall heat transfer

The can-wall heat transfer is modeled considering the above combinations of geometrical configuration and heat transfer paths. A typical energy equation of the temperature node m is written as:

$$\frac{\partial \bar{\rho}_m e_m}{\partial t} = h_{m,\mathrm{m-1}} a_{m,\mathrm{m-1}} (T_{m-1} - T_m) + h_{\mathrm{m+1,m}} a_{\mathrm{m+1,m}} (T_{\mathrm{m+1}} - T_m)\,. \tag{5-5}$$

The calculation is performed for up to five structure-component nodes at fluid time steps in either a slab geometry to represent LMFR subassembly duct or a cylinder geometry to simulate a circular pipe wall. Updates of specific internal energy and temperature of outer-most structure node, which contacts the fluid flow, have been performed in the heat and mass transfer model in fluid-dynamics Step 1 before can wall heat transfer. The update of internal energy due to nuclear heating is performed outside the structure model.

A solution method is implicit similarly to the fuel-pin heat transfer model. The end-of-time-step temperatures on the right side of Eq. (5-5) are expanded to a Taylor series with respect to specific internal energies. The resultant set of linearized equations, of up to 5 temperature nodes in Case 8d, are solved by a direct method.

5.2.3. Structure volume fraction and hydraulic diameter

The total volume fraction of structure, α_S, is an important variable, since it provides a basis to define the volume fraction of flow, $(1 - \alpha_S)$, and vapor volume fraction (void fraction), $(1-\alpha_S - \alpha_L)$. α_S is simply a summation of the volume fractions of individual structure components and no-flow volumes. The volume fraction of pin-fuel interior, not defined as a fluid-dynamics structure component, is also added.

$$\alpha_S = \alpha_{int} + \sum_{m=1}^{9} \bar{\rho}_{Sm} v_{Sm} + \alpha_{nf,PIN} + \alpha_{nf,LCW} + \alpha_{nf,RCW}\,. \tag{5-6}$$

This is a nominal formulation with no inter-cell thermal coupling. When one of two can walls at a cell boundary is missing as treated in Case 8, a complex set-over procedure is implemented in which a part of can-wall mass is transferred from cell *IJ* to the adjacent cell *IJ*+1, or from cell *IJ*+1 to cell *IJ*, as a new surface node. Inter-cell can wall heat transfer and the heat and mass transfer in these two cells are calculated in a consistent way. However, when the total structure volume fraction is calculated, the volume fraction of the transferred surface node must be brought back to the original transferring cell to conserve volume. A complete logical formulation of this procedure is described in the structure model report15).

$$\begin{aligned}\alpha_S = \alpha_{int} + \sum_{m=1}^{3} \bar{\rho}_{Sm} v_{Sm} + \alpha_{nf,PIN} + \alpha_{nf,LCW} + \alpha_{nf,RCW} + \bar{\rho}_{S9} v_{S9} \\ + \bar{\rho}_{S5}(ij) v_{S5}(ij) H\big(NCANL(ij)\big) + \bar{\rho}_{S6}(ij) v_{S6}(ij) \\ + \bar{\rho}_{S7}(ij) v_{S7}(ij) H\big(NCANR(ij)\big) + \bar{\rho}_{S8}(ij) v_{S8}(ij) \\ + \bar{\rho}_{S5}(ij+1) v_{S5}(ij+1) H\big(NCANL(ij+1)\big) \frac{V_{ij+1}}{V_{ij}} \\ + \bar{\rho}_{S7}(ij-1) v_{S7}(ij-1) H\big(NCANR(ij-1)\big) \frac{V_{ij-1}}{V_{ij}},\end{aligned} \tag{5-7}$$

where $H(x)$ is the Heaviside function, $NCANL$ and $NCANR$ are flags to recognize the presence of can wall in the left and right cell boundaries, respectively. The macroscopic densities of can wall components are denoted as energy components for simplicity.

The hydraulic diameter, D_h, is another important variable in fluid dynamics, and is defined as

$$D_h = \frac{4 \times [\text{flow area}]}{[\text{wetted perimeter}]} = \frac{4A_{flow}}{P_{flow}} = \frac{4(1-\alpha_S)}{a_{pin} + a_{LCW} + a_{RCW}}, \tag{5-8}$$

where a_{pin}, a_{LCW}, and a_{RCW} are the structure surface areas per unit volume of the fuel pin, left can wall and right can wall, respectively. When there is no structure existing in a cell, the hydraulic diameter is set to a large value,

$$D_h = 10^{20}\,, \tag{5-9}$$

such that the effects of structure on heat transfer and momentum exchange (friction) are eliminated. The hydraulic diameter in a pool configuration with an outer wall is determined from a mesh-cell width and the structure volume fraction as:

$$D_h = (1-\alpha_S)\Delta R\,, \tag{5-10}$$

where ΔR denotes the mesh cell width in cylindrical geometry.

It is also noted that the selection of flow regimes, pool or channel, in a mesh cell is determined from the hydraulic diameter. If the hydraulic diameter D_h is larger than the input threshold, $D_{h,pool}$, the flow in the cell is regarded as “pool flow”. Otherwise, the cell is considered to be a channel flow. The default value of $D_{h,pool}$ is 1.0.

5.2.4. Hydraulic diameter to simulate transient heat transfer

The hydraulic diameter is included in the fluid-to-structure HTC. When there is a large temperature difference between fluids and structure, the effect of transient heat transfer becomes important. Although it is beyond the scope of SIMMER-III quasi-steady-state HTC model, a simple time constant model has been developed for parametrically examining this effect. The effective heat transfer lengthscale is represented by a thermal penetration length, similarly to the structure surface node representation, as

$$D_h = 2\delta_M = 2\sqrt{3}\sqrt{\frac{\kappa_M v_M}{c_M}\tau_M}\,, \tag{5-11}$$

where κ_M, v_M and c_M are the thermal conductivity, specific volume, and specific heat of the fluid mixture, and τ_M is the input time constant to simulate the effect of transient heat transfer. The time constant must be determined considering a timescale of a problem. This model improvement has been developed as an input option after the structure model report$^{15)}$ was issued.

5.3. Structure Melting, Breakup and Other Modes of Mass Transfer

5.3.1. Modes of structure-related mass transfer

Various modes of structure-related mass transfer processes are modeled in SIMMER-III/SIMMER-IV. Non-equilibrium melting/freezing mass transfers occurring at the interfaces between structure surface and fluid are treated in the fluid-dynamics heat and mass transfer model$^{14)}$. Equilibrium melting/freezing mass transfers, on the other hand, are modeled in the structure model. The modes of mass transfer related to the structure include:

- equilibrium melting of solid components
- equilibrium freezing of liquid components
- fission gas release from liquid-field fuel
- fuel pin breakup
- collapse of unsupported pin fuel
- can-wall and crust fuel breakups

Equilibrium melting and freezing have already been discussed in the heat and mass transfer model (see **Section 4.5**); however, they are repeated here for completeness as structure-related mass-transfer processes.

All the above operations are included in the fluid-dynamics Step 1 procedure and mass and energy updates are performed in series, each of which deals with a different mass-transfer process. The structure breakup mass transfer is calculated at the beginning of the fluid-dynamics Step 1, before the structure configuration is updated, because the breakup transfer instantaneously and drastically changes the structure configuration, the structure volume fraction and the cell hydraulic diameter. The equilibrium melting/freezing transfer is calculated at the end of Step 1, to determine whether the component thermal condition after nuclear heating and a series of intra-cell transfers satisfies the phase transition criteria.

The equations for energy and mass transfers in these processes are described in the original structure model report$^{15)}$, and only modeling concepts are described below.

5.3.2. Equilibrium melting of solid components

Equilibrium melting occurs when the specific internal energy of a solid component exceeds its solidus energy and thereby a condition for phase transition (melting) is satisfied. The mass-transfer rate is determined such that the remaining mass stays at the solidus energy. This process includes: equilibrium melting of crust fuel, fuel particles, steel particles and fuel chunks. Since the mass transfers of pin fuel/control and cladding are treated as structure breakup processes, no equilibrium melting is modeled.

Equilibrium melting of can wall component s is rather complex. The surface node in a thick can wall or the interior node of a thin can wall undergoes equilibrium melting similarly to the above. Even when the crust fuel is present on the can wall, underlying can wall is allowed to melt and mass is transferred. When two cells are thermally coupled and a surface node is set over to an adjacent cell, the melting of this surface node occurs in the adjacent cell but the mass transferred to the liquid field must be brought back to the original cell to conserve mass and volume.

As a result of equilibrium melting of solid components, the thermodynamic state of the liquid field is updated. The macroscopic density of a liquid component is simply updated using the mass transfer rate. The specific internal energy of liquid fuel is updated assuming that the mass transferred is at the liquidus energy. The equilibrium melting of the fuel particles and fuel chunks is accompanied by fission-gas mass transfer to liquid fuel.

5.3.3. Equilibrium freezing of liquid components

Liquid fuel can freeze into either crust fuel or solid fuel particles. The former mode of mass transfer is modeled as non-equilibrium fuel freezing on a structure surface. This mode of freezing corresponds to the so-called “conduction-limited freezing” model and is treated in the heat and mass transfer model. It is noted the fission gas mass in liquid fuel is lost because no fission gas mass in crust fuel is modeled. This loss of mass is considered not important since most of fission gas resolved in liquid fuel has released before molten fuel re-freezes. Equilibrium freezing occurs when the specific internal energy of liquid fuel falls below the liquidus energy and results in formation of solid fuel particles. This mode of fuel freezing is important, since it describes the so-called “bulk freezing” mechanism. The mass-transfer rate is determined such that the remaining mass stays at the liquidus energy. This fuel mass transfer is accompanied by fission gas mass transfer from liquid fuel to fuel particles.

Equilibrium freezing of liquid steel is modeled similarly to the bulk freezing of fuel. In the initial modeling in SIMMER-III, liquid steel was assumed to freeze predominantly into steel particles. When liquid-steel-rich mixture flows into a cold structure channel, it should freeze not only into solid particles but also onto the structure surfaces. Therefore, an optional model has been later added to treat steel freezing onto cladding and can-wall surfaces. In this improved model, liquid steel is partitioned into dispersed droplets and continuous liquid, the latter of which freezes onto cladding and can walls based on individual binary contact areas. This optional treatment is controlled by user input specification.

5.3.4. Fission-gas release from liquid-field fuel

The fission gas masses can be retained in the liquid-field components, liquid fuel, fuel particles and fuel chunks. The release of fission gas from the liquid-field components to the vapor field is simply modeled by user specified release time constants, typical values being 10^{-3} and 10^{-1} s for liquid fuel and fuel particles/chunks, respectively. The vapor state is updated accordingly.

5.3.5. Fuel-pin breakup

The criteria for breakup of the pin fuel and cladding are determined from input threshold melt fractions, typically 0.5 for pin fuel and the solidus energy for the cladding. All the mass of pin fuel or cladding is transferred instantaneously into liquid and solid particles, for which the partition of mass is based on the threshold melt fraction, at the liquidus and solidus energies, respectively. It is unlikely that the cladding stays intact after pin fuel breakup, and therefore the cladding is assumed to break up simultaneously with pin fuel breakup.

The mass transfer to fine fuel particles is a rational assumption when fuel breakup mode is of a rapid disruption type under highly overpower conditions. At lower heating rates, on the other hand, pin fuel breaks up into larger solid particles. For this reason, the mass transfer from pin fuel to fuel chunks is optionally treated based on user input specification. The pin fuel breakup is accompanied by fission-gas mass transfer to the liquid-field fuels. The liquid and vapor states are updated following these mass transfers.

5.3.6. Collapse of unsupported pin fuel

A special fuel breakup model is implemented to simulate the collapse of a pellet column or the downfall of unsupported pellets. In this model, it is assumed that a fuel pellet column loses it mechanical integrity when: the cladding is lost and subassembly can wall is lost (collapse of pellet column); or the cladding is lost and the pin structure in the lower cell is lost (downfall of pellets). If one of these conditions is satisfied, the mass of pin fuel is transferred either to fuel particles or fuel chunks depending on user specification.

The control is assumed to break up into particles when the cladding is lost. The control particles, and no liquid control, are only modeled in a liquid field.

5.3.7. Can-wall and crust fuel breakup

A criterion to predict breakup of can wall is based on the melt fraction of can wall interior node. A part of can-wall mass is transferred to liquid steel at the liquidus energy depending on the melt fraction. The remaining mass is partitioned, based on user input specification, into the can wall structure and solid steel particles. Considering the mechanical stability of a can wall structure, additional structure breakup mechanisms are implemented which predict can wall failure based on the minimum thickness of remaining can wall and the threshold temperature above which structural strength is assumed to be practically lost.

Since the crust fuel itself is thought to be very brittle and fragile, it is assumed that it can stay on a structure wall surface only when underlying structure is intact. Namely, if the can wall structure disappears or undergoes extensive melting on its surface, the crust fuel is assumed to break up.

After the issuance of the structure model report[15)], other can-wall failure models have been later added as input options. Since the can-wall and crust fuel failure and breakup modes are becoming complex, the entire modeling framework is completely re-documented in **Section 5.6**.

5.4. Multi-node Can Wall Heat-Transfer Model

5.4.1. Background and objectives

In the standard model, a can wall structure is represented by two nodes, surface and interior. This simplified model is considered sufficient and practical in many cases of the code applications. For example, in a typical LMFR unprotected loss-of-flow accident, the core melt-out progresses sooner or later, and detailed resolutions of subassembly can wall temperature and failure timing are not necessarily important. However, in such situations that relatively cold structures are present in the core and the accuracy in predicting their failure timing becomes important, a more detailed treatment is desired. Calculations of small-scale experiments may require to calculate heat losses to the structure accurately.

From these observations, a multi-node can wall heat transfer model has been developed for SIMMER-III and SIMMER-IV. The model is available as an input option and can be used in reactor and non-reactor applications when detailed treatment of heat flow into and temperature profile in the can wall is needed. The model is documented as a JAEA report (in Japanese)[36)], and the model description specific to the multiple nodalization is reproduced concisely in this section. The verification and validation of the developed model are also included in the above JAEA report.

5.4.2. Multi-node representation

The model has been developed to completely fit into the standard two-node model[15)]. That is, keeping the same framework of can-wall configuration and heat-transfer model, only the interior node is subdivided into multiple nodes as shown in **Fig. 5-4**. Other parts of can-wall related models stay the same as the standard two-node model. Both the slab and cylindrical geometries can be treated optionally. The cylindrical geometry is applied only to the left-right (index i) direction.

Consider the left can wall in a mesh cell, and the total thickness of the can wall and the thickness of the surface node are defined as W_{LCW} and $2\delta_S$. respectively. It is reminded the latter is defined as the thermal penetration length in consideration of transient thermal response, and typically much less than 1/10 of total thickness. The number of sub-divided nodes, N_{LCWI}, is specified by user input or determined such that the node width is almost equal to $2\delta_S$.

$$N_{LCWI} = \min(\,(W_{LCW} - 2\delta_S)/2\delta_S\,,\; N_{DCWLM})\,, \tag{5-12}$$

where N_{DCWLM} is the maximum number of nodes, with the default value of 20. Then the node width is calculated uniformly as

$$D_{LCWI} = \frac{W_{LCW} - 2\delta_s}{N_{LCWI}}. \tag{5-13}$$

The macroscopic density of the node is calculated as

$$\bar{\rho}_{LCWI} = \bar{\rho}_{s9} \frac{D_{LCWI}}{\alpha_{S6}/a_{LCW}}, \tag{5-14a}$$

for the slab geometry in which the node volumes are equal, and

$$\bar{\rho}_{LCWI,L} = \bar{\rho}_{s9} \frac{r_{LCWI,L}^2 - r_{LCWI,L-1}^2}{(r_{S5} - 2\delta_s)^2 - r_{c0}^2}, \tag{5-14b}$$

for L-th node in the cylindrical geometry. The geometry of the slab geometry is illustrated in **Fig. 5-5**, and the complex node radii are shown in **Fig. 5-6** for different configuration cases in the cylindrical geometry.

5.4.3. Can wall configuration

For the can wall structure configuration, the same variations in configuration, shown in **Table 5-1**, are considered. The treatment of thick can walls is relevant to multiple nodalization and the thin can walls are treated in the same way as the standard two-node model. Thus, only Cases 2, 5, 7b, 7d, 8c and 8d with the multi-node can wall interior are described below.

Case 2 and Case 7b (left thick can wall): slab geometry

The treatment is the same for the two cases, in which only one left thick can wall with or without crust is modeled. Since the surface node thickness is always kept to $2\delta_s$, a rezoning operation is performed, using the updated can wall thickness, W_{LCW}.

For the standard two-node model, the macroscopic densities and specific internal energies are updated first, and the heat-transfer coefficients are calculated.

$$\tilde{\bar{\rho}}_{s8}^{n+1} = \frac{2\delta_s}{W_{LCW}} (\bar{\rho}_{s8}^n + \bar{\rho}_{s9}^n), \tag{5-15a}$$

$$\tilde{\bar{\rho}}_{s9}^{n+1} = \bar{\rho}_{s8}^n + \bar{\rho}_{s9}^n - \tilde{\bar{\rho}}_{s8}^{n+1}, \tag{5-15b}$$

$$\tilde{e}_{S5}^{n+1} = \begin{cases} e_{S5}^n & \tilde{\bar{\rho}}_{s8}^{n+1} < \bar{\rho}_{s8}^n \\ \dfrac{[\bar{\rho}_{s8}^n e_{S5}^n + (\tilde{\bar{\rho}}_{s8}^{n+1} - \bar{\rho}_{s8}^n) e_{S6}^n]}{\tilde{\bar{\rho}}_{s8}^{n+1}} & \tilde{\bar{\rho}}_{s8}^{n+1} \geq \bar{\rho}_{s8}^n \end{cases}, \text{and} \tag{5-15c}$$

$$\tilde{e}_{S6}^{n+1} = \begin{cases} \dfrac{[\bar{\rho}_{s9}^n e_{S6}^n + (\tilde{\bar{\rho}}_{s9}^{n+1} - \bar{\rho}_{s9}^n) e_{S5}^n]}{\tilde{\bar{\rho}}_{s9}^{n+1}} & \tilde{\bar{\rho}}_{s9}^{n+1} \geq \bar{\rho}_{s9}^n \\ e_{S6}^n & \tilde{\bar{\rho}}_{s9}^{n+1} < \bar{\rho}_{s9}^n \end{cases}. \tag{5-15d}$$

The internal heat transfer coefficients of the can wall nodes (crust, surface and interior) are defined respectively by

$$h_{S2} = \frac{2\kappa_f a_{LCW}}{\alpha_{S2}^n}\ ,\ h_{S5} = \frac{2\kappa_s a_{LCW}}{\tilde{\alpha}_{S5}^{n+1}}\ \text{ and }\ h_{S6} = \frac{2\kappa_s a_{LCW}}{\tilde{\alpha}_{S6}^{n+1}}. \tag{5-16}$$

The heat transfer coefficients between structure nodes are

$$h_{S2,S5} = \frac{h_{S2} h_{S5}}{h_{S2} + h_{S5}}\ \text{ and }\ h_{S5,S6} = \frac{h_{S5} h_{S6}}{h_{S5} + h_{S6}}. \tag{5-17}$$

The structure-side heat transfer coefficients, with and without crust, used in the fluid dynamics are determined with applying the limiters to avoid numerical problems when the heat capacity of the crust or surface node becomes very small.

$$h_{k2} = \begin{cases} \min\left[\dfrac{(\bar{\rho}_{s3}^n + \bar{\rho}_{s4}^n) c_{S2}}{\Delta t a_{LCW}}, h_{S2}\right] & \text{with crust} \\ \min\left[\dfrac{\tilde{\bar{\rho}}_{s8}^{n+1} c_{S5}}{\Delta t a_{LCW}}, h_{S5}\right] & \text{without crust} \end{cases}. \tag{5-18}$$

The above equations are the same as the standard model. In the multiple nodalization of the interior node, a change in can wall thickness from the previous time step may change the number of nodes (from $NLCWP$ to $NLCWI$), the node width (from D_{LCWP} to D_{LCWI}) and the node location (from $r_{LCWI,m}^n$ to $\tilde{r}_{LCWI,L}^{n+1}$). This requires a complex rezoning procedure for the specific internal energy. The results are:

$$\tilde{\bar{\rho}}_{LCWI,L}^{n+1} = \tilde{\bar{\rho}}_{S9}^{n+1} \frac{D_{LCWI}}{W_{LCW} - \tilde{\bar{\rho}}_{S8}^{n+1} \upsilon_s / a_{LCW}}, \tag{5-19}$$

$$\tilde{e}_{LCW,L}^{n+1} = \begin{cases} \dfrac{\left[\bar{\rho}_{LCWI,m-1}^n e_{LCWI,m-1}^n \dfrac{r_{LCWI,m-1}^n - \tilde{r}_{LCWI,L-1}^{n+1}}{r_{LCWI,m-1}^n - r_{LCWI,m-2}^n} + \bar{\rho}_{LCWI,m}^n e_{LCWI,m}^n \dfrac{\tilde{r}_{LCWI,L}^{n+1} - r_{LCWI,m-1}^n}{r_{LCWI,m}^n - r_{LCWI,m-1}^n}\right]}{\tilde{\bar{\rho}}_{LCWI,L}^{n+1}} \\ \qquad \text{if } \tilde{r}_{LCWI,L}^{n+1} \le r_{LCWI,NLCWP}^n \\ \dfrac{\left[\bar{\rho}_{LCWI,m}^n e_{LCWI,m}^n \dfrac{r_{LCWI,m}^n - \tilde{r}_{LCWI,L-1}^{n+1}}{r_{LCWI,m}^n - r_{LCWI,m-1}^n} + \bar{\rho}_{S8}^n e_{S5}^n \dfrac{\tilde{r}_{LCWI,L}^{n+1} - r_{LCWI,m}^n}{r_{LCWI,m+1}^n - r_{LCWI,m}^n}\right]}{\tilde{\bar{\rho}}_{LCWI,L}^{n+1}} \\ \qquad \text{if } \tilde{r}_{LCWI,L-1}^{n+1} \le r_{LCWI,NLCWP}^n \le \tilde{r}_{LCWI,L}^{n+1} \\ e_{S5}^n \ \text{ if } r_{LCWI,NLCWP}^n < \tilde{r}_{LCWI,L-1}^{n+1} \end{cases}, \tag{5-20}$$

$$h_{LCWI,L} = \frac{2\kappa_s}{D_{LCWI}}\ ,\text{and} \tag{5-21a}$$

$$h_{(LCWI,L),(LCWI,L-1)} = \frac{h_{LCWI,L-1} h_{LCWI,L}}{h_{LCWI,L-1} + h_{LCWI,L}}. \tag{5-21b}$$

Case 2 and Case 7b (left thick can wall): cylindrical geometry

The treatment is identical for the two cases, in which only one left thick can wall with or without crust is modeled. For the cylindrical geometry for the standard two-node model, rezoning is performed

Since the surface node thickness is always kept to $2\delta_s$, a rezoning operation is performed using the radii of node boundaries and temperature points.

$$r_5 = \sqrt{r_{C0}^2 + (r_{C1}^2 - r_{C0}^2)(\alpha_{S5}^n + \alpha_{S6}^n)} \text{ and } r_4 = r_5 - 2\delta_s\,. \tag{5-22}$$

The macroscopic densities are calculated as

$$\tilde{\bar{\rho}}_{s8}^{n+1} = \frac{1}{v_s}\frac{r_5^2 - r_4^2}{r_{C1}^2 - r_{C0}^2} \text{ and } \tilde{\bar{\rho}}_{s9}^{n+1} = \frac{1}{v_s}\frac{r_4^2 - r_{C0}^2}{r_{C1}^2 - r_{C0}^2}\,. \tag{5-23}$$

The specific internal energies are the same as Eq. (5-20). Where there is no crust, the can wall surface area, heat transfer coefficient of the surface node and the structure-side heat transfer coefficient are:

$$a_{LCW} = \frac{2r_5}{r_{C1}^2 - r_{C0}^2}\,, \tag{5-24a}$$

$$h_{S5} = \frac{\kappa_s}{r_5\, ln(r_5/r_{t5})}\,,\text{ where } r_{t5} = \sqrt{(r_4^2 + r_5^2)/2}\,,\text{and} \tag{5-24b}$$

$$h_{k2} = min\left[\frac{\tilde{\bar{\rho}}_{s8}^{n+1} c_{S5}}{\Delta t a_{LCW}}, h_{S5}\right]. \tag{5-24c}$$

With crust, required equations are:

$$h_{S6} = \frac{\kappa_s}{r_4 \ln(r_4/r_{t4})}\,,\text{where } r_{t4} = \sqrt{(r_4^2 + r_{C0}^2)/2}\,, \tag{5-25a}$$

$$a_{S5,S6} = \frac{2r_4}{r_{C1}^2 - r_{C0}^2} \text{ and } h_{S5,S6} = \frac{1}{r_4[{\kappa_s}^{-1}\ln(r_{r5}/r_4) + {\kappa_s}^{-1}\ln(r_4/r_{t4})]}\,, \tag{5-25b}$$

$$a_{S2,S5} = \frac{2r_5}{r_{C1}^2 - r_{C0}^2} \text{ and } h_{S2,S5} = \frac{1}{r_4[{\kappa_s}^{-1}\ln(r_5/r_{r5}) + {\kappa_s}^{-1}\ln(r_{r6}/r_5)]}\,,\text{and} \tag{5-25c}$$

$$r_6 = \sqrt{r_{C0}^2 + (r_{C1}^2 - r_{C0}^2)(\alpha_{S2}^n + \alpha_{S5}^n + \alpha_{S6}^n)} \text{ and } r_{t6} = \sqrt{(r_5^2 + r_6^2)/2}\,. \tag{5-25d}$$

For the multiple nodalization of the interior node, the macroscopic density and specific internal energy of subdivided node *L* are:

$$\tilde{\bar{\rho}}_{LCWI,L}^{n+1} = \tilde{\bar{\rho}}_{s9}^{n+1}\frac{\tilde{r}_{LCWI,L}^2 - \tilde{r}_{LCWI,L-1}^2}{r_4^2 - r_{C0}^2}\,,\text{and} \tag{5-26}$$

$$\tilde{e}^{n+1}_{LCW,L} = \begin{cases} \dfrac{\left[\bar{\rho}^{n}_{LCWI,m-1} e^{n}_{LCWI,m-1} \dfrac{{r^{n}_{LCWI,m-1}}^{2} - {\tilde{r}^{n+1}_{LCWI,L-1}}^{2}}{{r^{n}_{LCWI,m-1}}^{2} - {r^{n}_{LCWI,m-2}}^{2}} + \bar{\rho}^{n}_{LCWI,m} e^{n}_{LCWI,m} \dfrac{{\tilde{r}^{n+1}_{LCWI,L}}^{2} - {r^{n}_{LCWI,m-1}}^{2}}{{r^{n}_{LCWI,m}}^{2} - {r^{n}_{LCWI,m-1}}^{2}}\right]}{\tilde{\bar{\rho}}^{n+1}_{LCWI,L}} \\ \text{if } \tilde{r}^{n+1}_{LCWI,L} \le r^{n}_{LCWI,NLCWP} \\ \dfrac{\left[\bar{\rho}^{n}_{LCWI,m} e^{n}_{LCWI,m} \dfrac{{r^{n}_{LCWI,m}}^{2} - {\tilde{r}^{n+1}_{LCWI,L-1}}^{2}}{{r^{n}_{LCWI,m}}^{\square} - {r^{n}_{LCWI,m-1}}^{2}} + \bar{\rho}^{n}_{s8} e^{n}_{S5} \dfrac{{\tilde{r}^{n+1}_{LCWI,L}}^{2} - {r^{n}_{LCWI,m}}^{2}}{{r^{n}_{LCWI,m+1}}^{2} - {r^{n}_{LCWI,m}}^{2}}\right]}{\tilde{\bar{\rho}}^{n+1}_{LCWI,L}} \\ \text{if } \tilde{r}^{n+1}_{LCWI,L-1} \le r^{n}_{LCWI,NLCWP} \le \tilde{r}^{n+1}_{LCWI,L} \\ e^{n}_{S5} \text{ if } r^{n}_{LCWI,NLCWP} < \tilde{r}^{n+1}_{LCWI,L-1} \end{cases} . \tag{5-27}$$

The heat transfer coefficients are:

$$h_{LCWI,L} = \frac{\kappa_s}{\tilde{r}^{n+1}_{LCWI,L} \ln\left(\tilde{r}^{n+1}_{LCWI,L} / r_{tLCWI,L}\right)} \text{ , where } r_{tLCWI,L} = \sqrt{\left({\tilde{r}^{n+1}_{LCWI,L}}^{2} + {\tilde{r}^{n+1}_{LCWI,L-1}}^{2}\right)/2} \, , \tag{5-28a}$$

$$h_{(LCWI,L),(LCWI,L+1)} = \frac{1}{\tilde{r}^{n+1}_{LCWI,L}\left[\kappa_s^{-1}\, ln\left(r_{tLCWI,L+1}/\tilde{r}^{n+1}_{LCWI,L}\right) + \kappa_s^{-1}\, ln\left(\tilde{r}^{n+1}_{LCWI,L}/r_{tLCWI,L}\right)\right]} . \tag{5-28b}$$

Case 5 and Case 7d (right thick can wall)

The treatment is the same as left thick can wall described above, except for the subscripts of the symbols are replaced by those representing the right can wall. Hence no repetition seems necessary.

Case 8c (thick can wall without crust): slab geometry

A part on the interior node is taken to the adjacent cell to create a new surface node with the $2\delta_s$ thickness. The thickness of the interior node is reduced by $2\delta_s$ and rezoned. When the macroscopic density of can wall is transferred to the adjacent cell, a volume ratio of the two cells is applied to conserve can wall mass. For the standard two-node representation in the slab geometry, the updated masses and energies for the left can wall are

$$\tilde{\bar{\rho}}^{n+1}_{s8}(ij+1) = \frac{2\delta_s}{W_{LCW}}\left[\bar{\rho}^{n}_{s8}(ij+1) + \bar{\rho}^{n}_{s9}(ij+1) + \bar{\rho}^{n}_{s10}(ij)\frac{V_{ij}}{V_{ij+1}}\right] \tag{5-29}$$

$$\tilde{\bar{\rho}}^{n+1}_{s10}(ij) = \frac{2\delta_s}{W_{LCW}}\left[\bar{\rho}^{n}_{s8}(ij+1)\frac{V_{ij+1}}{V_{ij}} + \bar{\rho}^{n}_{s9}(ij+1)\frac{V_{ij+1}}{V_{ij}} + \bar{\rho}^{n}_{s10}(ij)\right] \tag{5-30}$$

$$\tilde{\bar{\rho}}^{n+1}_{s9}(ij+1) = \bar{\rho}^{n}_{s8}(ij+1) + \bar{\rho}^{n}_{s9}(ij+1) + \bar{\rho}^{n}_{s10}(ij)\frac{V_{ij}}{V_{ij+1}} - \tilde{\bar{\rho}}^{n+1}_{s8}(ij+1) - \bar{\rho}^{n}_{s10}(ij)\frac{V_{ij}}{V_{ij+1}} \tag{5-31}$$

$$\tilde{e}^{n+1}_{S5}(ij) = \begin{cases} e^{n}_{S5}(ij+1) & \tilde{\bar{\rho}}^{n+1}_{s8}(ij+1) < \bar{\rho}^{n}_{s8}(ij+1) \\ \dfrac{\bar{\rho}^{n}_{s8}(ij+1) e^{n}_{S5}(ij+1) + \left[\tilde{\bar{\rho}}^{n+1}_{s8}(ij+1) - \bar{\rho}^{n}_{s8}(ij+1)\right] e^{n}_{S6}(ij+1)}{\tilde{\bar{\rho}}^{n+1}_{s8}(ij)} & \tilde{\bar{\rho}}^{n+1}_{s8}(ij+1) \ge \bar{\rho}^{n}_{s8}(ij+1) \end{cases} \tag{5-32}$$

$$\tilde{e}_{S7}^{n+1}(ij) = \begin{cases} e_{S7}^{n}(ij) & \tilde{\bar{\rho}}_{s10}^{n+1}(ij) < \bar{\rho}_{s10}^{n}(ij) \\ \dfrac{\bar{\rho}_{s10}^{n}(ij) e_{S7}^{n}(ij) + [\tilde{\bar{\rho}}_{s10}^{n+1}(ij) - \bar{\rho}_{s10}^{n}(ij)] e_{S6}^{n}(ij+1)}{\tilde{\bar{\rho}}_{s10}^{n+1}(ij)} & \tilde{\bar{\rho}}_{s10}^{n+1}(ij) \geq \bar{\rho}_{s10}^{n}(ij) \end{cases}, \text{and} \tag{5-33}$$

$$\begin{aligned} &\tilde{e}_{S6}^{n+1}(ij+1) \\ &= \left\{ \begin{array}{c} e_{S6}^{n}(ij+1) \\ \tilde{\bar{\rho}}_{s8}^{n+1}(ij+1) \geq \bar{\rho}_{s8}^{n}(ij+1) \text{ and } \tilde{\bar{\rho}}_{s10}^{n+1}(ij) \geq \bar{\rho}_{s10}^{n}(ij) \\ \dfrac{\bar{\rho}_{s9}^{n}(ij+1) e_{S6}^{n}(ij+1) - [\tilde{\bar{\rho}}_{s8}^{n+1}(ij+1) - \bar{\rho}_{s8}^{n}(ij+1)] e_{S6}^{n}(ij+1) - [\tilde{\bar{\rho}}_{s10}^{n+1}(ij) - \bar{\rho}_{s10}^{n}(ij)] e_{S7}^{n}(ij)}{\tilde{\bar{\rho}}_{s9}^{n+1}(ij+1)} \\ \tilde{\bar{\rho}}_{s8}^{n+1}(ij+1) \geq \bar{\rho}_{s8}^{n}(ij+1) \text{ and } \tilde{\bar{\rho}}_{s10}^{n+1}(ij) < \bar{\rho}_{s10}^{n}(ij) \\ \dfrac{\bar{\rho}_{s9}^{n}(ij+1) e_{S6}^{n}(ij+1) - [\tilde{\bar{\rho}}_{s8}^{n+1}(ij+1) - \bar{\rho}_{s8}^{n}(ij+1)] e_{S5}^{n}(ij+1) - [\tilde{\bar{\rho}}_{s10}^{n+1}(ij) - \bar{\rho}_{s10}^{n}(ij)] e_{S6}^{n}(ij+1)}{\tilde{\bar{\rho}}_{s9}^{n+1}(ij+1)} \\ \tilde{\bar{\rho}}_{s8}^{n+1}(ij+1) < \bar{\rho}_{s8}^{n}(ij+1) \text{ and } \tilde{\bar{\rho}}_{s10}^{n+1}(ij) \geq \bar{\rho}_{s10}^{n}(ij) \\ \dfrac{\bar{\rho}_{s9}^{n}(ij+1) e_{S6}^{n}(ij+1) - [\tilde{\bar{\rho}}_{s8}^{n+1}(ij+1) - \bar{\rho}_{s8}^{n}(ij+1)] e_{S5}^{n}(ij+1) - [\tilde{\bar{\rho}}_{s10}^{n+1}(ij) - \bar{\rho}_{s10}^{n}(ij)] e_{S7}^{n}(ij)}{\tilde{\bar{\rho}}_{s9}^{n+1}(ij+1)} \\ \tilde{\bar{\rho}}_{s8}^{n+1}(ij+1) < \bar{\rho}_{s8}^{n}(ij+1) \; and \; \tilde{\bar{\rho}}_{s10}^{n+1}(ij) < \bar{\rho}_{s10}^{n}(ij) \end{array} \right. . \end{aligned} \tag{5-34}$$

The heat transfer areas and coefficients, and the structure-side heat transfer coefficients are calculated as follows.

$$a_{LCW}(ij+1) = a_{LCW}^{i}(ij+1) \text{ for } S5, \text{ and}, a_{RCW}(ij) = a_{LCW}^{i}(ij+1) \frac{V_{ij+1}}{V_{ij}} \text{ for } S7, \tag{5-35a}$$

$$h_{S5}(ij+1) = \frac{2\kappa_s a_{LCW}(ij+1)}{\tilde{\alpha}_{S5}^{n+1}(ij+1)} \text{ and } h_{S7}(ij) = \frac{2\kappa_s a_{RCW}(ij)}{\tilde{\alpha}_{S7}^{n+1}(ij)}, \tag{5-35b}$$

$$h_{k2}(ij+1) = \min\left[\frac{\tilde{\bar{\rho}}_{s8}^{n+1}(ij+1) c_{S5}(ij+1)}{\Delta t a_{LCW}(ij+1)}, h_{S5}(ij+1)\right], \tag{5-35c}$$

$$h_{k3}(ij) = \min\left[\frac{\tilde{\bar{\rho}}_{s10}^{n+1}(ij) c_{S7}(ij)}{\Delta t a_{RCW}(ij)}, h_{S7}(ij)\right], \tag{5-35d}$$

$$h_{S5,S6}(ij+1) = \frac{h_{S5}(ij+1) h_{S6}(ij+1)}{h_{S5}(ij+1) + h_{S6}(ij+1)}, \text{and} \tag{5-35e}$$

$$(ha)_{S7(ij),S6(ij+1)} = \frac{a_{LCW}(ij+1) h_{S6}(ij+1) h_{S7}(ij)}{h_{S6}(ij+1) + h_{S7}(ij)}. \tag{5-35f}$$

The above equations for the left can wall are for the standard model, and the right can wall can be treated sin the same procedure.

In the multiple nodalization of the interior node, a change in can wall thickness from the previous time step may change the number of nodes (from $NLCWP$ to $NLCWI$), the node width (from D_{LCWP} to D_{LCWI}) and the node location (from $r_{LCWI,m}^{n}$ to $\tilde{r}_{LCWI,L}^{n+1}$). This requires a complex rezoning procedure for the specific internal energy. The results are:

$$\tilde{\bar{\rho}}_{LCWI,L}^{n+1}(ij+1)=\tilde{\bar{\rho}}_{s9}^{n+1}(ij+1)\frac{D_{LCWI}(ij+1)}{W_{LCW}-\tilde{\bar{\rho}}_{s8}^{n+1}(ij+1)\nu_s/a_{LCW}-\tilde{\bar{\rho}}_{s10}^{n+1}(ij)\dfrac{V_{ij}}{V_{ij+1}}\upsilon_s/a_{RCW}}, \tag{5-36a}$$

$$\tilde{e}_{LCW,L}^{n+1}=\begin{cases} e_{S7}^{n}(ij) \\ \text{if } \tilde{r}_{LCWI,L}^{n+1}\le r_{LCWI,1}^{n}\left(=\bar{\rho}_{s10}^{n}(ij)\dfrac{V_{ij}}{V_{ij+1}}\nu_s/a_{RCW}\right) \\ \dfrac{\begin{bmatrix}\bar{\rho}_{s10}^{n}(ij)\dfrac{V_{ij}}{V_{ij+1}}e_{S7}^{n}(ij)\dfrac{r_{LCWI,1}^{n}-\tilde{r}_{LCWI,L}^{n+1}}{r_{LCWI,1}^{n}} \\ +\bar{\rho}_{LCWI,1}^{n}(ij+1)e_{LCWI,1}^{n}(ij+1)\dfrac{\tilde{r}_{LCWI,L+1}^{n+1}-r_{LCWI,1}^{n}}{r_{LCWI,2}^{n}-r_{LCWI,1}^{n}}\end{bmatrix}}{\tilde{\bar{\rho}}_{LCWI,L}^{n+1}(ij+1)} \\ \text{if } r_{LCWI,1}^{n}<\tilde{r}_{LCWI,L+1}^{n+1}\le r_{LCWI,2}^{n} \\ \dfrac{\begin{bmatrix}\bar{\rho}_{LCWI,m-1}^{n}(ij+1)e_{LCWI,m-1}^{n}(ij+1)\dfrac{r_{LCWI,m}^{n}-\tilde{r}_{LCWI,L}^{n+1}}{r_{LCWI,m}^{n}-r_{LCWI,m-1}^{n}} \\ +\bar{\rho}_{LCWI,m}^{n}(ij+1)e_{LCWI,m}^{n}(ij+1)\dfrac{\tilde{r}_{LCWI,L+1}^{n+1}-r_{LCWI,m}^{n}}{r_{LCWI,m+1}^{n}-r_{LCWI,m}^{n}}\end{bmatrix}}{\tilde{\bar{\rho}}_{LCWI,L}^{n+1}(ij+1)} \\ \text{if } r_{LCWI,2}^{n}<\tilde{r}_{LCWI,L+1}^{n+1}\le r_{LCWI,NLCWP(ij+1)+1}^{n} \\ \dfrac{\begin{bmatrix}\bar{\rho}_{LCWI,m-1}^{n}(ij+1)e_{LCWI,m-1}^{n}(ij+1)\dfrac{r_{LCWI,m}^{n}-\tilde{r}_{LCWI,L}^{n+1}}{r_{LCWI,m}^{n}-r_{LCWI,m-1}^{n}} \\ +\bar{\rho}_{LCWI,m}^{n}(ij+1)e_{LCWI,m}^{n}(ij+1)\dfrac{\tilde{r}_{LCWI,L+1}^{n+1}-r_{LCWI,m}^{n}}{r_{LCWI,m+1}^{n}-r_{LCWI,m}^{n}}\end{bmatrix}}{\tilde{\bar{\rho}}_{LCWI,L}^{n+1}(ij+1)} \\ \text{if } \tilde{r}_{LCWI,L}^{n+1}\le r_{LCWI,NLCWP(ij+1)+1}^{n}<\tilde{r}_{LCWI,L+1}^{n+1} \\ e_{S5}^{n}(ij+1) \\ \text{if } r_{LCWI,NLCWP(ij+1)+1}^{n}<\tilde{r}_{LCWI,L}^{n+1} \end{cases}, \tag{5-36b}$$

$$h_{LCWI,L}(ij+1)=\frac{2\kappa_s(ij+1)}{D_{LCWI}(ij+1)}\text{, and} \tag{5-36c}$$

$$h_{(LCWI,L),(LCWI,L-1)}(ij+1)=\frac{h_{LCWI,L-1}(ij+1)h_{LCWI,L}(ij+1)}{h_{LCWI,L-1}(ij+1)+h_{LCWI,L}(ij+1)}. \tag{5-36d}$$

Case 8c (thick can wall without crust): cylindrical geometry

For the standard two-node representation, the macroscopic densities of can wall components are expressed as:

$$\tilde{\bar{\rho}}_{s8}^{n+1}(ij+1)=\frac{1}{\upsilon_s}\frac{r_5^2-r_4^2}{r_{C2}^2-r_{C1}^2}, \tag{5-37a}$$

$$\tilde{\bar{\rho}}_{s10}^{n+1}(ij)=\frac{1}{\upsilon_s}\frac{r_2^2-r_{C1}^2}{r_{C2}^2-r_{C1}^2}\frac{V_{ij+1}}{V_{ij}}\text{, and} \tag{5-37b}$$

$$\tilde{\bar{\rho}}_{S9}^{n+1}(ij+1) = \frac{1}{v_S}\frac{r_4^2 - r_2^2}{r_{C2}^2 - r_{C1}^2}\,, \tag{5-37c}$$

where the radii r_5, r_4 and r_2 are defined by

$$r_5 = r_{C1} - W_{LCW}\ ,\ r_4 = r_5 - 2\delta_S \ \text{ and } r_2 = r_{C1} + 2\delta_S\,.$$

The heat transfer areas and coefficients required are calculated as

$$a_{LCW}(ij+1) = \frac{2r_5}{r_{C2}^2 - r_{C1}^2}\ \text{ for } S5,\ \text{ and } a_{RCW}(ij) = \frac{2r_{C1}}{r_{C1}^2 - r_{C0}^2}\ \text{ for } S7\text{, and} \tag{5-38a}$$

$$h_{S5}(ij+1) = \frac{\kappa_S}{r_5\, ln(r_5/r_{t5})}\ \text{ and }\ h_{S7}(ij) = \frac{\kappa_S}{r_{C1}\, ln(r_{C1}/r_{t2})}\,, \tag{5-38b}$$

where the radii r_{r5} and r_{r2} are defined by

$$r_{t5} = \sqrt{(r_5^2 + r_4^2)/2}\ \text{ and } r_{t2} = \sqrt{(r_{C1}^2 + r_2^2)/2}\,.$$

The remaining heat transfer areas and coefficients are:

$$h_{S5,S6}(ij+1) = \frac{\kappa_S}{r_4[ln(r_4/r_{t4}) + ln(r_{t5}/r_4)]}\ \text{, where } r_{t4} = \sqrt{(r_4^2 + r_2^2)/2}\ , \tag{5-38c}$$

$$a_{S7(ij),S6(ij+1)}(ij+1) = \frac{2r_2}{r_{C2}^2 - r_{C1}^2}\,, \tag{5-38d}$$

$$a_{S5(ij+1),S6(ij+1)}(ij+1) = \frac{2r_4}{r_{C2}^2 - r_{C1}^2}\ \text{, and} \tag{5-38e}$$

$$(ha)_{S7(ij),S6(ij+1)} = \frac{a_{S7(ij),S6(ij+1)}}{r_2[\kappa_S^{-1}\, ln(r_2/r_{t2}) + \kappa_S^{-1}\, ln(r_{t4}/r_2)]}\,. \tag{5-38f}$$

For the multiple nodalization of the interior node, the macroscopic density and specific internal energy of subdivided node *L* are:

$$\tilde{\bar{\rho}}_{LCWI,L}^{n+1}(ij+1) = \tilde{\bar{\rho}}_{S9}^{n+1}(ij+1)\frac{{r_{LCWI,L+1}^{n+1}}^2 - {r_{LCWI,L}^{n+1}}^2}{r_4^2 - r_2^2}\ \text{, and} \tag{5-39a}$$

$$\tilde{e}_{LCW,L}^{n+1} = \begin{cases} e_{S7}^{n}(ij) \\ \quad \text{if } \tilde{r}_{LCWI,L+1}^{n+1} \le r_{LCWI,1}^{n} \left(= \bar{\rho}_{s10}^{n}(ij) \dfrac{V_{ij}}{V_{ij+1}} \upsilon_s / a_{RCW} \right) \\ \dfrac{\left[\begin{aligned} & \bar{\rho}_{s10}^{n}(ij) \dfrac{V_{ij}}{V_{ij+1}} e_{S7}^{n}(ij) \dfrac{{r_{LCWI,1}^{n}}^{2} - {\tilde{r}_{LCWI,L}^{n+1}}^{2}}{{r_{LCWI,1}^{n}}^{2} - r_{C1}^{2}} \\ & + \bar{\rho}_{LCWI,1}^{n}(ij+1) e_{LCWI,1}^{n}(ij+1) \dfrac{{\tilde{r}_{LCWI,L+1}^{n+1}}^{2} - {r_{LCWI,1}^{n}}^{2}}{{r_{LCWI,2}^{n}}^{2} - {r_{LCWI,1}^{n}}^{2}} \end{aligned} \right]}{\tilde{\bar{\rho}}_{LCWI,L}^{n+1}(ij+1)} \\ \quad \text{if } r_{LCWI,1}^{n} < \tilde{r}_{LCWI,L+1}^{n+1} \le r_{LCWI,2}^{n} \\ \dfrac{\left[\begin{aligned} & \bar{\rho}_{LCWI,m-1}^{n}(ij+1) e_{LCWI,m-1}^{n}(ij+1) \dfrac{{r_{LCWI,m}^{n}}^{2} - {\tilde{r}_{LCWI,L}^{n+1}}^{2}}{{r_{LCWI,m}^{n}}^{2} - {r_{LCWI,m-1}^{n}}^{2}} \\ & + \bar{\rho}_{LCWI,m}^{n}(ij+1) e_{LCWI,m}^{n}(ij+1) \dfrac{{\tilde{r}_{LCWI,L+1}^{n+1}}^{2} - {r_{LCWI,m}^{n}}^{2}}{{r_{LCWI,m+1}^{n}}^{2} - {r_{LCWI,m}^{n}}^{2}} \end{aligned} \right]}{\tilde{\bar{\rho}}_{LCWI,L}^{n+1}(ij+1)} \\ \quad \text{if } r_{LCWI,2}^{n} < \tilde{r}_{LCWI,L+1}^{n+1} \le r_{LCWI,NLCWP(ij+1)+1}^{n} \\ \dfrac{\left[\begin{aligned} & \bar{\rho}_{LCWI,m-1}^{n}(ij+1) e_{LCWI,m-1}^{n}(ij+1) \dfrac{{r_{LCWI,m}^{n}}^{2} - {\tilde{r}_{LCWI,L}^{n+1}}^{2}}{{r_{LCWI,m}^{n}}^{2} - {r_{LCWI,m-1}^{n}}^{2}} \\ & + \bar{\rho}_{s8}^{n}(ij+1) e_{S5}^{n}(ij+1) \dfrac{{\tilde{r}_{LCWI,L+1}^{n+1}}^{2} - {r_{LCWI,m}^{n}}^{2}}{{r_{LCWI,m+1}^{n}}^{2} - {r_{LCWI,m}^{n}}^{2}} \end{aligned} \right]}{\tilde{\bar{\rho}}_{LCWI,L}^{n+1}(ij+1)} \\ \quad \text{if } \tilde{r}_{LCWI,L}^{n+1} \le r_{LCWI,NLCWP(ij+1)+1}^{n} < \tilde{r}_{LCWI,L+1}^{n+1} \\ e_{S5}^{n}(ij+1) \\ \quad \text{if } r_{LCWI,NLCWP(ij+1)+1}^{n} < \tilde{r}_{LCWI,L}^{n+1} \end{cases}. \tag{5-39b}$$

The heat transfer coefficients are:

$$h_{LCWI,L}(ij+1) = \frac{\kappa_s(ij+1)}{\tilde{r}_{LCWI,L+1}^{n+1} \, ln\left(\tilde{r}_{LCWI,L+1}^{n+1} / r_{tLCWI,L}\right)} \text{ , where } r_{tLCWI,L} = \sqrt{\left({\tilde{r}_{LCWI,L+1}^{n+1}}^{2} + {\tilde{r}_{LCWI,L}^{n+1}}^{2}\right)/2}\,, \tag{5-40a}$$

$$h_{(LCWI,L),(LCWI,L+1)} = \frac{1}{\tilde{r}_{LCWI,L+1}^{n+1}\left[\kappa_s^{-1} \, ln\left(r_{tLCWI,L+1} / \tilde{r}_{LCWI,L+1}^{n+1}\right) + \kappa_s^{-1} \, ln\left(\tilde{r}_{LCWI,L+1}^{n+1} / r_{tLCWI,L}\right)\right]}. \tag{5-40b}$$

Case 8d (thick can wall with crust)

The only difference from Case 8c is the presence of crust. The treatment of multiple nodalization of the interior node is the same as Case 8c. The formulation of the crust related heat transfer coefficients is unchanged from the standard two-node representation, and hence it is not repeated here.

5.4.4. Multi-node can wall heat transfer model

The basic model and solution method are the same as the standard two-node model, except that the number of temperature nodes is increased when the multiple nodalization is used for the interior node. Only the model for the interior node is described below, since overall model covering other configuration cases are documented already in the structure model report[15)]. When the interior node is subdivided into $NLCWI$ nodes (for left can wall), the energy equation for a subdivided node L is expressed as:

$$\frac{\partial \bar{\rho}_{LCW,L} e_{LCW,L}}{\partial t} = -a_{LCW} h_{(LCW,L),(LCW,L+1)} \left(\tilde{T}^{n+1}_{LCW,L} - \tilde{T}^{n+1}_{LCW,L+1} \right) \text{ for L} = 1 \, , \tag{5-41a}$$

$$\begin{aligned} \frac{\partial \bar{\rho}_{LCW,L} e_{LCW,L}}{\partial t} &= a_{LCW} h_{(LCW,L-1),(LCW,L)} \left(\tilde{T}^{n+1}_{LCW,L-1} - \tilde{T}^{n+1}_{LCW,L} \right) \\ &\quad - a_{LCW} h_{(LCW,L),(LCW,L+1)} \left(\tilde{T}^{n+1}_{LCW,L} - \tilde{T}^{n+1}_{LCW,L+1} \right) \text{ for L} = 2 \sim NLCWI \text{ , and} \end{aligned} \tag{5-41b}$$

$$\frac{\partial \bar{\rho}_{LCW,L} e_{LCW,L}}{\partial t} = a_{LCW} h_{(LCW,L-1),(LCW,L)} \left(\tilde{T}^{n+1}_{LCW,L-1} - \tilde{T}^{n+1}_{LCW,L} \right) \text{ for L} = NLCWI + 1 \, . \tag{5-41c}$$

where the node $NLCWI + 1$ corresponds to the surface node.

The end-of-time-step temperatures appearing on the right side of equations are expanded into a Taylor series as

$$\tilde{T}^{n+1}_{L} = T^{n}_{L} + \left(\frac{\partial T_L}{\partial e_L} \right)^{n} \Delta e_L \, . \tag{5-42}$$

By substituting Eq. (5-37) to Eq. (5-36), we obtain the expression for the L-th node.

$$\begin{aligned} &-\left[(ah)_{L-1,L} \Delta t \frac{\partial T_{L-1}}{\partial e_{L-1}} \right] \Delta e_{L-1} + \left[\bar{\rho}_L + \left\{ (ah)_{L-1,L} + (ah)_{L,L+1} \right\} \Delta t \frac{\partial T_L}{\partial e_L} \right] \Delta e_L \\ &\qquad + \left[(ah)_{L,L+1} \Delta t \frac{\partial T_{L+1}}{\partial e_{L+1}} \right] \Delta e_{L+1} \\ &\qquad = \Delta t \left[(ah)_{L-1,L} (T^n_{L-1} - T^n_L) + (ah)_{L,L+1} (T^n_{L+1} - T^n_L) \right] . \end{aligned} \tag{5-43}$$

This is a set of $NLCWI$ linear equations and is solved using the Newton's method, together with the equations for crust nodes, if present, and the surface node that has been set over to an adjacent cell (in configuration cases 8c and 8d). Finally, the specific internal energy is simply updated explicitly.

$$\tilde{e}^{n+1}_L = e^n_L + \Delta e_L \, . \tag{5-44}$$

5.5. Can Wall and Crust Fuel Breakup Model

5.5.1. Background

The can wall and crust breakup model has been documented in the structure model report[15)], and is briefly explained in **Section 5.3.7**. The original breakup model is, more or less, based on thermal criteria such as a melt fraction and temperature of the can wall. Other mechanisms of can wall breakup or failure have been later added as optional models controlled by input specifications. This section describes all the modes of can wall and crust fuel failure and breakup in detail and replaces **Section 5.3.7**.

In the original model in SIMMER-III/SIMMER-IV, a criterion to predict breakup of can wall is based on the melt fraction of can wall interior node. Although the structural dynamics of can wall is not modeled in the code, a consideration is made on the structural integrity at an elevated temperature range close to the melting point of steel. The terminology of “breakup” means the structure is completely disintegrated and its mass is transferred to either liquid or solid particles, while “failure” means the integrity of the structure is lost but its mass remains as structure without mass transfer. The modes of structure breakup and failure as modeled in SIMMER-III are listed below, where NC’s denote the breakup or failure ID numbers. For SIMMER-IV, the same modeling approach is used for the front/back can walls.

- Breakup of right/left thin can wall from adjacent cell (NC1/NC2)
- Breakup of cladding (NC3)
- Breakup of left/right can wall (NC4/NC5)
- Mechanical failure of left/right can wall (NC6/NC7)
- Mechanical breakup of left/right can wall (NC8/NC9)
- Breakup of suspended left/right can wall (NC8B/NC9B)
- Breakup of left/right crust fuel

Whether each model is made active or not is controlled by input option flags, as listed in **Table 5-2**. Some of the models are redundant and seem duplicating; for example, NC1/NC2 and NC8/NC9 both model the breakup of thin can wall. However, this duplication is left untouched, such that the user can flexibly specify input options depending on application problems. It is noted that since a thin can wall without crust is broken up, the can wall structure configuration Case 8a is no longer applicable.

The concept and models of these modes are described in detail in the following section, including the breakup of cladding for completeness.

5.5.2. Breakup of thin can wall in adjacent cell (NC1/NC2)

This is a special case treatment with a single thin can wall at a mesh-cell boundary. When a can wall is missing at the left boundary of cell *IJ* and the right can wall in cell *IJ*-1 becomes thin without crust, the heat and mass transfer model can no longer calculate energy transfer with the remaining thin can wall in the adjacent cell. This may generate an unphysical situation that the melting of the can wall is suddenly ceased when it becomes thin. Assuming a thin can wall is weak and cannot stay intact for a long time, it is unconditionally broken up and the mass is transferred to solid steel particles. This mode of breakup applies only to a thin coupled can wall, without crust, in an adjacent cell. For the left mesh cell boundary of cell *IJ* (Case NC1) where only a thin can wall is present in cell *IJ*-1 without crust, the mass is transferred to steel particles instantaneously in cell *IJ*-1.

$$\tilde{\bar{\rho}}_{l7}^{n+1} = \bar{\rho}_{l7}^{n} + \bar{\rho}_{s11}^{n} \,, \qquad (5\text{-}45a)$$

$$\tilde{\bar{\rho}}_{s11}^{n+1} = 0 \,, \qquad (5\text{-}45b)$$

$$\tilde{e}_{L5}^{n+1} = \frac{\bar{\rho}_{l7}^{n} e_{L5}^{n} + \bar{\rho}_{s11}^{n} e_{S8}^{n}}{\tilde{\bar{\rho}}_{l7}^{n+1}} \text{ , and} \tag{5-45c}$$

$$\tilde{e}_{S8}^{n+1} = e_{S,2}^{0} \text{ .} \tag{5-45d}$$

The same treatment is implemented at the right cell boundary of cell IJ (Case NC2), and the thin can wall interior mass in cell *IJ*+1 is transferred to solid steel particles.

5.5.3. Breakup of cladding (NC3)

The criterion to predict breakup of cladding is based on a thermal condition, that is the melt fraction of cladding.

$$\frac{e_{S4} - e_{Sol,2}}{e_{Liq,2} - e_{Sol,2}} \geq f_c^i \text{ ,} \tag{5-46}$$

where f_c^i is an input threshold melt fraction. Molten cladding mass is transferred to liquid steel at the liquidus energy as follows:

$$f_c = \frac{e_{S4} - e_{Sol,2}}{e_{Liq,2} - e_{Sol,2}} \text{ ,} \tag{5-47a}$$

$$\tilde{\bar{\rho}}_{l3}^{n+1} = \bar{\rho}_{l3}^{n} + f_c \bar{\rho}_{s7}^{n} \text{ , and} \tag{5-47b}$$

$$\tilde{e}_{L2}^{n+1} = \frac{\bar{\rho}_{l3}^{n} e_{L2}^{n} + f_c \bar{\rho}_{s7}^{n} e_{Liq,2}}{\tilde{\bar{\rho}}_{l3}^{n+1}} \text{ .} \tag{5-47c}$$

The remaining solid mass is transferred to the liquid field as steel particles or stays as cladding at the solidus energy. That is

$$\tilde{\bar{\rho}}_{l7}^{n+1} = \bar{\rho}_{l7}^{n} + (1 - f_c)(1 - X_{clad}) \bar{\rho}_{s7}^{n} \text{ ,} \tag{5-48a}$$

$$\tilde{e}_{L5}^{n+1} = \frac{\bar{\rho}_{l7}^{n} e_{L5}^{n} + (1 - f_c)(1 - X_{clad}) \bar{\rho}_{s7}^{n} e_{Sol,2}}{\tilde{\bar{\rho}}_{l7}^{n+1}} \text{ ,} \tag{5-48b}$$

$$\tilde{\bar{\rho}}_{s7}^{n+1} = \bar{\rho}_{c}^{n} - \tilde{\bar{\rho}}_{l3}^{n+1} - \tilde{\bar{\rho}}_{l7}^{n+1} \text{ , and} \tag{5-48c}$$

$$\tilde{e}_{S4}^{n+1} = e_{Sol,2} \text{ .} \tag{5-48d}$$

where X_{clad} is an input fraction of the solid mass that is left as cladding at the solidus energy.

An optional criterion for cladding breakup is the input threshold temperature, reflecting the fact that the structural strength of cladding is significantly reduced at a higher temperature range. The criterion is

$$T_{S4} > T_{clad,fail} \text{ .} \tag{5-49}$$

The cladding mass is transferred to solid steel particles.

$$\tilde{\bar{\rho}}_{l7}^{n+1} = \bar{\rho}_{l7}^{n} + \bar{\rho}_{s7}^{n} \text{ ,} \tag{5-50a}$$

$$\tilde{e}_{L5}^{n+1} = \frac{\bar{\rho}_{l7}^{n} e_{L5}^{n} + \bar{\rho}_{s7}^{n} e_{S4}^{n}}{\tilde{\bar{\rho}}_{l7}^{n+1}} , \tag{5-50b}$$

$$\tilde{\bar{\rho}}_{s7}^{n+1} = 0 \text{ , and} \tag{5-50c}$$

$$\tilde{e}_{S4}^{n+1} = e_{S,2}^{0} . \tag{5-50d}$$

5.5.4. Breakup of can wall (NC4/NC5)

This is an original SIMMER-III model. The criterion to predict breakup of can wall is based on a thermal condition, that is the melt fraction of a can wall interior node.

$$\frac{e_{SM} - e_{Sol,2}}{e_{Liq,2} - e_{Sol,2}} \geq f_{CW}^{i} \quad \text{for } M = 6 \text{ or } 8 , \tag{5-51}$$

where f_{CW}^{i} is an input threshold melt fraction. Molten can-wall mass is transferred to liquid steel at the liquidus energy as follows:

$$f_{CW} = \frac{e_{SM} - e_{Sol,2}}{e_{Liq,2} - e_{Sol,2}} , \tag{5-52a}$$

$$\tilde{\bar{\rho}}_{l3}^{n+1} = \bar{\rho}_{l3}^{n} + f_{CW} \bar{\rho}_{sm}^{n} \quad \text{for } m = 9 \text{ or } 11 \text{ , and} \tag{5-52b}$$

$$\tilde{e}_{L2}^{n+1} = \frac{\bar{\rho}_{l3}^{n} e_{L2}^{n} + f_{CW} \bar{\rho}_{sm}^{n} e_{Liq,2}}{\tilde{\bar{\rho}}_{l3}^{n+1}} . \tag{5-52c}$$

The remaining solid mass is transferred to the liquid field as steel particles or stays as a can wall at the solidus energy. That is

$$\tilde{\bar{\rho}}_{l7}^{n+1} = \bar{\rho}_{l7}^{n} + (1 - f_{CW})(1 - X_{CW}) \bar{\rho}_{sm}^{n} , \tag{5-53a}$$

$$\tilde{e}_{L5}^{n+1} = \frac{\bar{\rho}_{l7}^{n} e_{L5}^{n} + (1 - f_{CW})(1 - X_{CW}) \bar{\rho}_{sm}^{n} e_{Sol,2}}{\tilde{\bar{\rho}}_{l7}^{n+1}} , \tag{5-53b}$$

$$\tilde{\bar{\rho}}_{sm}^{n+1} = \bar{\rho}_{sm}^{n} - \tilde{\bar{\rho}}_{l3}^{n+1} - \tilde{\bar{\rho}}_{l7}^{n+1} \text{ , and} \tag{5-53c}$$

$$\tilde{e}_{SM}^{n+1} = e_{Sol,2} , \tag{5-53d}$$

where X_{CW} is an input fraction of the solid mass that is left as the can wall interior at the solidus energy.

Upon breakup of a thick can wall interior node, the accompanying surface node is assumed to break up simultaneous, since it cannot exist without its interior. When a single thick can wall that couples two adjacent cells breaks up, a special treatment is necessary for the surface node set over from the adjacent donor cell containing the interior node. The mass of this surface node being transferred to steel particles must be returned back to the donor cell; otherwise, the volume fractions of steel in the two cells cannot be conserved. It is noted that this tricky procedure of can wall surface node set-over is to enable the heat and mass transfer calculations in the acceptor cell and thereby to thermally couple the two cells, but its volume is not transferred (See the definition of the structure volume fraction in Eq. (5-7)). When the surface node in cell *IJ*-1 breaks up and is transferred to steel particles in cell *IJ*, for example in case NC4, the macroscopic density of steel particles being transferred must be multiplied by the ratio of cell volumes to conserve steel mass. Although this special-case treatment was implemented only recently as an input option, it must be always used.

5.5.5. Mechanical failure of can wall (NC6/NC7)

Two additional mechanisms have been developed in consideration of mechanical strength of a can wall structure to simulate an early can wall failure, which results in crack formation that allows lateral (radial) fluid motion. There is no mass transfer in these mechanisms. First, when the can wall becomes thinner than an input threshold value, it is assumed that the can wall structure can no longer stay intact. Namely, the can wall failure is predicted when the following condition is satisfied.

$$W_{CW} < W_{CW,fail}\,, \tag{5-54}$$

where $W_{CW.fail}$ is an input threshold of can-wall failure thickness. The mode of failure is crack formation and no mass transfer to the liquid field takes place until a thermal breakup condition is met.

Second, the can wall failure is modeled based on the thermal condition. Structural strength of steel decreases with increasing temperature in general and becomes zero at the solidus energy. It is therefore assumed that the structural integrity of the can wall is practically lost at high temperature and the can wall failure is predicted when the can wall interior temperature exceed an input threshold temperature $T_{CW,fail}$.

$$T_{Sm} > T_{CW,fail}\,. \tag{5-55}$$

The mode of failure is crack formation as well. Even though the can wall mass remains unchanged, lateral fluid motion is allowed through a crack or hole in these failure modes and the orifice pressure drop is applied to the lateral fluid flow.

5.5.6. Mechanical breakup of can wall (NC8/NC9)

In general, the structural strength of steel can wall decreases with increasing its temperature, and will be practically lost at an elevated temperature range close to the solidus point. In addition, when the can wall becomes thin and without crust, it is assumed the structural strength is practically lost. The latter criterion is similar to NC1/NC2, in which a thin can wall in an adjacent cell is broken up; but NC8/NC9 is applied to cell *IJ*. The criterion for mechanical breakup of left can wall is:

$$T_{S6} > T_{CW,mech} \text{ or [the fluid is in contact directly with left can wall interior]}\,, \tag{5-56}$$

where $T_{CW,mech}$ is the input breakup temperature (default value: 1513 K). The latter means the left can wall is thin with no surface node nor crust.

If the above criterion is met, the entire mass of a can wall interior node is transferred to steel particles. The surface node is also transferred simultaneously.

$$\tilde{\bar{\rho}}_{l7}^{n+1} = \bar{\rho}_{l7}^{n} + \bar{\rho}_{S8}^{n} + \bar{\rho}_{S9}^{n}\,, \tag{5-57a}$$

$$\tilde{e}_{L5}^{n+1} = \frac{\bar{\rho}_{l7}^{n} e_{L5}^{n} + \bar{\rho}_{s8}^{n} e_{S5}^{n} + \bar{\rho}_{s9}^{n} e_{S6}^{n}}{\tilde{\bar{\rho}}_{l7}^{n+1}}\,, \tag{5-57b}$$

$$\tilde{\bar{\rho}}_{s8}^{n+1} = \tilde{\bar{\rho}}_{s9}^{n+1} = 0\,, \text{and} \tag{5-57c}$$

$$\tilde{e}_{S6}^{n+1} = e_{S,2}^{0}\,. \tag{5-57d}$$

When the can wall energy is larger than the solidus energy, the mass being transferred is partitioned between liquid steel and steel particles, based on a melt fraction. The formulae are similar to the standard can wall breakup model in NC4/NC5. The same formulae apply to the right can wall, as well.

When the left can wall in cell *IJ* is coupled with the left adjacent cell *IJ*-1, breakup of a can wall interior node in cell *IJ* also causes simultaneous breakup of a can wall surface node in cell *IJ*-1.

$$\tilde{\bar{\rho}}_{l7}^{n+1}(ij-1) = \bar{\rho}_{l7}^{n}(ij-1) + \bar{\rho}_{s10}^{n}(IJ-1)\,, \tag{5-58a}$$

$$\tilde{e}_{L5}^{n+1}(ij-1) = \frac{\bar{\rho}_{l7}^{n}(ij-1) e_{L5}^{n}(ij-1) + \bar{\rho}_{s10}^{n}(ij-1) e_{S7}^{n}(ij-1)}{\tilde{\bar{\rho}}_{l7}^{n+1}(ij-1)}\,, \tag{5-58b}$$

$$\tilde{\bar{\rho}}_{s10}^{n+1}(ij-1) = 0\,, \text{and} \tag{5-58c}$$

$$\tilde{e}_{S7}^{n+1}(ij-1) = e_{S,2}^{0}\,. \tag{5-58d}$$

When the can wall energy is larger than the liquidus energy, the mass being transferred is partitioned between liquid steel and steel particles, based on a melt fraction. The same formulae apply to the right can wall, as well.

5.5.7. Breakup of suspended can wall (NC8B/NC9B)

In rare occasions during reactor core melt-out progression, the breakup of can wall may take place at two axial locations simultaneously. This produces an unphysical situation that the remaining can wall structure between the two breakup locations stays intact and stationary. This suspended (floating un-supported) can wall structure may fall down under gravity or move in a fluid flow. To simply simulate the mobility of a suspended can wall structure, a breakup model, almost the same as NC8/NC9, is optionally made available. When a suspended can wall structure is detected, the entire mass of suspended can wall is transferred to steel particles instantaneously.

5.5.8. Breakup of crust fuel

Since the crust fuel itself is thought to be very brittle and fragile, it is assumed that it can stay on a structure wall surface only when underlying structure is intact. Namely, if the can wall disappears or undergoes extensive melting on surface, the crust fuel is likely to fail at the same time. Thus, the breakup of crust fuel is assumed when one of the following two conditions is satisfied.

First, the crust fuel breaks up, when the can wall disappears. For the left crust, the criterion is

$$\bar{\rho}_{S5} + \bar{\rho}_{S6} = 0\,. \tag{5-59}$$

Second, the crust fuel becomes unstable, when the underlying wall surface starts to melt. However, a thick crust can stay intact even when the underlying structure starts to melt. Thus the crust fuel breakup is judged, for the left crust case, by one of the two criteria

$$T_{S5} \geq T_{Sol,2}\text{ , and} \tag{5-60a}$$

$$W_{cr} < W_{cr,min}\,. \tag{5-60b}$$

It is assumed the crust breakup occurs instantaneously, and the mass and energy of the left crust fuel are transferred to solid fuel particles as follows:

$$\tilde{\bar{\rho}}_{S2}^{n+1} = 0\,, \tag{5-61a}$$

$$\tilde{e}_{S2}^{n+1} = e_{S,1}^{0}\,, \tag{5-61b}$$

$$\tilde{\bar{\rho}}_{L4}^{n+1} = \bar{\rho}_{L4}^{n} + \bar{\rho}_{S2}^{n}\text{ , and} \tag{5-61c}$$

$$\tilde{e}_{L4}^{n+1} = \frac{\bar{\rho}_{L5}^{n} e_{L4}^{n} + \bar{\rho}_{S2}^{n} e_{S2}^{n}}{\tilde{\bar{\rho}}_{L4}^{n+1}}\,. \tag{5-61d}$$

The model for the right crust fuel is the same.

5.5.9. Lateral fluid flow restraint

Breakup of the uncoupled two can walls or the coupled can wall allows lateral (radial) fluid motion to take place across the mesh-cell boundary. When the can wall becomes completely melted or broken up with no can wall structure remaining, an entire area of mesh call boundary is available for lateral fluid flow. On the other hand, when can wall breakup is incomplete with a part of can wall mass still remaining as an intact structure, like in NC4/NC5 (breakup by thermal criterion) and NC6/NC7 (mechanical failure), the lateral fluid flow is restrained by the remaining can wall structure with a reduced cell boundary area available for flow.

To simulate the lateral fluid flow restraint caused by incomplete can wall failure, a simple orifice pressure drop is modeled with its coefficient defines as

$$C_{ORF} = C_{ORF.0}(1-\beta)(1-\beta^2)\frac{1}{\beta^2}\,, \tag{5-62}$$

where $C_{ORF.0}$ is an empirical constant with the value of 1.35, and

$$\beta = \beta_{CW} + f_{CW}(1-\beta_{CW})\,, \tag{5-63}$$

where f_{CW} is the melt fraction of the can wall and β_{CW} is a fractional area of the can wall available for lateral fluid flow across the mesh-cell boundary and the default value of 0.1.

5.6. Detailed Fuel-Pin Model

5.6.1. Background

The standard fuel pin model of SIMMER-III/SIMMER-IV is a simplified pin model (SPIN)[15], in which pin fuel is represented by two temperature nodes, a thin surface and thick interior nodes, for fuel pin heat-transfer calculations. This SPIN model is considered sufficient for many of code application areas, such as undercooling type accident sequences where a detailed behavior of intact fuel pin is unimportant. When rapid overpower transients are to be simulated, on the other hand, a more detailed fuel pin modeling is desired to describe the development of radial temperature distribution, fuel melting onset from the centerline, molten cavity formation, mechanical loading to cladding, and so on. The development of a detailed fuel pin model (DPIN) was initiated by JAEA and later taken over by CEA-Cadarache[37]. Although further development and refinement of DPIN-related models were required, the effort was interrupted due to limited resources available. It is noted a new project was recently initiated as a joint study by JAEA and CEA to develop some advanced technologies beyond SIMMER-III and SIMMER-IV. This project includes the development of a new detailed fuel pin model that can simulate various designs of future LMFRs.

In the rest of this section, the DPIN model incorporated in the current SIMMER-III and SIMMER-IV libraries is described, including the fuel-pin radial heat transfer model and the molten cavity model.

5.6.2. Geometry and assumptions

A concept of the fuel-pin radial heat transfer model is similar to one used in initiating-phase codes such as SAS4A, where a detailed fuel-pin thermo-mechanical model is used. Only a thermal behavior is modeled in SIMMER-III/SIMMER-IV, since detailed descriptions of pre-transient fuel irradiation phenomena and transient mechanical deformations are beyond the scope of the codes. However, it is expected that the treatment of radial temperature distribution in pin fuel should make connection from SAS4A more consistent or simulate overpower transients much better.

Like in SAS4A, a representative fuel pin is divided into a number of axial segments (*MZ*), and each axial segment of pin fuel is divided into radial temperature nodes (*NPB*). The geometrical arrangement of the initial radial node structure is illustrated in **Fig. 5-6**. The fuel pin heat transfer calculation is made from node *KS* to node *KE*, initially set to k=1 and k= *NPB* +1, respectively. In an overpower transient, pin fuel melting proceeds from the inner-most node and the inner radius changes. Then the radial nodes are rezoned and *KS* can be set to 2 or larger value for a new heat transfer calculation in the next cycle. The width of the outermost pellet node is set to the thermal penetration length $2\delta_f$, which is the same as the pin-fuel surface node as defined as a fluid-dynamics structure-field component. This means the pin fuel surface node is treated completely the same as the one in the SPIN option. The single interior node in SPIN is divided into *NPB-1* nodes in the DPIN option. For better thermal coupling of pin fuel and the cavity fuel, the width of innermost node is also set to $2\delta_f$.

The following assumptions are used in the detailed pin model.

- Thermal expansion of fuel is modeled using the standard equations of state (EOS) and thermophysical properties, but the expansion occurs only to a radial direction. Thus, an important reactivity effect of fuel-pin axial expansion cannot be calculated since the axial nodes are always fixed in space.

- A central hole and fuel restructuring during pre-transient irradiation can be specified by user input data. Radial distributions of porosities and fission gas retention are specified for each of radial nodes.
- Pellet-cladding gap conductance is modeled by a simple function.
- The mass transfer from the inner pellet surface to the cavity is treated only at the same axial segment, and a complete cavity treatment, including redistribution of cavity materials, has not been implemented in the present code version.
- Input specification

5.6.3. Fuel pin structure configuration

In the fuel pin heat-transfer code structure shown in **Fig. 5-6**, the heat-transfer area between the two nodes *k* and *k*-1 is defined at the node boundary as:

$$a_{k,k-1} = 2r_k \frac{\alpha_{pin,j}}{r_{co,j}^2} \text{ , for } k = KS+1 \text{ to } KE \text{ ,and} \tag{5-64a}$$

$$a_{k,k-1} = 0 \text{ , for } k = KS \text{ or } KE+1, \tag{5-64b}$$

where r_k, $\alpha_{pin,j}$ and $r_{co,j}$ are the inner radius of radial node *k*, the volume fraction of fuel pin at axial segment *j* and the outer radius of fuel pin at axial segment *j*, respectively.

Similarly to the simplified pin model formation, a temperature point to calculate radial heat transfer is placed at a volumetric centroid of each radial node for representing the cylindrical geometry of the fuel pin. The radius of temperature point of node *k* is calculated by

$$\hat{r}_k = \sqrt{\frac{r_k^2 + r_{k+1}^2}{2}}. \tag{5-65}$$

Then the heat-transfer coefficient between nodes *k* and *k*-1 is defined as

$$h_{k,k-1} = \frac{\kappa_{Sf}}{r_k[ln(r_k/\hat{r}_{k-1}) + ln(\hat{r}_k/r_k)]} \text{ , for } k = KS+1 \text{ to } NP, \tag{5-66}$$

where κ_{Sf} denotes the thermal conductivity of solid fuel.

The heat transfer coefficient between pellet outermost node ($k = NPB$) and cladding ($k = NPB+1$) includes the gap conductance

$$h_{NPB,NPB+1} = \left[\frac{r_{NP}}{\kappa_{Sf}} \ln\left(\frac{\hat{r}_{NP}}{r_{NP}}\right) + \frac{1}{h_{gap}} + \frac{r_{NP+1}}{\kappa_{Ss}} \ln\left(\frac{\hat{r}_k}{r_{NP}}\right)\right]^{-1}, \tag{5-67}$$

where κ_{Ss} denotes the thermal conductivity of solid steel and h_{gap} is the gap conductance. There are three options are available for the gap conductance as documented in the structure model report[15)].

- a constant value specified by user input,
- a simple conductance model based on gap gas conduction and radiation heat transfer, and
- a more elaborated model to consider fuel-cladding contact behavior as well as gap gas conductance and radiation.

The fuel pin outer surface area and the structure-side heat-transfer coefficient to be used in the fluid-dynamics heat and mass transfer operations are calculated in the same way as the simplified model.

5.6.4. Radial heat transfer model and solution method

The mass and energy equations for the fuel-pin radial node *k* are:

$$\frac{\partial \bar{\rho}_k}{\partial t} = \Gamma_k \text{ , and} \tag{5-68}$$

$$\frac{\partial \bar{\rho}_k e_k}{\partial t} = h_{k,k-1} a_{k,k-1} (T_{k-1} - T_k) + h_{k+1,k} a_{k+1,k} (T_{k-1} - T_k) + Q_{Hk} + Q_{Nk} \text{ ,} \tag{5-69}$$

where the mass transfer rate Γ_k and the energy transfer rate Q_{Hk} are applied only to the innermost node and the outermost node. Namely,

$\Gamma_k = 0$, for $k = KS$+1 to KE-1 , and

$Q_{Hk} = 0$, for $k = KS$+1 to KE-1 .

The time step sizes can be larger than the fluid-dynamics tie steps and hence Γ_k, Q_{Hk} and Q_{Nk}, calculated in the fluid-dynamics Step 1 operations, are summed over the fluid time steps involved in the current heat transfer time step.

Equations (5-68) and (5-69) are implicitly finite-differenced as:

$$\tilde{\bar{\rho}}_k^{n+1} - \bar{\rho}_k^n = \Delta \mathrm{t} \Gamma_k \text{ , and} \tag{5-70}$$

$$\begin{aligned} \tilde{\bar{\rho}}_k^{n+1} \tilde{e}_k^{n+1} - \bar{\rho}_k^n e_k^n & \\ &= \Delta \mathrm{t} \big[h_{k,k-1} a_{k,k-1} \big(\tilde{T}_{k-1}^{n+1} - \tilde{T}_k^{n+1} \big) + h_{k+1,k} a_{k+1,k} \big(\tilde{T}_{k+1}^{n+1} - \tilde{T}_k^{n+1} \big) + Q_{Hk} \\ &+ Q_{Nk} \big] \text{ ,} \end{aligned} \tag{5-71}$$

where $h_{k,k-1}$ and $a_{k,k-1}$ are the heat-transfer coefficient and heat-transfer area, respectively, between the nodes *k* and *k*-1. The end-of-time-step temperatures are used in this implicit formulation. Equation (5-70) is multiplied by $\tilde{e}_k^{n+1}$ and subtracted from Eq. (5-70) to produce:

$$\begin{aligned} \bar{\rho}_m^k \big(\tilde{e}_k^{n+1} - e_k^n \big) = \Delta \mathrm{t} \big[& h_{k,k-1} a_{k,k-1} \big(\tilde{T}_{k-1}^{n+1} - \tilde{T}_k^{n+1} \big) + h_{k+1,k} a_{k+1,k} \big(\tilde{T}_{k+1}^{n+1} - \tilde{T}_k^{n+1} \big) \\ & + Q_{Hk} + Q_{Nk} - \Gamma_k \tilde{e}_k^{n+1} \big] \text{ .} \end{aligned} \tag{5-72}$$

Then the end-of-time-step temperature and specific internal energy are expanded with respect to the change in internal energy Δe_k as:

$$\tilde{T}_k^{n+1} = T_k^n + \left(\frac{\partial \mathrm{T}_{Sk}}{\partial e_{Sk}}\right)^n \Delta e_k \text{ , and} \tag{5-73}$$

$$\tilde{e}_k^{n+1} = e_k^n + \Delta e_k , \tag{5-74}$$

where the partial derivative of temperature with respect to internal energy is evaluated at the beginning of time step in the EOS model. The variables with "tilde" denote tentative values during iterations.

Substituting Eqs. (5-73) and (5-74), Eq. (5-72) is rearranged into the form:

$$a_1 \Delta e_{k-1} + a_2 \Delta e_k - a_3 \Delta e_{k+1} = b , \tag{5-75}$$

where the coefficients are:

$$a_1 = -\Delta \mathrm{t} h_{k,k-1} a_{k,k-1} \left(\frac{\partial \mathrm{T}_{Sk}}{\partial e_{Sk}}\right)^n , \tag{5-76a}$$

$$a_2 = \bar{\rho}_k^n + \Delta \mathrm{t} h_{k,k-1} a_{k,k-1} \left(\frac{\partial \mathrm{T}_{Sk}}{\partial e_{Sk}}\right)^n + \Delta \mathrm{t} h_{k+1,k} a_{k+1,k} \left(\frac{\partial \mathrm{T}_{Sk}}{\partial e_{Sk}}\right)^n + \Delta \mathrm{t} \Gamma_k , \tag{5-76b}$$

$$a_3 = \Delta \mathrm{t} h_{k+1,k} a_{k+1,k} \left(\frac{\partial \mathrm{T}_{Sk}}{\partial e_{Sk}}\right)^n \text{ , and} \tag{5-76c}$$

$$b = \Delta \mathrm{t} \left[h_{k,k-1} a_{k,k-1} (T_{k-1}^n - T_k^n) + h_{k+1,k} a_{k+1,k} (T_{k+1}^n - T_k^n) + Q_{Hk} + Q_{Nk} - \Gamma_k e_k^n \right] . \tag{5-76d}$$

This is a tridiagonal linear matrix equation with respect to Δe_k and is solved using the standard solver available in SIMMER-III and SIMMER-IV. The solutions are substituted to Eq. (5-74) to determine the new estimates for end-of-time-step energy and temperature. This procedure is iterated until the convergence criterion,

$$\left| \frac{\Delta e_k}{e_k^i} \right| < \varepsilon , \tag{5-77}$$

is satisfied, where *i* in an iteration index. Finally, the end-of-time-step macroscopic densities are updated using Eq. (5-71).

5.6.5. Time step control

The same time-step control is employed as the SPIN model. Namely, fuel-pin heat transfer time steps are controlled based on changes in specific energies of pin fuel and cladding, and the change in power level. The latter accounts for close relationship between internal heating and fuel temperature.

$$\Delta t_k^{new} = 0.9 f_k \frac{\tilde{e}_k^{n+1}}{\left|\tilde{e}_k^{n+1} - e_k^n\right|} \Delta t^{old} \text{ , and} \tag{5-78a}$$

$$\Delta t_P^{new} = 0.9 f_P \frac{P^{n+1}}{\left|P^{n+1} - P^n\right|} \Delta t^{old} \text{ .} \tag{5-78b}$$

where P^n is the power amplitude, and f_k and f_P are the input multipliers used when a tighter control is desired. Other restrictions of time step sizes include input minimum and maximum values.

5.6.6. Molten cavity model

In an overpower transient, pin fuel starts to melt at an axial pin segment near the midplane from the inner-most radial node. The molten region of pin fuel grows, as long as internal heating continues, axially and radially to form an inter-connected central cavity. In the DPIN model at present, however, a molten cavity is modeled in a very simplified way. It is assumed that: there is no axial and redial relocation of molten fuel even after it joins the central cavity. This means the radial heat-transfer calculation is performed as if the molted fuel stays at the original intact location.

To determine the radius of the cavity at each axial segment, the melt fraction of node k, $f_{p,k}$, is checked against the input threshold value as:

$$f_{p,k} = \frac{e_k - e_{Sol,1}}{e_{Liq,1} - e_{Sol,1}} > f_p^i \text{ .} \tag{5-79}$$

Since the radius of cavity in included in the node *k*=*KC*, between r_{KC} and r_{KC+1}, the cavity radius is calculated from:

$$r_{cav}^2 = r_{KC}^2 + \frac{f_{p,KC} - f_p^i}{1 - f_p^i} \left(r_{KC+1}^2 - r_{KC}^2\right) \text{ .} \tag{5-80}$$

Once the cavity boundary is determined, the macroscopic densities of cavity fuel are obtained as:

$$\bar{\rho}_{c1} = \sum_{k=1}^{KC-1} \bar{\rho}_{s1,k} + \frac{f_{p,KC} - f_p^i}{1 - f_p^i} \bar{\rho}_{s1,KC} \text{ , and} \tag{5-81a}$$

$$\bar{\rho}_{c2} = \sum_{k=1}^{KC-1} \bar{\rho}_{s2,k} + \frac{f_{p,KC} - f_p^i}{1 - f_p^i} \bar{\rho}_{s2,KC} \text{ ,} \tag{5-81b}$$

where subscripts c1 and c2 denotes fertile and fissile cavity fuel components, respectively, and are summed to make an energy component, similarly to the convention of fluid-dynamics components.

$$\bar{\rho}_C = \bar{\rho}_{c1} + \bar{\rho}_{c2} \text{ .} \tag{5-82}$$

The specific internal energy of the cavity fuel is:

$$e_{C1} = \frac{1}{\bar{\rho}_{C1}} \left[\sum_{k=1}^{KC-1} \left(\bar{\rho}_{s1,k} + \bar{\rho}_{s2,k}\right) e_{C1,k} + \frac{f_{p,KC} - f_p^i}{1 - f_p^i} \left(\bar{\rho}_{s1,KC} + \bar{\rho}_{s2,KC}\right) e_{Liq,1} \right] \text{.} \tag{5-83}$$

The total cavity volume is calculated by summing over the axial segments. Then the cavity pressure is calculated based on the released fission gas pressure using an ideal gas law and the fuel saturation vapor pressure corresponding to the cavity fuel temperature. Many of the cavity related models are too preliminary to describe in detail at this stage of model development.

5.6.7. Options for input specifications

A standard input specification of the DPIN model is to input: the radii for radial node boundaries, fuel temperature and porosities in individual radial nodes. When a SAS4A calculation is connected to SIMMER-III, the detailed distributions can be directly transferred. Since this input specification is complicated, a new option has been developed in which an input file prepared for the SPIN model is converted to the input for the DPIN model. The number of radial nodes and the volume fraction of the central hole are specified by user input. Then the uniform distributions of fuel temperature and porosity are internally calculated.

5.7. Other Model Development

5.7.1. Fuel swelling model

In the original version of SIMMER-III/SIMMER-IV, the porosities of solid oxide fuel are specified by user input variables for pin fuel, crust fuel, fuel particles and fuel chunks and they are kept constant during transient calculations. It is known, however, from the available knowledge on in- and out-of-pile transient heating experiments, that the irradiated oxide fuel containing an amount of fission gas exhibits non-negligible solid-state swelling at high temperature and the rate of swelling increases with fuel temperature38). That is, the swelling initiates at fuel temperature around 2300 K and becomes prominent at higher temperature above 2700 K. A major mechanism of swelling is inter-granular gas bubble expansion and grain boundary separation, accompanied by transient fission gas release. The fuel swelling results in an increased fuel volume fraction and a reduced vapor volume fraction, and thereby it can influence the transient behavior of a disrupted core involving a large amount of solid fuel. From the above background, a simple fuel swelling model has been developed as an option. The model is applied only to pin fuel and fuel chunks that are larger in size and hence retain an amount of fission gas. The swelling of crust fuel and fuel particles are neglected because of their negligibly small effect. It is assumed, for pin fuel, that the swelling occurs only when the cladding is missing or its mechanical constraint is lost at high temperature.

Fuel swelling is modeled as an increase in the fuel porosity ε_f and the resultant specific volume of fuel υ_f is calculated by

$$\upsilon_f = \frac{\upsilon_{f,EOS}}{1-\varepsilon_f}, \tag{5-84}$$

where $\upsilon_{f,EOS}$ is the specific volume of fuel coming from EOS defined as a polynomial of fuel internal energy. From the effective specific volume, the fuel volume fraction is calculated as

$$\alpha_f = \bar{\rho}_f \upsilon_f , \tag{5-85}$$

where $\bar{\rho}_f$ is the macroscopic density of fuel. The swelling rate, the rate of porosity increase, is simply modeled using a swelling time constant.

$$\frac{d\varepsilon_f}{dt} = \frac{\varepsilon_f}{\tau_{sw}} . \tag{5-86}$$

The swelling time constant is defined as a function of fuel temperature, which is experimentally correlated, by fitting the condition of significant grain boundary separation[38], as

$$\log_{10}\tau_{sw} = -10.02 + \frac{23773}{T_f} . \tag{5-87}$$

The solution of Eq. (5-86) is the fuel porosity reflecting fuel swelling. For fuel chunks, the effect of inter-cell convection must be taken into account, as well. This is done by formulating an additional convection equation for the volume fraction of fuel chunks as

$$\frac{\partial\alpha_f}{\partial t} = \nabla \cdot \alpha_f \boldsymbol{v}_q , \tag{5-88}$$

where $\boldsymbol{v}_q$ is the velocity of velocity field q to which fuel chunks are assigned. Equation (5-88) is solved in the fluid-dynamics Step 4 using the end-of-time-step velocity in the same way as the mass convection. Using the updated volume fraction and Eqs. (5-84) and (5-85), the fuel porosity is updated as

$$\varepsilon_f = 1 - \frac{\bar{\rho}_f v_{f,EOS}}{\alpha_f} . \tag{5-89}$$

The convection of volume fraction in Eq. (5-88) is computed in Step 4 in the previous cycle, and the fuel swelling in Eq. (5-89) is calculated at the end of Step 1 in subroutine EOST.

Since Eq. (5-86) implies an exponential increase of fuel porosity, it is possible that the fuel volume fraction increases unrealistically. To avoid such an unrealistic situation, an input limiter is provided to ε_f with a default value of 0.5. Also controlled by input parameters are: the minimum fuel and cladding temperatures for swelling inception. Another important factor that is not modeled is the influence of fuel heating rate on solid fuel swelling. The experimental evidence of fuel swelling has been obtained from the out-of-pile heating tests of irradiated fuel pellet samples, in which transient fuel behaviors were visualized[39][40]. It was shown that obvious solid fuel swelling was observed in the tests with the heating rates of several tens to hundreds K/s. At higher heating rates, rapid grain boundary cracking and pellet disruption was observed. Finally, it is noted that this model must be carefully used in order not to predict unrealistically large and rapid swelling, because excessive swelling may significantly decrease the mobility of disrupted core materials and hence may well underestimate an important reactivity effect of fuel motion and fuel compaction.

5.7.2. Improvement of fission-gas release model

In the original SIMMER-III/SIMMER-IV, fission gas release from the liquid-field fuel components, liquid fuel, fuel particles and fuel chunks, is modeled simply by user-specified time constants (see **Section 5.3.4**). The default time constants are 10^{-3} and 10^{-1} s for liquid fuel and fuel particles/chunks, respectively.

No fission gas component is modeled in crust fuel, because the refrozen fuel crust is formed from once molten fuel and only a negligible amount of fission gas has been left in liquid fuel. The mass transfers involving fuel components, such as melting and freezing of fuel and pin fuel breakup, are accompanied by fission gas transfer at the same time, and no direct release to the vapor field is treated. These default time constants have not been calibrated through experimental analyses and might be too short, allowing rapid gas release especially from liquid fuel. The temperature dependence on fission gas release rate is not treated, either.

The above model is too simplistic, in the light of the available knowledge on in- and out-of-pile transient heating experiments investigating transient fission gas release from the irradiated oxide fuel[38]. It is known that the rate of fission-gas release depends on fuel temperature and closely related to solid-state fuel swelling, as discussed in the previous section. First, the fission gas release, in a lower fuel temperature range, is activated by an onset of significant grain boundary separation and a fraction of inter-granular fission gas is released rapidly. Second, fission gas release is further enhanced, in a higher fuel temperature range, beyond the onset of significant grain boundary separation, possibly involving intra-granular fission gas. These two mechanisms of fission gas release have been incorporated in an improved fission gas release model, which is applied to fuel chunks in the liquid field and pin fuel with no cladding constraint. The fission gas releases from liquid fuel and fuel particles are treated by the original temperature-independent release time constants.

In the improved temperature-dependent model, the rate of fission gas release is modeled by a time constant τ_{FG}, as well. For a fuel temperature range below a certain threshold value, $T_{f,sw}$, the time constant is determined, similarly to fuel swelling, by a function of fuel temperature, based on the condition of significant grain boundary separation, as

$$\log_{10}\tau_{FG} = -10.02 + \frac{23773}{T_f}\ , \text{ for } T_f \leq T_{f,sw}\ . \tag{5-90}$$

The threshold temperature $T_{f,sw}$ corresponds to the temperature above which fuel swelling becomes significant, with its default value of 2175.6 K. Above this temperature, the release time constant is modeled based on the experimental data of FGR-15, in which a pre-irradiated fuel pellet sample was placed in a tungsten capsule and was heated at the rate of 200 K/s and the fission gas release behavior was evaluated[41), 42)]. From the data on relationship between a released fraction of retained fission gas and fuel temperature, the fission gas release time constant has been derived as

$$\log_{10}\tau_{FG} = 0.86654 - (3.0967 \times 10^{-12})\left(T_f - T_{f,sw}\right)^4\ , \text{ for } T_f > T_{f,sw}\ . \tag{5-91}$$

The model is implemented in Step 1 (MASSPN) of the fluid dynamics. With the improved model, direct fission gas release from unclad pin fuel to the vapor field can be treated. Fast fission gas release to the vapor field upon fuel failure is also modeled. For the fuel pin breakup (**Section 5.3.5**), the fission gas from pin fuel is transferred, based on a threshold melt fraction, to liquid fuel and fuel particles (or fuel chunks). For the collapse of unsupported pin fuel (**Section 5.3.6**), the fission gas from pin fuel is transferred to fuel chunks. A fraction of direct release is specified by user input and the small release time constant, from liquid fuel, is applied in this case. All these model options are controlled by input parameters. Since the pressure rise due to fission gas release has a large effect on disrupted core material motion and the resultant reactivity change, the model parameters may have to be adjusted in order not to calculate unrealistically rapid gas release.

Table 5-1. Variations in can-wall structure configuration for 2D SIMMER-III

Location	Cases	Numbers of can walls and nodes	Can wall and crust fuel components
Left boundary of the first real cell (IJ=1)	Case 1	1 thin can wall (1 node)	S6 or S6+S2
	Case 2	1 thick can wall (2 nodes)	S6+S5 or S6+S5+S2
	Case 3	No can wall	Radial flow allowed, depending on the fluid-dynamics boundary condition.
Right boundary of the last real cell (IJ=IB)	Case 4	1 thin can wall (1 node)	S8 or S8+S3
	Case 5	1 thick can wall (2 nodes)	S8+S7 or S8+S7+S3
	Case 6	No can wall	Radial flow allowed, depending on the fluid-dynamics boundary condition.
Right boundary of normal real cells	Case 7	2 can walls (two cells, IJ and IJ+1, are decoupled)	
	7a	Left thin can wall in cell IJ+1	S6 or S6+S2 (same as Case 1)
	7b	Left thick can wall in cell IJ+1	S6+S5 or S6+S5+S2 (same as Case 2)
	7c	Right thin can wall in cell IJ	S8 or S8+S3 (same as Case 4)
	7d	Right thick can wall in cell IJ	S8+S7 or S8+S7+S3 (same as Case 5)
	Case 8	1 can wall (two cells, IJ and IJ+1, are coupled)	
	8a	Thin can wall without crust (1 node)	S6 (IJ+1) or S8 (IJ)
	8b	Thin can wall with crust (3 nodes)	[S6(IJ+1) or S8 (IJ)]+S2 (IJ+1)+S3(IJ)
	8c	Thick can wall without crust (3 nodes)	[S5(IJ+1)+S6(IJ+1)+S7 (IJ)] or [S7(IJ)+S8(IJ)+ S5(IJ+1)]
	8d	Thick can wall with crust (5 nodes)	[[S5(IJ+1)+S6(IJ+1)+S7 (IJ)] or [S7(IJ)+S8(IJ)+ S5(IJ+1)]+ S2 (IJ+1)+S3(IJ)
	Case 9	No can wall	Radial flow allowed

The same cases apply to the X (traverse) direction for 3D SIMMER-IV, and the Y (traverse) direction is treated in the same way.

Table 5-2. Input option flags for can wall breakup models

Case ID	Breakup mode	Option flag	Active	Remark
NC1/NC2	Thin can wall breakup	HTMOPT(63)	0	Thin can wall in adjacent cell
NC3	Cladding breakup	standard	--	Melt fraction
		HTMOPT(68)	1	Threshold temperature
NC4/NC5	Can wall breakup	standard	--	Melt fraction
NC6/NC7	Mechanical failure	HTMOPT(64)	1	Threshold thickness or temperature
NC8/NC9	Mechanical breakup	HTMOPT(61)	1	Threshold temperature
NC8B/NC9B	Suspended can wall breakup	HTMOPT(62)	1	Suspended (floating) can wall range
---	Crust fuel breakup	HTMOPT(65)	1	Threshold temperature and thickness

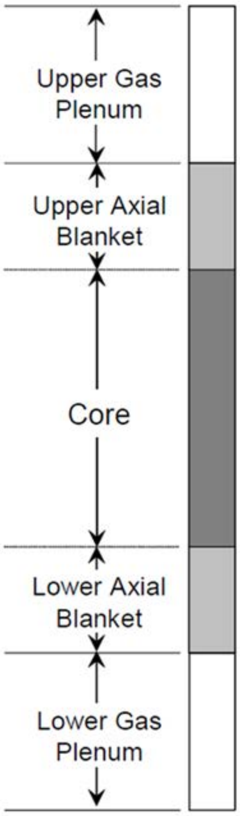

Fig. 5-1. Axial fuel pin representation (simplified pin model)

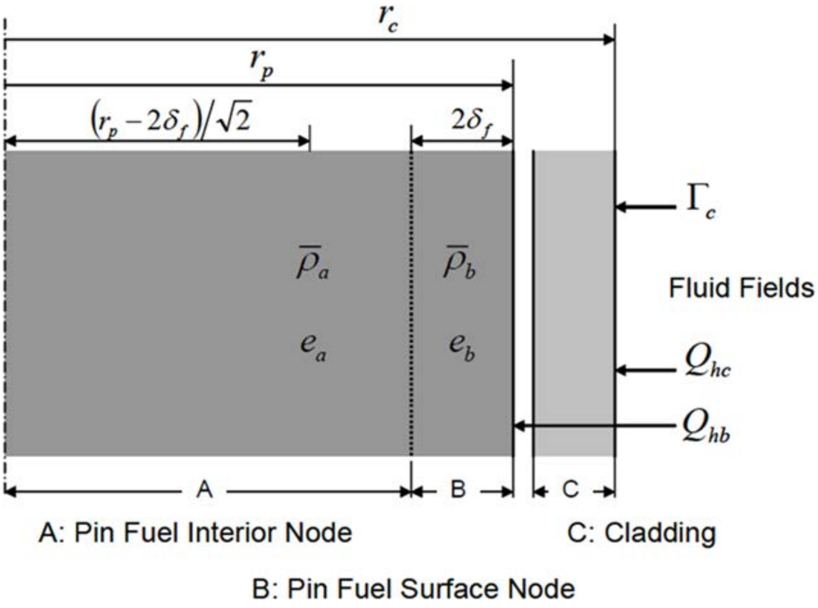

Fig. 5-2. Radial fuel pin representation (simplified pin model)

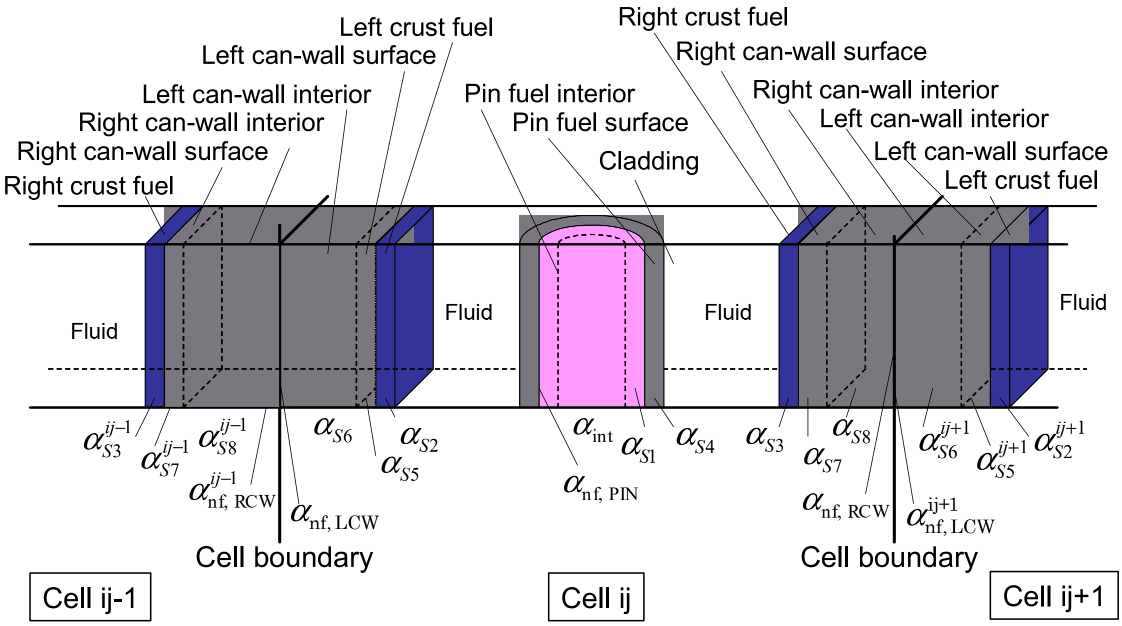

Fig. 5-3. Fuel pin and can wall structure configuration

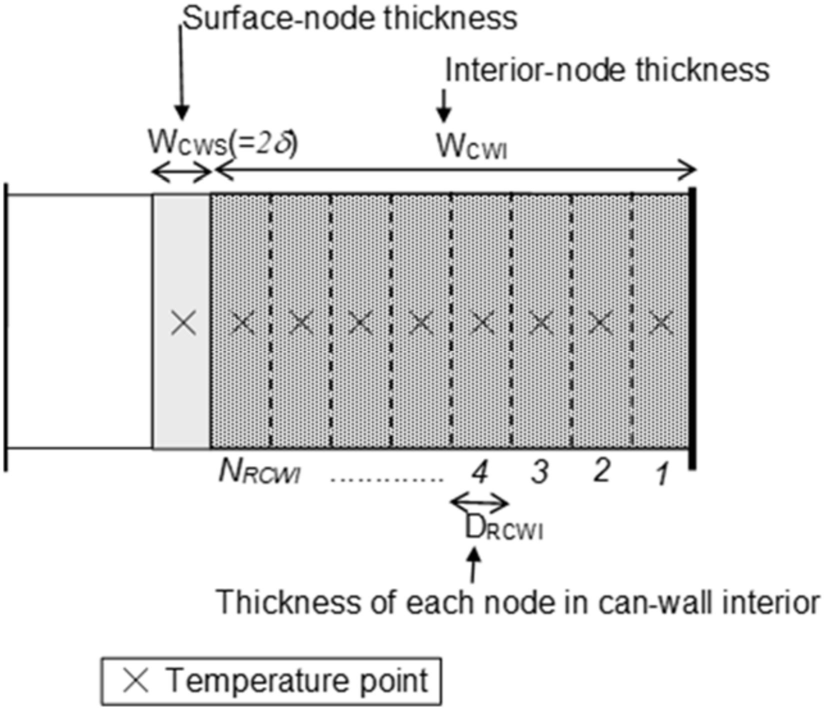

Fig. 5-4. Concept of multi-node can wall model (for left can wall).

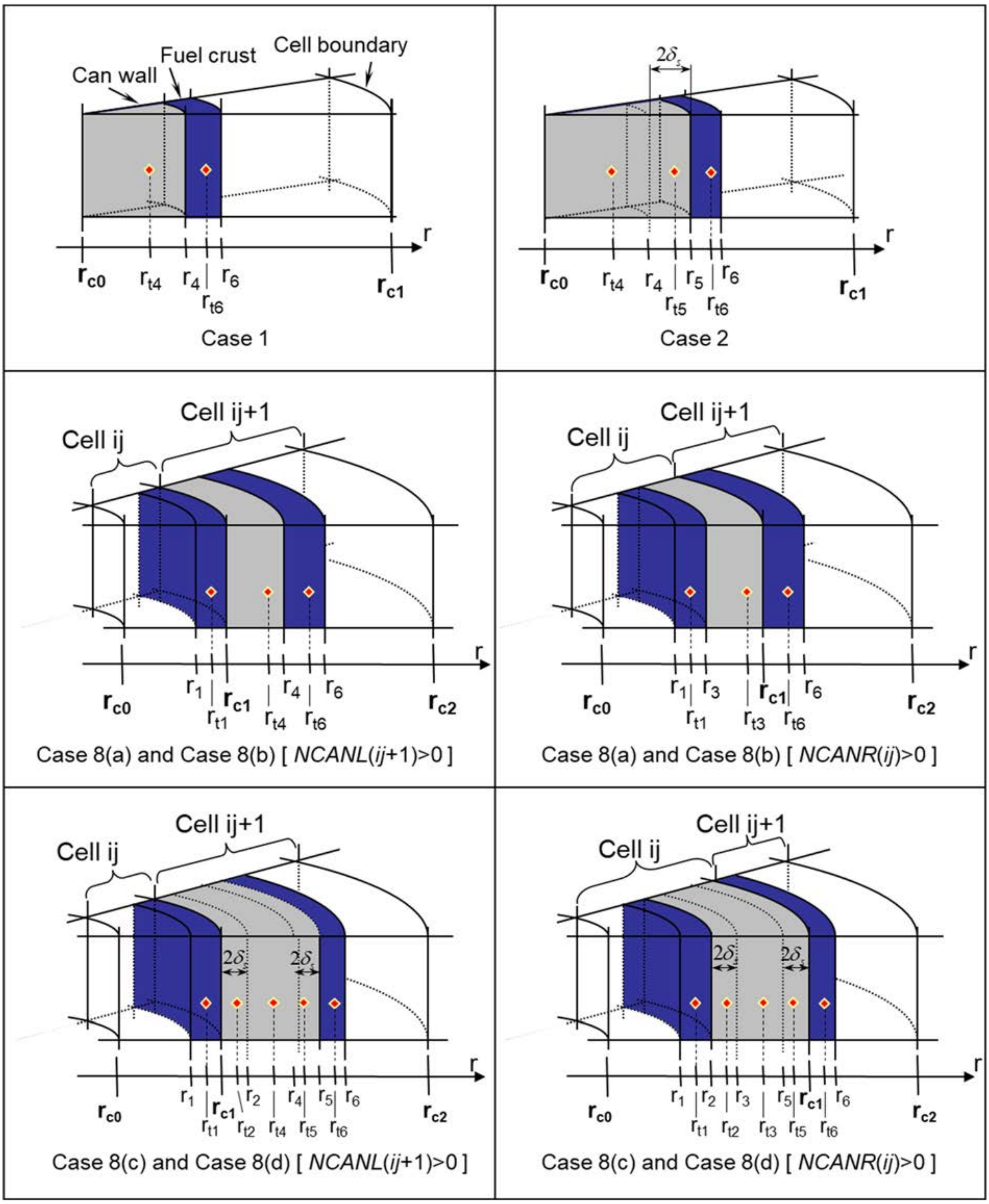

Fig. 5-5. Radii of can wall nodes and temperature points in cylindrical geometry.

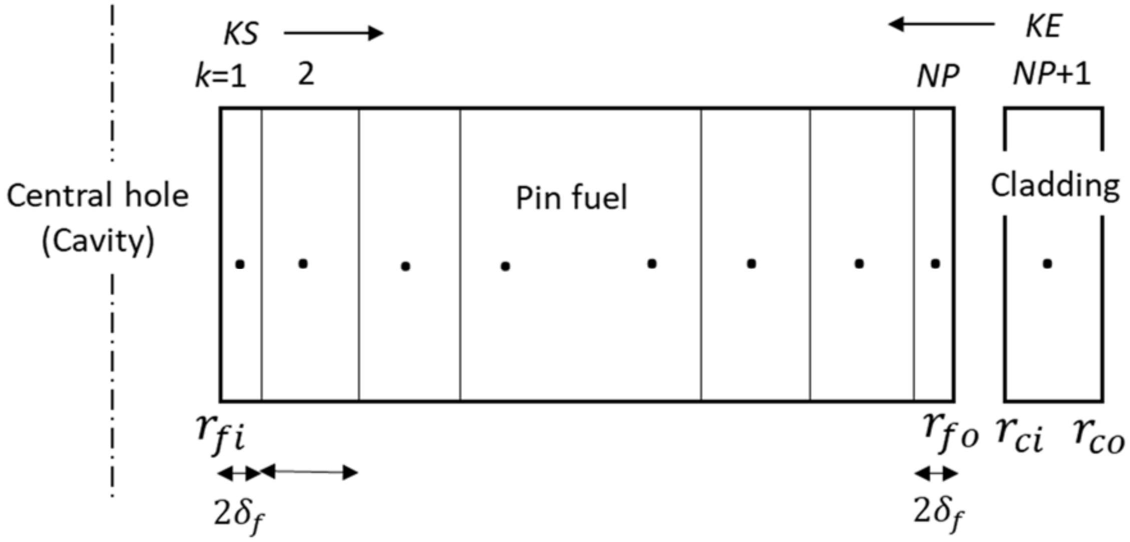

Fig. 5-6. Fuel pin radial heat-transfer nodes (DPIN).

6. Equations of State and Thermophysical Properties Models

6.0. Overview

6.0.1. Background of models and methods

The equations of state (EOS) and thermophysical properties (TPP) models for SIMMER-III and SIMMER-IV have been developed based on the experiences in the previous codes. In SIMMER–II1), inconsistencies in the simple analytic EOS introduced difficulty in determining vapor temperature at high pressure, resulting in many numerical problems. A use of a tabular EOS model was tried in AFDM43), but this was not successful due to the time-consuming table search and interpolation and the iteration to obtain mechanical equilibrium between the cell pressure and liquid compression.

Based on these past experiences, therefore, an improved analytic EOS model using flexible thermodynamic functions is newly developed to treat the basic reactor-core materials including mixed-oxide (MOX) fuel, steel, sodium, control (B_4C) and fission gas for the SIMMER-III/SIMMER-IV codes. This model assumes the immiscibility of the reactor-core materials, such that a unique EOS can be defined for each material. Proposed functions are formulated to have adequate accuracy in thermodynamic properties of the reactor materials at high temperature and high pressure, and to consistently satisfy basic thermodynamic relationships over the wide temperature range from a solid to supercritical state. The function forms use polynomial equations for the liquid and solid phases and a modified Redlich-Kwong (MRK) equation for the vapor phase. The MRK equation is almost as simple as the well-known van der Waals equation, but it is much more accurate at least for vapors44). Moreover, the original MRK equation is further extended to include the dimerization process of sodium vapor to better describe the properties of sodium vapor at high temperature. The heat and mas transfer model requires additional thermodynamic properties and their derivatives to evaluate heat- and mass-transfer rates at each pair of binary contact interfaces between different energy components. The present analytic EOS model also defines the saturation temperature, specific volumes, internal energies, and the heats of vaporization, based on the vapor partial pressure.

In the former SIMMER-II, material TPPs were treated as empirical correlations mostly as a simple function of temperature. Sometimes even constant values were used for properties where the temperature dependence is weak or for problems without large temperature change. However, for the generalized framework of SIMMER-III and SIMMER-IV, it is highly desired that TPPs are made consistent with the EOS model and are accurate at high temperature near the critical point. Therefore, a new set of analytic TPP functions have been developed, based on existing empirical functions and theoretical consideration, to fit better at a high temperature range including the vicinity of the critical point. The parameters in the TPP functions are determined using most up-to-date and reliable sources for uranium dioxide, MOX, stainless steel and sodium.

6.0.2. Interaction with other models

EOSs are required to close and complete the fluid-dynamic conservation equations. Moreover it is crucial from the viewpoints of numerical accuracy and stability, and computing efficiency. The EOS functions are called very frequently from various parts of fluid dynamics models. The derivatives of EOS variables are also used in the fluid convection algorithm and heat and mass transfer model. These derivatives are also modeled as EOS functions. The TPP functions are called from wherever the properties are used.

6.1. Analytic Equation-of-State Model

6.1.1. Outline of the EOS model

A complete model description of the EOS is available in a separate report[12)] and the modeling framework stays unchanged since then. Only the outline of the model is therefore given below.

The functions use polynomial equations for the liquid and solid phases. Structure-field components, such as can wall, cladding, pin fuel and crust fuel, are assumed to be incompressible, and the compressibility is modeled for real liquid components. For solid particles and fuel chunks, however, compression resulting from higher cell pressure is assumed such that they can be treated similarly to liquid materials. As examples, solid temperature and specific volume as functions of specific internal energy below the solidus energy are expressed as:

$$T_{Sm} = T_{Sol,M}\left[1 - a_{S1,M}(1-u_{Sm}) - a_{S2,M}(1-u_{Sm})^2 - a_{S3,M}(1-u_{Sm})^3\right], \text{and} \tag{6-1}$$

$$v_{Sm} = v_{Sol,M}\left[1 - b_{S1,M}(1-u_{Sm}) - b_{S2,M}(1-u_{Sm})^2 - b_{S3,M}(1-u_{Sm})^3\right]. \tag{6-2}$$

where $u_{Sm} = \mathrm{e}_{Sm}/\mathrm{e}_{Sol,M}$ and a's and b's are the fitting parameters.

For a vapor phase, a modified Redlich-Kwong (MRK) equation is used[44)]. The MRK EOS, similar to the van der Waals equation, but it can be made reasonably accurate especially at high temperatures, has the form:

$$p_{Gm} = \frac{R_M T_M}{v_{Gm} - a_{G1,M}} - \frac{a(T_G)}{v_{Gm}\left(v_{Gm} + a_{G3,M}\right)}, \tag{6-3}$$

where

$$a(T_G) = a_{G2,M}\left(\frac{T_G}{T_{Crt,M}}\right)^{a_{G4,M}}, \text{for } T_G < T_{Crt,M}, \text{and}$$

$$a(T_G) = a_{G2,M}\left[1 + a_{G4,M}\left(\frac{T_G}{T_{Crt,M}} - 1\right)\right], \text{for } T_G \ge T_{Crt,M},$$

and $a_{G1,M}$, $a_{G2,M}$, $a_{G3,M}$ and $a_{G4,M}$ are the EOS fitting parameters.

It was found that this EOS poorly reproduces the evaluated data of the internal energy and the heat capacity of sodium vapor. Therefore, the MRK EOS was extended to a reacting system, which describes the dimerization process of sodium vapor molecules at a high temperature range, and thereby satisfactory agreement was obtained.

In AFDM, an inner EOS iteration was implemented to obtain mechanical equilibrium to compress each liquid to a state that is consistent with an identical pressure, and thereby to define the vapor volume fraction. This treatment turned out to be inefficient and made the pressure iteration, a main element of fluid convection algorithm, very slow. In SIMMER–III/SIMMER-IV, an improved method is introduced to eliminate the inner EOS iteration by defining the EOS pressure as a function of the cell pressure, and thereby the mechanical equilibrium among liquid components with the cell pressure is automatically guaranteed when the pressure iteration is converged.

The EOS functions are fitted using the most up-to-date and reliable data sources available. The present SIMMER-III/SIMMER-IV EOS model has adequate accuracy at high temperature and high pressure and consistently satisfies basic thermodynamic relationships over the wide temperature range from the solid to supercritical state. The main analytic EOS functions currently defined is listed in **Table 6-1**, in which a's, b's, etc. are fitting parameters. The recommended EOS parameters, defaulted in the code, are presented in the EOS report[12)] for mixed oxide, UO_2, stainless steel and sodium. Historically, the saturated vapor pressure curve has played an important role in evaluating the work energy from the energetic accident sequences. The saturated liquid vapor pressure is expressed by a functional form of

$$p_{Lm}^{+} = \exp\left[b_{L1,M} + b_{L2,M}T_{Lm}^{+} + \frac{b_{L3,M}}{T_{Lm}^{+}} + b_{L4,M}\ln\left(\frac{T_{Lm}^{+}}{T_{Crt,M}}\right)\right], \tag{6-4}$$

where p_{Lm}^{+} is the saturated vapor pressure corresponding the saturated liquid temperature T_{Lm}^{+}. Based on the recent evaluation of the UO_2 vapor pressure measurement, the fuel vapor pressure p_{Sat} is fitted as[45)]:

$$\log p_{Sat} = 39.187 - \frac{34715}{T} + 0.1921 \times 10^{-3}\mathrm{T} - 3.8571\ln(T), \tag{6-5}$$

Which is used in SIMMER-III/SIMMER-IV. The critical temperature and pressure of fuel were evaluated as 10600 K and 157.873 MPa, respectively.

In many of the non-reactor applications of SIMMER-III/SIMMER-IV, such as experimental analyses, temperature changes are only small and hence the EOS properties valid for a narrow temperature range are sufficient. Also, when only limited property data are available for a material, it is difficult to prepare a complete set of the EOS parameters for this material. For these reasons, a simplified analytic EOS (SAEOS) model was developed, which is similar to that adopted in AFDM[43)] but is improved on thermodynamic consistency. The SAEOS model assumes simple EOS relationships: ideal gas equation, temperature-independent particle and liquid compressibilities, temperature-independent solid and liquid densities, and constant solid and liquid heat capacities. The SAEOS model is fully documented in Appendix B of the EOS report[12)].

The model improvements and changes after the issuance of the EOS report is described in the following sections.

6.1.2. Fitting-free EOS model

In the standard analytic EOS model, there are 12 EOS functions for which as many as 65 EOS parameters need to be prepared for liquid and vapor properties. For the LMFR materials this work was already done and the recommended parameters are documented in the EOS reports and included in the codes as defaulted values. When SIMMER-III/SIMMER-IV is to be applied to reactor or non-reactor systems with different materials, the preparation of the fitting parameters in the EOS functions for new materials requires a tedious procedure in advance. This procedure may introduce errors in fitting processes and more importantly it may cause numerical problems due to thermodynamic inconsistency.

To simplify this procedure, a fitting-free EOS (FFEOS) model is developed to minimize a tedious process of determining the parameters, still using formulation consistent with the standard analytic EOS. In the FFEOS model, only 3 EOS functions and 10 fitting parameters are required for liquid and vapor propertied. Other EOS properties are evaluated numerically based on thermodynamic relationships. Although the use of the FFEOS model deteriorates the numerical efficiency, taking about 30% or more CPU time for each material, it would be still useful for new materials where experimental data sources are limited.

Required EOS parameters are: energy, temperature and specific volume at the liquidus point; critical temperature and density; and specific heat of dilute vapor at constant volume. The EOS functions are: saturation vapor pressure as a function of temperature, liquid density as a function of temperature, and adiabatic compressibility of liquid as a function of temperature. The FFEOS model is further enhanced to iteratively evaluate saturation properties: saturation temperature, condensate volume and energy, and vaporization volume and energy. With these EOS parameters and functions, the EOS calculations are performed directly using the thermodynamic relationships, the MRK equations for vapor EOS and the Clapeyron equation for liquid EOSs.

The FFEOS model is available as an input option. The recommended and default FFEOS parameters for the reactor materials, MOX, steel and sodium, are included in the codes.

6.1.3. Treatment of EOS sub-materials and EOS regions

The EOS model treats five EOS materials, fuel, steel, coolant, control and fission gas. For LMFR systems, they correspond respectively to mixed-oxide fuel (MOX), type-316 stainless steel, sodium, B_4C and xenon (as a representative of fission gas). The SIMMER-III, since its early development, has been applied to a number of reactor and non-reactor systems, including coolant types such as water and lead, and fuel types such as UO_2 and light-water-reactor corium (uranium and zirconium oxide). A concept of "EOS sub-materials" is introduced, to each of which up to five EOS materials are assigned. Currently, seven EOS sub-materials are defined as shown in **Table 6-2** and the EOS parameters have been prepared and are contained in the code.

Another useful feature of the EOS material specification is EOS regions. An entire computational domain can be divided into multiple EOS regions and a different set of EOS materials can be assigned to each region. By combining the EOS regions with EOS sub-materials, the area of SIMMER-III/SIMMER-IV applications is significantly enhanced with flexible assignment of materials.

6.2. Analytic Thermophysical Properties Model

6.2.1. Outline of the TPP model

A complete description of the TPPs is available in a separate report[13)] and the modeling framework stays unchanged. Therefore, only the outline of the model is therefore given below.

A set of analytic TPP functions have been developed, based on existing empirical functions and theoretical consideration, to fit better at a high temperature range including the vicinity of the critical point. The TPPs used in SIMMER-III/SIMMER-IV include: thermal conductivity of solid, liquid and vapor materials; viscosity of liquid and vapor materials; surface tension and heat capacity of liquid materials; and vapor diffusion coefficient for binary system. The forms of the functions are not only taken from general formulae such as empirical equations and theoretical equations, but also newly designed to represent the dependency on major physical variables. For the thermal conductivity and viscosity, especially of sodium, improved formulation is newly proposed to represent the correct behavior of properties near the critical point. For fuel and steel, which have so high critical temperatures, properties in their vicinity should not become important in the reactor safety analysis. Therefore, a simple function model using polynomial and empirical equations as well as a model based on the kinetic theory of gases is also prepared to calculate the thermal conductivity and viscosity.

The TPP model is also designed to be consistent with a SIMMER-III/SIMMER-IV model on thermodynamic properties and the analytic EOS model. The parameters in the TPP functions are determined using most up-to-date and reliable sources for uranium dioxide, mixed-oxide fuel, stainless steel, and sodium. The recommended EOS parameters, defaulted in the code, are presented in the TPP report[13)]. The main analytic TPP functions currently defined is listed in **Table 6-3**, in which *a*'s, *b*'s, etc. are fitting parameters. The recommended TPP parameters, defaulted in the code, are presented in the TPP report for mixed oxide, UO_2, stainless steel and sodium. Only basic functions are listed in **Table 6-3**. For example, the diffusion coefficient for a binary system and the properties of vapor mixture are not shown because they cannot be expressed as a simple functional form. The partial derivatives appearing in several TPP functions are to be expanded using available EOS functions and thermodynamic relationships. These are detailed in the TPP report.

The liquid heat capacity at constant pressure can be evaluated using EOS functions based on thermodynamic relationships. However, this procedure poorly reproduces the sodium heat capacity in the lower temperature range where the experimental data are well developed. This is due to the simplification made when the MRK equation was extended to a reacting system to better describe thermodynamic states of sodium vapor at a high temperature range. The liquid heat capacity at constant pressure is therefore defined as a TPP function, because it is used to calculate Prandtl number in Nusselt number correlations and hence it is not necessary to consistently satisfy thermodynamic relationships among state variables.

Table 6-1. Main analytic EOS functions defined in SIMMER-III/SIMMER-IV. (1/3)

EOS properties	Analytic EOS functions
Structure temperature	$T_{Sm}=T_{Sol,M}\left[1-a_{S1,M}(1-u_{Sm})-a_{S2,M}(1-u_{Sm})^2-a_{S3,M}(1-u_{Sm})^3\right]$ for $\mathrm{e}_{Sm}<\mathrm{e}_{Sol,M}$ $T_{Sm}=T_{Sol,M}+\dfrac{T_{Liq,M}-T_{Sol,M}}{h_{f,M}}(\mathrm{e}_{Sm}-\mathrm{e}_{Sol,M})$ for $\mathrm{e}_{Sol,M}\le\mathrm{e}_{Sm}<\mathrm{e}_{Liq,M}$ $u_{Sm}=\mathrm{e}_{Sm}/\mathrm{e}_{Sol,M}$ and $h_{f,M}=\mathrm{e}_{Liq,M}-\mathrm{e}_{Sol,M}$
Structure specific volume	$v_{Sm}=v_{Sol,M}\left[1-b_{S1,M}(1-u_{Sm})-b_{S2,M}(1-u_{Sm})^2-b_{S3,M}(1-u_{Sm})^3\right]$ for $\mathrm{e}_{Sm}<\mathrm{e}_{Sol,M}$ $v_{Sm}=v_{Sol,M}+\dfrac{v_{Liq,M}-v_{Sol,M}}{h_{f,M}}(\mathrm{e}_{Sm}-\mathrm{e}_{Sol,M})$ for $\mathrm{e}_{Sol,M}\le\mathrm{e}_{Sm}<\mathrm{e}_{Liq,M}$
Particle temperature	$T_{Lm}=T_{Lm}^{+}+\left(\dfrac{\partial T_{Lm}}{\partial p}\right)_M^0 p$ Note: The terms with "+" lack pressure dependence and apply to the sublimation curve of a solid state. The pressure derivatives are assumed to be constant independent of specific internal energy.
Particle specific volume	$v_{Lm}=v_{Lm}^{+}+\left(\dfrac{\partial v_{Lm}}{\partial p}\right)_M^0 p$
Saturated liquid vapor pressure,	$p_{Lm}^{+}=\exp\left[b_{L1,M}+b_{L2,M}T_{Lm}^{+}+\dfrac{b_{L3,M}}{T_{Lm}^{+}}+b_{L4,M}\ln\left(\dfrac{T_{Lm}^{+}}{T_{Crt,M}}\right)\right]$ Note: The terms with "+" are saturated properties.
Inverted saturated-vapor pressure	$T_{Sat,Gm}=1/\left[a_{Sat1,M}+a_{Sat2,M}(\ln p_{Gm})+a_{Sat3,M}(\ln p_{Gm})^2+a_{Sat4,M}(\ln p_{Gm})^3\right]$
MRK equation for vapor	$p_{Gm}=\dfrac{R_M T_M}{v_{Gm}-a_{G1,M}}-\dfrac{a(T_G)}{v_{Gm}(v_{Gm}+a_{G3,M})}$ $a(T_G)=a_{G2,M}\left(\dfrac{T_G}{T_{Crt,M}}\right)^{a_{G4,M}}$ for $T_G<T_{Crt,M}$ $a(T_G)=a_{G2,M}\left[1+a_{G4,M}\left(\dfrac{T_G}{T_{Crt,M}}-1\right)\right]$ for $T_G\ge T_{Crt,M}$

Table 6-1. Main analytic EOS functions defined in SIMMER-III/SIMMER-IV. (2/3)

EOS properties	Analytic EOS functions
Modified MRK equation with vapor dimerization effect	$p_{Gm} = \frac{R_M T_M}{(1 + y_{B,Gm})(\upsilon_{Gm} - a_{G1,M})} - \frac{a(T_G)}{\upsilon_{Gm}(\upsilon_{Gm} + a_{G3,M})}$ $y_{B,Gm} = \frac{1 + 2x_{Gm} - \sqrt{1 + 8x_{Gm}}6}{2(x_{Gm} - 1)}$, where $x_{Gm} = \frac{k_{2,Gm} R_M T_G}{\upsilon_{Gm} - a_{G1,M}}$ $k_{2,Gm} = \exp\left(d_{G1,M} + \frac{d_{G2,M}}{T_G}\right)$
Spinodal volume	$\upsilon_{Spn} = \upsilon_{Crt,M}\left[1 + f_{S1,M}(1 - \eta_{G1,M})^{1/3} + f_{S2,M}(1 - \eta_{G2,M}) + f_{S3,M}(1 - \eta_{G3,M})^3 + f_{S4,M}(1 - \eta_{G4,M})^5\right]$ $\eta_{G1,M} = \frac{T_G}{T_{Crt,M}}$
Specific volume of saturated vapor (vaporization volume)	$\upsilon_{Vap,Gm} = \upsilon_{Crt,M}\exp\left[b_{G1,M}(1 - \eta_{Sat,Gm})^{1/3} + b_{G2,M}(1 - \eta_{Sat,Gm})^{2/3} + b_{G3,M}(1 - \eta_{Sat,Gm})^{4/3} + b_{G4,M}(1 - \eta_{Sat,Gm})^3 + b_{G5,M}(1 - \eta_{Sat,Gm})^{37/6} + b_{G6,M}(1 - \eta_{Sat,Gm})^{71/6}\right]$ for $T_{Sat.Gm} \le T_{Crt,M}$ $\eta_{Sat,Gm} = T_{Sat.Gm}/T_{Crt,M}$
Specific internal energy of saturated vapor (vaporization energy)	$e_{Vap,Gm} = e_{Liq,M} + c_{G1,M}(T_{Sat.Gm} - T_{Liq.M}) - c_{G2,M}(T_{Sat.Gm} - T_{Liq.M})^2 - c_{G3,M}(T_{Sat.Gm} - T_{Liq.M})^3$ for $T_{Liq.M} < T_{Sat.Gm} \le c_{G4,M} T_{Crt,M}$ $e_{Vap,Gm} = e_{Crt,M}\left[1 + c_{G5,M}(T_{Crt,M} - T_{Sat.Gm})^{1/2} + c_{G6,M}(T_{Crt,M} - T_{Sat.Gm})^2\right]$ for $c_{G4,M} T_{Crt,M} < T_{Sat.Gm} \le T_{Crt,M}$
Specific volume of saturated liquid (condensate volume)	$\upsilon_{Con,Gm} = \upsilon_{Liq,M}\left[1 + b_{Sat1,M}(T_{Sat.Gm} - T_{Liq.M}) + b_{Sat2,M}(T_{Sat.Gm} - T_{Liq.M})^2 + b_{Sat3,M}(T_{Sat.Gm} - T_{Liq.M})^3\right]$ for $T_{Liq.M} < T_{Sat.Gm} \le b_{Sat4,M} T_{Crt,M}$ $\upsilon_{Con,Gm} = \upsilon_{Crt,M}\left[1 + b_{Sat5,M}(T_{Crt,M} - T_{Sat.Gm})^{1/2} + b_{Sat6,M}(T_{Crt,M} - T_{Sat.Gm})^2\right]$ for $b_{Sat4,M} T_{Crt,M} < T_{Sat.Gm} \le T_{Crt,M}$

Table 6-1. Main analytic EOS functions defined in SIMMER-III/SIMMER-IV. (3/3)

EOS properties	Analytic EOS functions
Specific internal energy of saturated liquid (condensate energy)	$e_{Con,Gm} = e_{Liq,M} + c_{Sat1,M}\left(T_{Sat.Gm} - T_{Liq.M}\right) - c_{Sat2,M}\left(T_{Sat.Gm} - T_{Liq.M}\right)^2 - c_{Sat3,M}T_{Liq.M}\left(T_{Sat.Gm} - T_{Liq.M}\right)^3$ for $T_{Liq.M} < T_{Sat.Gm} \le c_{Sat4,M}T_{Crt,M}$ $e_{Con,Gm} = e_{Crt,M}\left[1 + c_{Sat5,M}\left(T_{Crt,M} - T_{Sat.Gm}\right)^{1/2} + c_{Sat6,M}\left(T_{Crt,M} - T_{Sat.Gm}\right)^2\right]$ for $c_{Sat4,M}T_{Crt,M} < T_{Sat.Gm} \le T_{Crt,M}$
Specific internal energy of saturated liquid	$e_{Lm,Sat} = e_{Gm,Sat} - \left(\upsilon_{Gm.Sat} - \upsilon_{Lm.Sat}\right)\left[T_{Sat}\left(\frac{dp}{dT}\right)_{Sat} - p_{Sat}\right]$
Saturated liquid temperature	$T_{Lm}^{+} = T_{Liq,M}\left[1 + a_{L1,M}(u_{Lm} - 1) + a_{L2,M}(u_{Lm} - 1)^2 + a_{L3,M}(u_{Lm} - 1)^3\right]$ for $\mathrm{e}_{Liq,M} < \mathrm{e}_{Lm} \le a_{L4,M}\mathrm{e}_{Liq,M}$ $T_{Lm}^{+} = T_{Crt,M}\left[1 - a_{L5,M}(1 - \xi_{Lm})^2 - a_{L6,M}(1 - \xi_{Lm})^3\right]$ for $a_{L4,M}\mathrm{e}_{Liq,M} < \mathrm{e}_{Lm} \le \mathrm{e}_{Crt,M}$ $u_{Sm} = \mathrm{e}_{Lm}/\mathrm{e}_{Liq,M}$ and $\xi_{Lm} = \mathrm{e}_{Lm}/\mathrm{e}_{Crt,M}$
Saturated liquid specific volume	$\upsilon_{Lm}^{+} = \upsilon_{Liq,M}\left[1 + d_{L1,M}(u_{Lm} - 1) + d_{L2,M}(u_{Lm} - 1)^2 + d_{L3,M}(u_{Lm} - 1)^3\right]$ for $\mathrm{e}_{Liq,M} < \mathrm{e}_{Lm} \le d_{L4,M}\mathrm{e}_{Liq,M}$ $\upsilon_{Lm}^{+} = \upsilon_{Crt,M}\left[1 + d_{L5,M}(1 - \xi_{Lm})^{1/2} + d_{L6,M}(1 - \xi_{Lm})^2\right]$ for $d_{L4,M}\mathrm{e}_{Liq,M} < \mathrm{e}_{Lm} \le \mathrm{e}_{Crt,M}$
Pressure derivative of liquid temperature	$\left(\frac{\partial T_{Lm}}{\partial p}\right)_{e_{Lm}} = \max\left\{\left(\frac{\partial T_{Lm}}{\partial p}\right)_M^o, f(\xi_{Lm})\right\}$ for $e_{Lm} < e_{Crt,M}$ $f(\xi_{Lm}) = \left(\frac{\partial T_{Lm}}{\partial p}\right)_{e_{Crt,M}} \exp\left[c_{L1,M}(1 - \xi_{Lm}) + c_{L2,M}(1 - \xi_{Lm})^{2/3} + c_{L3,M}(1 - \xi_{Lm})^2 + c_{G4,M}(1 - \xi_{Lm})^3\right]$
Pressure derivative of liquid specific volume	$\left(\frac{\partial \upsilon_{Lm}}{\partial p}\right)_{e_{Lm}} = \min\left\{\left(\frac{\partial \upsilon_{Lm}}{\partial p}\right)_M^o, \max\left[g(\xi_{Lm}), f_{L6,M}\right]\right\}$ for $e_{Lm} < e_{Crt,M}$ $g(\xi_{Lm}) = f_{L1,M}\exp\left[f_{L2,M}(1 - \xi_{Lm}) + f_{L3,M}(1 - \xi_{Lm})^2 + f_{L4,M}(1 - \xi_{Lm})^3 + f_{L5,M}(1 - \xi_{Lm})^4\right]$

Table 6-2. EOS sub-materials included in SIMMER-III/SIMMER-IV.

		EOS sub-materials							
EOS materials		1	2	3	4	5	6	7	8
1	fuel*	MOX	UO_2	C-100	C-8416	C-50	C-22	MSRE	MSBR
2	steel	316SS	316SS						
3	coolant*	sodium	water	lead	LBE	LBE**			
4	control	B_4C	B_4C						
5	fission gas	Xe	air						

* compositions of fuel and LBE (lead-bismuth eutectic alloy):

MOX: 80.0 mol% UO_2+20.0 mol% PuO_2

C-100: 77.8 wt% UO_2+22.2 wt% ZrO_2+0.0 wt% Zr

C-8416: 84.0 wt% UO_2+16.0 wt% ZrO_2+0.0 wt% Zr

C-50: 80.0 wt% UO_2+11.5 wt% ZrO_2+8.5 wt% Zr

C-22: 81.5 wt% UO_2+5.0 wt% ZrO_2+13.5 wt% Zr

MSRE: 65.0 mol% LiF+29.1 mol% BeF_2+5.0 mol% ZrF_4+0.9 mol% UF_4

(MSRE: Molten Salt Reactor Experiment)

MSBR: 71.7 mol% LiF+16.0 mol% BeF_2+12.0 mol% Th_{F4}+0.3 mol% UF_4

(MSBR: Molten Salt Breeder Reactor)

LBE: 44.5 wt% Pb+55.5% wt% Bi

** fitting-free EOS parameters are provided composition of fuel

Table 6-3. Main analytic TPP functions defined in SIMMER-III/SIMMER-IV. (1/3)

Thermophysical properties	Analytic TPP functions
Solid thermal conductivity, including solid particles	$\kappa_{Sm} = a_{KS1,M} + \frac{a_{KS2,M}}{T_{Sm}} + \frac{a_{KS3,M}}{{T_{Sm}}^2} + a_{KS4,M}T_{Sm} + a_{KS5,M}{T_{Sm}}^2$
Solid thermal conductivity with porosity, ε_{Sm}, for solid fuel	$\kappa_{Sm}^P = \kappa_{Sm}(1-\varepsilon_{Sm})^{2.5}$
Thermal conductivity and viscosity of liquid (simple function)	$\kappa_{Lm} = a_{KL1,M} + a_{KL2,M}T_{Lm} + a_{KL3,M}{T_{Lm}}^2$ $\mu_{Lm} = b_{ML1,M}\exp\left(\frac{b_{ML2,M}}{T_{Lm}}\right)$
Thermal conductivity and viscosity of vapor (simple function)	$\kappa_{Gm} = \exp\left(a_{KG1,M} + \frac{a_{KG2,M}}{T_G} + a_{KG3,M}T_G + a_{KG4,M}{T_G}^2 + a_{KG5,M}{T_G}^3\right)$ $\mu_{Gm} = b_{MG1,M} + b_{MG2,M}T_G + {b_{MG3,M}}^2$
Thermal conductivity of liquid (extended function for sodium)	$\kappa_{Lm} = a_{KL1,M} + a_{KL2,M}T_{Lm} + a_{KL3,M}{T_{Lm}}^2 \quad \text{for } T_{Lm} \le a_{KL4,M}T_{Lm}$ $\kappa_{Lm} = \kappa_{Crt,M} + a_{KL5,M}\left(T_{Crt,M} - T_{Lm}\right)^{1/2} + a_{KL5,M}\left(T_{Crt,M} - T_{Lm}\right)^2 \quad \text{for } a_{KL4,M}T_{Crt,M} < T_{Lm} \le T_{Crt,M}$ $\kappa_{Lm} = \kappa_{Crt,M} \quad \text{for } T_{Lm} > T_{Crt,M}$
Viscosity of liquid (extended function for sodium)	$\mu_{Lm} = b_{ML1,M}\exp\left(\frac{b_{ML2,M}}{T_{Lm}}\right) \quad \text{for } T_{Lm} \le b_{ML3,M}T_{Lm}$ $\mu_{Lm} = \mu_{Crt,M} + b_{ML4,M}\left(T_{Crt,M} - T_{Lm}\right)^{1/2} + b_{ML5,M}\left(T_{Crt,M} - T_{Lm}\right)^2 \quad \text{for } b_{ML3,M}T_{Crt,M} < T_{Lm} \le T_{Crt,M}$ $\mu_{Lm} = \mu_{Crt,M} \quad \text{for } T_{Lm} > T_{Crt,M}$
Thermal conductivity of vapor (extended function for sodium)	$\kappa_{Gm} = \kappa_{Gm}^D + \left[\kappa_{Crt,M} - \kappa_{Gm}^D\left(T_{Crt,M}\right)\right]\left(\frac{T_G}{T_{Crt,M}}\right)^{n_{f,M}}\frac{v_{Crt,M}}{v_{Gm}} \quad \text{for } T_G \le T_{Crt,M}$ $\kappa_{Gm}^D = a_{KG1,M} + a_{KG2,M}T_G$ $\kappa_{Gm} = \kappa_{Crt,M} \quad \text{for } T_G > T_{Crt,M}$

Table 6-3. Main analytic TPP functions defined in SIMMER-III/SIMMER-IV. (2/3)

Thermophysical properties	Analytic TPP functions
Viscosity of vapor (extended function for sodium)	$\mu_{Gm} = \mu_{Gm}^{D} + \left[\mu_{Crt,M} - \mu_{Gm}^{D}(T_{Crt,M})\right]\left(\frac{T_G}{T_{Crt,M}}\right)^{n_{f,M}} \frac{\upsilon_{Crt,M}}{\upsilon_{Gm}}$ for $T_G \leq T_{Crt,M}$ $\mu_{Gm}^{D} = b_{MG1,M} + b_{MG2,M} T_G$ $\mu_{Gm} = \mu_{Crt,M}$ for $T_G > T_{Crt,M}$
Specific heat at constant pressure of liquid	$c_{p,Lm} = f(\eta_{Lm})^{-1}$ $f(\eta_{Lm}) = d_{CL1,M}(1-\eta_{Lm}) + d_{CL2,M}(1-\eta_{Lm})^{3/2} + d_{CL3,M}(1-\eta_{Lm})^2 + d_{CL4,M}(1-\eta_{Lm})^3 + d_{CL5,M}(1-\eta_{Lm})^4 + d_{CL6,M}(1-\eta_{Lm})^5$ $\eta_{Lm} = T_{Lm}/T_{Crt,M}$
Vapor heat capacity at constant pressure	$c_{p,Gm} = c_{v,Lm} - T_G \left(\frac{\partial p_{Gm}}{\partial T_G}\right)_{\upsilon_{Gm}}^{2} \Big/ \left(\frac{\partial p_{Gm}}{\partial \upsilon_{Gm}}\right)_{T_G}$
Surface tension	$\sigma_{Lm} = c_{SL1,M}\left(1 - \frac{T_{Lm}}{T_{Crt,M}}\right)^{c_{SL2,M}}$
Coefficients of volumetric thermal expansion of liquid	$\alpha_{p,Lm} = \frac{1}{\upsilon_{Lm}}\left(\frac{\partial \upsilon_{Lm}}{\partial T_{Lm}}\right)_p$
Isothermal compressibility of liquid	$\beta_{T,Lm} = -\frac{1}{\upsilon_{Lm}}\left(\frac{\partial \upsilon_{Lm}}{\partial p}\right)_{T_{Lm}}$
Adiabatic compressibility of liquid	$\beta_{S,Lm} = -\frac{1}{\upsilon_{Lm}}\left(\frac{\partial \upsilon_{Lm}}{\partial p}\right)_{s_{Lm}}$
Speed of sound of liquid	$\nu_{S,Lm} = \upsilon_{Lm}/\beta_{S,Lm}\sqrt{\upsilon_{Lm}/\beta_{S,Lm}}$
Coefficients of volumetric thermal expansion of vapor	$\alpha_{p,Gm} = -\frac{1}{\upsilon_{Gm}}\left(\frac{\partial \mathrm{p_{Gm}}}{\partial \mathrm{T_G}}\right)_{\mathrm{p}} \Big/ \left(\frac{\partial p_{Gm}}{\partial \upsilon_{Gm}}\right)_{T_G}$

Table 6-3. Main analytic TPP functions defined in SIMMER-III/SIMMER-IV. (3/3)

Thermophysical properties	Analytic TPP functions
Isothermal compressibility of vapor	$\beta_{T,Gm} = -\frac{1}{v_{Gm}}\left(\frac{\partial p_{Gm}}{\partial v_{Gm}}\right)_{T_G}^{-1}$
Adiabatic compressibility of vapor	$\beta_{S,Gm} = \beta_{T,Gm}\frac{c_{v,Gm}}{c_{p,Gm}}$

7. Neutronics Model

7.0. Overview

7.0.1. Background of models and methods

The SIMMER-III/SIMMER-IV neutron kinetics is modeled by an improved quasi-static method, in which a time-dependent neutron transport equation is factorized into: a shape function that represents the neutron flux distribution but changes only slowly with time, and an amplitude function that accounts for time evolution of the reactor power. The time-dependent neutron cross sections are updated based on the distributions of material densities and energies calculated in the fluid-dynamics and structure modules. A basic approach of the neutronics model is the same as the former SIMMER-II code1), except that the neutron diffusion and point-kinetics models are not included in SIMMER-III/SIMMER-IV.

The development of the neutronics model has been performed in the following steps:

- The fluid-dynamics system of SIMMER-III without neutronics was developed and underwent extensive V&V testing in the Phase 1 assessment program.
- The neutronics model of SIMMER-II was transplanted into SIMMER-III but re-programmed in a fashion consistent with other parts of the code. It includes: the cross-section model, the quasi-static method and the discrete-ordinate S_n neutron transport model based on TWOTRAN-II46). This version of SIMMER-III was used in the Phase 2 assessment program.
- An advanced neutron transport model based on the diffusion-synthesis acceleration method of TWODANT47) was coupled with SIMMER-III by G. Buckel et al.48) of the present KIT, and was made available as an alternative neutronics option.
- The three-dimensional fluid-dynamics module then developed for SIMMER-IV was interfaced, at first, with the two-dimensional neutronics module, either TWODANT- or TWOTRAN-based.
- The SIMMER-IV neutronics module was replaced with the THREEDANT9) model in collaboration with KIT, again taking advantage of the open-source DANTSYS package49).
- After successful implementation of DANTSYS coupled with SIMMER-III/SIMMER-IV and confirmation of their performance both in accuracy and efficiency, the option of the TWOTRAN-based neutronics module was removed from the program library.
- Major improvements from the former SIMMER-II, in addition to the flux shape solution method, include: the neutron up-scattering capability for possible application to thermal neutron systems, and the treatment of an external neutron source for simulating sub-critical systems.
- Other neutronics-related models are: a simple decay heat model based on the SAS4A modeling, and the specified power history capability without neutronics calculation.

In this chapter the models and methods of the neutronics module are described for the fundamental models, cross-section methods, quasi-static method, amplitude function and shape function solution methods, decay heat model, and so on. The model and method descriptions are rather concise, since many of the models have been documented by the original authors. The neutronics model is common to SIMMER-III and SIMMER-IV, except for dimensions 2-D and 3-D, respectively. The mesh-cell index "*ij*" is commonly used in this chapter and this denotes (i,j) in SIMMER-III and (i,k,j) in SIMMER-IV.

7.0.2. Interaction with other models

Coupling with the fluid-dynamics part is carefully designed, because the neutronic state of an LMFR core during a severe accident is determined primarily from time-dependent mass and energy distribution of the core materials. It is because of this time dependence that the shielded (effective) macroscopic cross sections are calculated within the code. To connect with the initiating phase calculations, a capability of transient-state neutronics initialization is available for connecting non-zero reactivity level.

The neutronics calculation provides: the power distributions (specific internal energy generation rates due to nuclear heating) for each of the five heat-source materials (fertile fuel, fissile fuel, steel, sodium and control); and the parabolic fitting coefficients to extrapolate the power amplitude to the subsequent fluid-dynamics time steps. They are then used in fluid dynamics Step 1 to explicitly update the component internal energies due to nuclear heating.

7.1. Fundamental Models

7.1.1. Time-dependent neutron transport equation

In LMFR accident calculations, the time-dependent power and its spatial distribution are the desired objective of the neutronics calculation. The neutron flux must first be obtained to determine the power. The general, linear Boltzmann transport equation for the time-dependent angular flux is given below. It has been assumed that there is no neutron upscattering as is typical for fast neutron reactor calculations, and that anisotropic scattering effects can be approximated satisfactorily by modifications to isotropic cross sections$^{50)}$. The treatment of neutron upscattering has been added later for potential applications to thermal spectrum systems. Also made available is an external neutron source for simulating sub-critical systems.

With these assumptions with new additions, the multi-group time-dependent neutron transport equation is

$$\begin{aligned}\frac{1}{V(E)}\frac{\partial\Psi}{\partial \mathrm{t}} + \vec{\Omega}\cdot\nabla\Psi + \Sigma_t\Psi \\ &= \frac{1}{4\pi}\int_E^\infty \Sigma_s(t,r,E'\to E)\Phi dE' + \frac{\chi_p(E)}{4\pi k_0}\int_0^\infty \nu_p\Sigma_f(t,r,E')\Phi dE' \\ &+ \frac{1}{4\pi}\sum_{d=1}^{IGD}\chi_d(E)\,\lambda_d C_d + S(t,r,E)\,,\end{aligned} \tag{7-1}$$

where

$\Psi = \Psi\left(t,r,\vec{\Omega},E\right)$	angular neutron flux per unit volume, per unit solid angle, per unit energy at the spatial point *r* with direction $\vec{\Omega}$ and energy *E* at time *t*,
$V(E)$	magnitude of the neutron velocity,

$\Sigma_t = \Sigma_t(t,r,E)$	macroscopic total cross section,
$\Sigma_s(t,r,E' \to E)$	macroscopic cross section for isotropic neutron scattering from neutron energy *E'* to neutron energy *E*,
$\Phi = \Phi(t,r,E')$	neutron scalar flux,
$S(t,r,E)$	external neutron source,
k_0	initial stationary k-effective for the reactor system,
$\chi_p(E)$	prompt neutron fission emission spectrum,
ν_p	prompt neutron fission yield,
$\Sigma_f(t,r,E)$	macroscopic fission cross section,
IGD	number of delayed neutron precursor groups,
χ_d	delayed neutron emission spectrum from delayed neutron precursor group *d*,
λ_d	decay constant for delayed neutron precursor group *d*, and
C_d	delayed neutron precursor concentration for precursor group *d*.

In addition to the neutron transport equation, the equations for the delayed neutron precursor concentrations are

$$\frac{\partial C_d}{\partial \mathrm{t}} = -\lambda_d C_d + \frac{1}{k_0}\int_0^\infty \nu_d \Sigma_f(t,r,E')\Phi(t,r,E')dE' , \tag{7-2}$$

where ν_d is the delayed neutron yield for precursor group *d*. As in the neutron transport equation, the delayed neutron precursor equations are converted into difference equations. The time, space, and energy dependencies are treated consistently with those in the transport equations. However, a complete treatment of the delayed neutron precursor dynamics, such as their fluid-dynamic transport independent of other fluid-dynamics components, was considered beyond the scope of the code and hence was neglected.

In these equations, the neutron scalar flux Φ, instead of the angular flux Ψ, is used on the right-hand sides since no anisotropic scattering is explicitly modeled. The scalar flux, found as the solution in Eq. (7-1), is used to determine the power distribution in the materials in the reactor. The specific power in each material is determined from

$$Q_{Nm} = \int_0^\infty \left[\alpha_c^m \Sigma_c^m(t,r,E') + \alpha_f^m \Sigma_f^m(t,r,E')\right]\Phi(t,r,E')dE' , \tag{7-3}$$

where

$Q_{Nm} = Q_{Nm}(t,r,z)$	specific power (W/kg) in material *m*,
α_c^m	energy conversion factor per neutron captured in material *m*,
$\Sigma_c^m(t,r,E')$	macroscopic capture cross section per unit density of material *m*,
α_f^m	energy conversion factor per fission in material *m*,
$\Sigma_f^m(t,r,E')$	macroscopic fission cross section per unit density of material *m*, and

NNMAT=5 number of material mixtures used to compute the neutron flux: fertile fuel, fissile fuel, steel, sodium, and control.

Equation (7-3) considers only the energy production resulting from neutron capture and fission. Therefore, the energy deposition as a result of absorption of gamma photons must be included in the neutron capture term, which then leads to an error in the location of the energy deposition. The power represented in Eq. (7-3) only accounts for the recoverable energy from fission; the decay heat generated in fission and neutron capture products is not explicitly included. A simple decay heat model is later made available and added as an input option.

7.1.2. Cross-section model

In SIMMER-III/SIMMER-IV, the same cross-section model and method as SIMMER-II are used. Anisotropic scattering is treated in an approximated way[50)] similarly to SIMMER-II as well. Treatment of neutron up-scattering, not included in SIMMER-II, has been made available in the cross-section model as an input option, although this is unimportant in fast-spectrum reactor applications.

Several steps are involved in the cross-section calculations. Because the compositions and temperatures of individual cells change with time, microscopic cross sections are input as infinitely dilute (or unshielded) quantities. Cell-wise effective (shielded) microscopic cross sections are calculated according to the Bondarenko formalism after cell compositions and temperatures are known. The effective cross sections then are multiplied by the isotopic atom densities and summed to obtain the macroscopic cross sections to be used in the neutron transport equation.

In the Bondarenko formalism, the capture, fission, elastic scattering, inelastic scattering and transport cross sections for each isotope are calculated for selected temperatures by multiplying input microscopic cross sections by self-shielding factors, *f*, interpolated from input tables. Thus,

$$\bar{\sigma} = f\sigma \,, \tag{7-4}$$

where

$\bar{\sigma}$	effective self-shielded cross section, and
σ	infinitely dilute cross section.

The shielding factor depends on temperature and a background cross section (an effective shielded microscopic cross section for all isotopes in a mixture other than the isotope being considered). Because the background cross section depends on *f*, the iterative process is required for determining cross sections.

During the time-dependent calculations, the background cross section, $\sigma_{o,i}$, is determined for each isotope *i* at each mesh cell as

$$\sigma_{o,i} = \frac{1}{N_i} \sum_{j \neq i} N_j \bar{\sigma}_{t,j} \,, \tag{7-5}$$

where

N_i	atom number density for the isotope *i*, and

N_j atom number density for the isotope j .

From the isotope temperature and background cross sections, the values of the shielding factors are interpolated from tables and the effective cross section is calculated from Eq. (7-4).

As an option, also taken from SIMMER-II, the codes may use a neutronics preprocessor, MXS[51)], to improve both the physics treatment (interpolation methods) and the efficiency of the cross-section shielding calculation. One of the techniques used to improve the efficiency is the combination of isotopes into materials. Some error may be introduced if, during a calculation, the composition of some cell includes materials with a common isotope. The assessment of such errors is covered in Appendix R of the SIMMER-II Manual.

7.2. Cross-Section Methods

7.2.1. Introduction to the cross-section model

The cross sections represent the coupling from the fluid dynamics solution and they vary as the cell-wise isotopic densities and temperatures vary. In SIMMER-III/SIMMER-IV, several steps are involved in the cross-section calculations. Because of the time dependence of individual cell compositions and temperatures, microscopic cross sections are input as infinitely dilute, or unshielded, quantities. Cell-wise shielding factors are calculated according to the Bondarenko formalism after cell compositions and temperatures are known. Macroscopic cross sections for each mesh cell then are calculated by summing the various isotopic cross sections weighted by the appropriate isotopic concentrations and the previously determined shielding factors.

7.2.2 Neutronics mesh structure and coupling with fluid dynamics

The spatial mesh structure used for the neutronics calculations is based on the fluid-dynamics mesh, but the entire domain of the fluid-dynamics mesh need not be used. For the neutronics methods, each mesh cell is considered to be homogeneous; that is, only averaged quantities are described. For some problems, the size of the neutronics cells must be limited to obtain realistic flux shapes or to enhance iteration convergence. Thus, an option is provided to subdivide specified rows or columns of fluid-dynamics cells to reduce computing cost in cross-section calculations. The number of subdivisions desired is user-specified, and a fluid-dynamics cell is subdivided into equal-volume neutronics cells. When a fluid-dynamics mesh cell is subdivided into neutronics mesh cells, it is not necessary to calculate the atom number densities, average temperatures and the macroscopic cross sections for each neutronics mesh cell since the neutronics mesh cells belonging to the relevant fluid-dynamics mesh cell are uniform. An input option is available to calculate cross sections for each fluid-dynamics mesh cell and thereby to save computing cost.

An entire neutronics computational domain can be divided into several cross-section regions, for each of which the isotopic compositions of each material component are fixed. The method is sufficiently general to allow the same isotope to exist in more than one material components.

The neutronics and fluid-dynamics equations are partially decoupled; that is, the equations are not solved simultaneously at each time step. The neutronics state is updated at intervals determined by the fluid-dynamics solution for densities and temperatures at that time. Information transferred from the neutronics module to the fluid-dynamics module includes the cell-wise specific powers and the time dependence of the integral power. The time-dependent behavior of the reactor power is extrapolated from current and previous neutronics solutions, modified to enforce energy conservation between the neutronics and fluid-dynamics solutions, and used for a series of fluid-dynamics steps. This approach permits the separation of the neutronics and fluid-dynamics methods and requires only the communication of such key quantities as component temperatures, densities, and powers.

The interactions between the fluid-dynamics and neutronics calculations occur in both directions. Changes in material densities and temperatures affect the reactor criticality by changing the neutron cross sections, and the neutron flux affects material motion by time- and space-dependent energy deposition caused by neutron capture and fission processed.

The total atom number density and average temperature for each isotope in a cell are determined by

$$\widehat{N}_{ij}^{i} = \sum_{m=1}^{NC} N_{ij}^{im} \bar{\rho}_{ij}^{m} \text{ , and} \tag{7-6}$$

$$\bar{T}_{ij}^{i} = \sum_{m=1}^{NC} N_{ij}^{im} \bar{\rho}_{ij}^{m} \bar{T}_{ij}^{m} \Big/ \widehat{N}_{ij}^{i} \text{ ,} \tag{7-7}$$

where

$\widehat{N}_{ij}^{i}$	total atom number density of isotope *i* for mesh cell *ij*,
N_{ij}^{im}	atom number density of isotope *i* in component *m* for mesh cell *ij*,
$\bar{\rho}_{ij}^{m}$	average density of component *m* for mesh cell *ij*,
$\bar{T}_{ij}^{i}$	average temperature of isotope *i* in each mesh cell *ij*, and
$\bar{T}_{ij}^{m}$	average temperature of component *m* in each mesh cell *ij*.

7.2.3. Calculation of macroscopic cross sections

Changes in the resonance self-shielding of the cross sections are caused by changes in the temperature and/or the background from other isotopes. This is modeled by self-shielding factors that multiply the infinitely dilute cross sections to give the effective (self-shielded) microscopic cross sections. To determine the macroscopic cross section for a particular reaction in a mesh cell, the isotopic number densities and appropriate shielding factors multiply the infinitely dilute (unshielded) cross sections.

$$\Sigma_{x,ijg} = \sum_{i=1}^{LNISIP} \widehat{N}_{ij}^{i} \sigma_{x,g}^{i} f_{x,ijg}^{i} \text{ ,} \tag{7-8}$$

where

x	particular reaction type,
$\sigma_{x,g}^{i}$	infinitely-dilute cross section of reaction type *x* for isotope *i* (input),

$f^i_{x,ijg}$	shielding factor for isotope *i* for reaction type *x* evaluated for the background cross section and temperature of mesh cell *ij*, and
$LNISIP$	total number of isotopes.

The former SIMMER-II could treat only 5 types of self-shielding factors: total, fission, capture, transport, and elastic down-scatter, since this was judged sufficient for simulating fast neutron systems. For potential application to thermal neutron systems, however, the SIMMER-III/SIMMER-IV codes have been improved to model neutron upscattering. As a result, a total of nine types of self-shielding factors are treated: total, fission, capture, transport, elastic upscatter, elastic in-group scatter, elastic downscatter, inelastic in-group scatter, and inelastic downscatter.

The microscopic cross sections used in SIMMER-III/SIMMER-IV are listed in **Table 7-1**, and the shielding factors required for the cross sections are listed in **Table 7-2**. The formulae required for the different macroscopic cross sections are given in **Table 7-3**, for the standard code option with "ISOTOPE on" and the approximate treatment of P_1 anisotropic scattering. It is noted that the fission cross section is always accompanied by the neutron yield per fission as:

$$\left(\nu_f \Sigma_f\right)_{ijg} = \sum_{i=1}^{LNISIP} \hat{N}^i_{ij} \left(\nu^i_f \sigma^i_f\right)_g f^i_{f,ijg} \,, \tag{7-9}$$

where

ν^i_f	total neutron yield per fission.

Equation (7-8) is not used in calculating the energy deposition cross sections. For nuclear heating, the energy deposition is proportional to the mass of the component. During the fluid-dynamics calculation, the mass of each component in a cell may be changing continuously; hence, it is appropriate to calculate the energy source for each component as the energy per unit mass and then multiply this result by the component density during the fluid-dynamics calculation. The cross sections for determining energy deposition are calculated as

$$\Sigma^m_{e,ijg} = \sum_{i=1}^{LNISIP} N^{im}_{ij} \left(\alpha^i_f \sigma^i_{f,ijg} + \alpha^i_c \sigma^i_{c,ijg}\right) , \tag{7-10}$$

where

$\Sigma^m_{e,ijg}$	energy deposition macroscopic cross section per unit density of component *m* for neutron energy group *g* in mesh cell *ij*,
α^i_f	energy conversion factor per fission in isotope *I*, and
α^i_c	energy conversion factor per neutron capture in isotope *i*.

After the neutron flux is calculated, the power per unit mass (W/kg), or the specific internal energy generation rate, of component *m* in each cell is calculated as

$$Q_{Nm,ij} = \sum_{g=1}^{IGM} \Sigma^m_{e,ijg} \phi_{ijg} \,, \tag{7-11}$$

where $\phi_{ijg}$is the spatial flux shape (The product of the flux shape and the flux amplitude equals the flux). The power densities are passed to the fluid-dynamics calculation and are multiplied by the flux amplitude, and by the component densities in the structure-, liquid-, and vapor-field energy equations.

7.2.4. Determination of shielding factors

The resonance self-shielding of the cross sections due to the temperature changes and the presence of other isotopes is modeled by self-shielding factors that multiply the infinitely dilute cross sections to give the effective (self-shielded) microscopic cross sections. At each reactivity time step, these effective microscopic cross sections are computed to form the various macroscopic cross sections required for each mesh cell.

The Bondarcnko method uses a background cross section to represent the total macroscopic cross section caused by all isotopes except for isotope j in mesh cell *ij*. Since the background cross section cannot be determined until the total shielded cross sections of all isotopes are known, an iteration must be used to obtain both the shielding factors and the shielded total cross section. The total macroscopic cross section for a group is:

$$\Sigma_{t,ijg} = \widehat{N}_{ij}^{j}\sigma_{t,ijg}^{j} + \sum_{j\neq k}\widehat{N}_{ij}^{k}\sigma_{t,ijg}^{k} \, , \tag{7-12}$$

where

$\sigma_{t,ijg}^{j} = f_{t,ijg}^{j}\sigma_{t,g}^{j}$ total microscopic cross section for isotope j, and

$f_{x,ijg}^{i} = f(\sigma_{o}, T)$ resonance self-shielding factor defined as a function (input table) of background cross section and temperature.

Dividing Eq. (7-10) by $\widehat{N}_{ij}^{j}$,

$$\frac{\Sigma_{t,ijg}}{\widehat{N}_{ij}^{j}} = \sigma_{t,ijg}^{j} + \frac{1}{\widehat{N}_{ij}^{j}}\sum_{j\neq k}\widehat{N}_{ij}^{k}\sigma_{t,ijg}^{k} \, . \tag{7-13}$$

The second term on the right side of Eq. (7-13) is defined as the background cross section:

$$\sigma_{o,ijg}^{j} = \frac{1}{\widehat{N}_{ij}^{j}}\sum_{j\neq k}\widehat{N}_{ij}^{k}\sigma_{t,ijg}^{k} \, . \tag{7-14}$$

The background cross section describes the effect of other isotopes in a mixture. The effect is especially significant in the vicinity of a large cross-section resonance. The background cross section cannot be determined until the total shielded cross sections of all isotopes are known. Because $\sigma_{x,ijg}^{k}$ is a function of the shielding factor $f_{x,ijg}^{k}$ for isotope k and reaction type x and hence it depends on its background cross section, an iterative procedure is used to obtain both the shielding factors and the shielded total cross section, as described in the SIMMER-II Manual.

Shielding factors are interpolated first over background and then over temperature. The interpolation is logarithmic for background and linear for temperature. First, the range of tabular values is searched to determine the tabulation points closest to the isotopic temperature and background values desired. Next, the background interpolated values are obtained for each tabular temperature point. Finally, a second interpolation over temperature is performed.

7.2.5. Use of neutronics preprocessor

In the standard cross-section method described in the previous sections, the operations are performed with individual isotopes as the basic quantity. This method therefore is called the code option "ISOTOPE on". Alternative approach is implemented to reduce the computing cost of isotope-wise cross-section data handling. In this option, invoked with ISOTOPE off, the MXS51) neutronics preprocessor is used to create material cross sections prior to transient calculations.

Since the method developed for SIMMER-II are described elsewhere in detail1), only the summary of this approach is given below:

- The isotopic cross sections are premixed by the MXS preprocessor to create material cross sections. This permits the number of different cross sections to be reduced.
- Interpolation of the background dependence of shielding factors has been replaced by the evaluation of interpolation formulas. This significantly reduces computational effort of table search and interpolation.
- Quantities that need to be calculated only once for a transient calculation have been placed in the MXS preprocessor.

7.3. Quasistatic Method Equations

The improved quasistatic method52) is used in SIMMER-III/SIMMER-IV, which is essentially the same as SIMMER-II, to treat the time dependence of the discrete-ordinate transport equation. The approach is based on the fact that the power level, or flux amplitude, changes much more rapidly than the power distribution, or the spatial flux shape. Thus, the amplitude equation contains most of time dependence, where it can be treated easily because it is described as an ordinary differential equation. The flux-shape equation requires most of the computational effort; however, it is solved only as needed, that is, when transient flux shape change becomes significant.

Because changes in flux-shape and flux amplitude occur with different characteristic time scales, the quasistatic algorithm is well suited to respond to varying degree of fluid dynamic-neutronic coupling. The algorithm is based on a three-tiered time-step structure: the smallest time steps apply only to the amplitude-equation solution, the intermediate steps (reactivity steps) are associated with evaluating the shape equation and amplitude equation coupling terms, and the largest steps (shape steps) are associated with the flux-shape solution interval.

7.3.1. Flux factorization

The approach used in the quasistatic method is based on factoring the time-dependent spatial flux into a scalar amplitude function that contains the major time dependence and a spatial flux shape function that contains all the space dependence of the flux but is slowly varying with time. The time dependent flux shape may be either the angular flux, Ψ, or the total (scalar) flux, Φ; the factorization approach is the same in both cases. Thus, the flux is

$$\Psi\left(t,r,\vec{\Omega},E\right) = N(t)\psi\left(t,r,\vec{\Omega},E\right)\text{, or} \tag{7-15a}$$

$$\Phi(t,r,E) = N(t)\phi(t,r,E)\,, \tag{7-15b}$$

where $N(t)$ is the amplitude function and $N(0) = 1$. The use of the flux-shape constraint condition makes the factorization unique.

$$\sum_{i,j} V_{ij} \sum_{g=1}^{IGM} \frac{\Phi_{ijg}^{*}\phi_{ijg}}{V_g} = 1\,, \tag{7-16}$$

where

V_g	average neutron velocity in energy group *g*,
V_{ij}	volume of mesh cell *ij*, and
Φ_{ijg}^{*}	integrated adjoint neutron flux-shape function for mesh cell *ij* and energy group *g*.

7.3.2. Procedure for fluid-dynamics/neutronics. coupling

The neutronics and fluid dynamics solutions are coupled by a tine-dependent amplitude function and spatial distribution of specific material powers for use during a series of fluid-dynamics steps; in turn, these neutronics parameters depend on the current fluid-dynamic configuration. Prediction of the amplitude-function time dependence is based on an extrapolation of the previous neutronics history. The validity of this approach requires that changes in the power level result from phenomena that do not change in character instantaneously. The spatial distribution of specific material powers is assumed to change slowly because it depends on the flux shape. Thus, although its magnitude changes, this distribution remains unchanged during a series of fluid-dynamic steps.

After a series of fluid-dynamic steps, the reactivity is recalculated based on the new material densities and temperatures predicted by the fluid-dynamic calculation. The amplitude function is recalculated and compared with the previously predicted function actually used in the fluid-dynamics calculations. If the difference between the predicted and updated amplitude function is not great, only a small error correction is made by adjusting the amplitude-function projection for the next series of fluid-dynamic steps to account for the energy mismatch. This approach limits the number of fluid-dynamic steps that can be used with a single amplitude function projection.

After a series of reactivity steps, the quasistatic constraint integral may begin to deviate significantly from unity. This is a result of the flux shape changing in response to the material motion and temperature changes; the neutron sources and sinks in the amplitude equation become out of balance with the sources and sinks in the shape equation. Therefore, the flux should be refactored. This is accomplished by performing a γ-iteration at the end of a shape step, where the amplitude function used over the shape step is modified by a series of flux-shape recalculations until the quasistatic constraint integral is satisfied. The modification of the amplitude function again introduces a discrepancy between the energy integrated in the fluid-dynamics calculation and that predicted in the neutronics calculation because the fluid-dynamics calculation is not included in the iteration. This discrepancy is treated by adjusting the amplitude function used in the next series of fluid-dynamic steps rather than performing an iteration between the fluid dynamics and neutronics. The amplitude function is projected for a series of fluid-dynamic steps by first extrapolating the reactivity state and then solving the amplitude equations. The reactivity state time dependence is modeled by a parabola with coefficients determined by the reactivities at two previous reactivity steps. After the amplitude equation is solved, a parabola in the logarithm of the amplitude is fitted to the extrapolated point and two previous ones. This function then is evaluated in the fluid-dynamics calculation.

The spatial distribution of material specific powers is based on the flux shape and cell cross sections at the most recent reactivity step. Cell power shape is calculated in the fluid-dynamics module by multiplying the material specific powers by their respective masses and summing over materials. The actual power then is obtained by multiplication with the amplitude function. This results in a first-order-accurate prediction of the effects of fluid motion and temperature change, with only the corresponding flux-shape changes and cross-section shielding changes neglected during the fluid-dynamics calculation.

7.3.3. Flux-shape equations

The procedure to calculate the flux shape function $\psi(t,r,\vec{\Omega},E)$ is briefly described below. For convenience, the equations of the time-dependent neutron transport and flux factorization are repeated below.

$$\begin{aligned}\frac{1}{V(E)}\frac{\partial\Psi}{\partial \mathrm{t}}+\vec{\Omega}\cdot\nabla\Psi+\Sigma_t\Psi & \\ &=\frac{1}{4\pi}\int_E^\infty \Sigma_s(t,r,E'\to E)\Phi(t,r,E')dE' \\ &+\frac{\chi_p(E)}{4\pi k_0}\int_0^\infty \nu_p\Sigma_f(t,r,E')\Phi(t,r,E')dE'+\frac{1}{4\pi}\sum_{d=1}^{IGD}\chi_d(E)\,\lambda_d C_d \\ &+S(t,r,\vec{\Omega},E)\,,\end{aligned} \tag{7-1}$$

$$\Psi(t,r,\vec{\Omega},E)=N(t)\psi(t,r,\vec{\Omega},E)\,,\text{and} \tag{7-15a}$$

$$\Phi(t,r,E)=N(t)\phi(t,r,E). \tag{7-15b}$$

By substituting Eq. (7-15) to Eq. (7-1) and dividing by $N(t)$, we obtain:

$$\begin{aligned}\frac{1}{V(E)}\left[\frac{\partial\psi}{\partial \mathrm{t}}+\frac{1}{N(t)}\frac{dN(t)}{dt}\psi\right]&+\vec{\Omega}\cdot\nabla\psi+\Sigma_t\psi\\ &=\frac{1}{4\pi}\int_E^{\infty}\Sigma_s(t,r,E'\to E)\phi(t,r,E')dE'\\ &+\frac{\chi_p(E)}{4\pi k_0}\int_0^{\infty}\nu_p\Sigma_f(t,r,E')\phi(t,r,E')dE'+\frac{1}{4\pi N(t)}\sum_{d=1}^{IGD}\chi_d(E)\,\lambda_d C_d\\ &+S\big(t,r,\vec{\Omega},E\big)\,.\end{aligned} \tag{7-17}$$

In the improved quasistatic approach, the partial derivative of angular flux, $\partial\psi/\partial \mathrm{t}$, is replaced by a linear backward-difference relation as

$$\frac{\partial\psi\big(t,r,\vec{\Omega},E\big)}{\partial \mathrm{t}}\approx\frac{\psi\big(t,r,\vec{\Omega},E\big)-\psi\big(t-\Delta t,r,\vec{\Omega},E\big)}{\Delta t}, \tag{7-18}$$

where $t-\Delta t$ is the previous time step of the flux-shape calculation. This means the explicit temporal dependence of ψ is no longer needed. This approximation is justified because the neutron flux shape changes only slowly with time and the time step sizes are appropriately controlled to take any larger changes in flux shape into account. The time derivative on the amplitude, $dN(t)/dt$, is calculated outside the flux shape calculation and is replaced simply by the numerical value. The resultant shape equation becomes:

$$\begin{aligned}\vec{\Omega}\cdot\nabla\psi\big(t,r,\vec{\Omega},E\big)&+\left[\frac{1}{V(E)\Delta t}+\frac{1}{V(E)N(t)}\frac{dN(t)}{dt}+\Sigma_t\right]\psi\big(t,r,\vec{\Omega},E\big)\\ &=\frac{1}{4\pi}\int_E^{\infty}\Sigma_s(t,r,E'\to E)\phi(t,r,E')dE'\\ &+\frac{\chi_p(E)}{4\pi k_0}\int_0^{\infty}\nu_p\Sigma_f(t,r,E')\phi(t,r,E')dE'+\frac{1}{4\pi N(t)}\sum_{d=1}^{IGD}\chi_d(E)\,\lambda_d C_d\\ &+\frac{1}{V(E)\Delta t}\psi\big(t-\Delta t,r,\vec{\Omega},E\big)+\frac{1}{N(t)}S(t,r,E)\,.\end{aligned} \tag{7-19}$$

The form of Eq. (7-19) is essentially the same as the equation of the time-independent (stationary) neutron transport theory with an external neutron source. The Solver module from the DANTSYS system is applied as a solution method for the flux-shape equation as described later.

7.3.4. Delayed-neutron precursor equations

The delayed-neutron precursor equation, Eq. (7-2), is rewritten in a multigroup form

$$\frac{\partial C_{ijd}}{\partial \mathrm{t}}=-\lambda_d C_{ijd}+N(t)F_{ijd}^d\;,\ \mathrm{d}=1,\cdots,\mathrm{IGD}\,, \tag{7-20}$$

where F_{ijd}^d is the delayed-neutron precursor shape term:

$$F_{ijd}^d=\frac{1}{k_0}\sum_{g=1}^{IGM}\big(\nu_d\Sigma_f\big)_{ijg}\,\phi_{ijg}\,, \tag{7-21}$$

where $\left(\nu_d \Sigma_f\right)_{ijg}$ denotes the product of the delayed-neutron yield ν_d and the fission cross section Σ_f for neutron energy group g.

7.3.5. Amplitude equation

The equation for the amplitude function, N, is obtained by summing flux-shape equation over m, multiplying by the initial stationary adjoint flux, Φ^*_{ijg}, and summing over all energy groups and all mesh cells. The resulting equation is

$$\frac{dN}{dt} = \frac{\rho - \beta}{\Lambda} N + \sum_{d=1}^{IGD} \lambda_d c_d + s \,. \tag{7-22}$$

In this derivation, the reactivity, ρ, the effective delayed-neutron fraction, β, the neutron generation time, Λ, the effective delayed-neutron precursor concentrations, c_d, and the effective external neutron source, s, are defined. These terms couple the amplitude equation to the flux-shape equation. Solution of the amplitude equation also involves the simultaneous solution of the delayed-neutron source equations. This set of equations is obtained by multiplying Eq. (7-20) by $\Phi^*_{ijg}\chi_{dg}V_{ij}$ (where Φ^*_{ijg} is the initial stationary adjoint flux) and summing over all energy groups and mesh cells:

$$\frac{dc_d}{dt} = -\lambda_d c_d + \frac{\beta_d}{\Lambda} N \,, \ \text{d=1}, \cdots, \text{IGD} \,. \tag{7-23}$$

7.3.6. Flux-shape/amplitude coupling terms

The amplitude equation parameters that couple the flux-shape and amplitude equations are defined as follows:

Effective delayed-neutron fraction:

$$\beta_d = \frac{1}{F} \sum_{ij} V_{ij} \sum_{g=1}^{IGM} \Phi^*_{ijg} \frac{\chi_{dg}}{k_o} \sum_{g'=1}^{IGM} \left(\nu_d \Sigma_f\right)_{ijg'} \phi_{ijg'} \tag{7-24}$$

Total effective delayed-neutron fraction:

$$\beta = \sum_{d=1}^{IGD} \beta_d \tag{7-25}$$

Effective neutron generation time:

$$\Lambda = \frac{1}{F} \sum_{ij} V_{ij} \sum_{g=1}^{IGM} \frac{\Phi^*_{ijg} \phi_{ijg}}{V_g} = \frac{1}{F} \tag{7-26}$$

Effective delayed-neutron precursor concentrations:

$$c_d = \sum_{ij} V_{ij} \sum_{g=1}^{IGM} \Phi^*_{ijg} \chi_{dg} C_{ijd} \tag{7-27}$$

Effective external neutron source:

$$s = \sum_{ij} V_{ij} \sum_{g=1}^{IGM} \Phi^*_{ijg} S \tag{7-28}$$

The effective neutron source, F, is given by,

$$F = \frac{1}{k_o} \sum_{ij} V_{ij} \sum_{g=1}^{IGM} \Phi^*_{ijg} \left[\chi_{pg} \sum_{g'=1}^{IGM} \left(\nu_p \Sigma_f\right)_{ijg'} \phi_{ijg'} + \sum_{d=1}^{IGD} \chi_{dg} \sum_{g'=1}^{IGM} \left(\nu_d \Sigma_f\right)_{ijg'} \phi_{ijg'} \right]. \tag{7-29}$$

Equation (7-27) is not needed formally because both the effective delayed-neutron concentration, c_d, and the spatial delayed-neutron precursor concentration, C_{ijd}, are defined by initial conditions. These two concentrations are calculated by numerical methods with quite different error characteristics, and hence they may become out of balance during a long calculation, and as a result, the quasistatic constraint integral will not converge to unity during the γ-iteration at shape recalculation steps. Equation (7-27) is used to rebalance the delayed neutron sources in the amplitude and shape equations periodically.

The products of the prompt and delayed neutron yields per fission and the fission cross section, appearing in the above equations, are currently evaluated using the total neutron yield per fission obtained from input cross-section file and the effective delayed-neutron fraction as:

$$\left(\nu_p \Sigma_f\right)_{ijg} = (1-\beta)\left(\nu_f \Sigma_f\right)_{ijg}\text{, and} \tag{7-30a}$$

$$\left(\nu_d \Sigma_f\right)_{ijg} = \beta_d \left(\nu_f \Sigma_f\right)_{ijg}, \tag{7-30b}$$

where ν_f is the neutron yield per fission that is divided into prompt and delayed neutron contributions and the values of β and β_d used in these equations are taken from the user input, not using Eqs. (7-24) and (7-25), in the present coding.

Because the amplitude equation was derived by integrating the time-dependent transport equation, the terms in the reactivity equation can be associated with terms in the transport equation. Thus, the total reactivity is expressed by the sum of the contributions:

$$\rho = \rho_{FP} + \rho_{FD} + \rho_S - \rho_L - \rho_T, \tag{7-31}$$

where ρ_{FP} is the prompt fission, ρ_{FD} is the delayed fission, ρ_S is the scatter, ρ_L is the leakage, and ρ_T is the total (associated with total cross section) contribution to the reactivity. The two fission contributions are:

$$\rho_{FP} = \frac{1}{F} \left[\sum_{ij} V_{ij} \sum_{g=1}^{IGM} \Phi^*_{ijg} \frac{\chi_{pg}}{k_o} \sum_{g'=1}^{IGM} \left(\nu_p \Sigma_f\right)_{ijg'} \phi_{ijg'} \right]\text{, and} \tag{7-32}$$

$$\rho_{FD}=\frac{1}{F}\left[\sum_{ij}V_{ij}\sum_{g=1}^{IGM}\Phi_{ijg}^{*}\sum_{d=1}^{IGD}\frac{\chi_{dg}}{k_o}\sum_{g'=1}^{IGM}\left(\nu_d\Sigma_f\right)_{ijg'}\phi_{ijg'}\right]. \tag{7-33}$$

The other contributions are:

$$\rho_S=\frac{1}{F}\sum_{ij}V_{ij}\sum_{g=1}^{IGM}\Phi_{ijg}^{*}\sum_{g'=1}^{IGM}\Sigma_{S,ijg'\to g}\,\phi_{ijg'}\text{ , and} \tag{7-34}$$

$$\rho_T=\frac{1}{F}\sum_{ij}V_{ij}\sum_{g=1}^{IGM}\Phi_{ijg}^{*}\,\Sigma_{T,ijg}\phi_{ijg}\,. \tag{7-35}$$

The leakage component of reactivity, ρ_L, cannot be defined by cell-wise scalar fluxes, like used in other reactivity components. The angular fluxes are used as

$$\rho_L=\frac{1}{F}\sum_{ij}V_{ij}\sum_{m}\sum_{g=1}^{IGM}\Phi_{ijg}^{*}\,\omega_m\nabla\psi_{ij,m,g}\,, \tag{7-36}$$

where ω_m is the solid angle for the direction with angular discrete-ordinate index *m*.

The calculative approach to solving the amplitude equation is based on the standard method, as detailed in Appendix M of the SIMMER-II Manual.

7.3.7. Fluid-dynamics/neutronics coupling terms

After the fluid-dynamics calculation is interrupted for a neutronics reactivity step, the total macroscopic densities and mass-averaged temperatures needed for the cross-section calculation are determined from the appropriate fluid-dynamics quantities for each of the five components (fertile fuel, fissile fuel, steel, sodium, and control). The following equations are used for the density calculations for SIMMER-III:

$$\bar{\rho}_{Fert}=\bar{\rho}_{int1}+\bar{\rho}_{s1}+\bar{\rho}_{s3}+\bar{\rho}_{s5}+\bar{\rho}_{l1}+\bar{\rho}_{l5}+\bar{\rho}_{l9}+\bar{\rho}_{g1}\,, \tag{7-37a}$$

$$\bar{\rho}_{Fiss}=\bar{\rho}_{int2}+\bar{\rho}_{s2}+\bar{\rho}_{s4}+\bar{\rho}_{s6}+\bar{\rho}_{l2}+\bar{\rho}_{l6}+\bar{\rho}_{l10}+\bar{\rho}_{g2}\,, \tag{7-37b}$$

$$\bar{\rho}_{SS}=\bar{\rho}_{s7}+\bar{\rho}_{s8}+\bar{\rho}_{s9}+\bar{\rho}_{s10}+\bar{\rho}_{s11}+\bar{\rho}_{l3}+\bar{\rho}_{l7}+\bar{\rho}_{g3}\,, \tag{7-37c}$$

$$\bar{\rho}_{Na}=\bar{\rho}_{l4}+\bar{\rho}_{g4}\text{ , and} \tag{7-37d}$$

$$\bar{\rho}_{Cont}=\bar{\rho}_{s12}+\bar{\rho}_{l8}\,. \tag{7-37e}$$

The fission gas component is not considered in the neutronics calculations because the effect of fission gas is negligible. The following set of equations is used for the component temperature calculations in SIMMER-III:

$$T_{Fert}=\frac{\bar{\rho}_{int1}T_{Int}+\bar{\rho}_{s1}T_{S1}+\bar{\rho}_{s3}T_{S2}+\bar{\rho}_{s5}T_{S3}+\bar{\rho}_{l1}T_{L1}+\bar{\rho}_{l5}T_{L4}+\bar{\rho}_{l9}T_{L7}+\bar{\rho}_{g1}T_G}{\bar{\rho}_{Fert}}, \tag{7-38a}$$

$$T_{Fiss} = \frac{\bar{\rho}_{int2}T_{Int} + \bar{\rho}_{s2}T_{S1} + \bar{\rho}_{s4}T_{S2} + \bar{\rho}_{s6}T_{S3} + \bar{\rho}_{l2}T_{L1} + \bar{\rho}_{l6}T_{L4} + \bar{\rho}_{l10}T_{L7} + \bar{\rho}_{g2}T_G}{\bar{\rho}_{Fiss}}, \tag{7-38b}$$

$$T_{SS} = \frac{\bar{\rho}_{s7}T_{S4} + \bar{\rho}_{s8}T_{S5} + \bar{\rho}_{s9}T_{S6} + \bar{\rho}_{s10}T_{S7} + \bar{\rho}_{s11}T_{S8} + \bar{\rho}_{l3}T_{L2} + \bar{\rho}_{l7}T_{L5} + \bar{\rho}_{g3}T_G}{\bar{\rho}_{SS}}, \tag{7-38c}$$

$$T_{Na} = \frac{\bar{\rho}_{l4}T_{L3} + \bar{\rho}_{g4}T_G}{\bar{\rho}_{Na}}\text{ , and} \tag{7-38d}$$

$$T_{Cont} = \frac{\bar{\rho}_{s12}T_{S12} + \bar{\rho}_{l8}T_{L6}}{\bar{\rho}_{Cont}}. \tag{7-38e}$$

Here the macroscopic densities and temperature of the pin-fuel interior node, $\bar{\rho}_{int1}$, $\bar{\rho}_{int2}$ and T_{Int}, calculated in the fuel-pin model outside the fluid-dynamics model, are added. The above is for the standard SPIN option (and the pin fuel radial temperature distribution is considered in the DPIN option). For SIMMER-IV, the additional structure-field steel components, which represent the front and back can walls, must be added to Eqs. (7-37c) and (7-38c).

7.4. Flux Shape Solution Method

The discrete-ordinates flux shape equation presented in Eq. (7-19) is solved numerically using an iterative procedure. This procedure involves two levels of iteration referred to as inner (within-group) and outer (energy-group-dependent source) iterations. The acceleration of these iterations is of crucial importance to transport codes in order to reduce the computation time involved. The iterative procedure employs the diffusion synthetic acceleration (DSA) method developed by Alcouffe53), an extremely effective method for accelerating the convergence of the iterations.

7.4.1. Iterative solution procedure for flux shape

The Solver Modules of the open-source DANTSYS system package49) have been transplanted to SIMMER-III and SIMMER-IV from TWODANT and THREEDANT Solvers, respectively. Since the solution method and procedure of DANTSYS are documented in detail elsewhere in the original Los Alamos report9), they are not reproduced in the present report. Only the summary of the iterative procedure is described in the following.

In the Solver Modules, a standard inner (within-group) iteration, outer (energy-group-dependent source) iteration technique is used. The inner iterations are concerned with the convergence of the pointwise scalar fluxes in each group for a given source distribution. The outer iterations are concerned with: the convergence of the eigenvalue, the fission-source distribution and the energy-group upscatter source if any or all are present. Both the inner and outer iterations are accelerated using the DSA method. The diffusion solver uses the standard multigrid method and Chebychev acceleration of the fission source.

For problems containing fissionable material the iterative procedure begins with the calculation of a diffusion coefficient for each space-energy point. Using the diffusion coefficients, a standard diffusion calculation is performed for each energy group. With the fluxes for all groups, a new fission source rate distribution is calculated and this is then used to generate new diffusion fluxes. The process is repeated until both the fission source rate and the pointwise fluxes are converged. Each such recalculation is called a “diffusion sub-outer iteration.”

Next, using the diffusion-converged fission source rate and using the first energy-group diffusion scalar fluxes to fix the within-group scattering sources, a single discrete-ordinates transport sweep through the spatial mesh is made for the first energy group. In this sweep angular fluxes are generated and they are used to calculate an effective diffusion coefficient at each mesh cell. With these effective diffusion coefficients, a diffusion sweep for the group is performed to determine the group scalar flux at each point. This transport sweep, followed by a calculation of the diffusion coefficients, followed by a diffusion sweep is called an “inner iteration”. Since the new diffusion calculated group scalar flux changes the within-group scattering source term, the inner iterations may be repeated before proceeding to the next energy group.

When the inner iterations for the first energy group are completed, the group scalar fluxes and flux moments are used to calculate the scattering source for the next group. One or more inner iterations are performed for the next group and the process is repeated until all energy groups have been completed.

When all energy groups have been calculated via inner iterations, the group fluxes are used to calculate a new fission source rate distribution. Following this a series of diffusion sub-outer iterations is performed. In these diffusion sub-outer iterations, however, the effective diffusion coefficients from the last-completed inner iteration for each group are used, thus making the sub-outer iteration calculation a synthetic diffusion calculation.

Each completion of the diffusion sub-outer iteration process based on the current set of diffusion coefficients defines the completion of an outer iteration. The first outer iteration is seen to be a pure diffusion calculation, while all subsequent outer iterations are synthetic diffusion in nature. Outer iterations continue until convergence is achieved.

One improvement for SIMMER-III/SIMMER-IV made to the original DANTSYS iterative procedure is an additional remedy to cope with convergence failure in outer iterations. A diffusion sub-outer iteration is turned off when the maximum change of fission source does not decrease due to mismatch of diffusion and transport fission sources.

7.4.2. Negative flux treatment

The discrete-ordinates form of approximation is used for treating the angular variation of the neutron flux and the diamond-difference scheme is used for space-angle discretization. It is well known negative fluxes can be calculated when implementing this diamond-difference scheme. Negative fluxes are eliminated by a local “set-to-zero-and-correct” algorithm, or so-called “flux fixup” remedy. The logic of this algorithm is that if any one flux is negative at a cell edge, it is set to zero and the cell-centered flux is recomputed assuming that particular flux is zero. Lathrop54) observed that “in many cases the negative fluxes can be tolerated because they occur in regions in which fluxes are small and unimportant”. The experience with SIMMER-II using different schemes suggested1) that the flux fixup scheme should be accurate because it is the minimum deviation from the second-order accuracy of the diamond-difference equations.

In the DANTSYS system, an adaptive weight diamond-difference (AWDD) scheme is available as an alternative option as a remedy to the negative flux problem. It was argued that there remains some difficulty in determining input weighting parameters used in the AWDD option. It was therefore decided that this option is not implemented in SIMMER-III/SIMMER-IV until future applications necessitate such a remedy be taken into consideration.

7.4.3. Adjoint equation solution method

The quasistatic method requires a weighting function to calculate the amplitude-equation parameters. Normally, this weighting function is taken as the adjoint flux for the stationary reactor state before initiating the transient. However, for SIMMER transient calculations that begin from transient reactor states predicted by other computer codes, the stationary reactor state is not available. The stationary adjoint flux for the transient reactor state at the beginning of the SIMMER calculation is considered to be a reasonably good weighting function that does not differ significantly from the normal adjoint-flux weighting function. The adjoint flux is evaluated only once at the beginning of the transient.

The adjoint transport equation is solved by transposing the scattering and fission source matrices and inverting the group order of the problem. Transposition of the scattering matrix converts the normal downscattering problem to an upscattering problem. The downscattering dominance is restored by inverting the group order. The adjoint equation is solved before the real flux equation because the adjoint fluxes are required for the transient-state initialization. The capability of adjoint flux calculations is available in the DANTSYS system9), and the same solution method implemented in SIMMER-III/SIMMER-IV.

Although the initial adjoint flux is normally used as a weighting function in the quasistatic method, use of an alternative functions is possible. There is an input option to specify “unity” (uniform distribution over the entire neutronics computational domain). This option may be used in such an extreme case such as a major portion of the core fuel has relocated in large scale.

7.5. Quasistatic Calculative Procedure

The quasistatic algorithm requires three different calculations characterized by different time scales in the order from the largest:

- determination of the flux shape,
- determination of reactivity and other amplitude equation parameters, and
- solution of the amplitude equations.

7.5.1. Overall calculative flow

First, new cross sections are calculated from the material densities and temperatures predicted by the fluid-dynamics calculation for the end of the previous reactivity step. These cross sections and updated fluxes are used to calculate new amplitude-equation parameters. The spatial distribution of specific material powers is updated in preparation for the next series of fluid-dynamics steps. The amplitude equation then is solved again for the current reactivity step. Next, the amplitude equation parameters are extrapolated quadratically to the end of the next reactivity step, and the amplitude equation is solved for the amplitude.

The logarithm of this amplitude and the amplitude for the two previous reactivity steps is fitted to a parabola and used to calculate the power level for the subsequent fluid-dynamics calculation. This description summarizes the neutronics calculations that occur at the end of a reactivity step and prepare for the initiation of the next reactivity step. After the fluid-dynamics calculation for the next reactivity step is completed, the cycle continues until the end of the current flux-shape step is reached.

If the end of a shape step is reached, the cycle is interrupted after the calculation of the reactivity state resulting from the previous series of fluid-dynamic steps. Thus, a new flux shape is calculated after the new cross sections are determined. Amplitude-equation parameters resulting from the new flux shape are compared with the parameters from the extrapolated flux shape. Any change in the parameters is assumed to have accumulated linearly during the shape step. The amplitude-equation parameters are corrected for each reactivity step within the shape step, and the corresponding amplitude-equation solutions are recalculated. If the constraint condition is satisfied to within a given tolerance, the amplitude-equation parameters are extrapolated into the next reactivity step, and the calculation proceeds as from the beginning. Otherwise, the calculation proceeds as from the end of the shape step with the recalculation of the flux shape.

The correction of the amplitude-equation parameters for the difference between the initial quadratically extrapolated values and the final shape-step values results in a power discrepancy between the fluid-dynamics and neutronics calculations. To maintain a consistent total energy between the two calculations, the amplitude function is adjusted after its calculation from the amplitude equation to include the discrepancy in energy from the previous shape step. This discrepancy is generally a small fraction of the total energy calculated for the shape step.

The quasistatic calculative algorithm and procedure briefly described above were transplanted from SIMMER-II and re-programmed. The detailed description is found in the original SIMMER-II Manual1), and only a short summary is provided in the rest of this section.

7.5.2. Time-step controls

The time-step controls for the quasistatic method regulate the length of both the reactivity step and the shape step. The controls become very tight for a reactivity near prompt critical, but they are relaxed for a reactivity not near prompt critical.

The shape time step is predicted or limited by the following seven separate controls, and determined as the minimum of them.

(1) Previous step size

(2) Change in leakage

(3) Number of reactivity steps

(4) Problem time

(5) Maximum shape step

(6) Change in shape

(7) Maximum change in reactivity

The reactivity time step is predicted or limited by the following six separate controls, and determined as the minimum of them.

(1) Previous reactivity step

(2) Change in reactivity

(3) Shape-step size

(4) Maximum reactivity step size

(5) Change in amplitude

(6) Maximum inverse period

In addition, a reactivity step also may be forced by changes that occur during the fluid-dynamics calculation. The limits are applied to changes in amplitude, material component masses, and component energies.

The further details of the neutronics time step control are presented in **Section 8.3**.

7.5.3. Initialization

The specific power shape for each material *m* in each mesh cell *ij* is calculated as

$$Q_{Nm,ij} = \frac{1}{\rho_{ij}^{m}} \sum_{g=1}^{IGM} \left(\alpha_f^m \Sigma_{f,ijg}^m + \alpha_c^m \Sigma_{e,ijg}^m\right)\phi_{ijg} , \tag{7-39}$$

where

$Q_{Nm,ij}$	specific energy generation rate for nuclear heating of material *m*,
ρ_{ij}^m	microscopic density of material *m*,
α_f^m	energy conversion factor per fission,
$\Sigma_{f,ijg}^m$	macroscopic fission cross section,
α_c^m	energy conversion factor per neutron captured, and
$\Sigma_{e,ijg}^m$	macroscopic capture cross section.

The fission power in the reactor system is calculated as

$$P_f = N(0)\sum_{ij} V_{ij}\sum_{m=1}^{NC} Q_{Nm,ij}\bar{\rho}_{ij}^m , \tag{7-40}$$

where

$N(0)$	initial value of the amplitude function (=1.0),

V_{ij}	volume of mesh cell ij,
$\bar{\rho}_{ij}^{m}$	macroscopic density of material m, and
NC	number of neutronics materials (fertile fuel, fissile fuel, steel, sodium and control).

The initial flux solution is unnormalized. To obtain the desired initial power, the fluxes are multiplied by the ratio of the desired power to the calculated power. The initial precursor concentrations and the material-specific power also are normalized by this factor. The quasistatic constraint constant normalizes the adjoint flux.

Equation (7-40) only accounts for fission and capture contributions to the reactor power. When the decay heat model (see **Section 7.6**) is used, the contribution of decay heat power is considered as well.

7.5.4. Transient-state initialization

An initial neutronics state may not be the pre-transient stationary state. For example, if a SIMMER-III/SIMMER-IV calculation is connected and continued from an initiating-phase calculation using such as SAS4A, the neutronics calculations must be initialized for a nonstationary reactor state with a non-zero reactivity level. The method developed for the transient initialization uses quasistatic methodology to give consistency between the constant point-kinetics parameters used for the initiating-phase calculation and the time-dependent amplitude-equation parameters. As a result, reactivity, power, and other integral kinetics parameters remain continuous at the connection between the two codes. This is done by computing the factors, using the quasistatic approach, that adjust the basic physical neutronics data to permit continuity of two consecutive calculations.

Details of the transient initialization are provided in Appendix H of the SIMMER-II Manual.[1)] The initial flux shape, stationary-state eigenvalue, data adjustment factors, and the delayed-neutron source normalization factor are calculated iteratively. The usual normalization procedure is followed. First, the real flux shape is normalized to yield the desired initial (transient state) reactor power. Then the adjoint flux is normalized to satisfy the quasistatic constraint condition.

7.5.5. Reactivity evaluation steps

There are two approaches concerning how the flux shape is treated in a reactivity step, as a user input option. The first and standard approach is “flux-shape extrapolation”, in which the flux shape used to recalculate the reactivity after a series of fluid-dynamic steps is extrapolated from the two previous flux-shape solutions at shape steps. This approach requires less computational effort; however, it simply assumes linear changes in flux shape. The effect of threshold or nonlinear changes in fluid-dynamic behavior will not be recognized until the end of the shape step when the flux shape is recalculated. If significant changes in reactivity result from the flux-shape change, the iteration that occurs over the series of reactivity steps and at the end of shape steps will not produce accurate results. The second approach is called “flux-shape update”, in which the flux shape updated at each reactivity step. An abbreviated series of outer iterations is performed to improve the flux shape but not to provide a fully converged solution[55)].

Thus, the effect of changes resulting from fluid-dynamic effects appears in the flux shape at each reactivity step, although much computational effort is required.

In both approaches, the first step is to calculate new cell-dependent cross sections corresponding to the new configuration with new cell material densities and temperatures. If the flux-shape extrapolation option is used, the flux shape is extrapolated to the end of the current reactivity step based on flux shapes calculated at the two previous shape steps. Next, the amplitude equation coefficients are calculated from the current cross sections and the extrapolated flux shapes or, if the flux-shape update option is used, the flux shape from the previous reactivity step. In both methods, the amplitude equation then is solved for the current reactivity step based on the updated coefficients. The spatial delayed-neutron source is updated based on the current and previous reactivity-step fission sources and the integrating factors determined in the amplitude-equation solution.

In the flux-shape update option, the calculation is continued by the flux shape calculation module, with the flux shape from the previous reactivity step provided as an initial guess. Convergence criteria are provided that are less restrictive than the criteria used at shape steps. For small changes in the reactor configuration, usually one outer iteration will meet the convergence criteria. More unusually, significant changes may require three or four outer iterations. After the flux shape is converged, the amplitude-equation coefficients are recalculated based on the new flux shape. The spatial material power distribution also is recalculated. The amplitude equation again is solved for the current reactivity step.

If the current shape step has not been completed, the amplitude equation parameters are projected in both the extrapolation and the update method. The projection is parabolic and based on the current and two previous reactivity step values. The amplitude equation then is solved for the next reactivity step. The amplitude variation over the next reactivity step is characterized by fitting a parabola in log amplitude to the amplitude at the end of the next reactivity step, the current amplitude, and the amplitude at the previous reactivity step.

The calculation then is transferred to the fluid-dynamics modules. A series of fluid-dynamics steps is completed, and the reactivity-step cycle begins again.

7.5.6. Flux-shape evaluation steps

A fully converged flux shape is calculated. The amplitude-equation coefficients then are calculated based on the new flux shape. The spatial material power distribution is calculated for the next reactivity step. Next, the changes in the amplitude-equation coefficients, from the previous iteration or the first iterate values at the end of the current shape step, are distributed linearly over all the reactivity steps composing the current shape step. The series of amplitude-equation solutions for each reactivity step then is repeated. The current value of the amplitude function is available for the next iterative solution of the flux-shape equation or extrapolation of the power for the next series of fluid-dynamics steps. During this procedure, the spatial delayed neutron-precursor concentrations are integrated, and the value is compared with the effective precursor concentrations used in the amplitude equations. If a significant difference is detected, the spatial concentrations are modified so as to agree with the amplitude-equation value.

This iterative process is completed when the quasistatic constraint condition is satisfied to within a user-specified tolerance, until the change in between two consecutive iterations is less than a tenth of the tolerance, or until the number of iterations exceeds a user-specified maximum.

7.6. Decay Heat Model

7.6.1. Model and method

The simple decay heat model for SIMMER-III/SIMMER-IV is based on SAS4A56); thus, decay heating is treated consistently in the two codes. The decay heat precursors, such as fission products and neutron capture products, are grouped into several decay heat groups depending on the rates and characteristics of their decay. The original SAS4A model has been simplified on the two points. First, the region-dependent decay characteristics (curves) modeled in SAS4A is not treated. Second, the treatment of irradiation history to determine the initial decay heat energy is not modeled. In the present SIMMER decay heat model, the time variation of decay heat power is determined by a point reactor model similarly to the fission power amplitude, and its spatial distribution is assumed to be the same as the fission power distribution. The decay heat power is added only to the fuel components since it is reasonable to assume the decay heat precursors always stay with fuel materials.

The normalized total power T_t is defined by the sum of fission power and decay heat power as

$$T_t(t) = T_f(t) + T_h(t)\,, \tag{7-41}$$

and $T_t(0) = 1$, where the fission power T_f represents all the recoverable energy generation resulted from fission reaction, including both the direct fission and neutron capture contributions as shown in Eq. (7-39).

Let h_n be the normalized decay heat energy, defined as the precursor concentration times energy release for decay heat, for decay heat group *n*. Then it is assumed that the change of decay heat energy is determined from the generation of the precursors due to fission and their decay characterized by time constants.

$$\frac{dh_n(t)}{dt} = \beta_{hn} T_f(t) - \lambda_{hn} h_n(t)\ , \tag{7-42}$$

where

β_{hn}	effective decay heat power fraction in decay heat group *n*,
λ_{hn}	effective decay constant for decay heat group n, and
$T_f(t)$	normalized fission power.

The decay heat fractions β_{hn} and the decay constants λ_{hn} are specified by user input variables. It is noted that β_{hn} is defined as the ratio of decay heat power to fission power (not total power), in the same way as SAS4A. The normalized fission power T_f is replaced by the fission amplitude as

$$T_f(t) = T_f(0) N(t)\,, \tag{7-43}$$

where $T_f(0)$ is the initial normalized fission power and $N(t)$ is the fission power amplitude obtained by solving the amplitude function equation. Equation (7-42) is re-written with the amplitude as

$$\frac{dh_n(t)}{dt} = \beta_{hn} T_f(0) N(t) - \lambda_{hn} h_n(t)\,. \tag{7-44}$$

Given the time dependence of the fission-power amplitude by solving the amplitude function equation, the equation for the normalized decay heat energy production, Eq. (7-44), is integrated directly to obtain the advanced time step value. The integration yields:

$$h_n(t+\Delta t) = h_n(t) e^{-\lambda_{hn}\Delta t} + \beta_{hn} T_f(0) e^{-\lambda_{hn}(t+\Delta t)} \int_t^{t+\Delta t} N(t') e^{\lambda_{hn} t'} dt'\,, \tag{7-45}$$

where the initial values of $T_f(0)$ and $h_n(0)$ must be determined during the initialization, as described later. In the solution procedure of the amplitude equation, the fission power amplitude is represented by a second order polynomial for time variation as

$$N(t+\Delta t) = N_f(t) + N_1 \Delta t + N_2 (\Delta t)^2\,, \tag{7-46}$$

and the fitting coefficients N_1 and N_2 have been determined.

The integral in Eq. (7-44) is evaluated as:

$$e^{-\lambda_{hn}(t+\Delta t)} \int_t^{t+\Delta t} N(t') e^{\lambda_{hn} t'} dt' = \left(\frac{1}{\lambda_{hn}}\right) \left[I_{1n} N_f(t) + I_{2n} \frac{N_1}{\lambda_{hn}} + I_{3n} \frac{N_2}{\lambda_{hn}^2} \right], \tag{7-47}$$

where

$$I_{1n} = 1 - e^{\lambda_{hn}\Delta t}\,, \tag{7-48a}$$

$$I_{2n} = \lambda_{hn}\Delta t - I_{1n}\,, \text{and} \tag{7-48b}$$

$$I_{3n} = (\lambda_{hn}\Delta t)^2 - 2 I_{2n}\,. \tag{7-48c}$$

Evaluating Eqs. (7-48) in the above order for small time steps ($\lambda_{hn}\Delta t < 0.01$) may result in unacceptable propagation of small numerical round-off errors in the calculations of the exponential in I_{1n}. Therefore, for small time steps, a series expansion of the exponential term is used along with an inverted recursion order as:

$$I_{3n} = 2 \left[\frac{(\lambda_{hn}\Delta t)^3}{3!} - \frac{(\lambda_{hn}\Delta t)^4}{4!} + \frac{(\lambda_{hn}\Delta t)^5}{5!} - \cdots \right], \tag{7-49a}$$

$$I_{2n} = \frac{1}{2} \left[(\lambda_{hn}\Delta t)^2 - I_{3n} \right], \text{and} \tag{7-49b}$$

$$I_{1n} = \lambda_{hn}\Delta t - I_{2n}\,, \tag{7-49c}$$

where the first two terms of the right side of Eq. (7-49a) are actually included in the code.

7.6.2. Input and initialization of decay heat model

For decay heat parameters, β_{hn} and λ_{hn}, the same input variables can be used as SAS4A if a SIMMER calculation is initiated by connecting from SAS4A. When only the data for decay heat power fractions of total power $\bar{\beta}_{hn}$ are available, the input β_{hn} are internally calculated as

$$\beta_{hn} = \bar{\beta}_{hn} \Bigg/ \left(1 - \sum_{n=1}^{\mathrm{NDKGRP}} \bar{\beta}_{hn} \right). \tag{7-50}$$

The initial decay heat energy $h_n(0)$ must be also supplied by user input. The solution of Eq. (7-44) at $t = 0$ is:

$$h_n(0) = \beta_{hn} T_f(0) \int_{-\infty}^{0} N(t') e^{\lambda_{hn} t'} dt' . \tag{7-51}$$

If the values of $N(t')$ for the reactor power history ($t' \leq 0$) are known, the initial decay heat energies are calculated by Eq. (7-51). When a SIMMER calculation is initiated by connecting from a SAS4A calculation, the values of $h_n(t)$ from the SAS4A calculation must be adjusted in SIMMER input because the amplitude is re-normalized in SIMMER initialization while maintaining the decay heat power fractions. The decay heat energy h_n and normalized total power T_t in the SAS4A calculation at the time of connection t_c are used to initialize the initial decay heat energy $h_n(0)$ in the SIMMER calculation as:

$$h_n(0) = h_n^{SAS4A}(t_c) / T_t^{SAS4A}(t_c) . \tag{7-52}$$

When a SIMMER calculation is initiated after a long-term steady-state reactor operation, the initial decay heat energy is simply evaluated, by ignoring the time dependence in Eq. (7-44),

$$h_n(0) = \frac{\beta_{hn}}{\lambda_{hn}} T_f(0) , \tag{7-53}$$

where the initial normalized fission power $T_f(0)$ is determined from

$$T_f(0) = T_t(0) - T_h(0) = 1 - T_h(0) , \tag{7-54}$$

and the initial normalized decay heat power is simply calculated by

$$T_h(0) = \sum_{n=1}^{\mathrm{NDKGRP}} \lambda_{hn} h_n(0) . \tag{7-55}$$

The initial decay heat power $T_h(0)$ is normalized to the initial total power, which is specified by the input variable $P_t(0)$.

7.6.3. Update of power shape with decay heat power

From the updated decay heat energy in Eq. (7-44), the normalized decay heat power is calculated by

$$T_h(t) = \sum_{n=1}^{\mathrm{NDKGRP}} \lambda_{hn} h_n(t) , \tag{7-56}$$

and the normalized fission power is given by Eq. (7-43), or

$$T_f(t) = T_f(0)N(t) = N(t)\left(1 - \sum_{n=1}^{\mathrm{NDKGRP}} \lambda_{hn} h_n(0)\right). \tag{7-57}$$

To determine the specific power distribution with decay heat contribution, the fission power (W) of the system for each material is first shown below, as defined in the cross-section model in Eq. (7-10).

$$P_{f,m} = \sum_{ij} V_{ij} \bar{\rho}_{m,ij} Q_{Nm,ij}\,, \tag{7-58}$$

where $Q_{Nm,ij}$ is the specific power per unit mass (W/kg) for material *m* in mesh cell i, V_{ij} is the mesh cell volume and $\bar{\rho}_{m,ij}$ is the macroscopic density of material *m*. Then the total decay heat power in the system (W) is:

$$P_h = T_h(t) P_t(0)\,. \tag{7-59}$$

Since the specific power shape $Q_{Nm,ij}$ accounts only for fission power generation, the contribution of decay heat power generation must be added. This is done by adjusting the power shape using the ratio of the total decay heat power to the total fission power of fuel materials. Since the decay heat is only generated by the fuel materials, the power shape of only the fuel materials (*m* = 1 and 2) is adjusted. The power shapes of other materials are unadjusted.

$$\hat{Q}_{Nm,ij} = Q_{Nm,ij}\left(1 + \frac{P_h}{P_{f,1} + P_{f,2}}\right)\,,\ \text{for } m = 1 \text{ and } 2\,. \tag{7-60}$$

7.7. Recent Model Addition

7.7.1. Isotope-wise delayed neutron yields

In the standard treatment in the quasi-static neutron kinetics, the delayed-neutron fractions β_d are calculated using Eqs. (7-24) and (7-29), which are repeated below.

$$\beta_d = \frac{1}{F}\sum_{ij} V_{ij} \sum_{g=1}^{IGM} \Phi^*_{ijg} \frac{\chi_{dg}}{k_o} \sum_{g'=1}^{IGM} \left(\nu_d \Sigma_f\right)_{ijg'} \phi_{ijg'}\,, \tag{7-24}$$

where the total neutron source is given by

$$F = \frac{1}{k_o}\sum_{ij} V_{ij} \sum_{g=1}^{IGM} \Phi^*_{ijg}\left[\chi_{pg} \sum_{g'=1}^{IGM} \left(\nu_p \Sigma_f\right)_{ijg'} \phi_{ijg'} + \sum_{d=1}^{IGD} \chi_{dg} \sum_{g'=1}^{IGM} \left(\nu_d \Sigma_f\right)_{ijg'} \phi_{ijg'}\right]. \tag{7-29}$$

The delayed neutron spectra χ_{dg} are specified by user input variable (Prompt fission neutron spectrum χ_{pg} is taken from the cross-section file (ISOTXS) by specifying a representative fissile isotope, typically Pu^{239}). The $\left(\nu_p \Sigma_f\right)_{ijg'}$ and $\left(\nu_d \Sigma_f\right)_{ijg'}$ terms are evaluated by Eq. (7-30) using β_d, in which the total neutron yield per fission times fission cross section $\left(\nu_f \Sigma_f\right)_{ijg}$ is calculated from the cross-section file. Isotope dependence of neutron yield is taken into account only for the total neutron yield, but the isotope dependence of delayed neutron yield is not treated.

A new option, proposed by the French partner, is available in which the isotope-wise delayed neutron yields ν_d^i are specified directly by an input variable. The delayed-neutron fractions in this option are calculated by,

$$\beta_d = \frac{1}{F'}\sum_{ij} V_{ij} \sum_{g=1}^{IGM} \Phi^*_{ijg} \frac{\chi_{dg}}{k_o} \sum_{g'=1}^{IGM} \sum_{i=1}^{LNISIP} \hat{N}^i_{ij} \left(\nu^i_d \sigma^{i,eff}_{f,ijg}\right)_{ijg'} \phi_{ijg'} , \tag{7-61}$$

where ν_d^i is the input delayed neutron yield for isotope *i*,

$$\sigma^{i,eff}_{f,ijg} = \sigma^i_{f,ijg} f^i_{f,ijg} \tag{7-62}$$

is self-shielded effective microscopic fission cross section, and

$$F' = \frac{1}{k_o}\sum_{ij} V_{ij} \sum_{g=1}^{IGM} \Phi^*_{ijg} \left[\chi_{pg} \sum_{g'=1}^{IGM} \left(\nu_p \Sigma_f\right)_{ijg'} \phi_{ijg'} + \sum_{d=1}^{IGD} \chi_{dg} \sum_{g'=1}^{IGM} \sum_{i=1}^{LNISIP} \hat{N}^i_{ij} \left(\nu^i_d \sigma^{i,eff}_{f,ijg}\right)_{ijg'} \phi_{ijg'}\right], \tag{7-63}$$

where $\left(\nu_p \Sigma_f\right)_{ijg}$ is evaluated as,

$$\left(\nu_p \Sigma_f\right)_{ijg} = (1-\beta) \sum_{i=1}^{LNISIP} \hat{N}^i_{ij} \left(\nu^i_f \sigma^{i,eff}_{f,ijg}\right)_{ijg} . \tag{7-64}$$

Note that application of the option has not been fully tested in the code, including transient-state initialization (ITR=1).

7.7.2. Flexible fuel isotope composition (Pu vector)

In the standard SIMMER-III neutronics model, two fuel materials, fertile and fissile fuel, are modeled to represent a variation of fissile enrichment in different regions, like in a two-zoned LMFR core design. Our common practice is to assign uranium isotopes to fertile fuel and plutonium isotopes and minor actinides to fissile fuel, both including oxygen. This simple assignment is justified in the homogeneous core design because the isotopic composition of plutonium is reasonably assumed to be uniform even in different enrichment zones. Although multiple cross-section regions can be defined in SIMMER-III, allowing to use different materials and isotope composition in different regions, a single region is usually preferred especially for cases with possible fuel movement across the cross-section region boundary.

For simulation of a large heterogeneous core, in which the isotope composition of plutonium produced in the internal blanket region may significantly differ from the composition of the initially loaded plutonium in the active core, a current simplistic assignment of uniform plutonium composition over the entire core is inappropriate. For this reason, a new model, called as “Pu vector”, has been developed to flexibly model the spatial and temporal variation of isotopic composition of the fuel components and thereby to accurately calculate reactivity changes due to fuel motion[57)].

In the Pu vector model, the fertile fuel and fissile fuel density components are no longer distinguished. To represent the variations in fuel isotopic composition, a new input variable $f_{M,n,ij}$ is introduced to denote the mass fraction of isotope *n* included in fuel component *M*,

$$f_{M,n,ij} = \bar{\rho}_{M,n,ij} \Big/ \sum_{n \in M} \bar{\rho}_{M,n,ij} \text{ ,} \tag{7-65}$$

where

$\bar{\rho}_{M,n,ij}$ macroscopic density of n-th isotope in fuel component *M* in mesh cell *ij*,

M fuel components (pin fuel interior and surface, crust fuel on each can wall, liquid fuel, fuel particles, fuel chunks and fuel vapor), and

n isotope ID numbers of each fuel component.

The fuel components are the same as the fluid-dynamics energy components, except that pin fuel involves pin fuel interior node treated in the structure model. The macroscopic density of each isotope is generally not known, but they can be calculated from the neutronics input variables of the theoretical density and atom number density of each fuel component.

To generalize the Pu vector model, it is assumed that 7 fuel energy components in SIMMER-III (9 components in SIMMER-IV) in cell *ij* may have different isotope compositions. The fuel isotope mass fractions $f_{M,n,ij}$ are specified in the fluid-dynamics mesh cell input, either region-wise or cell-wise. The number of isotopes for each fuel component is also specified by user input. Note that the same isotope fraction is used for both the pin-fuel interior node and the surface node (fluid-dynamics energy component *S*1).

The local intra-cell mass transfers and convection of fuel components result in changes in isotope composition. An example of intra-cell mass transfer from fuel component M_c to $M_{c\prime}$, the isotope mass fractions are updated using the mass transfer rate $\Gamma_{Mc,Mc\prime}$ as:

$$f_{M_{c\prime},n,ij}^{n+1} = \frac{\bar{\rho}_{M_{c\prime},n,ij}^{n} f_{M_{c\prime},n,ij}^{n} + \Delta t \Gamma_{M_c,M_{c\prime}} f_{M_{c},n,ij}^{n}}{\bar{\rho}_{M_{c\prime},n,ij}^{n+1}} \text{ , and} \tag{7-66a}$$

$$f_{M_{c},n,ij}^{n+1} = f_{M_{c},n,ij}^{n} \text{ .} \tag{7-66b}$$

This operation is performed for all the fuel mass transfer paths at the end of fluid-dynamics Step 1.

The update of the isotope mass fractions due to fluid convection is performed in fluid-dynamics Step 4 using the end-of-time-step velocity. The 4 fuel components, liquid fuel, fuel particles, fuel chunks and fuel vapor, are treated separately. For three-dimensional SIMMER-IV, the fuel isotope mass fractions are updated, similarly to the convection of internal energy, as:

$$f_{M,n,ikj}^{n+1} = \frac{1}{\bar{\rho}_{M,n,ikj}^{n+1}} \left\{ \bar{\rho}_{M,n,ikj}^{n} f_{M,n,ikj}^{n} - \Delta t \left[\frac{\Delta_i \left\langle \bar{\rho}_M^n f_{M,n}^n r^{\zeta} u_q^{n+1} \right\rangle_{k,j}}{r_i^{\zeta} \Delta x_i} + \frac{\Delta_k \left\langle \bar{\rho}_M^n f_{M,n}^n w_q^{n+1} \right\rangle_{j,i}}{r_i^{\zeta} \Delta y_k} + \frac{\Delta_j \left\langle \bar{\rho}_M^n f_{M,n}^n v_q^{n+1} \right\rangle_{i,k}}{\Delta z_j} \right] \right\}, \tag{7-67}$$

where the notation of the equation is the same as those used in **Chapter 3**. Subscript *q* denotes the velocity field to which fuel component *M* is assigned.

After the fluid-dynamics calculation is interrupted for a neutronics reactivity step, the total macroscopic densities and mass-averaged temperatures needed for the cross-section calculation are determined from the appropriate fluid-dynamics quantities for each of the heat-source components. In the Pu-vector model, fuel component densities are calculated for individual isotopes which are used in the neutronics. The following equations are used for the fuel density calculations for fuel isotope *n* in SIMMER-III:

$$\bar{\rho}_{fuel,n} = (\bar{\rho}_{int} + \bar{\rho}_{S1}) f_{S1,n} + \bar{\rho}_{S2} f_{S2,n} + \bar{\rho}_{S3} f_{S3,n} + \bar{\rho}_{L1} f_{L1,n} + \bar{\rho}_{L4} f_{L4,n} + \bar{\rho}_{L7} f_{L7,n} + \bar{\rho}_{G1} f_{G1,n}\,, \tag{7-68}$$

where the cell index *ij* is omitted. The following equation is used for the component temperature calculations:

$$T_{fuel,n} = \frac{1}{\bar{\rho}_{fuel,n}} \left[(\bar{\rho}_{int} T_{int} + \bar{\rho}_{S1} T_{S1}) f_{S1,n} + \bar{\rho}_{S2} T_{S2} f_{S2,n} + \bar{\rho}_{S3} T_{S3} f_{S3,n} + \bar{\rho}_{L1} T_{L1} f_{L1,n} + \bar{\rho}_{L4} T_{L4} f_{L4,n} + \bar{\rho}_{L7} T_{L7} f_{L7,n} + \bar{\rho}_{G1} T_G f_{G1,n} \right]. \tag{7-69}$$

The refinement and validation of the Pu-vector model is to be continued in collaboration with CEA, France.

7.8. Special Models for External Control

7.8.1. External neutron source

An external neutron source can be provided by user input specifications for possible applications to neutron-source-driven reactors or sub-critical systems. The neutron source is used in both the flux shape and power amplitude calculations. The source is specified by a neutron-source amplitude-versus-time table, a spatial distribution and an energy spectrum of the neutron source.

7.8.2. Specified external reactivity

In the quasistatic method, the reactivity is evaluated from the neutron flux shape reflecting material motion and energy change. The reactivity effects of those phenomena which are not modeled in the codes, such as control-rod movement, can be simulated by specifying a reactivity history externally via user input. The external reactivity history is specified either by an input reactivity-versus-time table or a reactivity ramp rate. In the reactivity calculation, the fission source terms are adjusted to take external reactivity into account.

7.8.3. Specified power history

The SIMMER-III and SIMMER-IV codes can be applied to a variety of multi-field, multi-component thermo-fluid-dynamics problems with or without neutronics. The historic code option “URANUS” is available for creating a code version with no neutronics capability. Even without the neutronics, internal heat sources can be specified by means of a power-versus-time table and specific power density distribution, based on user input variables.

7.8.4. Restart and neutronics re-initialization

The restart capability of SIMMER-III and SIMMER-IV is used to interrupt a computation and resume the same run continuously. The computer memory containing all the common block variables is dumped to restart dump files according to user input instruction. A new capability has been developed to re-initialize the neutronics calculation, using a fluid-dynamics restart dump file. The adjoint flux required for the quasistatic method is newly calculated at the restart point based on the mass and temperature distributions from the fluid dynamics. The initial conditions and parameters of the neutronics are supplied by user input, similarly to the initial run. This feature is useful when the re-initialization of the neutronics is desired with re-calculated adjoint flux.

In addition, a fluid-dynamics calculation without neutronics (URANUS) can be restarted with the neutronics using the restart dump file. This feature is useful when a simulation of a long-lasting accident sequence is switched from a neutronically inactive core state to an active state.

Table 7-1. Microscopic cross sections

Symbol	Variable	Definition
σ_c	LISCAP	Capture (n,γ)
σ_{tr}	LISTRN	Transport
σ_t	LISTOT	Total
σ_f	LISFIS	Fission (n,f)
$\sigma_{el,dw}$	LISELO	Elastic downscatter
$\sigma_{el,g\to g}$	LISELI	Elastic in-group scatter
$\sigma_{inel,dw}$	LISINO	Inelastic downscatter
$\sigma_{inel,g\to g}$	LISINI	Inelastic in-group scatter
$\sigma_{(n,2n),dw}$	LISN2O	(n,2n) downscatter
$\sigma_{(n,2n),g\to g}$	LISN2I	(n,2n) in-group scatter
σ_{msc}	LISMSC	(n,α) + (n,d) + (n,t) + (n,p), etc.
$\nu_f\sigma_f$	LISNSF	Neutron yield per fission times fission cross section
$\sigma_{\mathrm{el,P1},g\to g}$	LISEI1	P1 component of elastic in-group scatter
$\sigma_{\mathrm{el,P1,dw}}$	LISEO1	P1 component of elastic downscatter
$\sigma_{\mathrm{inel,P1},g\to g}$	LISII1	P1 component of inelastic in-group scatter
$\sigma_{\mathrm{inel,P1,dw}}$	LISIO1	P1 component of inelastic downscatter
$\sigma_{(n,2n),\mathrm{P1},g\to g}$	LISNI1	P1 component of (n,2n) in-group scatter
$\sigma_{(n,2n),P1,dw}$	LISNO1	P1 component of (n,2n) downscatter
$\sigma_{\mathrm{el,up}}$	LISEU0*	Elastic upscatter
$\sigma_{\mathrm{el,P1,up}}$	LISEU1*	P1 component of elastic upscatter

* used when ISOTOPE is on with up-scattering

Table 7-2. Isotopic shielding factors

Symbol	Variable	Definition
f_t	LIFTT	Total
f_f	LIFFF	Fission
f_c	LIFFC	Capture
f_{tr}	LIFTR	Transport
$f_{el,up}$	LIFEU*	Elastic upscatter
$f_{el,g\rightarrow g}$	LIFEI	Elastic in-group scatter
$f_{el,dw}$	LIFEO	Elastic downscatter
$f_{inel,g\rightarrow g}$	LIFII	Inelastic in-group scatter
$f_{inel,dw}$	LIFIO	Inelastic downscatter

* used when ISOTOPE is on with up-scattering

Table 7-3. Macroscopic cross sections

(ISOTOPE on, approximate treatment of P_1 anisotropic scattering, no up-scattering)

Symbol	Definition*
$\Sigma_{s,g\to g}$	$\sum_{i=1}^{LNISIP} \hat{N}^i\left(\sigma_{el,g\to g}^i f_{el,g\to g}^i + \sigma_{inel,g\to g}^i f_{inel,g\to g}^i + \sigma_{(n,2n),g\to g}^i\right) - \sum_{i=1}^{LNISIP} \hat{N}^i\left(\sigma_{el,P1,g\to g}^i f_{el,g\to g}^i + \sigma_{inel,P1,g\to g}^i f_{inel,g\to g}^i + \sigma_{(n,2n),\mathrm{P1},g\to g}^i\right) - \sum_{i=1}^{LNISIP} \hat{N}^i\left(\sigma_{el,P1,dw}^i f_{el,dw}^i + \sigma_{inel,P1,dw}^i f_{inel,dw}^i + \sigma_{(n,2n),\mathrm{P1},dw}^i\right)$
$\Sigma_{s,g'\to g}$	$\sum_{i=1}^{LNISIP} \hat{N}^i\left(\sigma_{el,\mathrm{dw}}^i f_{el,dw}^i + \sigma_{inel,dw}^i f_{inel,dw}^i + \sigma_{(n,2n),\mathrm{dw}}^i\right)$
$\Sigma_{t,g}$	$\sum_{i=1}^{LNISIP} \hat{N}^i\left(\sigma_{c,g}^i f_{c,g}^i + \sigma_{f,g}^i f_{f,g}^i + \sigma_{el,g\to g}^i f_{el,g\to g}^i + \sigma_{inel,g\to g}^i f_{inel,g\to g}^i + \sigma_{el,dw}^i f_{el,dw}^i + \sigma_{inel,dw}^i f_{inel,dw}^i + +\sigma_{(n,2n),g\to g}^i + \sigma_{(n,2n),\mathrm{dw}}^i + \sigma_{msc}^i\right)$
$\Sigma_{tr,g}$	$\Sigma_{t,g} - \sum_{i=1}^{LNISIP} \hat{N}^i\left(\sigma_{el,P1,g\to g}^i f_{el,g\to g}^i + \sigma_{inel,P1,g\to g}^i f_{inel,g\to g}^i + \sigma_{(n,2n),\mathrm{P1},g\to g}^i\right) - \sum_{i=1}^{LNISIP} \hat{N}^i\left(\sigma_{el,P1,dw}^i f_{el,dw}^i + \sigma_{inel,P1,dw}^i f_{inel,dw}^i + \sigma_{(n,2n),\mathrm{P1},dw}^i\right)$
$\left(\nu_f \Sigma_f\right)_g$	$\sum_{i=1}^{LNISIP} \hat{N}^i\left(\nu_f^i \sigma_f^i\right)_g f_{f,g}^i$
$\Sigma_{e,g}^m$	$\sum_{i=1}^{LNISIP} N^{im}\left(\alpha_c^i \sigma_c^i + \alpha_f^i \sigma_f^i\right)$

---

*The mesh cell index *ij* has been dropped, and the following apply.

i	Input isotopes
m	Components
$\hat{N}^i$	Cell-averaged number density for isotope *i*
N^{im}	Number density for isotope *i* in component *m*
α_c^i	Energy yield for neutron capture for isotope *i*
α_f^i	Energy yield for fission of isotope *i*

8. Initial and Boundary Conditions, and Time Step Control

8.1. Initial Conditions and Initialization

8.1.1. Fluid-dynamics cell initialization

Fluid-dynamics mesh-cell variables are specified by cell regions through the input group XRGN. The regions are defined by specifying the left, right, bottom, and top boundaries of fluid dynamics mesh cells. For SIMMER-IV, the front and back boundaries are specified, in addition. The mesh-cell variables in each region are assumed to be uniform. Region boundaries can overlap one another, and in this case later input overrides the former specification. In addition, all the cell variables can also be specified mesh-cell-wise through the input group XCWD. The cell-wise input overrides the region-wise specification.

For initial conditions of SIMMER-III/SIMMER-IV, volume fractions and temperatures of liquid- and structure-field components, vapor temperature, fission gas pressure, and single-phase pressure are specified by user-supplied input data. Before starting a calculation, initialization is required to define the thermodynamic state of cell components based on these input variables. For liquid and structure components, the specific internal energies and the specific volumes are determined from input temperatures using the EOS relationships.

The thermodynamic state of the vapor mixture depends on the vapor temperature and the specific volumes of vapor components. The condensable-gas partial pressures are defined to determine the specific volumes. Currently the following three options are available:

- The condensable-gas pressure is defined as the saturation pressure of liquid which exists in a cell.
- The condensable-gas pressure is defined as the pressure of liquid which exists in a cell, assuming that the liquid saturation temperature is the same as the vapor temperature.
- All the partial pressures are specified by inputs.

The specific volume of a vapor component is calculated using the relationship. Then the macroscopic density is defined by the volume fraction and the specific volume. The following two options are available:

- For liquid- and structure-field components, the macroscopic densities are defined using the volume fractions specified by inputs. For a vapor-field component, the effective volume fraction is calculated using the specified liquid- and structure-field volume fractions.
- The macroscopic densities of real liquid and vapor are calculated so as to conserve the mass in a cell, which is the real-liquid macroscopic density defined in the same way as described in the first option. Thus, the specified volume fraction of real liquid in a two-phase cell is decreased depending on the vapor macroscopic density.

It should be noted that there is no steady-state calculation capability to obtain equilibrated balanced mesh cell conditions. For example, when a single pressure is specified for a region-wise input, it normally takes several cycles of transient calculation before the axial pressure distribution is developed due to gravity.

8.1.2. Neutronics initialization

The spatial mesh structure used for the neutronics calculations is based on the fluid-dynamics mesh structure, but the entire domain of the fluid-dynamics mesh need not be used. The regions to be considered are defined by specifying the fluid-dynamics cells that arc the left, right, top, and bottom boundaries of the neutronics problem (for SIMMER-III). For the neutronics methods, each mesh cell is assumed to be homogeneous; that is, only averaged quantities arc described. For some problems, the size of the neutronics cells must be limited to obtain realistic flux shapes. Thus, an option to subdivide fluid-dynamics cells is provided, in which the number of subdivisions desired is user-specified, and the fluid-dynamics cells arc subdivided into equal-volume neutronics cells.

Isotopic compositions of five nuclear materials (fertile fuel, fissile fuel, steel, sodium, and control) are specified by user input instructions. Multiple sets of cross-section data can be specified in different regions, which are called “cross-section regions”. This means, for example, the composition of fissile fuel isotopes in one region may differ from one in another region. Since the cross-section regions are fixed in space, they must be used carefully when material motion across a region boundary is allowed.

The neutronics and fluid-dynamics equations are partially decoupled; that is, the equations are not solved simultaneously at each time step. This approach permits the separation of the neutronics and fluid-dynamics methods and requires only the communication of such key quantities as component temperatures, densities, and powers.

The neutronics initialization is performed in the following steps:

- Read input data and check for consistency
- Read cross-section binary files (ISOTXS and BRKOXS)
- Set up neutronics mesh geometry and cross-section regions
- Calculate an initial stationary flux and an initial adjoint flux
- Perform transient-state initialization if ITR=1
- Calculate material-wise power (specific internal energy generation rate) distribution to be used in the fluid dynamics

In the multi-group, neutron transport model, the multi-group cross-section data must be prepared by collapsing fine nuclear data from the nuclear library and input as standard-format files: ISOTXS for infinite-dilute microscopic cross sections and BRKOXS for self-shielding factors (f-table).

8.2. Boundary Conditions

8.2.1. Fluid-dynamics boundary conditions

The fluid-dynamics boundary conditions for SIMMER-III/SIMMER-IV have been made much more flexible than the previous SIMMER-II and AFDM codes. For implementing the boundary conditions, an extra layers of mesh cells are included around the surfaces of the computing mesh. These "fictitious" mesh cells, called also as boundary cells, provide exterior locations for the storage of boundary values that can be used automatically to evaluate the field equations.

Boundary conditions can be specified for each of the boundary cells. Currently, the following boundary conditions are available

- A rigid, free-slip boundary condition.
- A rigid, no-slip boundary condition.
- A continuous inflow/outflow boundary condition, where the same flow condition as the adjacent real cell is used also for inflow.
- The flow velocities and pressure in boundary cells are kept constant to the initial values.
- A pressure boundary condition specified by a constant value or a pressure-versus-time table.
- A velocity boundary condition specified by a constant value or a velocity-versus-time tables (for all fluid velocity components).
- A temperature boundary condition specified by a constant value or a temperature-versus-time tables (for all fluid energy components)

8.2.2. Virtual wall model

A concept of virtual walls is unique but extremely useful in flexibly restricting a flow direction or modeling flow channels within a computational mesh. Virtual walls can be placed at any mesh-cell boundaries according to user specifications, with the only purpose of restricting fluid flow across the walls. The model has the following features:

- The wall is bodiless, having no mass, volume nor energy.
- The velocities of the flow normal to the wall are set to zero.
- The free-slip condition, with no wall friction, is applied along the wall.
- Two cells with the wall in between are thermally decoupled.
- The virtual walls can be specified for each cell at four or six cell boundaries for SIMMER-III or SIMMER-IV, respectively.
- For further flexibility, ON and OFF timings of the walls can be specified by the user for individual cells.

8.2.3. Internal boundary conditions

Treatment of internal boundary conditions has been developed to model fluid inflows at certain locations within a computational mesh. The model was originally intended to simulate a phenomenon of high-pressure steam-water injection during an LMFR steam-generator accident. Even though the study has not been conclusive, this unique model is included in SIMMER-III/SIMMER-IV as an input option.

In the model, the inflow boundary conditions are applied to the mesh cells specified by the user, in which the fluid velocities in two or three directions are specified for all the velocity components. The velocities are specified as input constant values or time history tables.

8.2.4. Simple primary loop and pump model

In many of the former reactor calculations, the pressures at the reactor vessel inlet and outlet are specified by pressure boundary conditions with a constant value or a pressure-versus-time table. This treatment may become inappropriate when the vessel pressure changes largely, since an inertia of coolant in the cooling loop piping is neglected. To improve this situation, a simple primary loop and pump model has been developed, taking advantage of the internal boundary condition. The outline of the model is as follows:

A primary loop with a circulation pump is modeled as a one-dimensional axial channel, within a computational mesh but outside the reactor vessel internal that is the main region of SIMMER calculations. Hence the primary loop channel must be disconnected from the main region by means of “virtual walls”, except that the bottom and top of the loop are connected to the reactor lower and upper plena, respectively. The location of the pump cell is specified by the user. For the primary loop piping, the inertia of coolant is simulated by specifying the lengths above and below the pump cell and the diameter of the pipe. A simple momentum equation is used to calculate the dynamic response of the loop. The multipliers can be specified by the user to change the effects of inertia and gravity force terms in the momentum equation for the primary loop. The calculation is performed independent of the SIMMER fluid-dynamics.

The pump model is defined at a user-specified cell by giving the rated flow rate, inflowing coolant temperature, pressure head, the pump revolution-versus-time table to simulate flow coastdown characteristics. A coolant flow from the pump is limited to the downward direction to the cold leg and is led to the reactor lower plenum. The coolant circulated through the reactor vessel flows back to the pump via the hot leg. Although a heat exchanger is not modeled, the coolant temperature is reset to the constant initial value and thereby simulating the heat removal from the reactor vessel. More than one pumps can be defined for 2 or 3 loop calculations, especially with SIMMER-IV.

8.2.5. Neutronics boundary conditions

In the standard use of SIMMER-III/SIMMER-IV, the neutronics boundary conditions outside the neutronics mesh are vacuum, except that at the centerline of a cylindrical geometry a reflective boundary condition is employed. In the vacuum boundary condition, the value of the angular flux on the boundary is set to zero for all incoming directions. In the reflective boundary condition, the value of the flux on the boundary for incoming directions is set equal to the value of the outgoing flux in the direction corresponding to specular reflection. The options for boundary conditions available for the discrete-ordinate neutron transport solver model of TWODANT/THREEDANT can be used in SIMMER-III/SIMMER-IV, as well. They include: non-vacuum boundary condition such as reflective, periodic, and white boundary conditions.

8.3. Time Step Control

8.3.1. Fluid-dynamics time step control

The fluid-dynamics time step controls play important roles in computational efficiency, accuracy and stability. There are 16 controls that influence the fluid-dynamics time step size in SIMMER-III/SIMMER-IV. Based on the following controls, optimum time step sizes are automatically chosen; many of them are physics-based, taking advantage of experience in running SIMMER-III/SIMMER-IV and the previous codes.

(1) Initial time step (DTSTRT)

Since there is no steady-state initialization capability in SIMMER-III/SIMMER-IV, the fluid-dynamics calculation performs more smoothly if the first several cycles use a relatively small time step size (default: 10^{-5} s). The initial time step can be kept for an input number of cycles NDT0 unless some other time-step control requires a smaller time step.

(2) Maximum time step (DTMAX)

The time step is not permitted to exceed a user-specified maximum value DTMAX (default: 10^{-3} s).

(3) Twice the previous time step size (2*DTP)

The time step is limited to twice the previous time step.

(4) Velocity Courant condition (COURTN)

The semi-implicit fluid-dynamics algorithm requires a numerical stability criterion based on a velocity (not sonic) Courant condition, in which material is restricted to convect one mesh cell in a single time step. This leads to time-step size limitation such that

$$\Delta t^{n+1} < C_t \min\left(\frac{\min\left[r_i^{\zeta}\Delta x_i,\ r_{i+1}^{\zeta}\Delta x_{i+1}\right]}{\left[r^{\zeta}\max\limits_q\left(\left|u_q\right|\right)\right]_{i+1/2}},\ \frac{\min\left[\Delta y_k,\ \Delta y_{k+1}\right]}{\left[\max\limits_q\left(\left|w_q\right|\right)\right]_{k+1/2}},\ \frac{\min\left[\Delta z_j,\ \Delta z_{j+1}\right]}{\left[\max\limits_q\left(\left|v_q\right|\right)\right]_{j+1/2}} \right)\Delta t^n, \qquad (8\text{-}1)$$

where C_t is an input Courant number (default: 0.4).

(5) Optimum number of pressure iterations (OPTPIT)

The time-step size affects the number of pressure iterations required to converge to the end-of-time-step fluid state. An increase in the time-step size increases the number of pressure iterations. From four to six pressure iterations in each time step minimize the overall computational effort for typical problems. This time-step control is used to estimate the time-step size that yields a user-specified optimum number of pressure iterations, OPTPIT (default: 8). If the last time step Δt^n required ITERA pressure iterations, a next time step will be estimated by assuming the time-step size is proportional to the number of pressure iterations,

$$\Delta t^{n+1} = f_{IT}\Delta t^n, \tag{8-2}$$

(6) where the factor f_{IT} is evaluated as

$$f_{IT} = \begin{cases} f_{IT}^0 \Delta t^{inc} & \text{if } f_{IT}^0 \geq 1 \\ (f_{IT}^0)^2 & \text{if } f_{IT}^0 < 1 \end{cases}, \tag{8-3}$$

where Δt^{inc} is the user-specified maximum fractional change of the time-step size (default: 1.05) and the factor f_{IT}^0 is evaluated by assuming the time-step size is proportional to the number of pressure iterations,

$$f_{IT}^0 = \frac{\text{OPTPIT}}{\text{ITERA} + 1} + 10^{-10}\,. \tag{8-4}$$

(7) Source-term decoupling

The time step can be optionally restricted by monitoring the potential sources of source-term decoupling error. This is done by restricting the fractional changes in: the cell pressure between Step 1 and Step 2, and Step 2 and Step 4; and the vapor temperature between Step 1 and Step 2, and Step 2 and Step 4.

(8) Excessive V/C iteration (DTIVC)

If the number of the vaporization/condensation iterations exceeds a user-specified maximum, the next time step size is halved.

The minimum time step size of the criteria from (2) to (7) is used to calculate the next cycle. The predicted time step is compared with the following minimum values.

(9) Minimum time step (DTMIN)

The time step is not permitted to be reduced below a user-specified minimum value DTMIN (default: 10^{-6} s). The calculation is intended to terminate when the time step is decreased below DTMIN. Currently, however, this abortion is bypassed and the calculation is continued by setting the time step to DTMIN with printing an error message.

(10) Fuel-pin heat-transfer (reactivity) time step (DTHN)

The time step size cannot exceed the next fuel-pin heat transfer time step or neutronics reactivity step.

Furthermore, a capability of re-calculating the same cycle with a halved time step size is available, whenever non-convergence is detected in iterative operations in fluid dynamics. The time step is controlled by the following additional conditions.

(11) Non-convergence in V/C

Non-convergence occurred in the non-equilibrium V/C calculation.

(12) Excessive change in vapor temperature in V/C

The excessive change in vapor temperature is detected in the V/C iteration.

(13) Non-convergence in vapor temperature in EOS

Nonconvergence occurred in EOST called from either STEP1 or STEP4.

(14) Extremely low vapor temperature in EOS

The vapor temperature became lower than the minimum vapor temperature in EOST called either from STEP1 or STEP4.

(15) Non-convergence in velocity iteration in STEP2 or STEP4

Non-convergence occurred in the velocity iteration either in STEP2 or STEP4.

(16) Non-convergence in pressure iteration in STEP3

Non-convergence occurred in the velocity iteration either in STEP2 or STEP4.

(17) Keeping reduced time step size

This is a special control to avoid an oscillatory change in time step sizes in successive cycles. The time step size, which has been reduced by any of the above controls, is kept for a user-specified number of cycles.

8.3.2. Fuel-pin heat-transfer time step control

Fuel-pin heat-transfer time steps are controlled based on the changes of specific internal energies of pin fuel and cladding, and the change of the total power (or amplitude).

$$\Delta t_m^{new} = 0.9 f_m \frac{\tilde{e}_m^{n+1}}{\left|\tilde{e}_m^{n+1} - e_m^n\right|} \Delta t^{old}, \text{and} \tag{8-5a}$$

$$\Delta t_P^{new} = 0.9 f_P \frac{P^{n+1}}{\left|P^{n+1} - P^n\right|} \Delta t^{old}, \tag{8-5b}$$

where P^n is the power amplitude, and f_m and f_P are the input multipliers used when a tighter control is desired. The time step control also considers the user-specified minimum and maximum, the previous time step, the neutronics reactivity step and the fluid-dynamics time step. Finally the new time step is determined by

$$\Delta t^{new} = \max\left[\Delta t_{min}, \min\left(\Delta t_{max}, \Delta t_m, \Delta t_p, 4\Delta t^{old}\right)\right]. \tag{8-6}$$

When the neutronics calculation is performed, the time step size is set to be the same as the reactivity step for a standard use, because the reactivity feedback and fuel heat generation are closely related each other. However, the heat transfer time steps can be optionally controlled independently or forced to the fluid dynamics steps.

8.3.3. Neutronics shape time-step control

Most of the neutronics time-step controls are taken from SIMMER-II and they are briefly described in this section. More detailed description is available in the SIMMER-II manual[2)].

The neutronics time-step controls are used to anticipate the need to terminate a series of fluid-dynamic steps to update the amplitude function extrapolation (reactivity step) or to terminate a series of reactivity steps to update the flux shape (shape step). Generally, time-step controls monitor quantities that may affect the validity of the reactivity projection, such as a high reactivity derivative or a high reactivity state (implying a high power level) and significant system changes, such as the maximum change in internal energy or density. Time-step controls for shape steps generally monitor quantities that reflect the rate of flux-shape changes, such as the rate of flux tilt from previous steps and the deviation of the quasi-static constraint at reactivity steps.

The tightness of the control depends on the reactivity of the system. The controls become very tight for a reactivity near prompt critical, but they are relaxed for a reactivity not near prompt critical. There are two time-step reduction factors that appear in several of the individual time-step controls:

$$f_1(\rho) = 1 - (1 - \varepsilon_4)\exp\left[-\varepsilon_{17}\left(\frac{\rho - \beta}{\beta}\right)^2\right], \text{and} \tag{8-7a}$$

$$f_2(\rho) = f_1(\rho)^{1/5}, \tag{8-7b}$$

where ε_4 and ε_{17} are user-specified parameters (recommended values: 0,02 and 0.08515781). These recommended values tighten the time-step control as the system nears criticality and tighten even more as the system nears prompt critical.

During transient calculations, the shape time step is predicted or limited by the following individual controls.

(1) Previous shape step

The shape step is 1imitcd to 10 times the maximum of the previous two shape time steps.

(2) Change in leakage

The shape time step depends on the rate of change in the leakage contribution to the reactivity according to

$$\Delta t^{s2} = f_1(\rho)\varepsilon_6 \left|\frac{\Delta t^s I^r + (t^r - t^s)I^{s-1}}{I^r - I^{s-1}}\right|, \tag{8-8}$$

where

ε_6	the user-specified time-step control limiting the relative change in the leakage contribution to the reactivity,
I^r	the extrapolated leakage contribution to the reactivity for the most recent reactivity step,
I^r	the time for the most recent reactivity step,
t^s	the time for the most recent shape step, and
I^{s-1}	the leakage contribution to the reactivity for the previous shape calculation.

(3) Number of reactivity step

The shape time step cannot extend over more than a number of reactivity steps specified by the user.

(4) Last (largest) real time for the current run

A shape calculation is taken at the end of the problem time.

(5) Maximum shape step

The shape step is limited by a maximum size specified by the user.

(6) Change in neutron flux shape

The tilt of the total flux shape is calculated as the relative change in the flux at each mesh point:

$$T_{ij} = \left(\sum_{g=1}^{IGM} \phi_{ijg}^{s} - \sum_{g=1}^{IGM} \phi_{ijg}^{s-1} \right) \Bigg/ \sum_{g=1}^{IGM} \phi_{ijg}^{s} , \tag{8-9}$$

where ϕ_{ijg}^{s} and ϕ_{ijg}^{s-1} are the most recently calculated and the previous flux shapes, respectively. From this flus tilt through the mesh, the next time step is estimated as:

$$\Delta t^{s8} = \frac{f_1(\rho)\Delta t^{s}\varepsilon_9}{\max\limits_{ij}(|T_{ij}|) - \min\limits_{ij}(|T_{ij}|)} , \tag{8-10}$$

where Δt^{s} denotes the shape step between t^s and t^{s-1} and ε_9 is the user-specified parameter for monitoring the flux tilt.

(7) Change in reactivity

The shape step is predicted by the change in reactivity:

$$\Delta t^{s9} = (t^r - t^s) + \max\left[0.0, \frac{f_1(\rho)\varepsilon_{18}\beta^r - |\rho^r - \rho^s|}{\Lambda^r |a_1 - a_2 \Delta t^r|} \right] , \tag{8-11}$$

where

ε_{18}	the user-specified time-step control for the maximum reactivity change (in dollars) per

shape step,

β^r the effective delayed neutron fraction for the most recent reactivity step,

ρ^r the reactivity for the most recent reactivity step,

ρ^s the reactivity for the most recent shape calculation, and

Λ^r the neutron generation time for the most recent reactivity step.

and a_1 and a_2 are the first- and second-order coefficients of the parabolic fit ρ/Λ for the most recent reactivity time step.

(8) Deviation from quasistatic method constraint condition (optional)

If the option for flux shape update at reactivity steps is used, the shape step is halved to limit the deviation from unity of quasistatic constraint.

$$\Delta t^{s10} = \frac{\Delta t^s}{2}\ , \ \text{if } (\gamma - 1) > \varepsilon_{10}\ , \tag{8-12}$$

where ε_{10} is the maximum deviation from unity of quasistatic constraint (γ) specified by the user.

(9) Request of an external source model (optional)

If the external neutron source option is used, the shape step is forced to the time requested by user input specification.

(10) User-specified constant shape step (optional)

The shape time steps can be kept constant by user input specification.

The minimum of the controls (1) through (9) is taken, depending on the model option, and checked for the control (10). In addition, to avoid the situation that the shape step becomes unfavorably small, the minimum size is internally set to 10^{-7} s.

8.3.4. Neutronics reactivity time-step control

During the transient neutronics calculations, the reactivity time step is predicted or limited by eight individual controls in the neutronics.

(1) Previous reactivity step

The reactivity step is limited to twice the maximum of the previous two reactivity steps.

(2) Change in reactivity

The reactivity step is limited to twice the maximum of the previous two reactivity steps.

$$\Delta t^{r2} = \frac{f_1(\rho)\varepsilon_5\beta^r}{\Lambda^r|a_1 - a_2\Delta t^r|}\ , \tag{8-13}$$

where ε_5 denotes the time-step control specified by the user for limiting the maximum reactivity change per reactivity step.

(3) Next shape time step

The reactivity step is limited by the shape step.

(4) Maximum reactivity step

The reactivity step is limited to a maximum size specified by the user.

(5) Change in amplitude

The reactivity time step is limited by the rate of change in the flux amplitude solution by solving

$$\ln\left(\frac{N_0 + N_1\Delta t^{r3} + N_2(\Delta t^{r3})^2}{N^r}\right) = \frac{2.3 f_2(\rho)}{\varepsilon_7}, \tag{8-14}$$

for Δt^{r3}, where ε_7 denotes the time-step control specified by the user that determines the number of reactivity steps per power decade.

(6) Maximum inverse period

The reactivity time step is limited by the change in inverse period,

$$|\omega^r - \omega^s| \leq \varepsilon_8 f_2(\rho), \tag{8-15}$$

where ε_8 denotes the time-step control specified by the user for the maximum inverse period change per reactivity step. The reactivity time step is given by the minimum of these six time-step controls.

(7) Current shape step size

The reactivity time step is limited by the shape time step.

(8) User-specified constant reactivity step

The reactivity time steps can be kept constant by user input specification.

The reactivity time step is given by the minimum of (1) to (7) and then further checked for (8).

The reactivity steps are also controlled by the fluid dynamics, in order to take into account the influence of change, for example, in fuel mass or temperature on reactivity calculations. For this purpose, the total masses and internal energies for fuel, steel and sodium are summed up over a series of fluid-dynamics time steps. The following seven controls are tested against user-specified criteria, and the minimum is taken as the next reactivity step. The fluid dynamics control of reactivity steps works independently of the neutronics control of time steps described above.

(9) Fractional change in the total fuel mass

The change in material density per reactivity step is limited. For the fuel density, this control is given by

$$\sum_{n=n^r}^{n-1}\left\{\left[\sum_{ij}\left|\left(\bar{\rho}_{fuel}\right)_{ij}^{n+1}-\left(\bar{\rho}_{fuel}\right)_{ij}^{n}\right|V_{ij}\right]\Big/\left[\sum_{ij}\left(\bar{\rho}_{fuel}\right)_{ij}^{n+1}V_{ij}\right]\right\}<f_1(\rho)\varepsilon_{14}\,, \tag{8-16}$$

where

ε_{14} the control specified by the user that limits the maximum absolute fuel mass shift in a reactivity step,

n^r the number of the fluid-dynamics time step that began the current reactivity step, and

n the most recent fluid-dynamics time step number.

The total fuel macroscopic density $\bar{\rho}_{fuel}$ is calculated by summing over all fuel components. If the inequality is not satisfied after a fluid-dynamics time step, the fluid-dynamics calculation is suspended and a reactivity step is taken.

(10)Fractional change in the total steel mass

A similar control applies to the steel mass change and is controlled by the user input quantity ε_{15}.

(11)Fractional change in the total sodium mass

A similar control applies to the sodium mass change and is controlled by the user input quantity ε_{16}.

(12)Fractional change in the total fuel internal energy

The change in material energy per reactivity step is limited. For the fuel energy, this control is given by

$$\sum_{n=n^r}^{n-1}\left\{\left[\sum_{ij}\left|\left(\bar{\rho}_{fuel}e_{fuel}\right)_{ij}^{n+1}-\left(\bar{\rho}_{fuel}e_{fuel}\right)_{ij}^{n}\right|V_{ij}\right]\Big/\left[\sum_{ij}\left(\bar{\rho}_{fuel}e_{fuel}\right)_{ij}^{n+1}V_{ij}\right]\right\}<f_1(\rho)\varepsilon_{11}, \tag{8-17}$$

where ε_{11} denotes the control specified by the user that limits the maximum absolute fuel mass shift in a reactivity step and the total fuel energy $\left(\bar{\rho}_{fuel}e_{fuel}\right)$ is obtained by summing over all fuel components. If the inequality is not satisfied after a fluid-dynamics time step, the fluid-dynamics calculation is suspended and a reactivity step is taken.

(13)Fractional change in the total steel internal energy

A similar control applies to the steel energy change and is controlled by the user input quantity ε_{12}.

(14)Fractional change in the total sodium internal energy

A similar control applies to the sodium energy change and is controlled by the user input quantity ε_{13}.

(15)Change in amplitude projected to fluid dynamics

The number of reactivity steps per power decade is limited according to

$$\left|b_1\Delta t^h + b_2(\Delta t^h)^2\right| > \frac{f_2(\rho)}{2.3\varepsilon_7}, \tag{8-18}$$

where

Δt^h	the time interval from the start of the most recent reactivity step to the end of the most recent fluid-dynamics step,
$b_1. b_2$	the first-and second-order coefficients in the exponential fit to the amplitude function over the most recent reactivity step, and
ε_7	the control specified by the user that determines the number of reactivity steps per amplitude decade.

If this inequality is satisfied, the fluid-dynamics calculation is suspended and control is returned to the neutronics calculation to perform the next reactivity step. In that case, the reactivity time-step size is set to Δt^h.

9. Special Models

During the long history of the SIMMER code study at JAEA, several special or ad hoc models have been developed. Some of them are included in the standard code library at JAEA and were documented in the previous chapters. However, not all the models developed thus far have not yet been completed to be used as standard models. In this chapter, the following three models are described briefly because of their possible use in the future studies with SIMMER-III or SIMMER-IV.

- Inter-subassembly gap model
- SIMMER-LT
- SIMMER-SW

9.1. Inter-Subassembly Gap Model

9.1.1. Background

Inter-subassembly gaps outside the active core region are known to provide an effective path for early fuel removal from the core and thereby to significantly reduce a recriticality potential during CDA sequences. The separate effect of this was first evaluated as a part of the comprehensive safety assessment of CDA energetics in Clinch River Breeder Reactor58). For a whole-core calculation, the gap flow channel, which spreads radially and axially, is too complex to be modeled. In the two-dimensional axisymmetric geometry of SIMMER-III, the gap cannot be simulated. The gap flow channels can be modeled in the SIMMER-IV three-dimensional rectangular geometry; however, they cannot be treated together with the intra-subassembly structure and flow at the same time.

A special model has been developed to simulate a flow of molten core materials into the inter-subassembly gap channels within the framework of the standard SIMMER fluid-dynamics model. The model is available as an input option for SIMMER-IV, but is not available for SIMMER-III because gap geometry cannot be modeled.

9.1.2. Model outline

The gap flow model simulates the molten core material flow through the inter-subassembly gap channels in the region of radial blanket, reflector and shield subassemblies which are located outside the active core. The gap channels in the active core (and internal blanket if any) cannot be simulated. The internal contents of the subassembly, which must be preserved for maintaining the neutronics state, cannot be modeled with a gap flow channel at the same time. Therefore, the present gap flow model requires special and rather tricky geometrical treatment as: allowing only a gap flow channel till it wall failure and combining.

The following assumptions are made in the model:

- The gap channel is initially filled with sodium, and the gap wall is modeled by cladding having the same macroscopic density and surface area as the can wall (wrapper tube) of the subassembly to which the gap channel is assigned. This means the flow area and hydraulic diameter of the gap are made consistent with the designed geometry.

- The gap channel is accessed by molten core material when the outermost can wall of the active core subassembly fails.
- Although the axial boundaries of the gap region can be specified by user input, an entire subassembly length is normally specified. The bottom of the gap region is blocked to avoid unphysical in-flow of cold sodium from the subassembly inlet region.
- The interior of a subassembly in the gap flow region is initialized as no-flow volume, which is thermally decoupled from the gap sodium and wall. The contents (macroscopic densities and internal energies of the components) are stored as they are at the initial state. They are excluded from the fluid-dynamics calculations, but are used in the neutronics calculation.
- When a gap wall, modeled as cladding, breaks up due mainly to melt attack from the molten core material, the contents of the subassembly except for sodium are restored in the relevant mesh cell and they are mixed with the gap fluids including sodium, core materials and the broken-up steel for fluid-dynamics calculations. Intra-subassembly sodium is removed to prevent unphysical pressure events caused by numerical mixing such as rapid cooling by cold sodium and rapid pressurization due to fuel-coolant interactions.
- The fluids in the mesh cell of a failed subassembly are connected to the surrounding mesh cells only through gap flow channels.

This model is simple but very useful for simulating fuel removal from the core at an early stage of core disruption without forming a bottled-up core pool which has a potential of large-scale fuel motion resulting in energetic recriticality events. There are some drawbacks in this model from the neutronics aspects. Intra-subassembly contents are kept at the initial state and hence the reactivity feedback effect of transient temperature changes is not calculated. Upon failure of the gap wall, intra-subassembly sodium is intentionally eliminated. This may increase neutron leakage and thereby have a negative reactivity feedback effect. Nevertheless, these neutronics effects are considered relatively small in comparison to a large negative reactivity effect of extended fuel motion out of the active core through the gap flow channels.

This special model is rather tricky and of limited scope. For example, the molten core material cannot move axially inside the subassembly from the gap wall failure node. Therefore, the model must be used carefully especially for a longer time simulation.

9.2. SIMMER-LT

9.2.1. Background

The SIMMER-III and SIMMER-IV codes provide a feature to comprehensively simulate transient multi-phase fluid-dynamics behaviors of core materials that are coupled with neutronic feedback effects. The codes have been applied to various analyses of neutronically active LMFR core-disruptive accident sequences that typically last for a few to tens of seconds. Because of an enormous computing effort required, the code application is usually limited to simulating transient of a few minutes at most. However, even after permanent neutronic shutdown of the accident, movement and interactions of disrupted core materials further continue into a long-term post-accident material relocation and heat-removal phase. No practically useful computer code has yet been made available for analyzing this phase.

From the above background, the development of SIMMER-LT (long term), a fast-running version of SIMMER-III, has been attempted in collaboration with Kyushu University[5]. Since no neutronics calculations are necessary for simulating the post-accident phase, the development of SIMMER-LT is restricted to the fluid-dynamics module of SIMMER-III only and consists of:

- Performance measurement of SIMMER-III
- Parallelization of the fluid-dynamics module
- Improved time-step control
- Simplification of the heat- and mass-transfer model

SIMMER-LT is not an independent code but is included in the standard program library of SIMMER-III. The improved time-step control and the simplified V/C models are respectively activated by user input specifications.

9.2.2. Performance measurement of SIMMER-III

As the first step, a computing cost distribution was measured for a typical reactor problem with 7 velocity fields and 3096 mesh cells, with no neutronics. The CPU time fractions spent in the fluid-dynamics modules are:

- 73% in Step 1 (intra-cell transfers) and 26% in Steps 2 to 4 (inter-cell convection)
- 41% of total in heat and mass transfer calculations (56% of Step 1)

It was shown that about 3/4 of the CPU time is spent in Step 1, which is characterized by complex intra-cell (local) heat and mass transfer processes involving multi-phase and multi-component fluids and structure. It was also shown that, among the various heat and mass transfer models in Step 1, non-equilibrium vaporization and condensation (V/C) model is most costly because an iterative procedure with frequent EOS function calls is implemented to solve non-linear mass and energy equations cell by cell. Thus, the speed-up of the V/C calculation is critical for SIMMER-LT, with consideration that rapid transient processes need not be simulated in the post-accident phase.

---

[5] The development of SIMMER-LT is performed partly under the task "Development of Severe Accident Evaluation Technology (Level 2 PSA) for Sodium-Cooled Fast Reactors" entrusted from the Ministry of Education, Culture, Sports, Science and Technology of Japan (2010).

9.2.3. Parallelization

Parallelization is one of the most powerful tools in speeding up many of scientific and engineering computations taking advantage of recent parallel computing technology. Considering the characteristics of SIMMER-III from the point view of parallelization, use of a symmetric multi-processor (SMP) machine is more suitable than a distributed-memory parallel (DMP) machine. Although the latter technology has become mainstream of today's supercomputers, the former SMP technology is used in SIMMER-III because typical numbers of mesh cells are not huge (ten thousands at most) and excessive data communications among processor elements can be avoided. It should be reminded that the computing cost of SIMMER-III fluid dynamics is not attributed to the large number of mesh cells to obtain good spatial resolution but to the accuracy of complex intra-cell heat and mass transfer operations that cannot be parallelized. Therefore, the SMP technology is selected for SIMMER-III and OpenMP (Open Multi-Processing) is used as a programming interface to process multiple threads in parallel. The previous experience gained at JAEA in parallelizing three-dimensional SIMMER-IV has been utilized fully.

In general, speed-up by parallel computation is attained only in a parallel portion of the program and a sequential portion cannot be sped up, even if the number of parallel processors increases. Hence it is essential to maximize the parallel portion (fraction) to gain practical speed-up of the entire program. A parallel fraction of about 90% has been attained for SIMMER-III and, for a 2870-cell LMFR core disruption problem, the speed-up by a factor of 6 was obtained with 16 processor elements. In addition, the standard pressure iteration matrix solver was parallelized, but its speed-up effect became significant only with large number of mesh cells (10^4 or more cells).

9.2.4. Time-step control

The fluid-dynamics time-step control, as described in **Section 8.3.1**, is mainly dominated by the Courant condition and the optimum number of pressure iterations, both of which are necessary for stable and accurate calculation of inter-cell fluid motions computed in Steps 2, 3 and 4. However, these two time-step controls, related to fluid convection, are not necessary for stable and accurate calculation of intra-cell heat and mass transfer operations in Step 1. In slow transient problems, to which SIMMER-LT is to be applied, with no rapid V/C occurring, larger time-step sizes can be used for Step 1.

From the above consideration, a new and independent time-step control for Step 1 has been developed as an input option, in which convection-related controls are eliminated. For a typical LMFR core disruption test problem without neutronics and with ca. 2000 mesh cells, Step 1 time-step sizes are more than an order-of-magnitude larger than the fluid-dynamics time step for fluid convection. With this revised two-level time-step control method, a factor of 3 speed-up in the overall fluid-dynamics calculation is achieved.

9.2.5. Simplification of the heat- and mass-transfer model

In slow transient problems, to which SIMMER-LT is to be applied, with no rapid V/C occurring, detailed and accurate treatment of non-equilibrium V/C processes is not always required. To simplify the standard V/C model, two approaches have been developed by eliminating the original complex procedure to solve non-linear processes.

In a simplified equilibrium V/C (SEVC) model, it is assumed that a certain vapor component becomes equilibrated with the corresponding liquid component instantaneously within the same time step. Since there is no need for iteratively solving matrix equation for individual cells, computing cost can be significantly reduced. However, there are some shortcomings that would limit its applicability compared to the second approach as described below. Namely, phase transition of different materials cannot be modeled simultaneously nor superheated vapor cannot be treated. Currently, the SEVC model is extended to treat steel boiling and condensation where liquid sodium is not present.

The second approach is still simpler than the original non-equilibrium model but is more sophisticated than the SEVC model and is called an equilibrium V/C (EVC) model. In the EVC model, a liquid-vapor heat transfer rate due to temperature difference is expressed by deviations of vapor and liquid enthalpies from the saturation condition. By introducing a relaxation time constant to the model, mass transfers associated with energy transfers are modeled as an equilibration process as:

$$\Gamma_{G,Lm}^{\mathrm{EQ}} = -\frac{1}{\tau_m}\frac{\left(i_{Con,Gm} - e_{Lm}\right)\bar{\rho}_{Lm} + \left(i_{Vap,,Gm} - i_{Gm}\right)\bar{\rho}_{Gm}}{h_{Con,Gm}}\text{ , if } \left(i_{Con,Gm} - e_{Lm}\right)\bar{\rho}_{Lm} + \left(i_{Vap,,Gm} - i\right)\bar{\rho}_{Gm} < 0 \qquad (9\text{-}1)$$

$$\Gamma_{Lm,G}^{\mathrm{EQ}} = \frac{1}{\tau_m}\frac{\left(i_{Con,Gm} - e_{Lm}\right)\bar{\rho}_{Lm} + \left(i_{Vap,,Gm} - i_{Gm}\right)\bar{\rho}_{Gm}}{h_{Con,Gm}}\text{ , if } \left(i_{Con,Gm} - e_{Lm}\right)\bar{\rho}_{Lm} + \left(i_{Vap,,Gm} - i_{Gm}\right)\bar{\rho}_{Gm} > 0 \qquad (9\text{-}2)$$

With this relaxation time constant, the transient thermodynamic state of vapor can be deviated from saturation and thereby non-equilibrium nature of real vapor is modeled to some extent. Potential numerical instabilities caused by rapid changes in vapor state can be avoided by this relaxation time constant, as well. The EVC model requires an iterative solution procedure, and thus the speed-up effect is less than the SEVC. In the EVC model, simultaneous V/C of steel and sodium can be treated,

The SEVC and EVC models have been validated against selected experiments including non-energetic phase transition processes, such as a long-lasting transient sodium boiling in a pin bundle.

9.3. SIMMER-SW

9.3.1. Background

Because of the generalized framework of the fluid-dynamics model of SIMMER-III and SIMMER-IV, broader application and extension of these codes have been proposed in the areas other than LMFR core disruptive accident analyses. One of such new areas of application studied in around 2000 is a simulation of sodium-water reaction postulated as a design basis accident of the LMFR steam generator (SG). In an event of SG tube rupture, a high-pressure water/steam mixture is injected into liquid sodium and energetically reacts with sodium. The reaction generates pressure events that may jeopardize the integrity of SG and the jet of corrosive reaction products may erode nearby intact tubes (wastage) with potential failure propagation. In this study, using the framework of SIMMER-III and SIMMER-IV, the model for sodium-water (SW) reaction was developed and was coupled with the original fluid dynamics[59]. Because of fundamental difficulties in simulating an entire sequence of the sodium-water reaction, the development has been suspended. SIMMER-SW is included in the program library at JAEA as a code option (active only if SW in on) for future possible continuation of the study.

9.3.2. Model outline

The outline of the sodium-water (SW) reaction model is summarized as follows:

- Sodium and water are simulated by the SIMMER-III materials fuel and sodium, respectively. Hydrogen generated by reaction is simulated by fission gas. The EOS and TPP parameters are specified by input.
- Ejection of the water/steam mixture is modeled using the internal boundary condition as described in **Section 8.2.3**.
- Chemical reactions with hydrogen generation is modeled assuming a limited reaction rate and limited reaction area.
- The pressure events, calculated by the original SIMMER fluid dynamics, include: rapid pressure spike upon SG tube rupture and single-phase pressure propagation, and broader pressure buildup due to heating by exothermic reaction, water vaporization and hydrogen generation.

The simulation of an early phase of the SW reaction requires a sufficiently fine spatial and temporal resolution (extremely small mesh-cell sizes and time-step sizes). Keeping the same order of fine resolution in a longer time simulation is judged to be impractical. Also, the experimental knowledge is not sufficient for further model refinement and validation.

10. Concluding Remarks

The development of SIMMER-III and SIMMER-IV has been a long-lasting effort starting from at around 1990. The initial code versions were made available by the mid-2000s with all the originally planned framework and models. A full code documentation was repeatedly proposed but has never been completed until the present report is finally issued this time. Although some of the individual models were documented as JNC (current JAEA) reports, there have been many model revisions and additions later. Thus, the purpose of this reports is to provide a complete documentation of the SIMMER-III/SIMMER-IV models and methods including recent model revisions and additions. For those individual models which are documented in detail, only the summaries of models and methods are described in this report. The verification and validation of the codes, an important element of software development, were already documented in detail elsewhere.

The SIMMER-III and SIMMER-IV codes provides today's standard and most advanced tool for LMFR CDA simulations. Actually, the codes have been already used widely in reactor safety analyses in Japan, including the safety assessment in licensing applications. It has been demonstrated that the limitations with respect to applicability, accuracy and stability in the former code is largely removed for more reliable calculations. With the generalized framework and flexible treatment of material components especially in the fluid-dynamics model, the codes can be applicable to non-liquid-metal reactors and non-reactor transient multi-phase problems.

Acknowledgments

There are many contributors who have been directly and indirectly involved in the code development in the past years. They are too many to mention individually, and hence only those who have directly and lately conducted the model development of SIMMER-III and SIMMER-IV at JAEA are listed as the authors of this report. Major contributors who have formerly and actively involved in the model development are listed as “Former Contributors.”

It must be mentioned that SIMMER-III and SIMMER-IV were developed based on the achievement and experience of the previous computer codes, SIMMER-II, AFDM and DANTSYS, and therefore the efforts of the contributors to these codes are gratefully acknowledged.

The international collaboration on the SIMMER-III development has been extremely fruitful. Many suggestions and experience from the European partners have been effectively taken into consideration for later code development and improvement. The SIMMER-III assessment program (verification and validation) jointly conducted with Germany and France has been extremely productive and useful. The coordinating efforts and management of W. Maschek of KIT, and J. Louvet and P. Coste of CEA are gratefully appreciated.

The authors are thankful to the significant assistance of JAEA programming staff, especially of M. Sugaya, M. Mizuno, S. Hosono, and F. Inoue, for undertaking numerous programming and code maintenance jobs and test calculations. Without their endeavor, SIMMER-III and SIMMER-IV have not been matured to the present level of completion. The contributors from JAEA’s contractors included: Y. Horie and N. Shirakawa of Toshiba Corp. for improving 3D fluid dynamics and K. Tsunoda of Mitsubishi Research Institute for initial neutronics programming and coupling with fluid dynamics. Special thanks go to the JAEA management at Oarai for giving the first author (Kondo) an opportunity to re-visit the SIMMER-III/SIMMER-IV models and compile this report at last.

References

1) W. R. Bohl and L. B. Luck: "SIMMER-II: A Computer Program for LMFBR Disrupted Core Analysis," Los Alamos National Laboratory, LA-11415-MS (1990).

2) L. L. Smith : "SIMMER-II: A Computer Program for LMFBR Disrupted Core Analysis," Los Alamos National Laboratory, NUREG/CR-0453, LA-7515-M, Rev. (1980).

3) W. R. Bohl, *et al.*: "AFDM: An Advanced Fluid Dynamics Model, Volume I: Scope, Approach, and Summary," Los Alamos National Laboratory, LA-11692-MS, Vol.1 (1990).

4) S. Kondo, et al.: "SIMMER-III: A Computer Program for LMFR Core Disruptive Accident Analysis - Version 2.H Model Summary and Program Description –," JNC TN9400 2001-002 (2000) 318p.

5) S. Kondo, et al.: "SIMMER-IV: A Three-Dimensional Computer Program for LMFR Core Disruptive Accident Analysis - Version 1.B Model Summary and Program Description -," JNC TN9400 2001-003 (2000) 307p.

6) H. Yamano, et al.: "SIMMER-III: A Computer Program for LMFR Core Disruptive Accident Analysis - Version 3.A Model Summary and Program Description -," JNC TN9400 2003-071 (2003) 304p.

7) H. Yamano, et al.: "SIMMER-IV: A Three-Dimensional Computer Program for LMFR Core Disruptive Accident Analysis - Version 2.A Model Summary and Program Description -," JNC TN9400 2003-070 (2003) 333p.

8) W. R. Bohl: "AFDM: An Advanced Fluid Dynamics Model, Volume V: The Convective Transport Algorithm," Los Alamos National Laboratory, LA-11692-MS, Vol. V (1990).

9) R. E. Alcouffe, et al.: "DANTSYS: A Diffusion Accelerated Neutral Particle Transport Code System," Los Alamos National Laboratory, LA-12969-M (1995).

10) S. Kondo and Y. Tobita (Ed.): "Phase 1 Code Assessment of SIMMER-III, A Computer Program for LMFR Core Disruptive Accident Analysis," JAEA-Research 2019-009 (2020) 382p.

11) S. Kondo, et al.: "Phase 2 Code Assessment of SIMMER-III, A Computer Program for LMFR Core Disruptive Accident Analysis," JNC TN9400 2000-105 (2000) 777p.

12) K. Morita, et al.: "SIMMER-III Analytic Equation-of-State Model," JNC TN9400 2000-005 (1999) 57p.

13) K. Morita, et al.: "SIMMER-III Analytic Thermophysical Property Model," JNC TN9400 2000-004 (1999) 38p.

14) K. Morita, et al.: "SIMMER–III/IV Heat- and Mass-Transfer Model -Model and Method Description-," JNC TN9400 2003-047 (2003) 116p.

15) K. Kamiyama, et al.: "SIMMER-III Structure Model - Model and Method Description -," JNC TN9400 2004-043 (2004) 94p.

16) D. J. Brear, et al.: “Heat Transfer Coefficients Model for SIMMER-III and SIMMER-IV,” JAEA-Research 2024-009 (2024) 134p.

17) Y. Tobita, et al.: “Multi-Phase Flow Topology and Interfacial Area Model for SIMMER-III and SIMMER-IV,” JAEA-Research 2024-010 (2024) 77p.

18) Y. Tobita, et al.: “Momentum Exchange Functions Model for SIMMER-III and SIMMER-IV,” JAEA-Research 2024-011 (2024) 39p.

19) Y. Horie and N. Shirakawa: private communications (1997).

20) D. Wilhelm: “AFDM: An Advanced Fluid Dynamics Model, Volume II: Topologies, Flow Regimes, and Interfacial Areas,” Los Alamos National Laboratory, LA-11692-MS, Vol. II (1990).

21) M, Ishii: “Thermo-Fluid Dynamics Theory of Two-Phase Flow,” Eyrolles, Paris (1975).

22) J. Berthier, et al.: “AFDM: An Advanced Fluid Dynamics Model, Volume III: AFDM Heat-Transfer and Momentum-Exchange Coefficients,” Los Alamos National Laboratory, LA-11692-MS, Vol. III (1990).

23) M. Ishii and N. Zuber: “Drag coefficient and Relative Velocity in Bubbly, Droplet or Particulate Flows,” AIChE J., Vol. 25, pp.843-855 (1979).

24) T. Ueda: “On the Upward Flow of Gas-Liquid Mixture in a Pipe,” Nihon-kikai-gakkai ronbunsyu (in Japanese), Vol.33, No.248, pp.601-625, (1967).

25) T. Suzuki, et al.: “Analysis of Gas–Liquid Metal Two-Phase Flows Using a Reactor Safety Analysis Code SIMMER-III,” Nuclear Engineering and Design, Vol. 220, pp. 207-223 (2003).

26) W. R. Bohl, et al.: “AFDM: An Advanced Fluid Dynamics Model, Volume IV: The AFDM Heat and Mass-Transfer Solution Algorithm,” Los Alamos National Laboratory, LA-11692-MS, Vol. IV (1990).

27) G. Berthoud and B. Duret: “The freezing of molten fuel: reflections and new results,” 4th Topical Meeting on Nuclear Reactor Thermal-hydraulics (NURETH-4), Karlsruhe, Germany, 1989.

28) K. Kamiyama: “Improvement of SIMMER-Ill Freezing Model - A Study on a Semi-empirical Correlation for the Supercooling Temperature at the Melt/Structure Interface -,” JNC TN9400 2003-039 (2003) 46p.

29) G. Berthoud: “Relocation of molten fuel: determination of the interfacial resistance,” Proc. IAEA/IWGFR Technical Committee Meeting on Material-Coolant Interactions and Material Movement and Relocation in Liquid Metal Fast Reactors, Oarai, Japan, June 6–9, (1994).

30) D. J. Brear: private communications (1997).

31) K. Kamiyama, et al.: “Establishment of Freezing Model for Reactor Safety Analysis,” J. Nucl. Sci. and Technol. Vol. 43, No. 10, pp.1206-1217 (2006).

32) K. Kamiyama, et al.: “Experimental Studies on the Upward Fuel Discharge for Elimination of Severe Recriticality During Core-Disruptive Accidents in Sodium-Cooled Fast Reactors,” Journal of Nucl. Sci. and Technol., Vol. 51, No. 9, pp.1114-1124 (2014).

33) J. Toyooka, et al.: “SIMMER-III Analysis EAGLE-1 In-Pile Tests Focusing on Heat Transfer from Molten Core Material to Steel-Wall Structure,” NTHAS7: The Seventh Korea-Japan Symposium on Nuclear Thermal Hydraulics and Safety, Chuncheon, Korea, November 14-17, (2010).

34) J. Toyooka, et al.: “Improvements to the SIMMER Code Model for Steel Wall Failure Based on EAGLE-1 Test Results,” NTHAS10: The Tenth Korea-Japan Symposium on Nuclear Thermal Hydraulics and Safety, Kyoto, Korea, November 27-30, (2016).

35) H. Yamano, private communications (2002).

36) H. Yamano, et al.: “Development of Multi-Node Can Wall Model for SIMMER-III/IV,” JAEA-Research 2007-054 (in Japanese) (2007) 89p.

37) T. Cadiou: private communications (2000).

38) I. Sato, et al.: “Transient Fuel Behavior and Failure Condition in the CABRI-2 Experiments,” Nucl. Tech., Vol. 145 (2004).

39) G. Bandyopadhyay: “Fuel and Fission Gas Response to Simulated Thermal Transients: Experimental Results and Correlation with Fission Gas Release and Swelling Model,” Nucl. Tech., Vol.40, pp.62-78, 1978.

40) S. A. Wright, et al.: “In-Pile Determination of Fuel Disruption Mechanisms under LMFBR Loss-of-Flow Accident Conditions,” Nucl. Tech., Vol.71, pp.326-340, (1985).

41) O. D. Slagle: “Experiments on Melting and Gas Release Behavior of Irradiated Fuel,” Hanford Engineering Development Laboratory report, HEDL-TME 74-17 (1974).

42) E. T. Weber, et al.: “Laboratory Studies of Melting and Gas Release Behavior of Irradiated Fuel,” Proc. Fast Reactor Safety Meeting, Beverly Hills, CA, U. S. A., pp.2-4 (1974).

43) G. Henneges and S. Kleinheins: “AFDM: An Advanced Fluid Dynamics Mode Volume VI: EOS-AFDM Interface,” Los Alamos National Laboratory, LA-11692-MS, Vol. VI (1994).

44) E. A. Fischer: “Fuel Equation of State Data for Use in Fast Reactor Accident Analysis Codes,” Kemforschungszentrum Karlsruhe, KfK 4889 (1992).

45) E. A. Fischer: “A New Evaluation of the Urania Equation of State Based on Recent Vapor Pressure,” Nucl. Sci. Eng. Vol.101, pp.97-116 (1989).

46) K. D. Lathrop and F. W. Brinkley: “TWOTRAN-II: An Interfaced, Exportable Version of the TWOTRAN Code for Two-Dimensional Transport,” Los Alamos Scientific Laboratory, LA-4848-MS (1973).

47) R. E. Alcouffe, et al.: “User's Guide for TWODANT: A Code Package for Two-Dimension, Diffusion-Accelerated, Neutral-Particle Transport,” Los Alamos National Laboratory, LA-10049-M, Rev. 1 (1984).

48) G. Buckel, et al.: “A new SIMMER-III Version with Improved Neutronics Solution Algorithms,” Forschungszentrum Karlsruhe report FZKA 6290 (1999).

49) RSICC COMPUTER CODE COLLECTION, DANTSYS 3.0, One-, Two-, and Three-Dimensional, Multigroup, Discrete Ordinates Transport Code System, contributed by: Los Alamos National Laboratory, Los Alamos, New Mexico, (1995).

50) G. I. Bell, G. E. Hansen, and H. A. Sandmeier: “Multiple Treatment of Anisotropic Scattering in Sn Multigroup Transport Calculations,” Nucl. Sci. Eng. 28, 376 (1967).

51) F. Parker, M. Ishikawa, and L. Luck: “MXS Cross-Section Preprocessor User's Manual,” Los Alamos National Laboratory, LA-10856-M, NUREG/CR-4765 (1987).

52) K. O. Ott and D. A. Meneley: “Accuracy of the Quasistatic Treatment of Spatial Reactor Kinetics,” Nucl. Sci. and Eng. Vol.36(3), pp.402-411 (1969).

53) R. E. Alcouffe: “Diffusion Synthetic Acceleration Methods for the Diamond-Difference Discrete-Ordinates Equations,” Nucl. Sci. Eng. Vol.64(2), pp.344-355 (1977).

54) K. D. Lathrop: “Spatial Differencing of the Transport Equation: Positivity vs Accuracy,” J. Comp. Phys. Vol.4(4), pp.475-498 (1969).

55) L. B. Luck: “An Improved Quasistatic Method for Transition-Phase Calculations,” Transactions of the American Nuclear Society, Vol.41, pp.317-318 (1982).

56) J. E. Cahalan, et al.: “The SAS4A/SASSYS-1 Safety Analysis Code System Chapter 4: Reactor Point Kinetics, Decay Heat, and Reactivity Feedback,” Argonne National Laboratory, ANL/NE-16/ (2016).

57) H. Tagami, S. Ishida and Y. Tobita: “Development of New Treatment of Fuel Isotope Vector in the Core Disruptive Accident Analysis of Fast Reactors,” J. Nucl. Sci. and Technol., Vol. 60 (12), pp. 1548-1562 (2023).

58) T. G. Theofaous and C. R. Bell: “An Assessment of CRBR Core Disruptive Accident Energetics,” Los Alamos National Laboratory, NUREG/CR-3224, LA-9716-MS (1984).

59) N. Shirakawa, et. al.: private communications (2000).

Nomenclature

Symbols

A_M	Convectible interfacial area per unit volume of energy component *M* associating the relevant interfacial area (m^{-1})
$A_{M,B}, A_{M,D}$	Convectible interfacial areas per unit volume of component *M* in bubbly and dispersed regions (m^{-1})
$A_{M,B\rightarrow D}, A_{M,D\rightarrow \mathrm{B}}$	Convectible interfacial area diffusion terms between bubbly and dispersed regions (m^{-1})
$A_{qq'}$, $B_{qq'}$	Laminar and turbulent terms of momentum exchange function between velocity fields q and q'
A_{qS} , B_{qS}	Laminar and turbulent terms of momentum exchange function between velocity field q and structure
a	Binary contact area per unit volume, structure surface area per unit volume (m^{-1})
a	Radius of discrete contact points between crust and structure (m)
$a_{C,D}$	Interfacial area between continuous and discontinuous (dispersed) phases (m^{-1})
$a_{qq'},\ b_{qq'}$	Parameters of momentum exchange function between velocity fields q and q'
$a_{qS},\ b_{qS}$	Parameters of momentum exchange function between velocity field q and structure
b	Separation distance of contact points between crust and structure (m)
C_{ORF}	Orifice pressure drop coefficient for lateral fluid flow
C_d	Drag coefficient based on Ishii's drag similarity hypothesis
C_d, c_d	Delayed neutron precursor concentration for precursor group *d* (m^{-3})
C_G	Virtual mass coefficient
CV	Convective term
c	Specific heat (J kg^{-1} K^{-1})
c_p	Specific heat capacity at constant pressure (J kg^{-1} K^{-1})
c_{Sat}	Specific heat capacity along a saturation curve (J kg^{-1} K^{-1})
c_v	Specific heat capacity at constant volume (J kg^{-1} K^{-1})
$D_{e_{G,ikj}}$	Residual error in vapor internal energy with pressure-volume work term in Step 3 pressure iteration (J m^{-3} s^{-1})
D_h	Hydraulic diameter (m)
$D_{m,ikj}$	Residual errors in mass conservation in Step 3 pressure iteration (kg m^{-3} s^{-1})
E	Neutron energy (J)
e	Specific internal energy (J kg^{-1})
F	Total effective neutron source
F_{ijd}^{d}	Delayed neutron precursor shape

f	Resonance self-shielding factor
f_c	Melt fraction of cladding
$f_{cr,stab}$	Factor to adjust the minimum stable crust thickness depending on the surface shape
f_{CW}	Melt fraction of can wall
f_l	Factor to adjust the heat-transfer area between two cells having different volume fractions in the inter-cell heat transfer
$f_{M,n}$	Mass fraction of isotope *n* included in fuel component *M* in the Pu-vector model
$f_{x,ijg}^{i}$	Shielding factor for isotope *i* for reaction type *x*
Gr	Grashof number
$\boldsymbol{g}$	Acceleration by gravity (m s^{-2})
$g(\xi)$	Parameter to represent the effect of multiple contact points
$\mathrm{H}(x)$	Heaviside unit function (=1 if x>0, =1/2 if x=0, =0, if x<0)
H	Heat transfer coefficient (W m^{-2} K^{-1})
H_P	Rigid particle internal heat transfer coefficient (W m^{-2} K^{-1})
H_{FP}	Fluid particle (droplet or bubble) internal heat transfer coefficient (W m^{-2} K^{-1})
H_{CPP}	Heat transfer coefficient in a continuous phase fluid to a particle (W m^{-2} K^{-1})
H_{CPS}	Heat transfer coefficient in a continuous phase fluid to structure (W m^{-2} K^{-1})
H_{AFS}	Heat transfer coefficient from a liquid film to structure (W m^{-2} K^{-1})
H_{DPS}	Heat transfer coefficient in a droplet or solid particle to structure (W m^{-2} K^{-1})
H_{DF}	Heat transfer coefficient between moving droplets in dispersed flow (W m^{-2} K^{-1})
H_{FB}	Film boiling heat transfer coefficient (W m^{-2} K^{-1})
h	Heat transfer coefficient (W m^{-2} K^{-1})
h	Specific enthalpy (J kg^{-1})
h_{Con}/h_{Vap}	Effective latent heat of condensation/vaporization (J kg^{-1})
h_f	Heat of fusion (J kg^{-1})
h_g^*	Effective mass-transfer coefficient, in the presence of mass transfer (kg m^{-3} s^{-1})
h_{IR}	Heat-transfer coefficient with interface resistance (W m^{-2} K^{-1})
$h_{IR,c-s}$	Interface resistance heat-transfer coefficient between crust and structure (W m^{-2} K^{-1})
$h_{IR,s}$	Structure-side heat-transfer coefficient with interface resistance (W m^{-2} K^{-1})
$h_{IR,scl}$	Liquid-side heat-transfer coefficient with interface resistance (W m^{-2} K^{-1})
h_L	Liquid-side heat-transfer coefficient (W m^{-2} K^{-1})
h_{lg}	Heat of vaporization (J kg^{-1})
h_n	Normalized decay heat energy fraction, defined as the precursor concentration times energy release for decay heat
$h_n(0)$	Initial normalized decay heat energy fraction

h_s	Structure-side heat-transfer coefficient (W m^{-2} K^{-1})
$h_{scl-s,sum}$	Overall heat-transfer coefficient between liquid and structure (W m^{-2} K^{-1})
IGD	Number of delayed neutron precursor groups
i	Specific enthalpy (J kg^{-1})
i_{lg}	Latent heat of vaporization (J kg^{-1})
K	Thermal conductivity (W m^{-1} K^{-1})
$K_{qq'}$	Momentum exchange function between velocity fields q and q' (kg m^{-3} s^{-1})
K_{qS}	Momentum exchange function between velocity field q and structure (kg m^{-3} s^{-1})
k_0	Initial stationary k-effective for the reactor system
k_B	Boltzmann's constant (J K^{-1})
k_k^*	Effective heat-transfer coefficient, in the presence of mass transfer (W m^{-2} K^{-1})
$LNISIP$	Total number of isotopes
l	Mixing length (m)
$N(0)$	Initial value of the amplitude function (=1.0)
N	Avogadro's number
N, N_f	Normalized fission power amplitude
N_c	Number of discrete contact points per unit surface area (m^{-2})
N_f^0	Steady-state reactor power amplitude before transient ($t < 0$)
N_f	Normalized fission power amplitude
N_h	Normalized decay heat power amplitude
N_i	Atom number density of isotope i (m^{-3})
$\hat{N}_{ij}^{i}$	Total atom number density of isotope i for mesh cell ij (m^{-3})
N_{ij}^{im}	Atom number density of isotope i in component m for mesh cell ij (m^{-3})
NC	Number of neutronics materials (fertile fuel, fissile fuel, steel, sodium and control)
$NNMAT$	Number of material mixtures used to compute the neutron flux: fertile fuel, fissile fuel, steel, sodium, and control
Nu	Nusselt number
P	Reactor power (W)
P_f	Total fission power (W)
P_h	Total decay heat power (W)
P_t	Total reactor power (W)
Pe	Peclet number
Pr	Prandtl number
p	Pressure (Pa)
p_{cell}	Cell pressure (Pa)

p_{EOS}	EOS pressure (Pa)
Q_{IC}	Specific internal energy source due to inter-cell heat transfer (W kg^{-1})
$Q_H(h, a, \Delta T)$	Specific internal energy source due to heat transfer (h: heat-transfer coefficient, a: binary contact area, ΔT: temperature difference) (W kg^{-1})
$Q_M(\Gamma_M)$	Specific internal energy source due to mass transfer (W kg^{-1})
Q_N	Specific internal energy source due to nuclear heating (W kg^{-1})
Q_{Nm}	Specific power (internal energy generation rate) for material *m* (W kg^{-1})
$\hat{Q}_{Nm}$	Specific power adjusted for decay heat contribution for material *m* (W kg^{-1})
q	Heat transfer rate, heat flux (W m^{-2})
$\boldsymbol{q}_{c,M}$	Heat fluxes in intra-cell heat transfer (W m^{-2})
R	Radius of fluid particle (solid particle, droplet, bubble) (m)
R	Gas constant (J kg^{-1} K^{-1})
R	Correction factor to take into account the effects of noncondensable gases and multicomponent mixture
R_k	Correction factor to account for diffusion-limited mass transfer behavior
R_{SS}	Thermal resistance of a single contact point (W^{-1} m^2 K)
Re	Reynolds number
r	Radius, radial direction (m)
r	Spatial coordinates, (r, z) for 2D or (x, y, z) for 3D
(r, z)	Radial and axial coordinates in 2D
(r, θ, z)	Radial, azimuthal and axial coordinates in 3D
S, s	External neutron source
S_f	Multiplication factor to determine effective particle viscosity
$S_{M,k}$	Interfacial area source term of interface *M* for mechanism *k* (m^{-1} s^{-1})
SS	Stainless steel
T	Temperature (K)
T_t	Normalized total power
T_f	Normalized fission power
T_h	Normalized decay heat power
T_G	Vapor temperature (K)
T^I	Instantaneous contact interface temperature without phase transition (K)
T^I_{con}	Instantaneous contact interface temperature between melt and structure (K)
T^I_{scl}	Temperature of supercooling layer (K)
$\bar{T}^i_{ij}$	Average temperature of isotope *i* in each mesh cell *ij* (K)
$\bar{T}^m_{ij}$	Average temperature of component m in each mesh cell *ij* (K)
t	Time (s)

x	Reaction type
u, v	Radial and axial velocities in 2D (r, z) cylindrical geometry (m s^{-1})
u, w, v	Velocities in three directions in 3D (x, y, z) rectangular geometry (m s^{-1})
V_q	Velocity of field q, representing either u, w or v (m s^{-1})
V_g	Average neutron velocity in energy group g (m s^{-1})
V_{ij}	Volume of mesh cell ij (m^3)
$\boldsymbol{v}_q$	Velocity (vector) of velocity field q (m s^{-1})
$\boldsymbol{VM}_q$	Virtual mass term (vector) for velocity field q
W	Pressure-volume work term (J)
W	Molecular weight (kg mol^{-1})
W	Thickness of liquid film, crust or can wall (m)
$W_{cr,min}$	Minimum stable crust thickness (m)
$W_{cr,min}^{in}$	User-specified minimum stable crust thickness on a flat surface (m)
ω_m	Solid angle (area) of angular discrete-ordinate m
X	Addition to the liquid equations when the vapor pressure-volume work term is zero
X	Fraction left as solid cladding or can wall after structure breakup
(x, z)	Cartesian (rectangular) coordinates in 2D geometry
(x, y, z)	Cartesian (rectangular) coordinates in 3D geometry
z_c	Critical compressibility

Greek symbols

α	Volume fraction, void fraction
α	Thermal diffusivity (m^2 s^{-1})
α_0	Minimum vapor volume fraction (default: 10^{-3})
α_G	Vapor volume fraction ($= 1 - \alpha_S - \alpha_L$)
$\alpha_{ge}, \alpha_{G,eff}$	Effective vapor volume fraction ($= \max[\alpha_0(1 - \alpha_S), 1 - \alpha_S - (1 - \alpha_0)\alpha_L]$)
α_L	Liquid volume fraction
α_p	Volumetric thermal expansion coefficient (K^{-1})
α_S	Structure volume fraction
α_c^m	Energy conversion factor per neutron captured in material m
α_f^m	Energy conversion factor per fission in material m
β	Thermal expansion coefficient
β	Total effective delayed neutron fraction
β_{CW}	Fraction of can wall area available for lateral fluid flow
β_d	Effective delayed neutron fraction for delayed neutron group d

β_{hn}	Effective decay heat power fraction in decay heat group *n*
β_{ht}	Total effective decay heat power fraction in decay heat group *n* (optional input)
β_S	Adiabatic compressibility (Pa^{-1})
β_T	Isothermal compressibility (Pa^{-1})
Γ_m	Mass-transfer rate per unit volume from component *m* (kg m^{-3} s^{-1})
γ	Calculated value of the constant used in the quasistatic method to separate the neutron flux into amplitude and shape functions, calculated quasistatic constraint
ΔE_r	Net energy outflow for component *r* (J)
ΔM_m	Net mass outflow for component *m* (kg)
ΔT_{con}	Supercooling temperature with no phase transition (K)
ΔT_{sc}	Supercooling temperature (K)
Δt	Time step size (s)
δ_{lm}	Kronecker delta operator
$2\delta_M$	Thermal penetration length of structure material *M* (m)
ε_{ikj}	Residual error in pressure in Step 3 pressure iteration (Pa)
ε_v	Convergence precision for the velocity iterations in Steps 2 and 4
ϵ_p	Convergence criterion for residual error in pressure in Step 3 pressure iteration
ϵ_T	Convergence criterion for residual error in vapor internal energy in Step 3 pressure iteration
ϵ_ρ	Convergence criterion for residual error in mass conservation in Step 3 pressure iteration
ζ	Coordinate indicator (=1 for cylindrical geometry, =0 for rectangular geometry)
Θ_q	Interfacial energy production per unit mass for an energy component belonging to momentum field *q* (W kg^{-1})
κ	Thermal conductivity (W m^{-1} K^{-1})
κ	Viscosity ratio: $\kappa = \mu_{dp}/\mu_{cp}$
$\kappa_{T,M}$	Turbulent thermal conductivity evaluated by Prandtl's mixing length theory (W m-1 K-1)
Λ	Neutron generation time (s)
λ, τ, θ	Spatial indexes ($\lambda+= (i+1/2,k,j)$, $\tau+= (i,k+1/2,j)$, $\theta+= (i,k,j+1/2)$)
λ_d	Decay constant for delayed neutron precursor group *d* (s^{-1})
λ_{hn}	Decay constant for decay heat for decay heat group *n* (s^{-1})
μ	Viscosity (Pa s)
μ_q	Mixture viscosity of velocity field *q* (Pa s)
ν	Kinematic viscosity (m^2 s^{-1})
ν_d	Delayed neutron yield per fission
ν_d^i	Isotope-wise delayed neutron yield per fission

ν_f	Total neutron yield per fission ($\nu_f = \nu_p + \nu_d$)
ν_p	Prompt neutron yield per fission
ν_S	Speed of sound (m s^{-1})
ξ	Spatial index representing either λ, τ or θ
ξ	Ratio of a contact point radius to separation distance
ρ	Microscopic (EOS) density
ρ	Ratio of discrete contact point radius to separation distance
$\bar{\rho}$	Macroscopic (smeared) density (kg m^{-3})
Σ_x	Macroscopic cross section of reaction type *x*
σ	Surface tension (kg m^{-2})
σ	Microscopic cross section
$\bar{\sigma}$	Effective self-shielded microscopic cross section
σ_0	Background cross section
$\sigma_{x,g}^{i}$	Infinitely-dilute cross section of reaction type *x* for isotope *i* (input)
τ_{str}	Time constant of structure thermal response (s^{-1})
τ_{ij}^{c}	Contact timescale for droplet components *i* and *j* in dispersed flow (s)
$\bar{\boldsymbol{\tau}}_q$	Viscous stress tensor used to calculate viscous drag terms
υ	Specific volume ($= 1/\rho$) (m^3 kg^{-1})
Φ	Neutron scalar flux (m^{-2})
Φ^*	Integrated adjoint neutron flux
ϕ	Phase (single or two)
ϕ	Scalar flux shape function
χ_d	Delayed neutron emission spectrum from delayed neutron precursor group *d*
χ_p	Prompt neutron fission emission spectrum
Ψ	Angular neutron flux per unit volume
ψ	Angular flux shape function
$\vec{\Omega}$	Angular direction of motion
ω	Mass fractions of vapor species
ω_m	Solid angle (area) of angular discrete-ordinate *m*

Superscripts and subscripts

B	Bubbly region, bubbly flow regime
BR	Mass transfer due to structure breakup
C, c, CP, cp	Continuous phase
Con	Saturated liquid (condensate)
CP	Continuous phase

Crt	Critical point
c, cr	Crust, crusted region
c	Capture
cd	Between continuous and discontinuous (dispersed) phases
cS	Between continuous phase and structure
D	Dilute vapor
D, d	Discontinuous phase, dispersed region, dispersed flow regime
d	Delayed neutron group
dS	Between discontinuous phase and structure
EQ	Equilibrium mass transfer
f	Fission
G, g	Vapor mixture, vapor phase, gas, vapor state
g	Neutron energy group
h	Decay heat group
I	Interface quantity
IC	Internal circulation of fluid particle
IC	Inter-cell heat transfer
IR	Interface resistance
i	Isotope
ij	Fluid-dynamics mesh cell index, (*i, j*) for 2D or (*i, k, j*) for 3D
ikj	Fluid-dynamics mesh cell index, (*i, k, j*) for 3D geometry
ij	Neutronics mesh cell index, (*i, j*) for 2D or (*i, k, j*) for 3D
ijg	Neutronics mesh cell and energy group indexes
k	Iteration index
L, l	Liquid component, liquid state
Liq	Liquidus point
M	Energy component, vapor material
m	Density component, material, component
m	Melting point
NE	Non-equilibrium mass transfer
n	Beginning of time step, previous time step
n+1	End of time step, current time step
nocr	Noncrusted region
OS	Oscillation of fluid particle
p	Particle
p	Prompt neutron

q	Velocity field (momentum component)
qq'	Between velocity fields q and q'
qS	Between velocity field q and structure
REL	Fission gas release
S, s	Structure component, solid state
SS	Structure surface
Sat	Saturation
Sol	Solidus point
s	Scattering
sc	Supercooling temperature
scl	Supercooling layer
$tran$	Transition flow regime
Vap	Saturated vapor
t	Total
$+$	No pressure dependence

This is a blank page.